

*K. Tausch*

DISS. ETH No. 9808

and report of the Institute for Intermediate Energy Physics (ETHZ)

**ISOSPIN MASS SPLITTING OF THE  $K^*(892)$  MESON**

A dissertation submitted to the  
**SWISS FEDERAL INSTITUTE OF TECHNOLOGY ZURICH**

for the degree of

**Doctor of Natural Sciences**

presented by

Christian Bula  
dipl. phys., ETHZ  
born November 7, 1961  
citizen of Kerzers FR, Switzerland

accepted on the recommendation of

Prof. Dr. H.-J. Gerber examiner

PD Dr. T. Nakada co-examiner

1992

Thesis-1992-Bula

CERN LIBRARIES, GENEVA

DISS. ETH No. 9808

and report of the Institute for Intermediate Energy Physics (ETHZ)

**ISOSPIN MASS SPLITTING OF THE  $K^*(892)$  MESON**

A dissertation submitted to the  
**SWISS FEDERAL INSTITUTE OF TECHNOLOGY ZURICH**

for the degree of

**Doctor of Natural Sciences**

CERN LIBRARIES, GENEVA



CM-P00081064

presented by

Christian Bula  
dipl. phys., ETHZ  
born November 7, 1961  
citizen of Kerzers FR, Switzerland

accepted on the recommendation of

Prof. Dr. H.-J. Gerber    examiner

PD Dr. T. Nakada        co-examiner

1992

To my family

Silke, Jonas and Linda

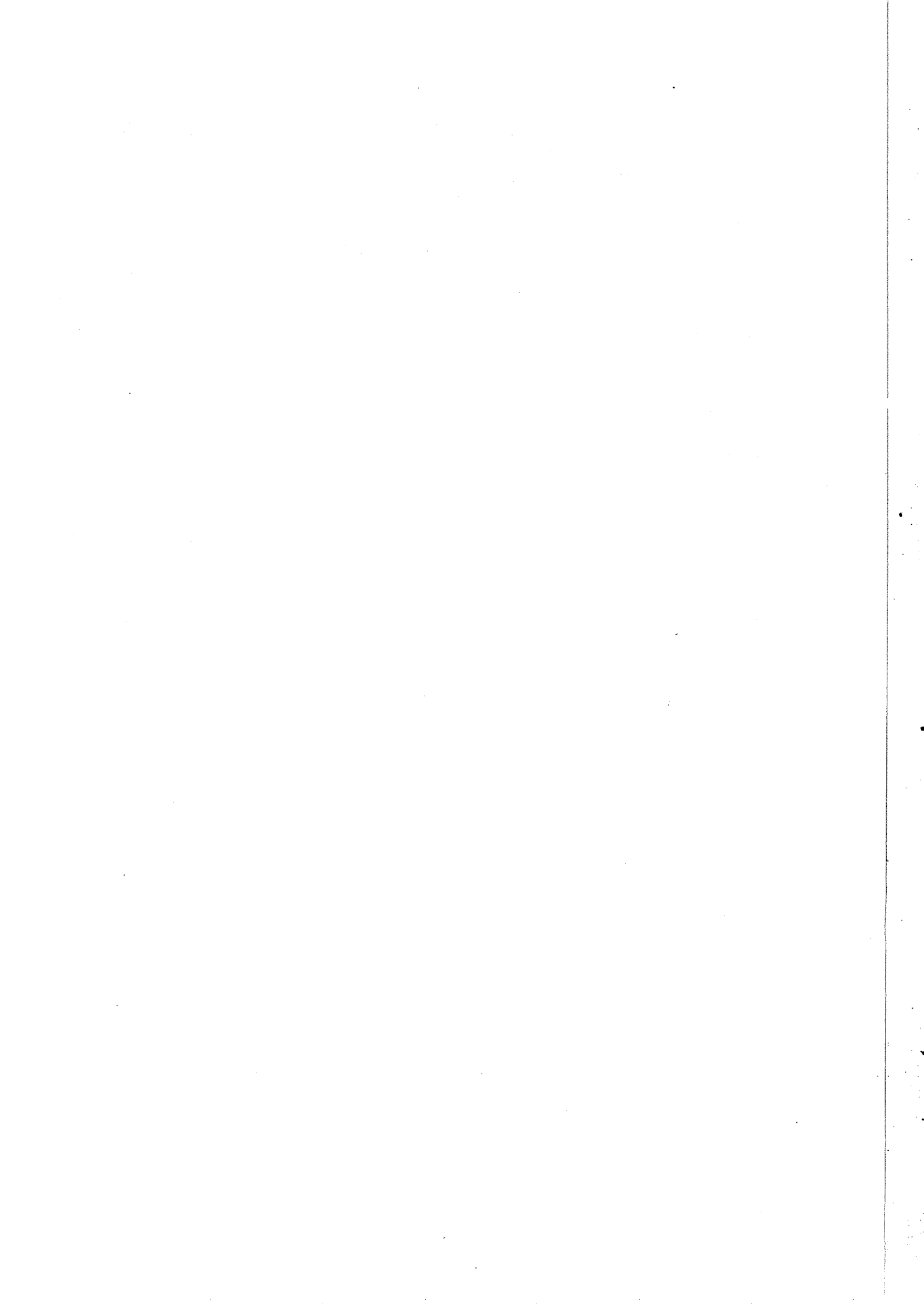


# Contents

<b>Abstract</b>	<b>1</b>
<b>Zusammenfassung</b>	<b>2</b>
<b>1 Introduction</b>	<b>3</b>
<b>2 CP Violation and the CPLEAR Experiment</b>	<b>5</b>
2.1 CP Violation in the Standard Model . . . . .	5
2.2 Phenomenology of CP Violation in the Neutral Kaon System . . . . .	7
2.3 The CPLEAR Experiment . . . . .	12
2.3.1 Decays into two Pions . . . . .	13
2.3.2 Decays into three Pions . . . . .	14
2.3.3 Semileptonic Decays . . . . .	14
2.4 The CPLEAR Detector . . . . .	16
<b>3 The Proportional Chambers PC1 and PC2</b>	<b>27</b>
3.1 Principle of Operation of Proportional Chambers . . . . .	27
3.2 Geometry of PC1 and PC2 . . . . .	31
3.3 Gas Mixture . . . . .	32
3.4 Materials Used in the Construction . . . . .	34
3.5 Construction of PC1 and PC2 . . . . .	36
3.6 Installation in the CPLEAR Detector . . . . .	42
3.6.1 Expected Sag of the Proportional Chambers . . . . .	44
3.7 Readout of the Wire Information . . . . .	46
3.7.1 The Cluster Processors . . . . .	46
3.7.2 Control of the Cluster Processors . . . . .	48
3.8 Performance . . . . .	48
3.8.1 Gas Amplification . . . . .	48
3.8.2 Chamber Efficiency . . . . .	52
3.8.2.1 Source Test Setup . . . . .	52
3.8.2.2 Beam Test Setup . . . . .	53
3.8.2.3 Anode Wire Efficiency Curve for two Gas Mixtures . . . . .	56
3.8.2.4 Cathode Strip Efficiency Curve . . . . .	57
3.8.2.5 Rate Dependence of Plateau Efficiency . . . . .	58
3.8.2.6 Inefficiency due to Wire Supports . . . . .	58
3.8.2.7 Efficiency of PC1 and PC2 for Run Periods 8 and 9 . . . . .	59
3.8.3 Spatial Resolution . . . . .	60
<b>4 Isospin Mass Splitting of the <math>K^*</math> (892) Meson</b>	<b>62</b>
4.1 Physics Motivation . . . . .	62
4.2 Event Selection . . . . .	66
4.2.1 Event Type . . . . .	67
4.2.2 Data Filtering . . . . .	68

4.2.2.1	The FILTER7 and the KAON4T . . . . .	69
4.2.2.2	The PREFILTER . . . . .	70
4.2.2.3	The 5CFIT . . . . .	71
4.2.3	Presentation of the Selected Data . . . . .	72
4.2.4	Background Analysis . . . . .	77
4.2.4.1	Semileptonic and three Pion Decays of $K_L^0$ . . . . .	77
4.2.4.2	Additional $\pi^0$ from the $p\bar{p}$ Annihilation . . . . .	78
4.2.4.3	Particle Misidentification . . . . .	79
4.3	Parameterization of the Dalitz-Plot Density . . . . .	80
4.3.1	Expansion of the Conforto-Model to P-Wave Annihilations . . . . .	82
4.3.1.1	Symmetry Properties of the Transition Amplitudes . . . . .	84
4.3.1.2	Partial Wave Decomposition and Separation of the Angular Variables . . . . .	85
4.3.1.3	The Spin-Parity Factors . . . . .	87
4.3.1.4	The Form Factors . . . . .	88
4.3.1.5	Dalitz-Plot Parameterization with the Conforto-Model . . . . .	89
4.3.2	Simplified Parameterization of the Dalitz-Plot Density . . . . .	91
4.4	Estimation of the Detector and Filter Acceptance . . . . .	95
4.5	Fit Results . . . . .	98
4.5.1	Least-Squares Fits . . . . .	98
4.5.2	The Method of Maximum Likelihood . . . . .	101
4.5.2.1	An Example of a Distribution Function . . . . .	103
4.5.2.2	Results for the Resonance Parameters . . . . .	106
4.5.3	Mean Value and Error Analysis for the $K^*$ Mass Difference . . . . .	108
4.5.3.1	Mean Value for the $K^*$ Mass Difference and Uncertainty due to the Parameterization . . . . .	108
4.5.3.2	Statistical Error and Correlations . . . . .	109
4.5.3.3	Uncertainty due to the Acceptance Function . . . . .	114
4.5.3.4	Effect of a Different Breit-Wigner Parameterization . . . . .	115
4.5.4	Result for the Isospin Mass Splitting of the $K^*$ (892) Meson . . . . .	117
<b>5</b>	<b>Conclusion</b> . . . . .	<b>120</b>
<b>A</b>	<b>The Kinematic Fit</b> . . . . .	<b>121</b>
A.1	Principle of Least Squares Fits with Constraints . . . . .	121
A.2	Application to "Golden $\pi^+\pi^-$ " Event Selection . . . . .	123
A.3	Improvement of the Measured Variables . . . . .	124
<b>B</b>	<b>The Simulated Data Samples</b> . . . . .	<b>128</b>
B.1	Data Samples Produced with CPGEANT . . . . .	128
B.2	The Simplified Simulation Program . . . . .	129
<b>C</b>	<b>The Amplitudes Contributing to the Reaction <math>p\bar{p} \rightarrow K\bar{K}\pi</math></b> . . . . .	<b>134</b>
C.1	Contributions to $A_0^{0-+}$ (initial $p\bar{p}$ state is $^1S_0$ ) . . . . .	134
C.2	Contributions to $A_1^{0-+}$ (initial $p\bar{p}$ state is $^3S_0$ ) . . . . .	135

C.3	Contributions to $A_0^{1--}$ (initial $p\bar{p}$ state is $^{13}S_0$ ) . . . . .	135
C.4	Contributions to $A_1^{1--}$ (initial $p\bar{p}$ state is $^{33}S_1$ ) . . . . .	136
C.5	Contributions to $A_0^{1+-}$ (initial $p\bar{p}$ state is $^{11}P_1$ ) . . . . .	136
C.6	Contributions to $A_1^{1+-}$ (initial $p\bar{p}$ state is $^{31}P_1$ ) . . . . .	137
C.7	Contributions to $A_0^{1++}$ (initial $p\bar{p}$ state is $^{13}P_1$ ) . . . . .	138
C.8	Contributions to $A_1^{1++}$ (initial $p\bar{p}$ state is $^{33}P_1$ ) . . . . .	138
C.9	Contributions to $A_0^{2++}$ (initial $p\bar{p}$ state is $^{13}P_2$ ) . . . . .	139
C.10	Contributions to $A_1^{2++}$ (initial $p\bar{p}$ state is $^{33}P_2$ ) . . . . .	139
<b>References</b>		<b>141</b>
<b>List of Figures</b>		<b>143</b>
<b>List of Tables</b>		<b>145</b>
<b>Curriculum Vitae</b>		<b>146</b>
<b>Acknowledgments</b>		<b>147</b>





## Abstract

The CPLEAR experiment at CERN is designed to study CP violation in the neutral kaon system.  $K^0$  and  $\bar{K}^0$  are produced in  $p\bar{p}$  annihilations at rest through the reactions  $p\bar{p} \rightarrow K^-\pi^+K^0$  and  $p\bar{p} \rightarrow K^+\pi^-\bar{K}^0$ . The strangeness of the neutral kaon is determined by identifying the charged kaon. The parameters describing CP violation are extracted from the asymmetries between the decay rates of initially pure  $K^0$  and  $\bar{K}^0$  states into a given final state.

The contribution of the PSI group to the CPLEAR detector are the two multi wire proportional chambers (PC1 and PC2). The two chambers were constructed successfully and thorough tests showed good performance. The efficiency for charged particles to be detected in PC1 and/or PC2 is

$$\eta_{(\text{PC1 or PC2})} = 99.5\% .$$

The spatial resolution of a chamber amounts to

$$\sigma_{r\varphi} = (336 \pm 6) \mu\text{m} .$$

A substantial fraction of the annihilations  $p\bar{p} \rightarrow K^\mp\pi^\pm K^0(\bar{K}^0)$  proceeds through an intermediate  $K^*(892)$  meson, i.e.  $p\bar{p} \rightarrow K\bar{K}^*$  ( $\bar{K}K^*$ ). In this work, 33'132 events of the type  $p\bar{p} \rightarrow K^\mp\pi^\pm K^0(\bar{K}^0)$  are used to determine the mass splitting between the neutral and charged modes of the  $K^*(892)$  meson. This search is stimulated by the systematic discrepancy in the mass difference for different experiments, measuring either only  $K^{*\pm}$  or  $K^{*0}(\bar{K}^{*0})$ , or both  $K^{*\pm}$  and  $K^{*0}(\bar{K}^{*0})$  simultaneously. The value for the  $K^*$  mass splitting is found to be

$$\Delta m_{K^*} \equiv m_{K^{*0}} - m_{K^{*\pm}} = (4.4 \pm 1.7) \text{ MeV}/c^2 ,$$

in excellent agreement with the difference between the world averages of the individual  $K^*$  masses,  $\langle m_{K^{*0}} \rangle - \langle m_{K^{*\pm}} \rangle = (4.27 \pm 0.37) \text{ MeV}/c^2$ , and lower by one standard deviation than the average of three previous measurements of  $\Delta m_{K^*}$ ,  $\langle \Delta m_{K^*} \rangle = (6.6 \pm 1.3) \text{ MeV}/c^2$ .

## Zusammenfassung

Das CPLEAR-Experiment am CERN untersucht die CP-Verletzung im System der neutralen Kaonen. Ursprünglich reine  $K^0$ - und  $\bar{K}^0$ - Zustände werden durch  $p\bar{p}$ -Annihilationen in Ruhe erzeugt,  $p\bar{p} \rightarrow K^-\pi^+K^0$  und  $p\bar{p} \rightarrow K^+\pi^-\bar{K}^0$ . Die Seltsamkeit des neutralen Kaons wird durch die Identifikation des entsprechenden geladenen Kaons bestimmt. Die Parameter der CP-Verletzung erhält man aus den Asymmetrien zwischen den Zerfallsraten von ursprünglich reinen  $K^0$ - und  $\bar{K}^0$ - Zuständen.

Die beiden Proportionalkammern PC1 und PC2 sind der Beitrag der PSI-Gruppe zum CPLEAR-Detektor. Die Kammern wurden am PSI gebaut und erfolgreich am CERN im Detektor installiert. Ausführliche Testmessungen zeigten, dass die Kammern gut funktionieren. Die Wahrscheinlichkeit, dass ein geladenes Teilchen von PC1 und/oder PC2 nachgewiesen wird ist

$$\eta_{(\text{PC1 oder PC2})} = 99.5\% .$$

Das räumliche Auflösungsvermögen einer Kammer beträgt

$$\sigma_{r\varphi} = (336 \pm 6) \mu\text{m} .$$

In einem wesentlichen Anteil der Annihilationen  $p\bar{p} \rightarrow K^\mp\pi^\pm K^0(\bar{K}^0)$  werden intermediäre  $K^*(892)$  Mesonen erzeugt, also  $p\bar{p} \rightarrow KK^*(\bar{K}K^*)$ . In dieser Arbeit wurden 33'132 Ereignisse vom Typ  $p\bar{p} \rightarrow K^\mp\pi^\pm K^0(\bar{K}^0)$  verwendet, um die Massendifferenz zwischen dem neutralen und dem geladenen Zustand des  $K^*(892)$  Mesons zu bestimmen. Die Motivation für diese neue Messung liegt in der systematischen Diskrepanz der Massendifferenz für verschiedene Experimente, die entweder nur  $K^{*\pm}$  oder  $K^{*0}(\bar{K}^{*0})$  oder beide Zustände  $K^{*\pm}$  und  $K^{*0}(\bar{K}^{*0})$  gleichzeitig messen. Der aus dieser Arbeit resultierende Wert für die Massendifferenz

$$\Delta m_{K^*} \equiv m_{K^{*0}} - m_{K^{*\pm}} = (4.4 \pm 1.7) \text{ MeV}/c^2$$

ist in guter Übereinstimmung mit der Differenz zwischen den Mittelwerten für die neutrale und geladene  $K^*$  Masse,  $\langle m_{K^{*0}} \rangle - \langle m_{K^{*\pm}} \rangle = (4.27 \pm 0.37) \text{ MeV}/c^2$ , und liegt um eine Standardabweichung tiefer als der Durchschnittswert der drei vorherigen Messungen von  $\Delta m_{K^*}$ ,  $\langle \Delta m_{K^*} \rangle = (6.6 \pm 1.3) \text{ MeV}/c^2$ .

# 1 Introduction

The origin of CP violation is one of the most fundamental and still unsolved questions in particle physics. So far, CP violation has only been observed in two-pion and semileptonic decays of the long-lived neutral kaon, i.e.

$$K_L^0 \rightarrow \pi^+\pi^- \quad (\pi^0\pi^0) \quad \text{and} \quad K_L^0 \rightarrow \pi^\pm l^\mp \nu.$$

In the standard model of electroweak interactions, the violation of CP symmetry is a consequence of the complex quark mixing matrix. However, with the present experimental data, other models suggesting different mechanisms for the breakdown of CP invariance cannot be excluded (see for example [1]). Thus, it is important to improve the precision of the parameters describing CP violation in the two-pion decay channels of the neutral kaon. In addition, other neutral kaon decay modes as well as processes outside the neutral kaon system should be searched for CP violation.

The CPLEAR experiment at CERN (PS195) uses the intense antiproton beam provided by LEAR to produce initially pure  $K^0$  and  $\bar{K}^0$  states in proton-antiproton annihilations at rest of the type

$$p\bar{p} \rightarrow K^-\pi^+K^0 \quad \text{and} \quad p\bar{p} \rightarrow K^+\pi^-\bar{K}^0.$$

In these reactions,  $K^0$  and  $\bar{K}^0$  are produced at equal rates with the same kinematics. The strangeness of the neutral kaon is identified through the observation of the accompanying charged kaon.

The intense and tagged sources of  $K^0$  and  $\bar{K}^0$  are used to measure the differential (time-dependent) and the integral (time-integrated) asymmetries between the decay rates of initially pure  $K^0$  and  $\bar{K}^0$  states into a given final state  $f$ , i.e.

$$A_f(t) \equiv \frac{R_{\bar{K}^0 \rightarrow f}(t) - R_{K^0 \rightarrow f}(t)}{R_{\bar{K}^0 \rightarrow f}(t) + R_{K^0 \rightarrow f}(t)}$$

and

$$I_f(t_0) \equiv \frac{\int_0^{t_0} R_{\bar{K}^0 \rightarrow f}(t) dt - \int_0^{t_0} R_{K^0 \rightarrow f}(t) dt}{\int_0^{t_0} R_{\bar{K}^0 \rightarrow f}(t) dt + \int_0^{t_0} R_{K^0 \rightarrow f}(t) dt},$$

where  $R_{K^0(\bar{K}^0) \rightarrow f}(t)$  is the time-dependent decay rate of  $K^0$  ( $\bar{K}^0$ ) into one of the final states  $f = \pi^+\pi^-$ ,  $\pi^0\pi^0$ ,  $\pi^+\pi^-\pi^0$ , and  $\gamma\gamma$ . This method allows the determination of CP violation parameters in two-pion decays of  $K^0$  and  $\bar{K}^0$  with different systematic errors as compared to earlier experiments.

The work of this thesis comprises two main parts, namely an instrumental work and a physics analysis:

- The construction of two multi wire proportional chambers, their installation in the CPLEAR detector and their testing.
- The physics analysis of the isospin mass splitting of the  $K^*(892)$  meson.

The resonances  $K^*(892)$  and  $a_2(1320)$  are produced as intermediate states in the reactions  $p\bar{p} \rightarrow K\bar{K}^* (\bar{K}K^*) \rightarrow K\bar{K}\pi$  and  $p\bar{p} \rightarrow \pi a_2 \rightarrow K\bar{K}\pi$ . The data collected by the CPLEAR experiment allows a determination of the masses and widths of these resonant states with high statistics. Of special interest is a new measurement of the mass splitting between the neutral and charged modes of the  $K^*$  meson. This is because the difference between the world averages of the  $K^*$  masses,  $\langle m_{K^{*0}} \rangle - \langle m_{K^{*\pm}} \rangle$ , differs by  $\sim 1.8$  standard deviations from the average value of previous measurements of the  $K^*$  mass splitting,  $\langle m_{K^{*0}} - m_{K^{*\pm}} \rangle$ .

Section two of this thesis gives an introduction to CP violation and to the CPLEAR experiment. First, CP violation in the standard model and the phenomenology of CP violation in the neutral kaon system are discussed. Then the physics program of the CPLEAR experiment is outlined and an overview of the CPLEAR detector is given.

Section three is dedicated to the multi wire proportional chambers, describing the construction of the chambers, their installation in the detector and their performance.

In section four, the physics analysis of the isospin mass splitting of the  $K^*(892)$  meson is presented. The mass difference between  $K^{*0}(\bar{K}^{*0})$  and  $K^{*\pm}$  is obtained by analysing the event density in the Dalitz-plot  $M_{inv}^2(K^\pm, \pi^\mp)$  vs  $M_{inv}^2(K^0, \pi^\pm)$ . After a description of the event selection algorithms and an estimation of the background in the selected data sample, two possible parameterizations of the Dalitz-plot population are discussed. One of these parameterizations is then used in a fit to the experimental Dalitz-plot.

In the last section, the result obtained for the isospin mass splitting of the  $K^*(892)$  meson is compared to previous measurements.

## 2 CP Violation and the CPLEAR Experiment

### 2.1 CP Violation in the Standard Model

In this part, a short description of CP violation within the framework of the standard model of electroweak interactions is given. More details on this subject can be found in [1],[2] and [3].

In the standard model, the mass eigenstates of the quarks are grouped into  $n$  left-handed weak isospin doublets and right-handed singlets, i.e.

$$\begin{pmatrix} U_i \\ D_i \end{pmatrix}_L \quad \text{and} \quad U_{iR}, D_{iR} \quad (i = 1, \dots, n),$$

where  $U_i$  represents an up-type quark ( $u, c, t, \dots$ ),  $D_i$  represents a down-type quark ( $d, s, b, \dots$ ) and  $i$  is the quark family index.

In charged weak interactions, only left-handed quarks take part. The Lagrangian density for the interactions of quarks with the charged gauge boson  $W$  is given by

$$\mathcal{L}_{int} \propto gW_\mu \bar{U}_{Li}^I \gamma^\mu D_{Li}^I + gW_\mu^* \bar{D}_{Li}^I \gamma^\mu U_{Li}^I, \quad (2.1)$$

where  $U_{Li}^I$  ( $D_{Li}^I$ ) are the weak interaction eigenstates of the left-handed up (down) quarks. In general, the interaction eigenstates are not identical to the mass eigenstates. However, without loss of generality, the up-quark interaction eigenstates can be identified with the mass eigenstates, i.e.

$$U_{Li}^I = U_{Li} \quad (i = 1, \dots, n). \quad (2.2)$$

The mass and interaction eigenstates of the down-quarks are then related by

$$D_{Li}^I = V_{ij} D_{Lj} \quad (i = 1, \dots, n), \quad (2.3)$$

where  $V$  is the  $n \times n$  unitary quark mixing matrix.  $V$  can be parameterized with  $n(n-1)/2$  real angles and  $(n-1)(n-2)/2$  physically meaningful phases ( $2n-1$  phases can be eliminated by redefining the phases of the quark fields).

With equation 2.3, the Lagrangian density can be written as

$$\mathcal{L}_{int} \propto gW_\mu \bar{U}_{Li} \gamma^\mu V_{ij} D_{Lj} + gW_\mu^* \bar{D}_{Lj} V_{ij}^* \gamma^\mu U_{Li}. \quad (2.4)$$

The CP-transformed Lagrangian density is obtained by substituting the quark operators by the CP-transformed ones. This yields

$$\mathcal{L}_{int}^{CP} \propto gW_\mu^* \bar{D}_{Lj} V_{ij} \gamma^\mu U_{Li} + gW_\mu \bar{U}_{Li} \gamma^\mu V_{ij}^* D_{Lj}. \quad (2.5)$$

Comparing equation 2.4 and 2.5, one sees that for a complex quark mixing matrix the Lagrangian density  $\mathcal{L}_{int}$  is not invariant under the CP transformation, i.e.

$$\mathcal{L}_{int} \neq \mathcal{L}_{int}^{CP} \quad \text{for} \quad V_{ij} \neq V_{ij}^*. \quad (2.6)$$

This shows that CP invariance can be broken by complex phases in the quark mixing matrix.

With two quark families,  $V$  is the Cabibbo matrix, which can be parameterized with one real angle. In order to have a complex mixing matrix, at least three quark families are needed. For three quark generations,  $V$  is the KM (Kobayashi-Maskawa) matrix of three angles ( $\theta_{12}$ ,  $\theta_{13}$ ,  $\theta_{23}$ ) and one complex phase ( $e^{i\delta}$ ). A possible parameterization is [4]

$$\begin{aligned} V &\equiv \begin{pmatrix} V_{ud} & V_{us} & V_{ub} \\ V_{cd} & V_{cs} & V_{cb} \\ V_{td} & V_{ts} & V_{tb} \end{pmatrix} \\ &= \begin{pmatrix} c_{12}c_{13} & s_{12}c_{13} & s_{13}e^{-i\delta} \\ -s_{12}c_{23} - c_{12}s_{23}s_{13}e^{i\delta} & c_{12}c_{23} - s_{12}s_{23}s_{13}e^{i\delta} & s_{23}c_{13} \\ s_{12}s_{23} - c_{12}c_{23}s_{13}e^{i\delta} & -c_{12}s_{23} - s_{12}c_{23}s_{13}e^{i\delta} & c_{23}c_{13} \end{pmatrix}, \end{aligned} \quad (2.7)$$

where  $c_{ij} = \cos \theta_{ij}$  and  $s_{ij} = \sin \theta_{ij}$ . Several conditions must be fulfilled for CP to be violated in the standard model with three quark generations [3]:

1. The imaginary part of  $e^{i\delta}$  should not vanish, i.e.  $\sin \delta \neq 0$ .
2. There should be no mass degeneracy among the three up-quarks ( $u, c, t$ ) or among the three down-quarks ( $d, s, b$ ).
3. The sines and cosines of the three mixing angles  $\theta_{12}$ ,  $\theta_{13}$  and  $\theta_{23}$  should be different from zero.

The above conditions for CP violation in the standard model with three quark families can be summarized as

$$U(M_u^2) \cdot D(M_d^2) \cdot J \neq 0, \quad (2.8)$$

where

$$U(M_u^2) = (m_t^2 - m_c^2)(m_c^2 - m_u^2)(m_t^2 - m_u^2), \quad (2.9)$$

$$D(M_d^2) = (m_b^2 - m_s^2)(m_s^2 - m_d^2)(m_b^2 - m_d^2), \quad (2.10)$$

$$J = c_{12} \cdot c_{23} \cdot c_{13}^2 \cdot s_{12} \cdot s_{23} \cdot s_{13} \cdot \sin \delta. \quad (2.11)$$

The function  $J$  of the mixing angles and the phase can be written in a form that is explicitly parameterization independent:

$$|J| = |\text{Im}(V_{ij}V_{lk}V_{ik}^*V_{lj}^*)|, \quad (2.12)$$

for any choice of  $i \neq l$  and  $j \neq k$ . It can be shown that all CP-violating observables are proportional to  $J$ .

## 2.2 Phenomenology of CP Violation in the Neutral Kaon System

This part gives a short introduction of the phenomenological description of the neutral kaon system and defines the parameters commonly used to describe CP violation in this system. The consequences of CPT non-conservation are ignored here. More detailed treatments of this topic can be found in many text books and articles, e.g. [1], [5], [6], [7] and [8].

The two neutral kaon states produced in hadronic interactions are called  $K^0$  and  $\bar{K}^0$ . The strong and electromagnetic interactions, responsible for the production of  $K^0$  and  $\bar{K}^0$ , conserve strangeness, i.e.

$$[H_{st} + H_{em}, S] = 0, \quad (2.13)$$

where  $S$  is the strangeness operator and  $H_{st}$  ( $H_{em}$ ) is the Hamiltonian of the strong (electromagnetic) interactions.  $K^0$  and  $\bar{K}^0$  are the simultaneous eigenstates of  $S$  and  $H_{st} + H_{em}$ , with

$$S|K^0\rangle = +|K^0\rangle \quad \text{and} \quad (2.14)$$

$$S|\bar{K}^0\rangle = -|\bar{K}^0\rangle. \quad (2.15)$$

Weak interactions do not conserve strangeness and allow the decay of  $K^0$  and  $\bar{K}^0$  into lighter, non-strange pions and leptons. This means that strangeness is not a good quantum number for the complete Hamiltonian  $H$ , i.e.

$$[H, S] \neq 0, \quad (2.16)$$

where  $H = H_{st} + H_{em} + H_{wk}$  and  $H_{wk}$  is the Hamiltonian for the weak interactions. Hence,  $K^0$  and  $\bar{K}^0$  are not eigenstates of the complete Hamiltonian  $H$ .

The time dependence of an arbitrary state

$$|\psi(t)\rangle = \alpha(t)|K^0\rangle + \beta(t)|\bar{K}^0\rangle = \begin{pmatrix} \alpha(t) \\ \beta(t) \end{pmatrix} \quad (2.17)$$

is described by a system of coupled Schrödinger equations:

$$i \frac{\partial}{\partial t} \begin{pmatrix} \alpha(t) \\ \beta(t) \end{pmatrix} = \left[ \begin{pmatrix} M_{11} & M_{12} \\ M_{21} & M_{22} \end{pmatrix} - \frac{i}{2} \begin{pmatrix} \Gamma_{11} & \Gamma_{12} \\ \Gamma_{21} & \Gamma_{22} \end{pmatrix} \right] \begin{pmatrix} \alpha(t) \\ \beta(t) \end{pmatrix}, \quad (2.18)$$

where  $M_{ij}$  and  $\Gamma_{ij}$  are two Hermitian matrices, called the mass and decay matrices, respectively. Using perturbation theory and the selection rule  $|\Delta S| \leq 1$  for first-order

weak interactions, the elements of the mass matrix can be expanded as

$$M_{11} = m_{K^0} + \langle K^0 | H_{wk} | K^0 \rangle + \sum_n \frac{|\langle K^0 | H_{wk} | n \rangle|^2}{m_{K^0} - E_n} + \dots, \quad (2.19)$$

$$M_{22} = m_{\bar{K}^0} + \langle \bar{K}^0 | H_{wk} | \bar{K}^0 \rangle + \sum_n \frac{|\langle \bar{K}^0 | H_{wk} | n \rangle|^2}{m_{\bar{K}^0} - E_n} + \dots, \quad (2.20)$$

$$M_{21} = M_{12}^* = \sum_n \frac{\langle \bar{K}^0 | H_{wk} | n \rangle \langle n | H_{wk} | K^0 \rangle}{m_{K^0} - E_n} + \dots, \quad (2.21)$$

where  $|n\rangle$  denotes any intermediate state with energy  $E_n$ . Conditions on the elements of the decay matrix are derived from the equation that describes conservation of probability, i.e.

$$\frac{d}{dt} \langle \psi(t) | \psi(t) \rangle + 2\pi \sum_F \rho(F) |\langle F | H_{wk} | \psi(t) \rangle|^2, \quad (2.22)$$

where the sum is over all possible final states  $|F\rangle$  resulting from  $K^0$  and  $\bar{K}^0$  decays, and  $\rho(F)$  is the phase space factor of the final state  $|F\rangle$ . With equation 2.18, one obtains for the elements of the decay matrix

$$\Gamma_{11} = 2\pi \sum_F \rho(F) |\langle F | H_{wk} | K^0 \rangle|^2, \quad (2.23)$$

$$\Gamma_{22} = 2\pi \sum_F \rho(F) |\langle F | H_{wk} | \bar{K}^0 \rangle|^2, \quad (2.24)$$

$$\Gamma_{21} = \Gamma_{12}^* = 2\pi \sum_F \rho(F) \langle \bar{K}^0 | H_{wk} | F \rangle \langle F | H_{wk} | K^0 \rangle. \quad (2.25)$$

CPT invariance implies  $M_{11} = M_{22}$  and  $\Gamma_{11} = \Gamma_{22}$ .

Under the CP operation, the states  $|K^0\rangle$  and  $|\bar{K}^0\rangle$  transform as

$$\text{CP}|K^0\rangle = +|\bar{K}^0\rangle \quad \text{and} \quad (2.26)$$

$$\text{CP}|\bar{K}^0\rangle = +|K^0\rangle, \quad (2.27)$$

where the choice of phase is convention. The CP eigenstates, named  $|K_1\rangle$  and  $|K_2\rangle$ , are then

$$|K_1\rangle = \frac{1}{\sqrt{2}} (|K^0\rangle + |\bar{K}^0\rangle) \quad \text{and} \quad (2.28)$$

$$|K_2\rangle = \frac{1}{\sqrt{2}} (|K^0\rangle - |\bar{K}^0\rangle), \quad (2.29)$$

with eigenvalues

$$\text{CP}|K_1\rangle = +|K_1\rangle \quad \text{and} \quad (2.30)$$

$$\text{CP}|K_2\rangle = -|K_2\rangle. \quad (2.31)$$



The observable particle states are the eigenstates of  $M_{ij} - \frac{i}{2}\Gamma_{ij}$ , for which the Schrödinger equation decouples, i.e.

$$i\frac{\partial}{\partial t} \begin{pmatrix} |K_S^0(t)\rangle \\ |K_L^0(t)\rangle \end{pmatrix} = \begin{pmatrix} m_S - \frac{i}{2}\Gamma_S & 0 \\ 0 & m_L - \frac{i}{2}\Gamma_L \end{pmatrix} \begin{pmatrix} |K_S^0(t)\rangle \\ |K_L^0(t)\rangle \end{pmatrix}. \quad (2.32)$$

The two solutions are given by

$$|K_S^0(t)\rangle = e^{-\Gamma_S t/2} e^{-im_S t} |K_S^0(0)\rangle \quad \text{and} \quad (2.33)$$

$$|K_L^0(t)\rangle = e^{-\Gamma_L t/2} e^{-im_L t} |K_L^0(0)\rangle, \quad (2.34)$$

where  $m_S$  ( $m_L$ ) is the mass and  $1/\Gamma_S$  ( $1/\Gamma_L$ ) is the lifetime of  $K_S^0$  ( $K_L^0$ ). The mass eigenstates can be written as

$$|K_S^0\rangle = \frac{1}{\sqrt{1+|\varepsilon|^2}} [|\bar{K}_1\rangle + \varepsilon|\bar{K}_2\rangle] \quad (2.35)$$

$$= \frac{1}{\sqrt{2(1+|\varepsilon|^2)}} [(1+\varepsilon)|K^0\rangle + (1-\varepsilon)|\bar{K}^0\rangle],$$

$$|K_L^0\rangle = \frac{1}{\sqrt{1+|\varepsilon|^2}} [\varepsilon|\bar{K}_1\rangle + |\bar{K}_2\rangle] \quad (2.36)$$

$$= \frac{1}{\sqrt{2(1+|\varepsilon|^2)}} [(1+\varepsilon)|K^0\rangle - (1-\varepsilon)|\bar{K}^0\rangle],$$

and the strangeness eigenstates as

$$|K^0\rangle = \frac{\sqrt{1+|\varepsilon|^2}}{\sqrt{2(1+\varepsilon)}} (|K_S^0\rangle + |K_L^0\rangle), \quad (2.37)$$

$$|\bar{K}^0\rangle = \frac{\sqrt{1+|\varepsilon|^2}}{\sqrt{2(1-\varepsilon)}} (|K_S^0\rangle - |K_L^0\rangle), \quad (2.38)$$

where the parameter  $\varepsilon$  is given by

$$\varepsilon = \frac{\text{Im}(\Gamma_{12})/2 + i\text{Im}(M_{12})}{i(\Gamma_S - \Gamma_L)/2 - (m_S - m_L)}. \quad (2.39)$$

If the relative phase between  $|K^0\rangle$  and  $|\bar{K}^0\rangle$  is chosen according to the Wu-Yang gauge [9] (see below), then  $|\varepsilon|$  is small compared to 1,  $\text{Re}(\varepsilon) \simeq \text{Im}(\varepsilon)$  and  $\varepsilon$  becomes a measurable quantity. With this phase convention, one finds from equation 2.35 and 2.36

$$\langle K_L^0 | K_S^0 \rangle \simeq 2 \text{Re}(\varepsilon), \quad (2.40)$$

i.e.  $|K_L^0\rangle$  and  $|K_S^0\rangle$  are only orthogonal if CP is conserved, which implies  $\varepsilon=0$ .

A consequence of CP violation in the decay matrix and/or in the mass matrix is therefore a CP impurity in the physical states, measurable by the parameter  $\varepsilon$ .

A possibility to determine  $\text{Re}(\varepsilon)$  is the measurement of the charge asymmetry in semileptonic  $K^0$  and  $\bar{K}^0$  decays. If one assumes the validity of the  $\Delta S = \Delta Q$  rule, the charge of the pion ( $\pi$ ) and the lepton ( $l = e, \mu$ ) in semileptonic  $K^0$  and  $\bar{K}^0$  decays is fixed as

$$\begin{aligned} K^0 &\rightarrow \pi^- l^+ \nu_l & (\Delta S = \Delta Q = -1) & \quad \text{and} \\ \bar{K}^0 &\rightarrow \pi^+ l^- \bar{\nu}_l & (\Delta S = \Delta Q = +1). \end{aligned}$$

Assuming again CPT invariance and using equation 2.36, the charge asymmetry  $\delta$  in  $K_L^0$  decays is given by

$$\delta \equiv \frac{R(K_L^0 \rightarrow \pi^- l^+ \nu_l) - R(K_L^0 \rightarrow \pi^+ l^- \bar{\nu}_l)}{R(K_L^0 \rightarrow \pi^- l^+ \nu_l) + R(K_L^0 \rightarrow \pi^+ l^- \bar{\nu}_l)} \simeq 2 \text{Re}(\varepsilon). \quad (2.41)$$

Another possible source of CP violation is in the transition matrix. This can be shown by analysing neutral kaon decays into  $\pi^+\pi^-$  and  $\pi^0\pi^0$ . Bose statistic and the conservation of angular momentum define the quantum numbers for the two pion final state as

$$\begin{aligned} \text{CP } |\pi\pi\rangle &= + |\pi\pi\rangle & (|\pi\pi\rangle = |\pi^+\pi^-\rangle \text{ or } |\pi^0\pi^0\rangle), \\ L_{\pi\pi} &= 0 & (\text{angular momentum}), \\ I_{\pi\pi} &= 0 \text{ or } 2 & (\text{isospin}). \end{aligned}$$

The observation of  $K_L^0 \rightarrow \pi\pi$  is proof of CP violation, since either the mass eigenstate  $|K_L^0\rangle$  is not equal to the CP eigenstate  $|K_2\rangle$  (i.e.  $\varepsilon \neq 0$ ), or the CP symmetry is violated in the decay process, or both.

The experimentally observable quantities are

$$\eta_{+-} \equiv |\eta_{+-}| e^{i\phi_{+-}} = \frac{\langle \pi^+\pi^- | H_{wk} | K_L^0 \rangle}{\langle \pi^+\pi^- | H_{wk} | K_S^0 \rangle} \quad \text{and} \quad (2.42)$$

$$\eta_{00} \equiv |\eta_{00}| e^{i\phi_{00}} = \frac{\langle \pi^0\pi^0 | H_{wk} | K_L^0 \rangle}{\langle \pi^0\pi^0 | H_{wk} | K_S^0 \rangle}. \quad (2.43)$$

To parameterize  $\eta_{+-}$  and  $\eta_{00}$ , one decomposes the  $2\pi$  final state into isospin eigenstates with  $I = 0$  and  $2$ , i.e.

$$\langle \pi^+\pi^- | = \sqrt{2/3} \langle I=0 | + \sqrt{1/3} \langle I=2 |, \quad (2.44)$$

$$\langle \pi^0\pi^0 | = \sqrt{2/3} \langle I=2 | - \sqrt{1/3} \langle I=0 |, \quad (2.45)$$

and defines the following two transition matrix elements for  $K^0$ :

$$A_0 = e^{-i\delta_0} \langle I=0, \pi\pi | H_{wk} | K^0 \rangle, \quad (2.46)$$

$$A_2 = e^{-i\delta_2} \langle I=2, \pi\pi | H_{wk} | K^0 \rangle. \quad (2.47)$$

Assuming CPT invariance and adjusting the relative phase between  $|K^0\rangle$  and  $|\bar{K}^0\rangle$  to make  $A_0$  real (Wu-Yang gauge), the corresponding matrix elements for  $\bar{K}^0$  are then given by

$$A_0 = e^{-i\delta_0} \langle I=0, \pi\pi | H_{wk} | \bar{K}^0 \rangle \quad \text{and} \quad (2.48)$$

$$A_2^* = e^{-i\delta_2} \langle I=2, \pi\pi | H_{wk} | \bar{K}^0 \rangle. \quad (2.49)$$

With the help of equation 2.35 and 2.36, one obtains

$$\eta_{+-} = \frac{\sqrt{2} \varepsilon A_0 + e^{i(\delta_2 - \delta_0)} (\varepsilon \operatorname{Re} A_2 + i \operatorname{Im} A_2)}{\sqrt{2} A_0 + e^{i(\delta_2 - \delta_0)} (\operatorname{Re} A_2 + i \varepsilon \operatorname{Im} A_2)} \quad \text{and} \quad (2.50)$$

$$\eta_{00} = \frac{\varepsilon A_0 - \sqrt{2} e^{i(\delta_2 - \delta_0)} (\varepsilon \operatorname{Re} A_2 + i \operatorname{Im} A_2)}{A_0 - \sqrt{2} e^{i(\delta_2 - \delta_0)} (\operatorname{Re} A_2 + i \varepsilon \operatorname{Im} A_2)}. \quad (2.51)$$

From the  $\Delta I = 1/2$  rule, the ratio  $A_2/A_0$  must be small. Expanding  $\eta_{+-}$  and  $\eta_{00}$  in powers of  $A_2/A_0$  and  $\varepsilon$  and keeping only the first order terms, one finds the relations:

$$\eta_{+-} \simeq \varepsilon + \varepsilon' \quad \text{and} \quad (2.52)$$

$$\eta_{00} \simeq \varepsilon - 2\varepsilon', \quad (2.53)$$

with

$$\varepsilon' = \frac{1}{\sqrt{2}} \frac{\operatorname{Im}(A_2)}{A_0} e^{i(\delta_2 - \delta_0 + \pi/2)}. \quad (2.54)$$

Thus CP violation in the decay  $K^0 (\bar{K}^0) \rightarrow \pi\pi$  is possible even for  $\varepsilon = 0$ . The parameter  $\varepsilon'$  is a measure of the CP violation in the decay and is suppressed by the  $\Delta I = 1/2$  rule. The relationship between  $\eta_{+-}$ ,  $\eta_{00}$ ,  $\varepsilon$  and  $\varepsilon'$  can be represented in the Wu-Yang triangle, shown in figure 2.1.

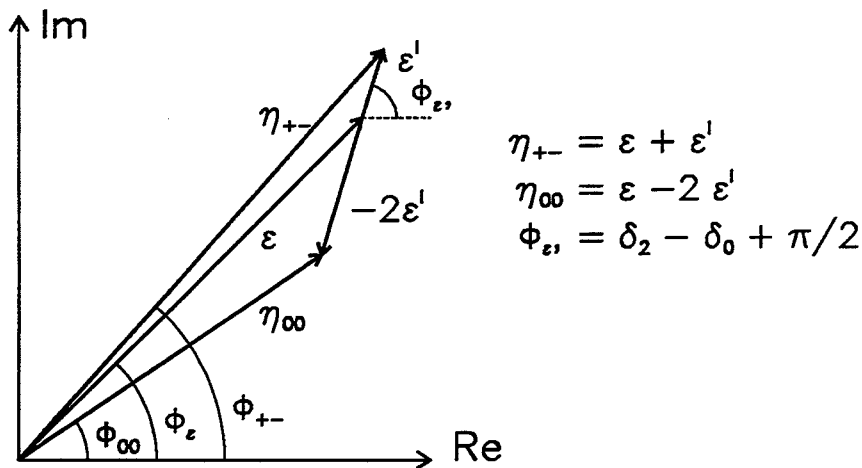


Figure 2.1: The Wu-Yang triangle, showing the relationship between the parameters  $\eta_{+-}$ ,  $\eta_{00}$ ,  $\varepsilon$  and  $\varepsilon'$ .

Combining equations 2.52 and 2.53, one finds:

$$\frac{\varepsilon'}{\varepsilon} \simeq \frac{1}{3} \left( 1 - \frac{\eta_{00}}{\eta_{+-}} \right). \quad (2.55)$$

## 2.3 The CPLEAR Experiment

CPLEAR is an experiment at the CERN Low Energy Antiproton Ring (LEAR). With the antiprotons from LEAR, it is possible to produce well defined and equal sources of  $K^0$  and  $\bar{K}^0$  at low energies through the two annihilation channels (the "golden" channels)

$$\begin{aligned} p\bar{p} \text{ ( at rest )} &\rightarrow K^+\pi^-\bar{K}^0 && (\text{BR} \simeq 2 \cdot 10^{-3}), \\ p\bar{p} \text{ ( at rest )} &\rightarrow K^-\pi^+K^0 && (\text{BR} \simeq 2 \cdot 10^{-3}). \end{aligned}$$

Because of strangeness conservation in strong interactions, the neutral kaon state ( $K^0$  or  $\bar{K}^0$ ) can be identified through the detection of the accompanying charged kaon (strangeness tagging). With a stop rate of  $\sim 10^6$   $\bar{p}$ 's per second, roughly  $10^8$   $K^0$  and  $\bar{K}^0$  are produced per day.

This intense sources of tagged  $K^0$  and  $\bar{K}^0$  allow to study CP violation in several decay channels of the neutral kaons. The method used by the CPLEAR experiment is to measure the differential and integral asymmetries between the decay rates of initially pure  $K^0$  and  $\bar{K}^0$  states into the final state  $f$ , e.g.  $\pi^+\pi^-$ ,  $\pi^0\pi^0$ ,  $\pi^+\pi^-\pi^0$  and  $\gamma\gamma$ . With this method, CP violation can be investigated with systematic errors of different nature compared to previous experiments and in decay channels where CP violation has never been observed before ( $\pi^+\pi^-\pi^0$  and  $\gamma\gamma$ ). In addition, many of the systematic errors cancel to first order in the asymmetries (differences and ratios of rates).

Using equation 2.37 and 2.38, one can write down the decay rates of initially pure  $K^0$  and  $\bar{K}^0$  states into the final state  $f$  as

$$\begin{aligned} R_{K^0 \rightarrow f}(t) &= \frac{1}{|4p^2|} \left[ |A_S|^2 e^{-\Gamma_S t} + |A_L|^2 e^{-\Gamma_L t} \right. \\ &\quad \left. + 2 |A_S||A_L| e^{-\frac{1}{2}(\Gamma_S+\Gamma_L)t} \cos(\Delta m t + \phi_S - \phi_L) \right], \end{aligned} \quad (2.56)$$

$$\begin{aligned} R_{\bar{K}^0 \rightarrow f}(t) &= \frac{1}{|4q^2|} \left[ |A_S|^2 e^{-\Gamma_S t} + |A_L|^2 e^{-\Gamma_L t} \right. \\ &\quad \left. - 2 |A_S||A_L| e^{-\frac{1}{2}(\Gamma_S+\Gamma_L)t} \cos(\Delta m t + \phi_S - \phi_L) \right], \end{aligned} \quad (2.57)$$

with

$$\begin{aligned} p(q) &= \frac{1 + (-)\varepsilon}{\sqrt{2(1 + |\varepsilon|^2)}}, \\ \Delta m &= m_L - m_S, \\ A_{S(L)} &= \langle f | H_{\text{wk}} | K_{S(L)}^0 \rangle, \end{aligned}$$

where  $\phi_{S(L)}$  is the phase of  $A_{S(L)}$  and  $t$  is the eigentime of  $K^0$  ( $\bar{K}^0$ ). The time-dependent asymmetry,  $A_f(t)$ , is then given by

$$\begin{aligned} A_f(t) &\equiv \frac{R_{\bar{K}^0 \rightarrow f}(t) - R_{K^0 \rightarrow f}(t)}{R_{\bar{K}^0 \rightarrow f}(t) + R_{K^0 \rightarrow f}(t)} \\ &= 2 \operatorname{Re}(\varepsilon) - \frac{2 |\eta_f| e^{\frac{1}{2}(\Gamma_S - \Gamma_L)t} \cos(\Delta m t - \phi_f)}{1 + |\eta_f|^2 e^{(\Gamma_S - \Gamma_L)t}}, \end{aligned} \quad (2.58)$$

where  $\eta_f = A_L/A_S$  and  $\phi_f$  is the phase of  $\eta_f$ .

Since  $\Delta m \sim \Gamma_S/2$ , it is possible to observe the oscillation of the interference term between  $A_S$  and  $A_L$  before the  $K_S^0$  component has died away. Therefore, both the magnitude and the phase of the ratio  $\eta_f$  can be obtained from the asymmetry function  $A_f(t)$  in the region of interference.

In the following, a brief description of the CPLEAR physics program is given. More details may be found in [10].

### 2.3.1 Decays into two Pions

We intend to determine  $|\eta_{+-}|$ ,  $|\eta_{00}|$ ,  $\phi_{+-}$  and  $\phi_{00}$  by measuring the time-dependent asymmetries  $A_{\pi^+\pi^-}(t)$  and  $A_{\pi^0\pi^0}(t)$  (see equation 2.58) in the region of interference between the decay amplitudes  $\langle \pi^+\pi^- | H_{wk} | K_S^0 \rangle$  and  $\langle \pi^+\pi^- | H_{wk} | K_L^0 \rangle$ , i.e. in the  $K^0$  ( $\bar{K}^0$ ) decay eigentime interval of  $5\tau_S$  to  $20\tau_S$ . In the interference region, the decay rates of  $K_S^0$  and  $K_L^0$  into  $\pi\pi$  are comparable and the asymmetry is large (see figure 2.2).

The measurement of the phase difference ( $\phi_{+-} - \phi_{00}$ ) will provide a valuable test of CPT invariance, since the Wu-Yang triangle (see figure 2.1) is expected to close if CPT is an exact symmetry.

The determination of  $\varepsilon'/\varepsilon$  is unlikely to be possible from the measurements of  $\eta_{+-}$  and  $\eta_{00}$  because of the limited vertex resolution and resulting eigentime resolution. An alternative way to determine  $\varepsilon'/\varepsilon$  is to measure the integral asymmetries, defined as

$$I_{\pi\pi}(t_0) \equiv \frac{\int_0^{t_0} R_{\bar{K}^0 \rightarrow \pi\pi}(t) dt - \int_0^{t_0} R_{K^0 \rightarrow \pi\pi}(t) dt}{\int_0^{t_0} R_{\bar{K}^0 \rightarrow \pi\pi}(t) dt + \int_0^{t_0} R_{K^0 \rightarrow \pi\pi}(t) dt}. \quad (2.59)$$

The integral asymmetries  $I_{\pi\pi}(t_0)$  are insensitive to the upper integration limit for  $t_0 > 20\tau_S$ , since the decay-rates for  $K^0$  and  $\bar{K}^0$  become equal. We expect to measure  $\varepsilon'/\varepsilon$  using the relationship

$$\frac{\operatorname{Re}(\varepsilon')}{\operatorname{Re}(\varepsilon)} \simeq \frac{1}{6} \left( 1 - \frac{I_{00}}{I_{+-}} \right). \quad (2.60)$$

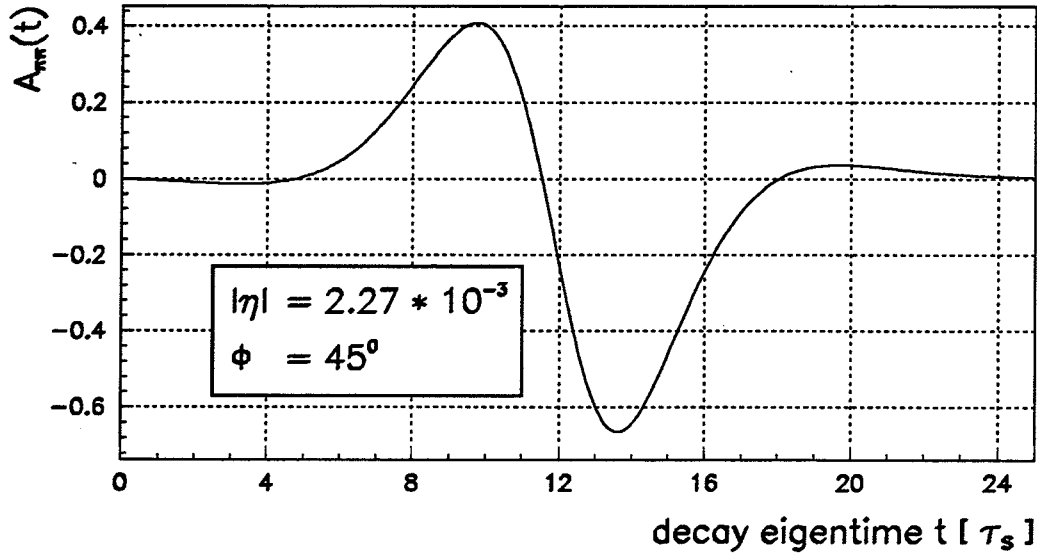


Figure 2.2: The expected asymmetry function  $A_{\pi\pi}(t)$  for neutral kaon decays into  $\pi^+\pi^-$  and  $\pi^0\pi^0$ .

### 2.3.2 Decays into three Pions

For the first time, it is intended to measure CP violation in the  $\pi^+\pi^-\pi^0$  decay mode of the neutral kaons. The corresponding observable is defined as

$$\eta_{+-0} = |\eta_{+-0}| e^{i\phi_{+-0}} = \frac{\langle \pi^+\pi^-\pi^0 | H_{wk} | K_S^0 \rangle}{\langle \pi^+\pi^-\pi^0 | H_{wk} | K_L^0 \rangle}. \quad (2.61)$$

The interference term in the time-dependent asymmetry function  $A_{+-0}(t)$  is expected to reach its maximum at early decay times ( $t < 5\tau_S$ ) and allows the determination of  $|\eta_{+-0}|$ . The real part of  $\eta_{+-0}$  can be obtained from the integral asymmetry  $I_{+-0}(t_0)$  and the phase  $\phi_{+-0}$  can then be extracted from

$$\cos \phi_{+-0} = \frac{\text{Re}(\eta_{+-0})}{|\eta_{+-0}|}. \quad (2.62)$$

### 2.3.3 Semileptonic Decays

One can define the following decay rates of initially pure  $K^0$  and  $\bar{K}^0$  states into the semileptonic final states  $\pi^-l^+\nu$  and  $\pi^+l^-\bar{\nu}$ :

$$R_+(t) \equiv R_{K^0 \rightarrow \pi^-l^+\nu}(t), \quad (2.63)$$

$$\bar{R}_-(t) \equiv R_{\bar{K}^0 \rightarrow \pi^+l^-\bar{\nu}}(t), \quad (2.64)$$

which are decays allowed by the  $\Delta S = \Delta Q$  rule for  $t = 0$ , and

$$R_-(t) \equiv R_{K^0 \rightarrow \pi^+ l^- \bar{\nu}}(t), \quad (2.65)$$

$$\bar{R}_+(t) \equiv R_{\bar{K}^0 \rightarrow \pi^- l^+ \nu}(t), \quad (2.66)$$

which are decays forbidden by the  $\Delta S = \Delta Q$  rule for  $t = 0$ . The semileptonic decays of the neutral kaons are of interest for the following three reasons:

1. We intend to test the  $\Delta S = \Delta Q$  rule. A violation of this rule can be expressed by the complex parameter  $x$ , defined as

$$x \equiv \frac{\langle \pi^- l^+ \nu | H_{\text{wk}} | \bar{K}^0 \rangle}{\langle \pi^- l^+ \nu | H_{\text{wk}} | K^0 \rangle} \quad (\text{CPT}) \quad \Rightarrow \quad x^* = \frac{\langle \pi^+ l^- \bar{\nu} | H_{\text{wk}} | K^0 \rangle}{\langle \pi^+ l^- \bar{\nu} | H_{\text{wk}} | \bar{K}^0 \rangle}. \quad (2.67)$$

The time-dependent total rate of semileptonic decays, defined as

$$R_{\text{tot}}(t) \equiv R_+(t) + R_-(t) + \bar{R}_+(t) + \bar{R}_-(t), \quad (2.68)$$

is sensitive to  $\text{Re}(x)$ , and the asymmetry

$$A_{\pi l \nu}(t) \equiv \frac{[\bar{R}_+(t) + \bar{R}_-(t)] - [R_+(t) + R_-(t)]}{[\bar{R}_+(t) + \bar{R}_-(t)] + [R_+(t) + R_-(t)]} \quad (2.69)$$

depends on  $\text{Im}(x)$ .

2. We expect to measure for the first time the T violation associated with CP violation, assuming CPT invariance holds. A non-zero value of the asymmetry function

$$A_T(t) = \frac{\bar{R}_+(t) - R_-(t)}{\bar{R}_+(t) + R_-(t)} \quad (2.70)$$

proves T violation, assuming the  $\Delta S = \Delta Q$  rule. This is because the rate of transitions  $\bar{K}^0 \rightarrow K^0$  is then not equal to the rate of the time-reversed process  $K^0 \rightarrow \bar{K}^0$ .

3. We intend to improve the accuracy of the mass difference value  $\Delta m = m_L - m_S$  by measuring the difference of the asymmetries

$$D(t) - \bar{D}(t) \equiv [R_+(t) - R_-(t)] - [\bar{R}_+(t) - \bar{R}_-(t)] \propto e^{(\Gamma_S + \Gamma_L)t/2} \cos(\Delta m t). \quad (2.71)$$

In table 2.1, the present precision in the determination of the various parameters is compared to the precision expected from the CPLEAR experiment, based on  $\sim 10^9$  reconstructed  $K^0$  and  $\bar{K}^0$  decays.

parameter	CPLEAR (expected)	present precision
$\sigma( \varepsilon'/\varepsilon )$	$1.5 \cdot 10^{-3}$	$\sim 1 \cdot 10^{-3}$
$\sigma( \eta_{+-} )/ \eta_{+-} $	$5 \cdot 10^{-3}$	$10 \cdot 10^{-3}$
$\sigma( \eta_{00} )/ \eta_{00} $	$< 2 \cdot 10^{-2}$	$1 \cdot 10^{-2}$
$\sigma(\phi_{+-})$	$0.3^\circ$	$1.2^\circ$
$\sigma(\phi_{00})$	$1^\circ$	$\sim 1.6^\circ$
$\sigma(\phi_{+-} - \phi_{00})$	$1^\circ$	$\sim 1.6^\circ$
$\sigma( \eta_{+-0} )$	$1 \cdot 10^{-3}$	$< 0.35$
$\sigma(\text{Re}(x)), \sigma(\text{Im}(x))$	$< 1 \cdot 10^{-3}$	$20 \cdot 10^{-3}$
$\sigma(A_T)/A_T$	$6 \cdot 10^{-2}$	...
$\sigma(\Delta m)/\Delta m$	$2 \cdot 10^{-3}$	$4.5 \cdot 10^{-3}$

Table 2.1: Comparison between the present precision for various parameters and the precision expected from the CPLEAR experiment.

## 2.4 The CPLEAR Detector

The CPLEAR detector has cylindrical geometry. The coordinate system defined for the experiment is explained in diagram 2.3. It is right-handed, with the origin at the center of the detector (the center of the target) and the  $z$ -axis pointing along the cylinder axis in the direction of the incoming antiproton beam. The transverse plane, the  $xy$ -plane, is perpendicular to the cylinder axis, with the  $y$ -axis pointing upwards.

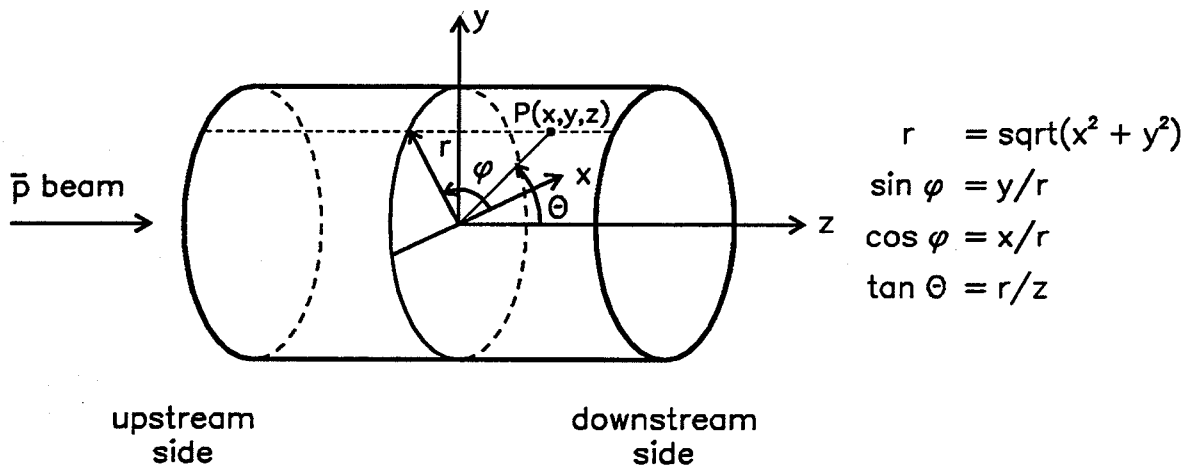


Figure 2.3: Definition of the coordinate system for the CPLEAR experiment.

Figure 2.4 shows a side view of the CPLEAR detector. The antiprotons from LEAR enter the detector with a momentum of 200 MeV/c and are stopped in the gaseous hydrogen target. The beam profile in the transverse plane is monitored with two small



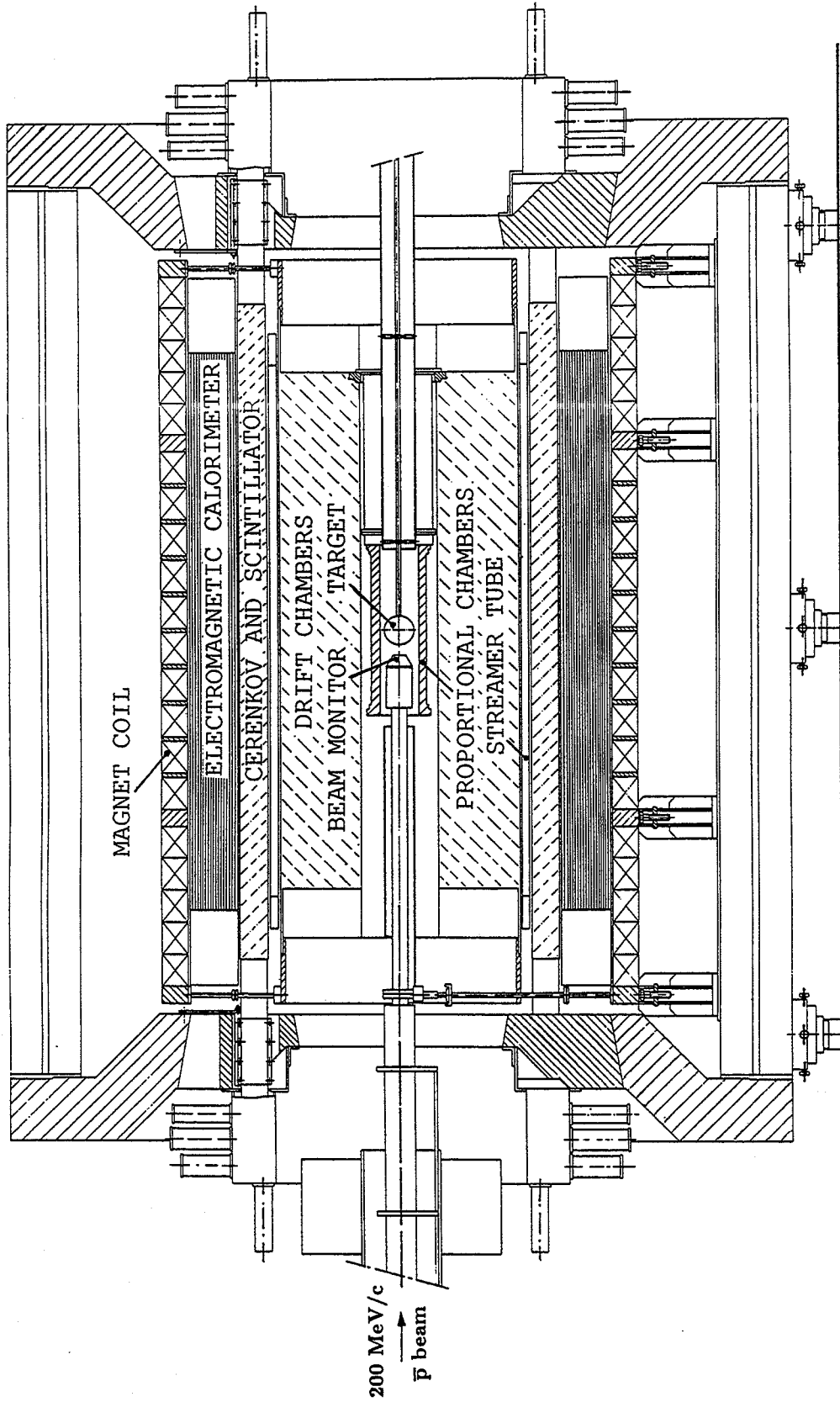


Figure 2.4: Side view of the CPLEAR detector.

multi wire proportional chambers, the beam monitor. The beam counter consists of a plastic scintillator in front of the entrance window of the target and signals an incoming antiproton. The target is surrounded by two cylindrical multi wire proportional chambers (PC1 and PC2), six drift chambers (DC1 to DC6), two layers of streamer tubes (ST1 and ST2), the Particle Identification Detector (PID), consisting of a 32 sector scintillator-Čerenkov counter-scintillator sandwich, and an 18-layer lead-gas-sampling electromagnetic calorimeter. The detector components are placed inside a solenoid of 3.6 m length and 1 m radius, which produces a magnetic field of 0.44 Tesla parallel to the  $z$ -axis.

In order to achieve the physics goals of the experiment, the main requirements on the detector are:

- **Definition of the strangeness (strangeness tagging)**

In order to determine the strangeness of the neutral kaon in a "golden" event, identification of the accompanying charged kaon and the sign of its charge are required. Since annihilations into pionic final states constitute  $\sim 95\%$  of all events, a fast and efficient pion/kaon separation is needed. This is realized with the PID, which provides the following possibilities for the particle identification:

1. Čerenkov signal discrimination.
2. Energy loss measurement ( $dE/dx$ ) in the inner scintillator layer (S1).
3. Time-of-flight (TOF) measurement with the beam counter ("START" signal) and S1 ("STOP" signal). Examined is the difference of TOF between two tracks. This is because the time difference between the passage of the incoming antiproton through the beam counter and the annihilation has an event-to-event fluctuation of the same order as the TOF of the pions and kaons themselves.

The sign of the kaon charge is obtained from the track curvature in the transverse plane due to the magnetic field. The curvature is measured with the tracking devices (PC's, DC's and ST's).

- **Minimization of regeneration**

Because strong interactions conserve strangeness, several reactions between  $\bar{K}^0$  and matter have no counterpart for  $K^0$ , and therefore the total cross-section of  $\bar{K}^0$  on a nucleus is bigger than the corresponding total cross-section of  $K^0$ . The interaction of  $K_L^0$  ( $K_S^0$ ) with matter leads then to an admixture of  $K_S^0$  ( $K_L^0$ ), since the two components  $K^0$  and  $\bar{K}^0$  of the mass eigenstates are altered differently. This regeneration of  $K_S^0$  and  $K_L^0$  must be accounted for in the analysis, since it changes the asymmetry functions  $A_f(t)$  (see equation 2.58). In order to minimize the effect of regeneration on  $A_f(t)$ , the amount of material in the  $K_S^0$  decay region is kept as low as possible by choosing

- a gaseous hydrogen target with thin walls and
- extremely light tracking chambers.

• **Detection of the neutral kaon decay products**

In  $p\bar{p}$  annihilations at rest, the decay products are isotropically distributed. Therefore, the detector must cover a large solid angle in order to have a good detection efficiency. This is realized with the cylindrical geometry, corresponding to a solid angle of  $\Omega \simeq 0.8 \cdot 4\pi$  steradians.

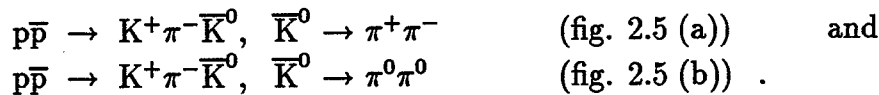
The tracking chambers should contain the region of interference between the decay amplitudes of  $K_S^0$  and  $K_L^0$  into  $\pi\pi$  ( $5 - 20\tau_S$ ). This requirement determines the outer radius of the detector.

The charged decay products are reconstructed with the tracking devices, while the neutral pions are detected by converting the two photons from the decay  $\pi^0 \rightarrow \gamma\gamma$  in the electromagnetic calorimeter.

• **Collection of the required number of events**

The determination of the parameters listed in table 2.1 with the intended precision requires  $\sim 10^9$  reconstructed  $K^0$  and  $\bar{K}^0$  decays. This corresponds to  $\sim 10^{13}$  antiproton annihilations in the target if the small branching ratios for the "golden" channels, the neutral kaon decays outside the detector and the detector inefficiency are taken into account. To collect the necessary number of events in a reasonable time ( $\sim 150$  days of data taking), the required stop rate is  $\sim 10^6$   $\bar{p}$ /sec. In order to handle this event rate, the "golden" channels must be recognized online. This is realized with a sophisticated multi-level trigger, which reduces the event rate to  $\sim 10^3$  Hz at low dead-time. The sequential decisions are provided by dedicated trigger processors.

Figure 2.5 shows a transverse view of the CPLEAR detector with typical events of the type



In the following, a brief description of the subdetectors, the trigger and the data acquisition system (DAQ) are given. Some of the physical parameters of the subdetectors are summarized in table 2.2. For a more detailed description of the CPLEAR detector see [11], and in particular section 3 for the proportional chambers, [12] for the drift chambers, [13] for the PID, [14] for the calorimeter, [15][16] for the trigger and [17] for the DAQ.

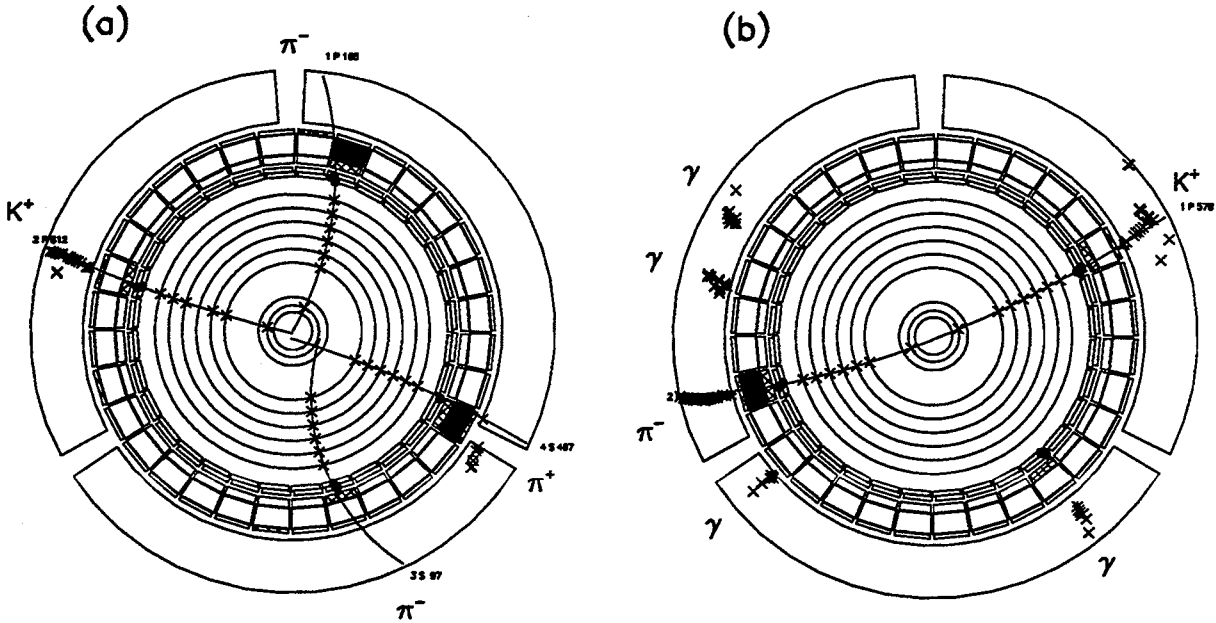


Figure 2.5: Transverse view of the CPLEAR detector with two typical events of the type  $p\bar{p} \rightarrow K^+\pi^-\bar{K}^0$ ,  $\bar{K}^0 \rightarrow \pi^+\pi^-$  (a) and  $\bar{K}^0 \rightarrow \pi^0\pi^0$  (b).

sub-detector	mid-plane radius [cm]	active thickness [cm]	active length [cm]	number of elements		
				wire	U-strips	V-strips
PC1	9.53	0.60	70.0	576	246	262
PC2	12.70	0.60	70.0	768	310	325
DC1	25.46	1.00	233.6	160	275	285
DC2	30.56	1.00	233.6	192	324	336
DC3	35.65	1.00	233.6	224	378	385
DC4	40.74	1.00	233.6	256	424	432
DC5	45.84	1.00	233.6	288	465	477
DC6	50.93	1.00	233.6	320	510	520
ST1	58.22	1.75	252.0	32 * 6 tubes		
ST2	59.97	1.75	252.0	32 * 6 tubes		
S1	63.84	3.00	310.0	32 sectors		
Č	69.43	8.00	310.0	32 sectors		
S2	74.21	1.40	310.0	32 sectors		
CAL	87.52	19.11	264.0	17'112	22'896	23'040

Table 2.2: Some physical parameters of the CPLEAR subdetectors

## The Target

The target is made of a laminated Kevlar sphere with a radius of 7 cm and a wall thickness of 800  $\mu\text{m}$ . It is filled with gaseous hydrogen at 15 bar pressure. The entrance window, made of mylar, has a diameter of 11 mm and is 120  $\mu\text{m}$  thick.

## The Proportional Chambers PC1 and PC2

The two multi wire proportional chambers are the innermost tracking devices. The radius of PC2 corresponds to a time of flight for neutral kaons of  $\sim 5\tau_S$  in eigentime, which allows online selection of neutral kaon events with  $t > 5\tau_S$ . This reduces the necessary number of recorded  $K^0$  ( $\bar{K}^0$ )  $\rightarrow \pi^+\pi^-$  decays for the determination of the asymmetry  $A_{\pi^+\pi^-}(t)$  by a factor of  $\sim 100$  without a loss in precision ( $A_{\pi^+\pi^-}(t) \simeq 0$  for  $t < 5\tau_S$ ). In addition, the fraction of events with semileptonic  $K^0$  and  $\bar{K}^0$  decays is enhanced in the recorded data.

The surface density of one chamber is only 41.5 mg/cm<sup>2</sup>, which corresponds to  $1.1 \cdot 10^{-3}$  radiation lengths. Both chambers provide anode wire and cathode strip information (the strip readout electronics is not yet installed). Due to the small wire pitch of 1 mm, the proportional chambers have a very short response time ( $\sim 30$  ns maximum drift time) and achieve a spatial resolution of  $\sigma_{r\varphi} \simeq 350 \mu\text{m}$ . The overall detection efficiency of the two chambers (signal in PC1 or PC2) is  $\sim 99.5\%$ .

## The Drift Chambers DC1 to DC6

The six drift chambers constitute the main part of the tracking devices. On average, the material represented by one chamber corresponds to only  $6.6 \cdot 10^{-4}$  radiation lengths. All drift chambers provide  $\varphi$  (wires) and  $z$  (strips) information. The sense wires are constructed in doublets in order to avoid left-right ambiguities. A small half drift cell size of 0.5 cm gives a fast detector response (200 ns maximum drift time). The mean detection efficiency is  $\sim 97\%$  for the wire plane and  $\sim 90\%$  for the strips. The spatial resolution was determined to be  $\sigma_{r\varphi} \simeq 300 \mu\text{m}$  and  $\sigma_z \simeq 2$  mm.

## The Streamer Tubes ST1 and ST2

The streamer tubes are arranged in two layers which are staggered by a half tube in order to avoid dead space. Each layer is divided into 32 modules consisting of 6 tubes. The streamer tubes provide a very fast (900 ns)  $z$  information for charged tracks by measuring the time difference between the signals arriving at the two ends of the tube. The overall detection efficiency is 97.5 % and the  $z$  resolution is  $\sigma_z \simeq 1$  cm.

The momentum resolution of the tracking devices is  $\sigma(p)/p \simeq 5\%$  at 300 MeV/c.

## The Particle Identification Detector (PID)

The PID is divided into 32 sectors, consisting of an inner scintillator (S1), a Čerenkov

counter (C) and an outer scintillator (S2). It is designed to give a high efficiency for the kaon/pion separation in the relevant momentum range of 300 to 750 MeV/c. The PID provides three methods for particle identification: Čerenkov signal discrimination, energy loss ( $dE/dx$ ) measurement in S1 and time-of-flight (TOF) measurement (S1) with an excellent time resolution of  $\sigma_{TOF} \simeq 180$  ps.

Requiring a  $S1 * \bar{C} * S2$  signature in a PID sector for a kaon candidate, i.e. coincident signals in the scintillators S1 and S2 and no signal in the corresponding Čerenkov sector, gives a pion rejection at the first trigger level (60 ns) of  $\sim 3 \cdot 10^{-3}$  with a kaon detection efficiency of  $\sim 75$  %. In a later trigger stage (2  $\mu$ s), using  $dE/dx$  and TOF information, the pion rejection can be improved by a further factor of 4. In the offline analysis, the PID achieves for

• 350 MeV/c tracks:	$\pi$ rejection:	$4 \cdot 10^{-6}$	K efficiency:	60 %
	K rejection:	$< 1 \cdot 10^{-6}$	$\pi$ efficiency:	90 % ,
• 650 MeV/c tracks	$\pi$ rejection:	$2 \cdot 10^{-4}$	K efficiency:	40 %
	K rejection:	$1 \cdot 10^{-3}$	$\pi$ efficiency:	40 % .

### The Electromagnetic Calorimeter (CAL)

The calorimeter is made of 18 layers corresponding to a total of 6.2 radiation lengths. A layer consists of an Al-Pb-Al converter plate (1.5 mm lead with 0.3 mm aluminium on each side) and a series of streamer tubes ( $4 \times 4.5$  mm<sup>2</sup>) sandwiched by cathode strips at an angle of  $\pm 30$  degrees with respect to the direction of the streamer tube wires. The high granularity of the calorimeter ( $\sim 64'000$  channels) provides a good shower foot resolution of the photons, which is important for the neutral vertex reconstruction ( $K^0 \rightarrow \pi^0 \pi^0$ ). The important characteristics of the calorimeter are

- spatial resolution :  $\sigma \sim 5$  mm,
- energy resolution :  $\sigma(E) \simeq 20\% / \sqrt{E[\text{GeV}]}$  ,
- efficiency for photons : 90 - 95 % for  $E_\gamma > 130$  MeV,
- $2 \pi^0$  vertex resolution :  $\sigma \simeq 1.5$  cm ( $0.5 c \cdot \tau_S$ ).

### The Trigger

The two main tasks of the trigger are to identify events containing a neutral kaon and to classify such events by the neutral kaon decay mode as well as the decay time. With  $\sim 10^6$  antiproton annihilations per second in the target, the neutral kaon production rate is a few times  $10^3$  Hz. In order to collect the required number of  $\sim 10^9$   $K^0$  and  $\bar{K}^0$  decays, it is thus important that the trigger keeps dead time to a minimum. This is realized by sequential trigger decisions in time regimes of 60 ns to 25  $\mu$ s as information becomes available from the subdetectors. The trigger is composed of ECL

trigger stage	task description	decision time	reduction factor
EDL	cut on: - n°. of S1 * $\bar{C}$ * S2 signatures in PID - n°. of hits in S1	60 ns	5.3
p <sub>T</sub> - cut	cut on: - transverse momenta of S1 * $\bar{C}$ * S2 tracks	500 ns	6.3
IDL	cut on: - n°. of primary tracks - n°. of charged tracks - n°. of kaon tracks	600 ns	1.9
Track Reconstruction	- reconstruct and parameterize all tracks - decide on event topology (total charge, charged or neutral K <sup>0</sup> ( $\bar{K}^0$ ) decay)	2 $\mu$ s	2.3
Charged Track Kinematics Trigger	cut on: - missing mass at primary vertex - invariant mass and opening angle of secondary tracks	3 $\mu$ s	4.7
<u>in parallel with :</u>			
PID Trigger	- confirm primary K <sup>±</sup> $\pi^{\mp}$ pair using <ul style="list-style-type: none"> <li>• dE/dx in the scintillators</li> <li>• time of flight</li> <li>• Čerenkov pulse height</li> </ul>		
Calorimeter Shower Trigger	- reconstruct and count shower clusters - veto events with K <sup>0</sup> decay outside the detector	25 $\mu$ s	2
Neutral Particle Trigger (not installed)	cut on: - number of photons - decay eigentime in K <sup>0</sup> $\rightarrow$ $\pi^0\pi^0$ decays	$\sim$ 1 ms	2

Table 2.3: The main stages of the CPLEAR trigger with the corresponding decision times and event rate reduction factors.

based electronics, except the last stage, which will be implemented in software on a RISC processor farm.

In table 2.3, the tasks of the major trigger parts are summarized, together with the corresponding decision times and reduction factors. Because the data used in the analysis of the K\*(892) mass difference (see section 4) were taken in run period P8 (October 1990), only the trigger stages already installed at that time will be described here.

The trigger logic is launched by the beam counter signal. In order to avoid a superposition of tracks in the detector, it is required that no other antiproton enters the target within the next 130 ns.

- **The Early Decision Logic (EDL)**

The very first trigger level uses information from the PID to estimate the number of charged tracks in the event and to look for a kaon candidate. A kaon candidate is identified by an  $S1 * \bar{C} * S2$  signature in a PID sector, and the number of charged tracks is estimated by counting the number of S1 sectors which gave a signal. In order to select events with a charged kaon, the EDL requires at least one kaon candidate and at least one additional hit in S1. For events accepted by the EDL, the trigger sends a strobe to the subdetectors front end electronics (FE) to start the conversion of data.

- **The  $p_T$  -cut**

The task of the  $p_T$ -cut is to reject events with a low momentum pion ( $p_\pi < 200$  MeV/c) that fakes a kaon in the Čerenkov counter. For this purpose, the transverse momentum of the  $S1 * \bar{C} * S2$  track is required to be above a certain threshold. The  $p_T$ -cut logic uses information from DC1 and DC6 to estimate the curvature of the kaon candidate track in the transverse plane, as explained in diagram 2.6. First, the wire hit by the  $S1 * \bar{C} * S2$  track in DC6 is identified and the corresponding wire number in DC1 (same  $\varphi$ ) is calculated. Then, assuming the kaon candidate track originates from the center of the target, the  $p_T$ -cut requires a hit in DC1 within a sector of  $\pm 4$ ,  $\pm 3$ ,  $\pm 2$  or  $\pm 1$  half drift cells around the calculated wire number in DC1, which corresponds to a minimum transverse momentum of 200, 270, 400 or 640 MeV/c, respectively. In order to define regions of half drift cells, left-right ambiguities must be solved online. For this reason, the sense wires of the drift chambers are constructed in doublets.

- **The Intermediate Decision Logic (IDL)**

The IDL tests whether there are enough hits in the tracking chambers to be associated with tracks, and counts the number of tracks originating from inside the PC's (primary tracks), the number of charged tracks and the number of kaon tracks.

Besides the S1 and the  $S1 * \bar{C} * S2$  sector hit maps obtained during the EDL and  $p_T$ -cut stage, the IDL decisions are based on the sector hit maps of (PC1 "OR" PC2), (DC1 "OR" DC2) and (DC5 "OR" DC6), where the tracking chambers are logically subdivided in 64 sectors. The different track types are then defined in the following way:

- primary track : hit in (PC1 "OR" PC2) AND (DC1 "OR" DC2) AND (DC5 "OR" DC6) AND (S1) ,
- charged track : hit in (DC5 "OR" DC6) AND (S1) ,



- kaon track : hit in (PC1 "OR" PC2) AND (S1 \*  $\bar{C}$  \* S2) AND ( $p_T > p_T\text{-cut value}$ ) .

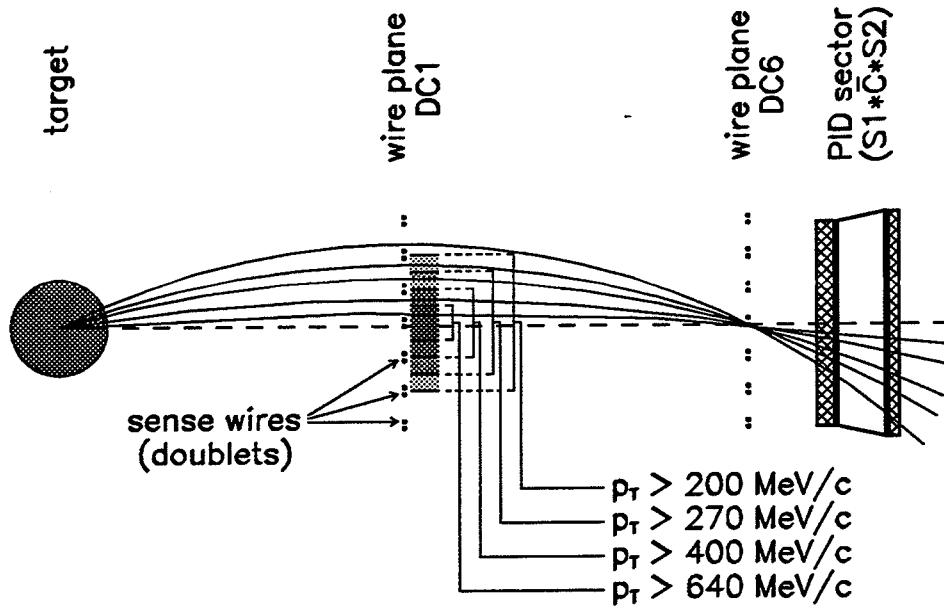


Figure 2.6: Principle of the  $p_T$ -cut logic.

In the run periods P7, P8 and P9 (second half of 1990), data were taken with the following trigger configurations:

- **The "minimum bias" trigger**

The data taken with this trigger type are used for detector calibration and to control the biases introduced on the selected data by the other trigger types. The only condition imposed by the trigger (EDL) is:

- At least one hit in S1.

- **The trigger 233 (short distance trigger)**

The data collected with the trigger 233 are used to study the detector performance, to investigate the fraction and type of background events, to determine the ratio between the number of tagged  $K^0$  and  $\bar{K}^0$  events and to measure the detector acceptance for  $K^0$  ( $\bar{K}^0$ ) decays as a function of the decay eigentime. The trigger conditions are:

- At least one kaon track (with a  $p_T$ -cut value of 400 MeV/c).
- At least two primary tracks.

- **The trigger 433 (long distance trigger)**

The trigger 433 selects data for the physics analysis of  $K^0 (\bar{K}^0) \rightarrow \pi^+\pi^-, \pi^\pm l^\mp \nu$  decays with a neutral kaon decay eigentime  $t > 5 \tau_S$ . The trigger conditions are:

- At least one kaon track (with a  $p_T$ -cut value of 400 MeV/c).
- Exactly two primary tracks.
- At least four charged tracks.

The data used in the analysis of the  $K^*(892)$  mass difference (section 4) were taken with the trigger 233.

### The Data Acquisition System (DAQ)

The CPLEAR data acquisition system is based on the VALET-Plus, a VME based microprocessor system [17], and controlled from the CPLEAR VAX cluster. It allows two simultaneous data streams:

1. In the **main data stream**, the complete detector and trigger information is written to tape ( $\sim 2500$  bytes/event) at a rate of  $\sim 800$  events per second. The events recorded in this data stream are used for the determination of the time-dependent asymmetries and in the analysis of the semileptonic decays. The data from the subdetectors are first converted in the front end electronics (FE). For events passing the trigger conditions, the data are sent from the FE to the corresponding Root-Read-Out (RRO) valet. The RRO allows online monitoring of the subdetector event information, and passes the data on to the event builder (EB) valet. In the EB, the data from the different subdetectors are merged to one event, which is then sent via an optical data link to tape recording and online event monitoring.
2. In the **fast data stream**, only certain information collected by the various trigger stages is written to tape ( $\sim 1000$  bytes/event), but at an increased rate of  $\sim 1200$  events per second. This fast data stream is needed to collect the required statistic of several  $10^9$   $K^0 (\bar{K}^0) \rightarrow \pi\pi$  events for the anticipated precision in the determination of  $\epsilon'/\epsilon$  with the integral asymmetries  $I_{+-}$  and  $I_{00}$ .

### 3 The Proportional Chambers PC1 and PC2

PC1 and PC2 are two extremely light, cylindrical multi wire proportional chambers with good spatial resolution. They are the innermost tracking devices of the CPLEAR detector. The two chambers are identical except for some geometrical quantities. They provide both wire and strip information, allowing the reconstruction of two points on each charged particle track traversing the chambers. The wire information is used by the online trigger-logic to validate a track and to identify it as primary or secondary track.

Since access to the chambers is only possible from the downstream side of the detector, PC1 and PC2 are supported and read out from this side, including high voltage and gas supply connections.

#### 3.1 Principle of Operation of Proportional Chambers

A brief description for the operation of such a multi wire proportional chamber is described below, whereas more details may be found in [18], [19].

Multi wire proportional chambers consist of an anode plane made of many thin parallel wires, placed between two cathode planes. The cathode planes are often foils, carrying a thin layer of metal in the form of strips. The volume between the cathode planes is filled with a suitable gas. Figure 3.1 shows the important geometrical parameters of such a chamber.

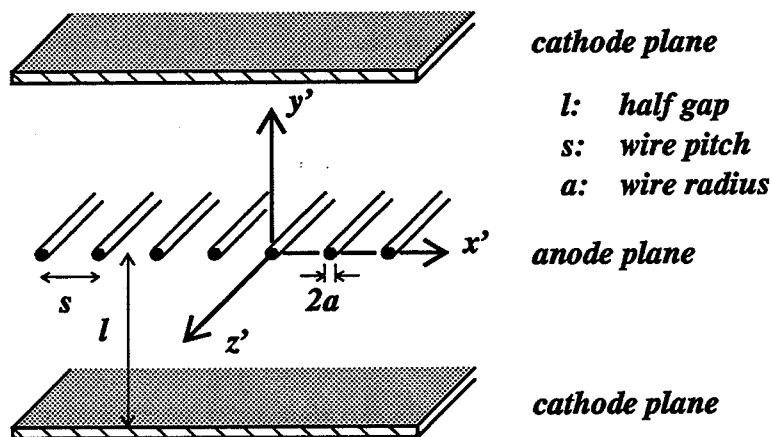


Figure 3.1: The important geometrical parameters of a multi wire proportional chamber. For PC1 and PC2 they are  $l = 3$  mm,  $s = 1$  mm and  $2a = 15$   $\mu$ m.

The analytic expressions for the electrical potential  $V(x', y')$  and the electric field  $\vec{E}(x', y')$  are given below. The formulae are obtained with the convention that the

potential is zero at the cathode planes and has the value  $V_o$  at the surface of the anode wires. The coordinate system  $(x', y', z')$  is defined in figure 3.1. The expressions for  $V$  and  $\vec{E}$  are [18]

$$V(x', y') = \frac{CV_o}{4\pi\epsilon_o} \cdot \left( \frac{2\pi l}{s} - \ln \left( 4 \left[ \sin^2\left(\frac{\pi x'}{s}\right) + \sinh^2\left(\frac{\pi y'}{s}\right) \right] \right) \right), \quad (3.1)$$

$$E_{x'}(x', y') = \frac{CV_o}{2\epsilon_o s} \cdot \frac{\sin\left(\frac{\pi x'}{s}\right) \cdot \cos\left(\frac{\pi x'}{s}\right)}{\sin^2\left(\frac{\pi x'}{s}\right) + \sinh^2\left(\frac{\pi y'}{s}\right)}, \quad (3.2)$$

$$E_{y'}(x', y') = \frac{CV_o}{2\epsilon_o s} \cdot \frac{\sinh\left(\frac{\pi y'}{s}\right) \cdot \cosh\left(\frac{\pi y'}{s}\right)}{\sin^2\left(\frac{\pi x'}{s}\right) + \sinh^2\left(\frac{\pi y'}{s}\right)}, \quad (3.3)$$

$$E_{z'}(x', y') = 0, \quad (3.4)$$

$$|\vec{E}(x', y')| = \frac{CV_o}{2\epsilon_o s} \cdot \sqrt{\frac{1 + \tan^2\left(\frac{\pi x'}{s}\right) \tanh^2\left(\frac{\pi y'}{s}\right)}{\tan^2\left(\frac{\pi x'}{s}\right) + \tanh^2\left(\frac{\pi y'}{s}\right)}}, \quad (3.5)$$

with

$$C = \frac{2\pi\epsilon_o}{\frac{\pi l}{s} - \ln\left(\frac{2\pi a}{s}\right)}, \quad (3.6)$$

where  $V_o$  is the potential difference between anode and cathode,  
 $C$  is the capacitance per unit length of one anode wire with respect to the cathode planes,  
 $l$  is the gap between anode and cathode planes (half gap),  
 $s$  is the distance between two wires (wire pitch) and  
 $a$  is the wire radius.

Figure 3.2 shows the electrical potential and the field strength for the geometry of PC1 and PC2 at a voltage of  $V_o = 2700$  V. The electric field strength at the anode wires ( $E_a$ ) and at the cathode planes ( $E_c$ ) are approximately given by

$$E_a \simeq \frac{CV_o}{2\pi\epsilon_o} \cdot \frac{1}{a} \quad \text{and} \quad E_c \simeq \frac{CV_o}{2\epsilon_o s}. \quad (3.7)$$

A charged particle traversing the chamber interacts with the chamber gas, mainly by Coulomb-interaction. The energy loss in the gas is given by the Bethe-Bloch formula [18]:

$$\frac{dE}{dX} \equiv \frac{dE}{dx} \rho = -K \frac{Z\rho}{A\beta^2} \cdot \left[ \ln \left( \frac{2mc^2\beta^2 E_M}{I^2(1-\beta^2)} \right) - 2\beta^2 \right], \quad (3.8)$$

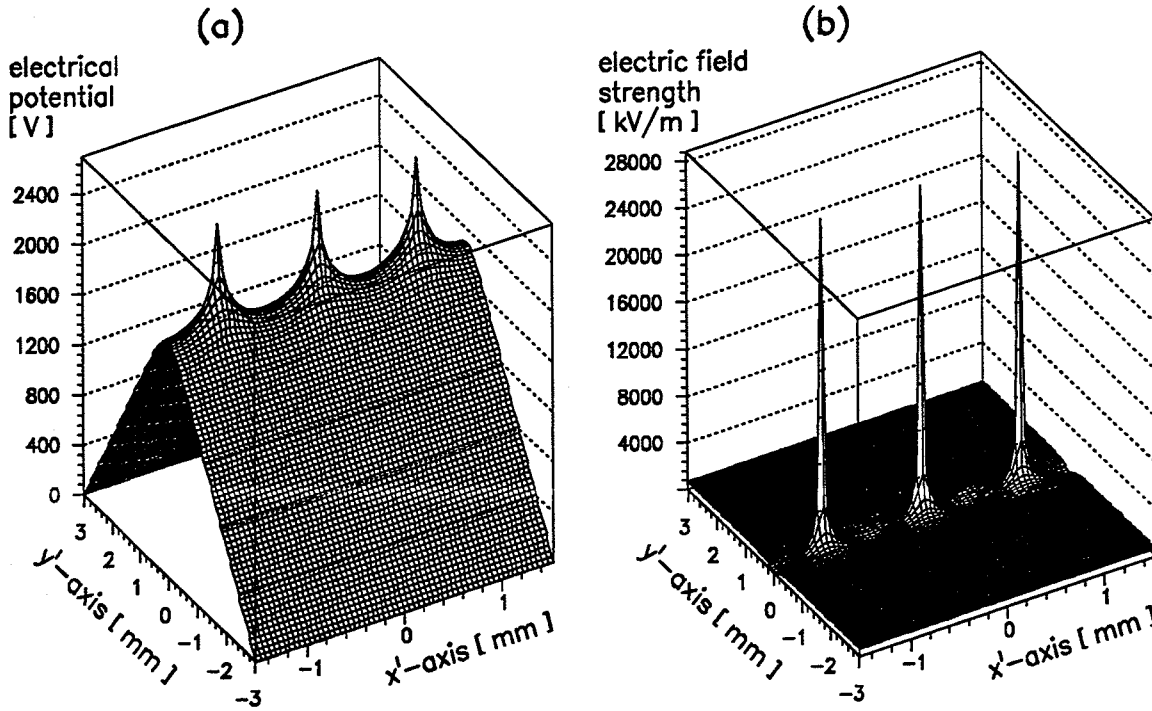


Figure 3.2: The electrical potential (a) and the electric field strength (b) for PC1 and PC2 with  $V_o = 2700$  V,  $s = 1$  mm,  $l = 3$  mm and  $a = 7.5$   $\mu$ m.

with

$$x = X \cdot \rho,$$

$$K = \frac{2\pi N z^2 e^4}{mc^2},$$

$$E_M = \frac{2mc^2 \beta^2}{1 - \beta^2},$$

where  $Z, A$  are the mediums atomic number and atomic mass,  
 $\rho, I$  are the density and effective ionization potential of the medium,  
 $z$  is the charge of the traversing particle,  
 $m, e$  are the mass and charge of the electron and  
 $N$  is Avogadro's number.

Gas molecules are ionized along the particle trajectory, due to the interaction of the particle with the chamber gas. The resulting number of electron-ion pairs,  $N_p$ , is

$$N_p = n_p \cdot t = \frac{\Delta E}{W_i} \cdot t, \quad (3.9)$$

where  $n_p$  = number of electron-ion pairs per unit length,  
 $t$  = track length in gas volume,  
 $\Delta E$  = total energy loss in the chamber and  
 $W_i$  = mean effective energy needed to produce one electron-ion pair.

This process of primary ionization is the basis for detecting charged particles in wire chambers. Under the influence of the electric field, the ions move towards the cathode, while the electrons drift to the closest anode-wire. Close to the wire, the electric field becomes very strong, and the electrons gain enough kinetic energy to ionize more gas molecules. This secondary ionization, also called gas amplification, leads to an avalanche of electrons and produces a charge large enough to be detected with electronic devices. The gas amplification factor,  $M$ , is usually in the range of  $10^4$  to  $10^6$ .

The drift of electrons and ions in the electric field reduces the electrostatic energy stored in the chamber, and hence induces a negative signal on the anode wire hit by the avalanche and a positive signal on the cathodes. The drift of electrons produces the fast rise of the output signal but contributes little to the pulse height. This is because the electron drift velocity is high, but the mean drift length is short, since most of the electron-ion pairs are produced by gas amplification, which starts only a few wire radii away from the anode wire. The main contribution to the pulse height comes from the positive ions, which have a long drift length.

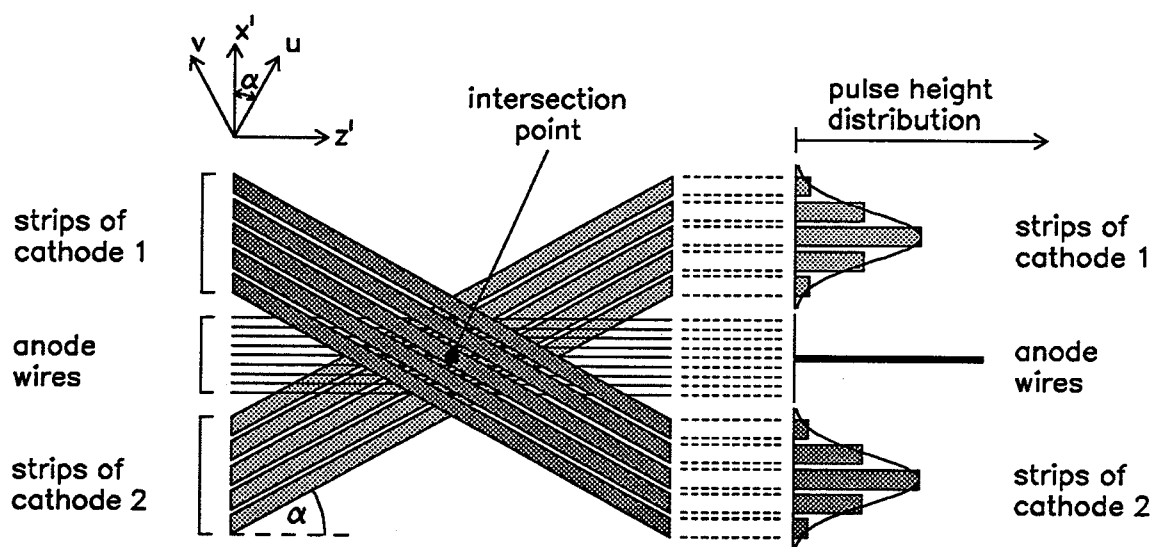


Figure 3.3: Pulse height distribution on anode wires and cathode strips, which allow the reconstruction of the intersection point between the particle trajectory and the anode plane.

The electric signals induced on anode wires and cathodes allow the reconstruction of the intersection point between the particle trajectory and the anode plane, as explained in figure 3.3. The anode wire signals determine the  $x'$ -coordinate with an intrinsic precision of  $\pm s/2$ . For the reconstruction of the  $z'$ -coordinate, the cathode planes are subdivided in strips which form an angle of  $\pm\alpha$  to the wires. Two planes of strips at different angles to the wires are needed in order to reconstruct more than one intersection point in the same event unambiguously. The induced pulse height

distributions on the strips, which is Gaussian and centered at the intersection point, allow the determination of the coordinates perpendicular to the strip direction ( $u$  and  $v$ ). The  $z'$ -coordinate can then be calculated from the  $u$ - and  $v$ -coordinates.

electrostatic properties		gas amplification properties	
$C$	$= 4.46$ pF/m	$dE/dX$	$= 2.85$ keV/cm
$E_a$	$= 2.88 \cdot 10^7$ V/m	$W_i$	$= 25.4$ eV
$E_c$	$= 6.80 \cdot 10^5$ V/m	$n_p$	$= 112$ cm <sup>-1</sup>
		$M$	$\simeq 2 \cdot 10^5$

Table 3.1: Electrostatic and gas amplification properties of PC1 and PC2 for  $V_o=2700$  V,  $l=3$  mm,  $s=1$  mm,  $a = 7.5$   $\mu$ m and a gas mixture of 79.5 % argon, 20.0 % isobutane and 0.5 % freon.

In table 3.1, the electrostatic and gas amplification properties for the geometry and gas mixture of PC1 and PC2 are listed. The quoted number of primary electron-ion pairs,  $n_p$ , does not take into account the freon in the gas mixture, which captures a fraction of the primary electrons (see section 3.8.1).

### 3.2 Geometry of PC1 and PC2

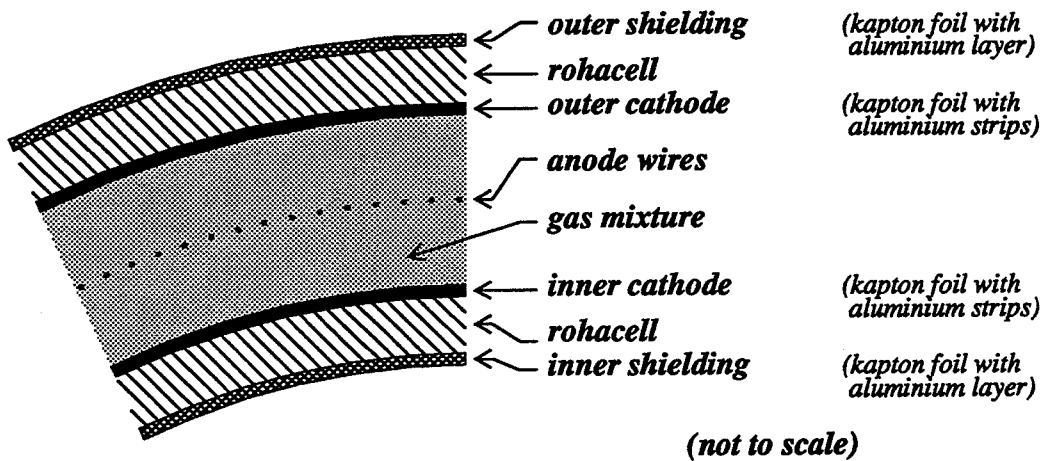


Figure 3.4: Transverse view of a chamber wall section.

Each of the proportional chambers PC1 and PC2 consists of two cylinders with different radii. The smaller cylinder carries the inner cathode and the anode wires, while the larger one supports the outer cathode. Figure 3.4 shows a transverse view of a chamber wall section.

parameter	PC1	PC2
outer radius	100.25 mm	132.00 mm
radius of outer strips	98.25 mm	130.00 mm
radius of wires	95.25 mm	127.00 mm
radius of inner strips	92.25 mm	124.00 mm
inner radius	90.25 mm	122.00 mm
active length	700.00 mm	700.00 mm
outer wall thickness	2.00 mm	2.00 mm
inner wall thickness	2.00 mm	2.00 mm
full gas gap	6.00 mm	6.00 mm
wire spacing	1.039 mm	1.039 mm
number of wires	576	768
wire diameter	15 $\mu\text{m}$	15 $\mu\text{m}$
strip width	1.721 mm	1.721 mm
strip gap	0.500 mm	0.500 mm
number of outer strips	262	325
number of inner strips	246	310
outer strip print pitch	2.356 mm	2.513 mm
inner strip print pitch	2.356 mm	2.513 mm
$d\varphi/dz$ of outer strips	-0.2062 Deg/mm	-0.2332 Deg/mm
$d\varphi/dz$ of inner strips	+0.2196 Deg/mm	+0.2445 Deg/mm
angle $\alpha$ betw. strips and wires	$\pm 19.474$ Deg	$\pm 27.888$ Deg
covered solid angle	$0.965 \cdot 4\pi$ steradians	$0.940 \cdot 4\pi$ steradians

Table 3.2: Geometrical parameters for PC1 and PC2.

The active length of a chamber is 700 mm and the radius of the anode plane is 95.25 mm for PC1 and 127.00 mm for PC2. The covered solid angle is  $(0.965 \cdot 4\pi)$  steradians for PC1 and  $(0.940 \cdot 4\pi)$  steradians for PC2.

With a wire pitch of 1.039 mm, both chambers have an intrinsic spatial resolution of  $\sigma_{r\varphi} = 300 \mu\text{m}$ . In table 3.2, the geometrical parameters are listed in more detail.

### 3.3 Gas Mixture

To find a good gas mixture, we made extensive tests with a small prototype chamber (see [19]). As a result of these tests, two mixtures were found with equally good characteristics, such as plateau length, plateau start, gain etc. (see section 3.8.2).



The two mixtures are:

- 79.5 % argon, 20.0 % isobutane, 0.5 % freon and
- 69.0 % argon, 30.0 % ethane, 1.0 % freon.

For PC1 and PC2, the latter mixture with ethane ( $C_2H_6$ ) as the main quenching component was initially chosen due to the then, supposedly less problematic consequences of aging in this mixture. However, both cathode foil etching (due to high electric field) and polymerization resulting in anode wire deposits (due probably to higher quencher concentration) were experienced after high rate source tests. After thorough cleaning of both chambers, we decided to change to the isobutane mixture with a lower quencher concentration and thus a lower working voltage. So far, no deposits have been noticed and no further cathode foil etching has occurred.

The functions of each gas component are [18]:

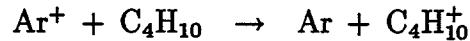
**Argon:** Avalanche multiplication can start at much lower electric fields in noble gases than in complex molecules, where many non-ionizing energy dissipation modes are available. Thus, a mixture with a noble gas as the main component has the advantage of a low working voltage. Within the family of noble gases, argon is the best compromise between a high ionization yield and low cost. However, using argon alone leads already with low gains to a permanent discharge for the following two reasons:

- In the process of the gas amplification, atoms are ionized and excited. The only way an excited argon atom can return to the ground state is by emitting a photon. Since the minimum energy of the photon (11.6 eV for argon) is always above the ionization potential of the cathode material (5.96 eV for aluminium), the photon can extract an electron from the cathode, which then initiates a new avalanche.
- Under the influence of the electric field, the argon ions drift to the cathode and are neutralized by extracting an electron from the cathode material. The difference in energy is compensated by the emission of a photon or the emission of a second electron from the cathode (secondary emission). Both processes can lead to a new avalanche.

**Isobutane:** Isobutane ( $C_4H_{10}$ ), the quenching component of the mixture, makes a stable high-gain operation of the chambers possible by:

**photon absorption:** Isobutane has many rotational and vibrational degrees of freedom. This allows the absorption of photons over a wide energy range. The excess energy can be dissipated either by elastic collisions or dissociation into simpler radicals.

**charge exchange:** The ionization potential for isobutane (10.8 eV) is lower than for argon (15.8 eV), resulting in a very efficient charge exchange mechanism:



Although most of the primary ions are argon atoms, mainly isobutane ions neutralize at the cathode.

**suppression of secondary emission:** When isobutane ions neutralize at the cathode, the radicals either break up into simpler molecules (dissociation) or form larger complexes (polymerization). Secondary emission is very unlikely.

**Freon:** Freon ( $\text{CF}_3\text{Br}$ ), an electronegative gas, captures free electrons and forms negative ions which are too heavy to induce avalanches. We added freon to the gas mixture for three reasons.

- If freon is present in the gas in such a concentration that the mean free path for electron capture,  $\lambda_{cap}$ , is shorter than the distance from the anode to the cathode, electrons liberated at the cathode (either by photon absorption or secondary emission) will have a very small probability to reach the anode.
- Freon reduces the mean wire hit multiplicity, especially for inclined tracks, since only electrons within a distance of  $\lambda_{cap}$  can reach the anode. This results in an improved spatial resolution of the chamber.
- Freon reduces the maximum electron drift time and hence improves the rate capability of the chamber.

### 3.4 Materials Used in the Construction

In order to minimize regeneration effects (see 2.4), the proportional chambers are required to have a low mass in the active region of the detector. This implies a construction of the chamber walls with either light or very thin materials. On the other hand, the chambers must be strong enough to withstand the stress produced by the wire tension ( $\sim 230$  N for PC2) and to be supported on one side in the detector, since access is only possible from the downstream side.

To meet these requirements, a self-supporting sandwich structure of rohacell and kapton foils was used for the chamber walls. The resulting surface density for one complete chamber is only  $41.5$  mg/cm<sup>2</sup>, representing  $1.1 \cdot 10^{-3}$  radiation lengths ( $X_0$ ). The different contributions are listed in table 3.3.

The chambers are made of rohacell (a polymethacrylimide hard foam), kapton polyimide films, stesalit rigid sheet materials, araldite glue and goldplated tungsten-rhenium wires. The purpose of each material is explained below, whereas their properties are summarized in table 3.4.

contribution from	surface density [mg/cm <sup>2</sup> ]	radiation lengths [10 <sup>-5</sup> X <sub>0</sub> ]
1 kapton foil (25 μm)	3.5	8.7
1 rohacell sheet ( 2 mm)	10.0	25.2
1 araldite layer	1.5	4.0
anode wires	0.3	5.1
gas ( 6 mm)	1.2	5.0
1 chamber wall	20.0	50.6
1 chamber	41.5	111.3

Table 3.3: The different contributions to the surface density and the radiation lengths of a chamber.

material constant	Rohacell 50	Kapton H	Luma Wire 861	Stesalit 4411 W	Araldite Standard
density [kg/m <sup>3</sup> ]	50	1.42 · 10 <sup>3</sup>	19.2 · 10 <sup>3</sup>	1.8 · 10 <sup>3</sup>	1.1 · 10 <sup>3</sup>
coefficient of thermal expansion [m/(m · ° K)]	3.3 · 10 <sup>-5</sup>	2.0 · 10 <sup>-5</sup>	4.5 · 10 <sup>-6</sup>	11.5 · 10 <sup>-6</sup>	≈ 7 · 10 <sup>-5</sup>
coefficient of hygroscopic expansion [m/(m · %rel.hum.)]	1.3 · 10 <sup>-5</sup>	2.2 · 10 <sup>-5</sup>	...	...	...
tensile modulus [N/m <sup>2</sup> ]	7.0 · 10 <sup>7</sup>	3.0 · 10 <sup>9</sup>	4.1 · 10 <sup>11</sup>	2.4 · 10 <sup>10</sup>	≈ 5 · 10 <sup>8</sup>
max. tensile strength [N/m <sup>2</sup> ]	1.9 · 10 <sup>6</sup>	1.7 · 10 <sup>8</sup>	3.5 · 10 <sup>9</sup>	6.6 · 10 <sup>8</sup>	1.5 · 10 <sup>7</sup>
dielectric strength [kV/mm]	...	280	...	19	17
radiation lengths [m]	7.94	0.29	3.5 · 10 <sup>-3</sup>	...	0.35

Table 3.4: The important properties of the materials used in the construction of PC1 and PC2.

**Rohacell** is a hard foam with a good relation between density and stiffness. The 2 mm thick plate gives the chamber wall the required rigidity.

**Kapton** polyimide film is a light and extremely tough insulator. The two 25 μm thick foils reinforce the chamber walls and help to keep the form as cylindrical as possible. The foils are aluminised, either completely for electrical shielding

or in strips for the cathodes. The aluminium layer for the shielding is  $0.03 \mu\text{m}$  thick, while the strips have a thickness of  $0.1 \mu\text{m}$ . Since the strips can be easily damaged by scratches, the foils must be handled with care.

**Stesalit** is made of layered glass fibre mats and epoxy. The rings support and protect the fragile chamber walls and the readout prints, contain the gas inlets, and provide connections to further support structures.

**Luma Wire** is made of a tungsten based alloy with 3 % rhenium and has a goldplated surface ( $0.15 \mu\text{m}$ ). The addition of rhenium increases the tensile strength of the wire, while the goldplated surface ensures good electrical properties.

### 3.5 Construction of PC1 and PC2

PC1 and PC2 consist of an inner cylinder (inner chamber wall) carrying the inner cathode and the anode wires and an outer cylinder supporting the second cathode plane. Both cylinders are made of a self-supporting sandwich structure, consisting of rohacell with two kapton foils glued on either side with araldite. At the ends of the cylinders, stesalit rings and the read-out prints are glued on. Diagram 3.5 shows a side view of the chambers.

For the construction of each chamber wall, a precisely machined hollow steel cylinder was used, with a vacuum pump connection and many small holes in the wall. This allowed an underpressure to be maintained in the steel cylinder which helped to press the different layers tightly against the cylinder. In this way, air-pockets were avoided and irregularities in the cathode radii could be reduced.

The construction of an inner wall is described here. Before the construction could start, the rohacell sheet had to be preshrunk in an oven for 6 hours at a temperature of  $180 \text{ }^\circ\text{C}$ . The sheet was then cut to the right form, wound around the steel cylinder and pressed against it with teflon tape. The whole cylinder was again placed in the oven under the same conditions, allowing the tension in the rohacell due to the bending to be removed and leaving the rohacell in a cylindrical form.

The next step is the sandwich construction of the chamber wall. In order to remove the completed chamber wall from the steel cylinder without damaging the innermost aluminium layer, a thin film of teflon was first sprayed onto the steel cylinder. Then we put a mylar foil around it which again was sprayed with teflon. This procedure is particularly important for the outer cylinder, where the cathode strips are on the inside (see figure 3.4).

For the inner wall, the first layer is the fully aluminised kapton foil with the aluminium layer on the inside of the cylinder. On top of it, the 2 mm thick rohacell sheet was

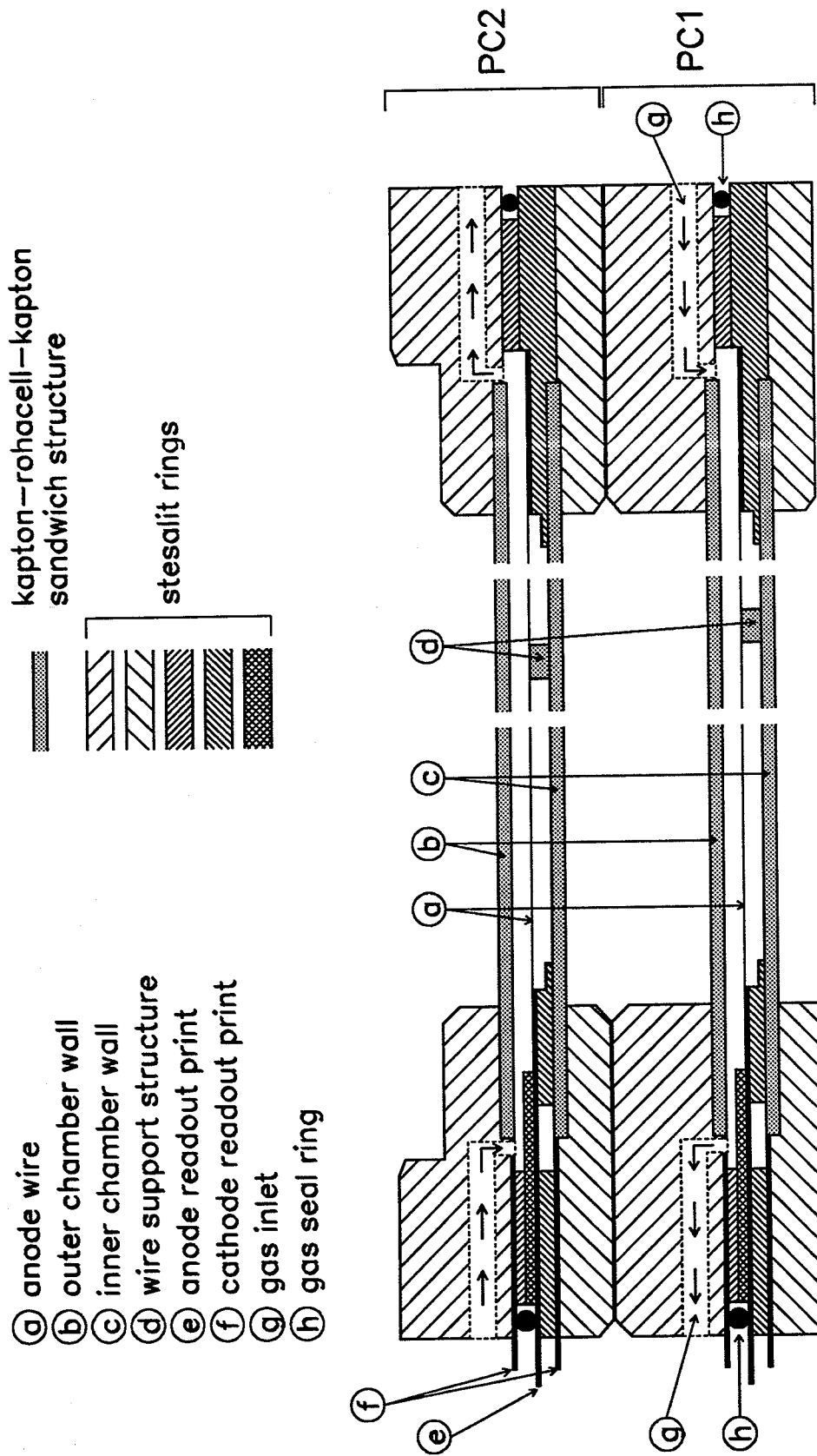


Figure 3.5: Cut along the z-axis through both chambers.

glued and finally the kapton foil with the aluminium strips was added with the strips being on the outside.

To glue the different layers together, an amount of araldite corresponding to  $3 \text{ mg/cm}^2$  was first spread on an separate mylar foil. The amount of glue was split between the cylinder and the foil by winding the foil around the cylinder and removing it again several times. In this way, we achieved an araldite layer of only  $1.5 \text{ mg/cm}^2$  uniformly spread on the cylinder surface and the next layer could be added.

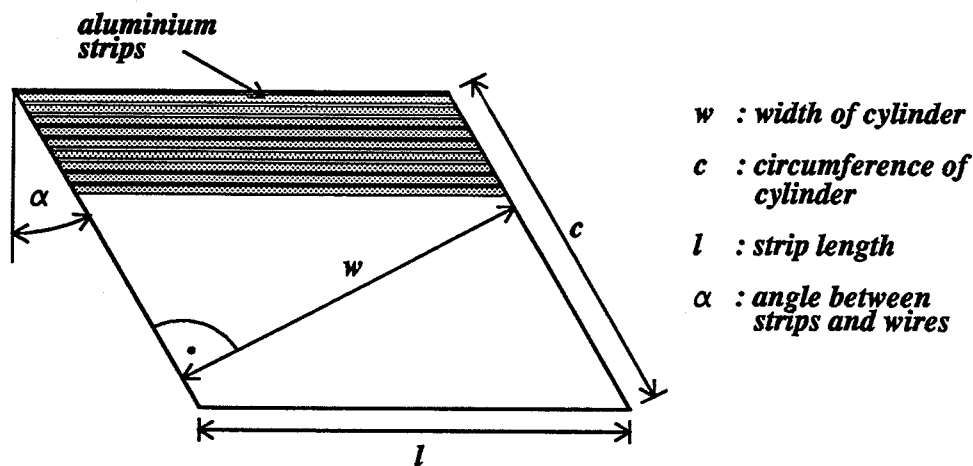


Figure 3.6: Preparation of a kapton foil.

The layers are cut in the form of a parallelogram, as shown in fig. 3.6. For the inner kapton foil and the rohacell sheet, the angle  $\alpha$  is 45 degrees, while for the cathode foils  $\alpha$  is equal to the angle between the strips and the anode wires (see table 3.2). The inner kapton foil, carrying the shielding layer, has a width of 740 mm, while the rohacell and the cathode foils are 750 mm wide. This difference in width is necessary to avoid sparking at the end of the cylinder due to the potential difference between the cathode and the shielding.

Before the cathode foil was added, the rohacell was ground down to the exact radius. In order to glue the cathode foil on the rohacell, a kapton band, 5 mm wide, was placed along the joint between the rohacell and the foil. This was necessary to ensure good contact between the cathode foil and the rohacell sheet along the joint, where the two ends must not overlap.

Two wire supports (see figure 3.5), made of rohacell bands 5 mm wide and 3 mm high, and the two stesalit rings carrying the anode prints were then glued in place on the cathode foil. The stesalit rings and the wire support structures were ground down until the anode prints matched perfectly. Finally, a kapton band was glued on top of the wire support bands.

The wire supports are necessary to avoid displacements of the anode wires due to electrostatic forces. The relationship between the wire tension  $\tau$  and the critical unsupported wire length  $L_c$  is given by [18]

$$L_c = \frac{s}{CV_o} \sqrt{4\pi\epsilon_o\tau}, \quad (3.10)$$

where  $s$  is the wire pitch,  $C$  is the capacitance per unit length of one anode wire with respect to the cathode planes (equation 3.6) and  $V_o$  is the potential difference between cathode and anode. The maximum allowed tension for the Luma wire is 0.62 N (see table 3.4). We choose a tension of 0.3 N, which corresponds to a critical length  $L_c=48$  cm for a high voltage of  $V_o=2700$  V. With the wire supports at  $z = \pm 17$  cm for PC1 ( $z=\pm 15$  cm for PC2), the maximum distance between two supports is 34 cm and hence uncritical.

The inner chamber wall was removed from the steel cylinder and most of the remaining stesalit rings and the cathode readout prints could be glued in place. We used small metal bands to connect the cathode strips to the printed circuit boards. The approximately 1 cm long and 0.2 mm wide bands had been soldered on the print in advance and suitably bent. Once the cathode print was in position, these metal bands pressed against the cathode strips and could easily be contacted with conductive silver paint. The connections were covered with araldite for protection.

At the non-readout side, all the cathode strips were interconnected with a high resistive graphite paint in order to avoid a charging up of partially disconnected strips. The resistance between two strips is in the range of 10 k $\Omega$  to 100 k $\Omega$  and hence has no effect on the cathode signals. The electronic components were then mounted on the cathode print and two layers of electrically insulating varnish (Scotchcal 3930) were sprayed to avoid sparking. Next, the anode print and the last stesalit rings were added. Both cathode and anode prints were reinforced with several smaller stesalit rings.

Finally, the anode wires had to be soldered. The Luma wire, on rolls of 800 m, was stretched by machine onto a large frame, with a tension of 0.3 N and a pitch of 1 mm. From this frame, the wire was soldered to smaller frames, leaving the tension and pitch unchanged. One of these smaller frames was then mounted together with the inner cylinder on a specially designed apparatus, from where the wires could be soldered directly on to the prints. The positional adjustment of the wire on the solder pad was made by eye, using a magnifying glass.

For PC2 with 768 wires, the wire tension produces a stress of 230 N on the chamber wall, causing the cylinder to shrink a little. To have equal tension for all wires, the inner cylinder was precompressed with a load equal to the total wire tension and then this load was reduced gradually during the soldering. In order to keep the stress on the inner chamber wall symmetric, only every eighth wire was soldered in one turn. When all the wires were soldered, they were glued to the wire supports with araldite.

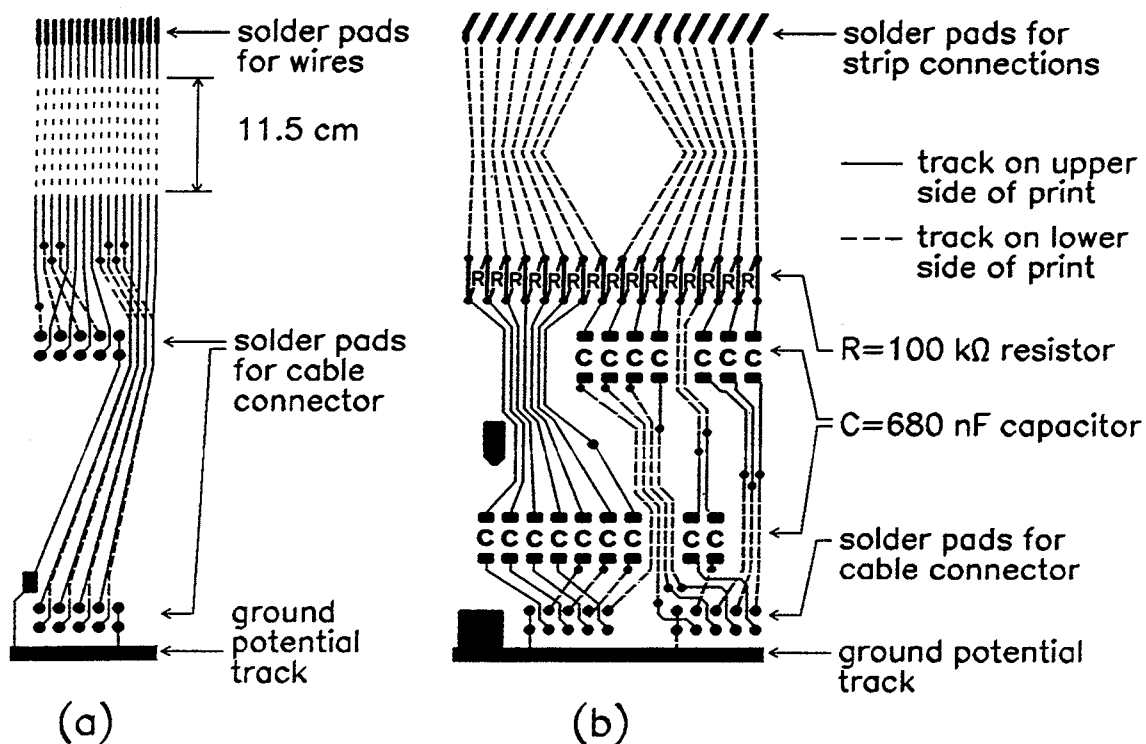


Figure 3.7: Design for the anode (a) and cathode (b) print sector, each containing 16 channels.

Figure 3.7 shows the design of the anode and cathode print sector, corresponding to 16 channels. The anode print contains an integer number of sectors and no high voltage connections. The cathode prints are more complicated, because they carry high voltage and ground potential tracks close together and contain not an integer number of sectors. The channels are interconnected with  $100\text{ k}\Omega$  resistors in order to keep disconnected strips (e.g. broken readout cables) from charging up. The cathode signals are decoupled from the high voltage with capacitors of  $680\text{ nF}$ . Due to the high density of strip channels on the print, we used small ( $5 \times 4 \times 2.5\text{ mm}^3$ ) surface mount device (SMD) capacitors and arranged them in two rows.

During the construction of the chamber, the following tests were performed:

1. The connections between the cathode strips and the readout prints were tested. Only connections with a resistance of less than  $8\ \Omega$  were accepted.
2. Before mounting the capacitors on the cathode prints, they were kept under a high voltage of  $1500\text{ V}$  for 24 hours. Capacitors showing any current were rejected.
3. Several kinds of varnish suitable for high voltage insulation were tested to cover the cathode prints. For each kind, a fully equipped print sector was prepared



and sprayed with two layers of varnish. The sector sprayed with Scotchcal 3930 held the highest voltages.

4. The tension of every wire was measured before it was glued to the wire supports. This was done by placing the wire in a magnetic field and inducing an alternating current in the wire. The frequency of the current was then varied until the first harmonic was observed. The basic frequency  $\nu_o$  and the wire tension  $\tau$  are related as [20]

$$\nu_o = \frac{1}{2L} \sqrt{\frac{\tau}{\rho_L}}, \quad (3.11)$$

where  $\rho_L = a^2\pi\rho$  is the wire mass per unit length,  $a$  is the wire radius and  $L$  is the wire length. The frequency for a wire tension of 0.3 N is 209 Hz. We accepted basic frequencies in the range of 205 Hz to 225 Hz. This corresponds to a lower limit for the wire tension of  $\tau_{min} = 0.29$  N and an upper limit of  $\tau_{max} = 0.35$  N.

5. The change of the critical high voltage  $V_{crit}$ , above which electrostatic instabilities of the anode wires may occur, was calculated for the following three effects:
  - A wire pitch reduction,  $\Delta s$ , due to inaccurate wire positioning on the solder pad.
  - A temperature change,  $\Delta T$ .
  - A change in the relative humidity,  $\Delta H$ .

From equation 3.10 and 3.6,  $V_{crit}$  is given by

$$V_{crit} = \frac{s}{CL} \cdot \sqrt{4\pi\epsilon_o\tau} = \frac{1}{L} \sqrt{\frac{\tau}{\pi\epsilon_o}} \left[ \pi l - s \ln\left(\frac{2\pi a}{s}\right) \right]. \quad (3.12)$$

The wires of PC1 were soldered at  $T_o = 21.5^\circ\text{C}$  and  $H_o = 42\%$ . PC1 is the more critical chamber, since the maximum unsupported wire length is  $L_{max} = 0.34$  m, while for PC2  $L_{max} = 0.30$  m. Inserting the values  $\tau_{min} = 0.29$  N and  $L_{max} = 0.34$  m in equation 3.12, one finds for PC1 a critical high voltage of  $V_{crit} \simeq 3800$  V.

The influence of a gap reduction on  $V_{crit}$  can be obtained from equation 3.12 as

$$\frac{\partial V_{crit}}{\partial s} = \frac{1}{L} \sqrt{\frac{\tau}{\pi\epsilon_o}} \left[ 1 - \ln\left(\frac{2\pi a}{s}\right) \right]. \quad (3.13)$$

The calculation of the dependence on temperature and relative humidity is based on the following assumptions:

- The values quoted above for  $\tau_{min}$  and  $V_{crit}$  are valid for the initial conditions  $T_o$  and  $H_o$  during the wire soldering.
- The gas mixture, which determines the conditions for the kapton foils adjoining to the gas volume, has a temperature  $T_G = 20^\circ\text{C}$  and a relative humidity  $H_G = 0\%$ .

- Outside the chamber (and for the outer kapton foils), the temperature and relative humidity change to  $T_{out} = T_o + \Delta T$  and  $H_{out} = H_o + \Delta H$ .
- In the rohacell between the kapton foils, the temperature and the relative humidity is given by  $(T_G + T_{out})/2$  and  $(H_G + H_{out})/2$ , respectively.
- Kapton foils and rohacell, as well as inner and outer cylinder are fixed rigidly.

The change in the cylinder length  $\Delta L$  (and thereby  $\Delta V_{crit}$ ) is then calculated by balancing of forces produced by all the changes in length of the different materials under the new conditions.

Taking into account the changes in temperature and relative humidity due to the gas mixture, but leaving the conditions outside the chambers unchanged,  $V_{crit}$  is lowered by  $\simeq 200$  V to

$$V_{crit} \simeq 3600 \text{ V}.$$

The dependence of  $V_{crit}$  on  $s$ ,  $T_{out}$  and  $H_{out}$  is, to a good approximation, linear in the considered range and was calculated to be

$$\frac{\partial V_{crit}}{\partial s} \simeq 1.2 \text{ V}/\mu\text{m}, \quad (3.14)$$

$$\frac{\partial V_{crit}}{\partial T_{out}} \simeq 6.8 \text{ V}/^\circ\text{C}, \quad (3.15)$$

$$\frac{\partial V_{crit}}{\partial H_{out}} \simeq 4.1 \text{ V}/\% \text{rel. humidity}. \quad (3.16)$$

Since the temperature in the experimental hall is guaranteed to be above  $10^\circ\text{C}$  and the wires are easily positioned within  $100 \mu\text{m}$  of the nominal position on the  $400 \mu\text{m}$  wide solder pads, the worst case is given by

$$\begin{aligned} s &= 800 \mu\text{m} \rightarrow \Delta s \simeq -200 \mu\text{m} \rightarrow \Delta V_{crit} \simeq -240 \text{ V}, \\ T_{out} &= 10^\circ\text{C} \rightarrow \Delta T_{out} \simeq -11.5^\circ\text{C} \rightarrow \Delta V_{crit} \simeq -80 \text{ V}, \\ H_{out} &= 0\% \rightarrow \Delta H_{out} \simeq -42.0\% \rightarrow \Delta V_{crit} \simeq -170 \text{ V}. \end{aligned}$$

Thus, one finds for the lower limit of the critical voltage

$$V_{crit} \simeq 3110 \text{ V},$$

which is still well above the required high voltage of  $\simeq 2750$  V for fully efficient anode wires (see section 3.8).

### 3.6 Installation in the CPLEAR Detector

The proportional chambers were assembled and connected to their support structure outside the experimental area. The support structure shown in diagram 3.8 consists of several flanges and two disks and has the following purposes:

- The PC coupling flange connects the support structure with PC1 and PC2.
- The drift chamber end flange is attached to the main PC support structure via the intermediate DC coupling flange, which allows both vertical and horizontal adjustment of the structure with the adjustment screws.
- The chariot coupling flange provides a connection to the "chariot", needed to insert the chambers into the detector.
- The support disks guide the target extraction tube and support the PC readout cables, high voltage cables and the gas tubes.

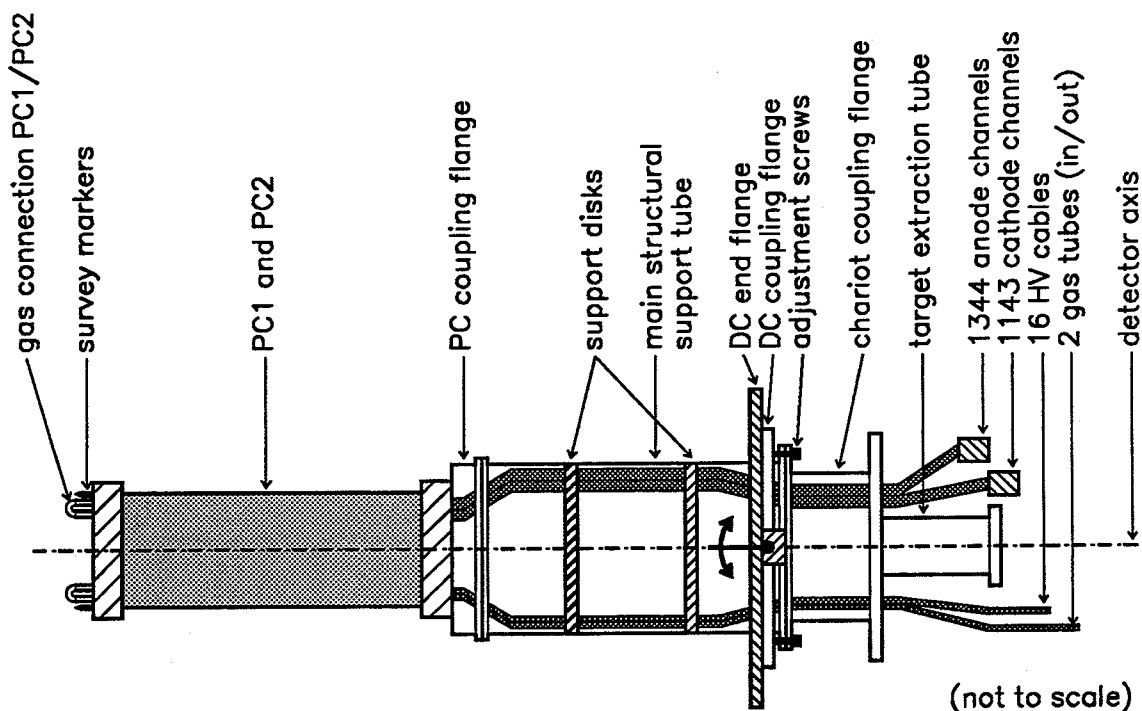


Figure 3.8: Support structure for the proportional chambers.

All readout cables were tested for continuity prior to mounting them on the prints. After the cabling, all channels were checked again for continuity and proper contact between cables and print connectors.

The proportional chambers were then transported to the experimental area, mounted on the "chariot" and inserted into the detector. The "chariot" was removed again after the support structure was fastened to the DC flange.

With the help of several survey markers and a set of cross wires, placed on the upstream stesalit rings, the chambers were surveyed and both vertically and horizontally adjusted.

### 3.6.1 Expected Sag of the Proportional Chambers

Since the proportional chambers are supported from only the downstream side, the opposite side sags mainly due to the weight of the stesalit rings. The size of this effect was calculated with the following assumptions:

1. The complete structure of PC1 and PC2 consists of
  - 8 kapton cylinders
  - 4 rohacell cylinders and
  - 2 tungsten-rhenium cylinders with a cross section equal to the sectional area of the anode wires.

The araldite layers are neglected.

2. All cylinders are fixed rigidly.
3. The bending radius at each point along the cylinder axis is calculated by balancing of the torques produced by the weight of the unsupported stesalit rings and the expansion and compression of the different cylinders. The weight of the chamber walls is neglected.

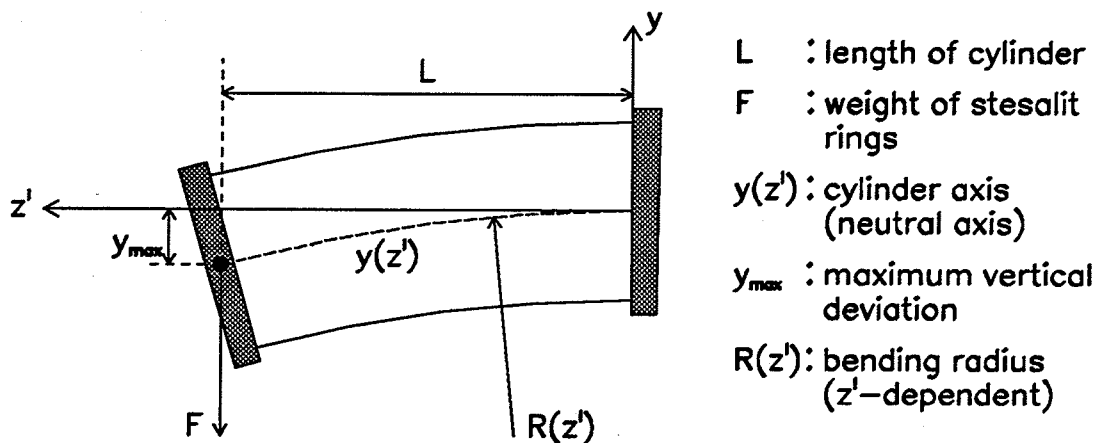


Figure 3.9: Sag of the proportional chambers due to the weight of the unsupported stesalit rings.

The definitions and the coordinate system used for the following calculation are explained in figure 3.9. For a slight bending of the chambers, the vertical displacement of the cylinder axis can be approximated by

$$-y(z') = \frac{F}{B_{tot}} \cdot \frac{z'^2}{2} \left( L - \frac{z'}{3} \right), \quad (3.17)$$

with

$$B_{tot} = \sum_{\text{all cylinders}} E_i \cdot J_i ,$$

$$J_i = \frac{\pi}{4} \left[ (r_i^{out})^4 - (r_i^{in})^4 \right] ,$$

where  $L$  is the length of the cylinders (0.71 m),  $F$  is the weight of the unsupported stesalit rings ( $\simeq 49$  N),  $E_i$  are the tensile moduli (or Young's moduli) of the cylinder material and  $r_i^{in}$  ( $r_i^{out}$ ) is the inner (outer) radius of the cylinder. With this model calculation, the following results were found:

1. The maximum vertical deviation of the PC cylinder axis from the detector axis is

$$-y_{max} = -y(L) = 0.98 \text{ mm} .$$

2. By adjusting the vertical position of the upstream cylinder end with the mechanism described above, this maximum deviation is reduced. Assuming both cylinder ends on the detector axis, one finds

$$-y_{max} = -y(z'_o) = 0.19 \text{ mm}$$

for  $z'_o = 0.30$  m.

3. The maximum gap reduction,  $\Delta l$ , due to bent cathode planes but straight anode wires between supports is

$$\Delta l = 0.045 \text{ mm} \quad (\text{PC1}) ,$$

and thus less than 2 %.

4. The weight of the stesalit rings is carried in the following way:

- 34.5 % ( $\simeq 16.9$  N) by the outer cylinder of PC2,
- 35.9 % ( $\simeq 17.6$  N) by the inner cylinder of PC2,
- 14.9 % ( $\simeq 7.3$  N) by the outer cylinder of PC1,
- 14.7 % ( $\simeq 7.2$  N) by the inner cylinder of PC1.

To verify the calculation, a stress test was performed with a chamber wall having the same geometry as the inner cylinder of PC2. One side of the chamber wall was rigidly attached to the test stand. The deviation of the unsupported cylinder end from its initial position was measured, while the load on this side was gradually increased up to 30 N. Good agreement was found between the measured and calculated values, as shown in diagram 3.10.

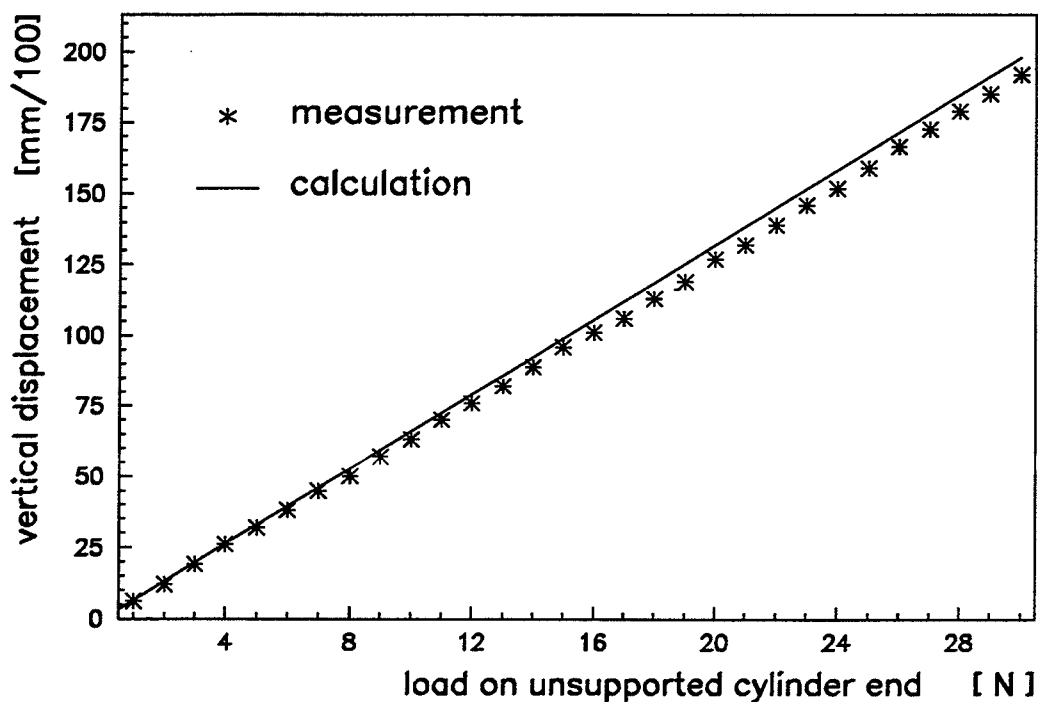


Figure 3.10: Result of the stress test with a cylinder equivalent to the inner wall of PC2.

### 3.7 Readout of the Wire Information

So far, only the wire information of the proportional chambers is read out. For the cathode strips, a readout with Analog-to-Digital Converters (ADC's) is planned in the near future at least for one chamber.

Figure 3.11 shows the readout chain for the PC wires. The wire signals are first passed through the preamplifier and discriminator module, and then arrive at the cluster processors (CP's). The preamplifier-discriminator cards are identical to those used for the drift chambers and are built by Saclay [12]. The cluster processors, built at PSI, communicate with the trigger and send the wire information to the PC Root Read Out (PC RRO). The CP's are controlled by an IBM AT.

#### 3.7.1 The Cluster Processors

Each proportional chamber has its own dedicated cluster processor, consisting of

- 1 cluster processor interface (CPI300) and
- 4 (6) cluster processor modules (CP300) for PC1 (PC2), each capable of handling 144 channels.

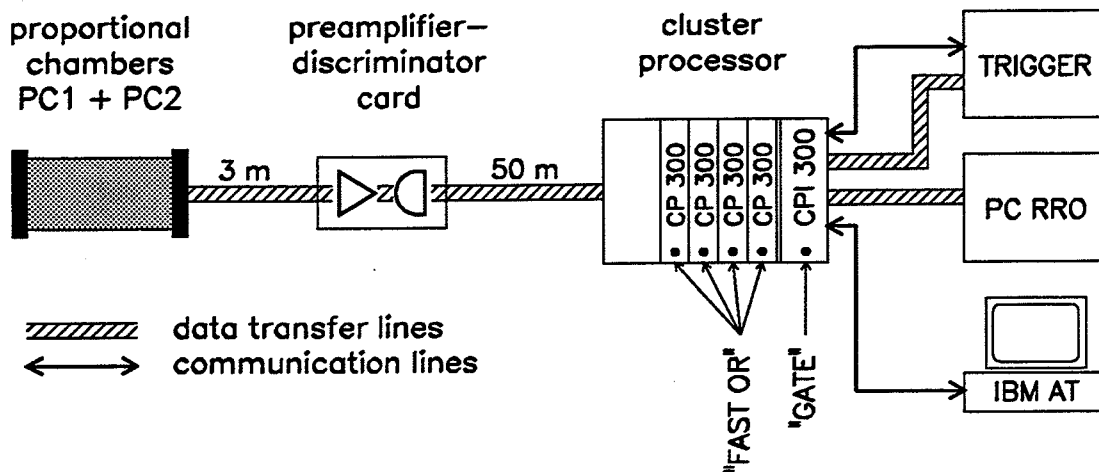


Figure 3.11: Readout chain for the proportional chamber wires.

The CP provides fast proportional chamber wire information to the trigger logic and, if an event is validated by the trigger, passes the wire information on to the PC RRO. The operation of the cluster processor is now discussed in more detail:

**"STROBE-FE" from trigger:** If an event passes the early decision logic (EDL), the trigger sends a "STROBE-FE" signal to the subdetectors front-end electronics (FE). Receiving the "STROBE-FE", the CPI300 generates and distributes a gate signal to the CP300 modules. The distributed gate signal opens the coincidence gate of the CP300 input registers for  $\simeq 80$  ns, and the wire hit signals are latched. The cluster processor then performs the following logical functions:

**gap filling:** Neighboring hits with no more than one missing wire between them are grouped together in hit clusters. The "gap filling" logic, which can be enabled or disabled, fills missing hits in a cluster.

**cluster center address:** The address of each cluster center is calculated.

**sector pattern of cluster centers:** For the communication with the trigger, each proportional chamber is logically subdivided in 64 sectors, one sector corresponding to 9 (12) wires for PC1 (PC2). The CP calculates the sector hit pattern of the cluster centers.

Approximately 150 ns after the input signals are latched, the sector pattern is sent to the intermediate decision logic (IDL). For events reaching the track parameterization stage, the cluster processor provides the trigger with the cluster center addresses.

**"READOUT" from trigger:** The trigger distributes a "READOUT" signal to the FE if an event is validated. This causes the CPI300 to initiate the data transfer to the PC RRO. The time needed for the transfer depends on the number of hits

and is  $\sim 20 \mu\text{s}$  for "golden" events. The data registers are reset as soon as the data transfer is completed.

**"CLEAR" from trigger:** For events failing the trigger conditions, a "CLEAR" signal is sent, causing the CPI300 to reset all data registers in  $\sim 200 \text{ ns}$ .

In addition, the cluster processor provides at the front panel a "FAST OR" of the wire hit signals and a "GATE" output, which may be used to set the gate timing and for test purposes.

### 3.7.2 Control of the Cluster Processors

An IBM AT compatible computer is used to program, setup and control the cluster processors. The AT, connected via the parallel ports to the CP's, has the following functions:

**chip loading:** The CP300 logic is realized with Xilinx circuits. The program determining the chips internal architecture and connections is loaded from the AT.

**gate setting:** The delay between the arrival of "STROBE-FE" and the distribution of the gate signal to the CP300 modules (0 - 200 ns), as well as the width of the gate (50 - 300 ns), can be set from the AT.

**wire masking:** The CP's allow masking of noisy channels. The AT controls the mask pattern and enables or disables the mask option.

**testing:** Two programs running on the AT perform an internal test of the cluster processors and test the data transfer between CP and PC RRO.

## 3.8 Performance

### 3.8.1 Gas Amplification

The gas amplification factor  $M$  (see section 3.1) can be determined by a measurement of the total current pulled by the proportional chamber,  $I_{PC}$ , for a known  $p\bar{p}$  annihilation rate,  $R_{p\bar{p}}$ . The current pulled by the chamber is given by

$$I_{PC} = R_{p\bar{p}} \cdot \bar{n}_{ch} \cdot \frac{\Omega_{PC}}{4\pi} \cdot n_p^{eff} \cdot M \cdot e, \quad (3.18)$$



where  $R_{p\bar{p}}$  is the  $p\bar{p}$  annihilation rate,  
 $\bar{n}_{ch}$  is the mean charged particle multiplicity,  
 $\Omega_{PC}$  is the solid angle covered by the proportional chamber,  
 $n_p^{eff}$  is the mean number of primary electron-ion pairs per track, within  
a distance  $\lambda_{cap}$  of an anode wire,  
 $M$  is the gas amplification factor and  
 $e$  is the electron charge magnitude.

**mean charged particle multiplicity  $\bar{n}_{ch}$ :** For the determination of  $\bar{n}_{ch}$ , only annihilations into pions are considered. The branching ratios for pionic annihilation channels, constituting approximately 95 % of all annihilations, are [21]:

• multi $\pi^0$	:	BR $\simeq$ 3.2 %
• $\pi^+ \pi^- + n \pi^0$ ( $n \geq 0$ )	:	BR $\simeq$ 41.4 %
• $2 \pi^+ 2 \pi^- + n \pi^0$ ( $n \geq 0$ )	:	BR $\simeq$ 47.6 %
• $3 \pi^+ 3 \pi^- + n \pi^0$ ( $n \geq 0$ )	:	BR $\simeq$ 3.6 %

With this branching ratios, one finds

$$\bar{n}_{ch} \simeq 3.1 .$$

**solid angle  $\Omega_{PC}$ :** The chamber current  $I_{PC}$  was measured for PC1. The solid angle covered by PC1 is (see table 3.2)

$$\Omega_{PC} = 0.965 \cdot 4\pi \text{ steradians.}$$

**effective number of primary ion pairs  $n_p^{eff}$ :** The electronegative freon ( $CF_3Br$ ) in the gas mixture captures a part of the primary electrons. The mean free path for electron capture,  $\lambda_{cap}$ , is approximately given by [18]

$$\lambda_{cap} \simeq \frac{1}{(1.5 \cdot P)} \text{ mm} \simeq 1.33 \text{ mm} , \quad (3.19)$$

where  $P$  is the concentration of freon in percent ( $P = 0.5$ ). We assume that only the primary electrons produced within a distance of  $\lambda_{cap}$  of an anode wire can initiate an avalanche. The freon thus defines an active gas volume around the anode wires with a mean thickness  $\bar{d}$  given by (see diagram 3.12)

$$\bar{d} = \frac{F}{s} = \frac{4}{s} \cdot \int_0^{s/2} \sqrt{\lambda_{cap}^2 - x'^2} dx' \simeq 2.6 \text{ mm} , \quad (3.20)$$

where  $F$  is the active area per wire and  $s$  is the wire pitch.

For isotropic track directions, the mean track length  $\bar{t}$  in the active gas volume (see figure 3.13) is derived to be

$$\bar{t} \equiv \frac{1}{(\pi/2 - \theta_{min})} \int_{\theta_{min}}^{\pi/2} t(\theta) d\theta = \frac{-\bar{d} \cdot \ln(\tan(\theta/2))}{(\pi/2 - \theta_{min})} \simeq 4 \text{ mm} , \quad (3.21)$$

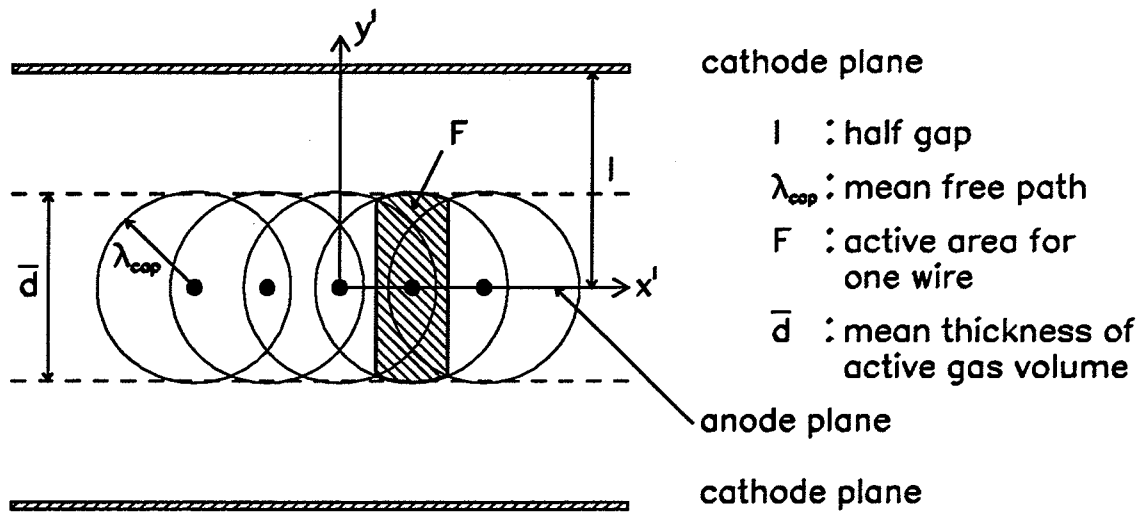


Figure 3.12: Active gas volume defined by the mean free path for electron capture.

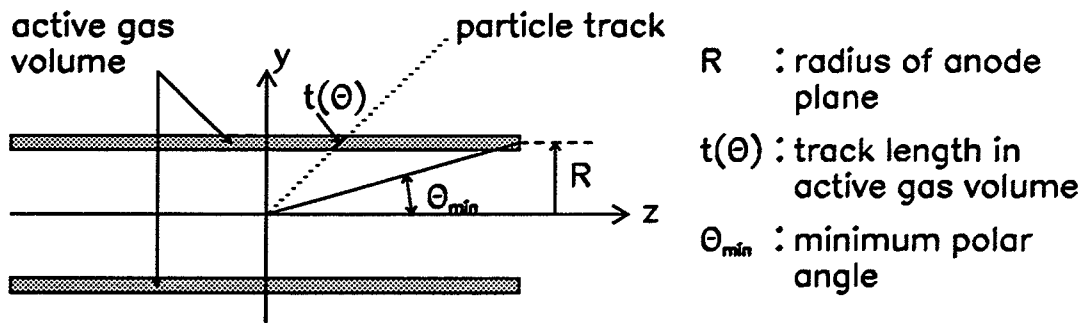


Figure 3.13: Track length in the active gas volume for a given polar angle.

where  $t(\theta)$  is the track length for a given polar angle  $\theta$ , and  $\theta_{min}$  is the minimum polar angle ( $\approx 15.2$  degrees for PC1).

With the approximation of minimum ionizing particles, one finds the effective number of primary electrons to be

$$n_p^{eff} \simeq n_p \cdot \bar{t} \simeq 45, \quad (3.22)$$

where  $n_p$  is the number of primary electron-ion pairs per unit length, listed in table 3.1.

Inserting the values for  $\bar{n}_{ch}$ ,  $\Omega_{PC}$  and  $n_p^{eff}$  into equation 3.18, one gets for the gas amplification factor  $M$ :

$$M \simeq (4.5 \cdot 10^7) \cdot \frac{I_{PC} [\mu A]}{R_{pp} [kHz]} \quad (3.23)$$

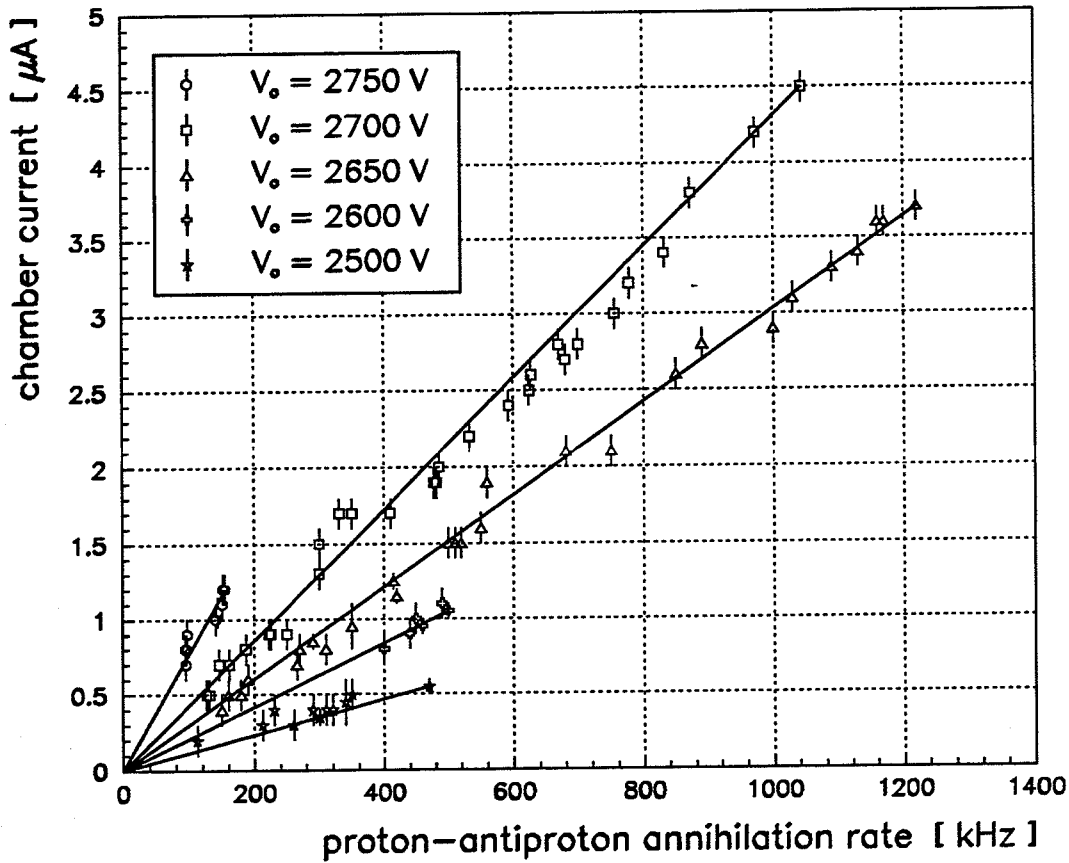


Figure 3.14: PC1 chamber current versus  $p\bar{p}$  annihilation rate, measured for five different high voltage values.

$V_0$ [V]	$I_{PC} [\mu A]/R_{p\bar{p}}$ [kHz]	M
2500	$1.2 \cdot 10^{-3}$	$0.6 \cdot 10^5$
2600	$2.1 \cdot 10^{-3}$	$1.0 \cdot 10^5$
2650	$3.0 \cdot 10^{-3}$	$1.4 \cdot 10^5$
2700	$4.2 \cdot 10^{-3}$	$1.9 \cdot 10^5$
2750	$7.7 \cdot 10^{-3}$	$3.5 \cdot 10^5$

Table 3.5: Gas amplification factors  $M$  for different high voltage values.

Figure 3.14 shows the PC1 chamber current for several high voltage values, plotted versus the  $p\bar{p}$  annihilation rate. The ratios  $I_{PC}/R_{p\bar{p}}$ , determined with straight line fits, and the gas amplification factors  $M$  are listed in table 3.5. For our working voltage of  $V_0 = 2750$  V, we obtained

$$M \simeq 3.5 \cdot 10^5.$$

### 3.8.2 Chamber Efficiency

The particle detection efficiency of a proportional chamber is determined by the total amount of charge produced in the chamber due to the traversing particle, the resulting pulse height on anode wires and cathode strips as well as the sensitivity of the readout electronics.

- The total amount of charge,  $Q_{tot}$ , is given by the product of the number of primary electrons produced within a distance  $\lambda_{cap}$  of an anode wire,  $n_p^{eff}$ , and the gas amplification factor,  $M$ . The gas mixture determines  $n_p^{eff}$ . The gas amplification factor is given to first order by the chamber geometry, the applied high voltage and the gas mixture. However, at high ionizing particle rates  $M$  can be reduced due to the accumulation of a positive space charge close to the anode wires, which distorts the electric field.
- The induced pulse height on wires and strips is proportional to  $Q_{tot}$  and depends further on the differentiation time constant  $\tau = R \cdot C$  [18], where  $R$  is the impedance of the wire (strip) termination and  $C$  is the capacitance of the wire (strip) with respect to the cathode (anode). High impedance terminations (and thus long differentiation time constants) have the advantage of maximum pulse heights, while low impedances shorten the pulses and thereby increase the rate capability of the chamber.
- The amplification factor and the discriminator threshold of the readout electronics finally decide whether the induced signal can be detected.

The results presented here for the chamber efficiency are based on:

1. Tests with a planar prototype chamber, using electrons from a  $^{90}\text{Sr}$  source.
2. Measurements with the test chamber under beam conditions.
3. An offline analysis of the PC performance during run periods 8 and 9.

First, the experimental setup of the source and beam tests with the prototype chamber are described.

#### 3.8.2.1 Source Test Setup

The experimental setup for the  $^{90}\text{Sr}$  source test is sketched in diagram 3.15. The prototype chamber has an active area of  $20 \times 20 \text{ cm}^2$  and is equipped with 167 anode wires and cathode strips at an angle of  $\pm 45$  degrees with respect to the wires. 32 anode wires and 27 strips for each cathode plane can be read out. The parameters of the chamber geometry (half gap, wire pitch and diameter), as well as the width and the gap between cathode strips, are the same as for PC1 and PC2.

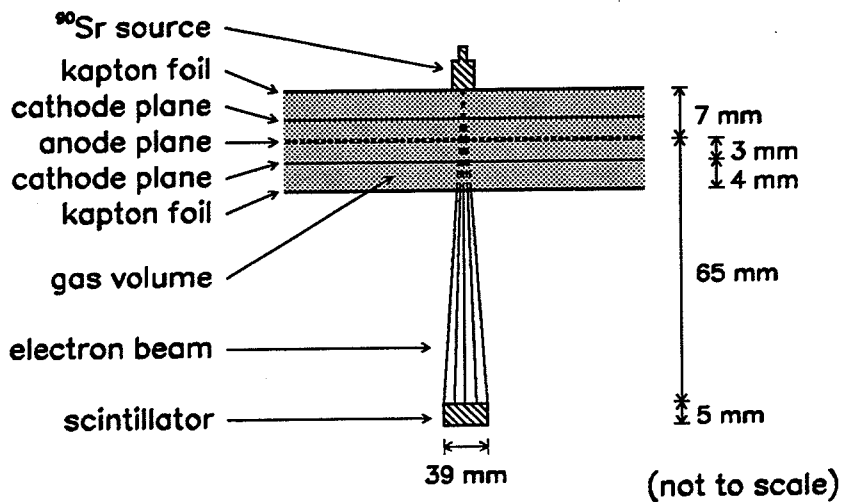


Figure 3.15: Experimental setup for the source test with the prototype chamber.

The  $^{90}\text{Sr}$  source, placed on top of the chamber, had an activity of  $10 \mu\text{Ci}$ . A traversing beam of electrons was defined with a plastic scintillator, positioned below the chamber. The electrons emitted by the source originate from the two  $\beta$ -transitions

- $^{90}\text{Sr} \rightarrow ^{90}\text{Y}$  with  $T_{1/2} = 28.5 \text{ y}$  and  $E_{\beta \text{ max}} = 0.55 \text{ MeV}$  and
- $^{90}\text{Y} \rightarrow ^{90}\text{Zr}$  with  $T_{1/2} = 64 \text{ h}$  and  $E_{\beta \text{ max}} = 2.28 \text{ MeV}$ .

Only electrons from the transition  $^{90}\text{Y} \rightarrow ^{90}\text{Zr}$  can have enough kinetic energy to produce a scintillator signal which is above the discriminator threshold.

For the efficiency measurements, the counting rate of the scintillator ( $\sim 250 \text{ Hz}$ ) was compared to the coincidence rate between the scintillator and the "OR" of 32 anode wires (27 cathode strips). More details about the prototype chamber and the readout electronics are given in [19].

### 3.8.2.2 Beam Test Setup

A test of the prototype chamber under beam conditions was performed at PSI in October 1987, using a  $220 \text{ MeV}/c$  momentum beam of pions and electrons. Figure 3.16 shows the setup for the test measurement.

Two pill counters (S1,S2), placed on either side of the test chamber, defined a very narrow, traversing particle beam. The type of particle could be identified by the time of flight measurement between the production target and the scintillator S1

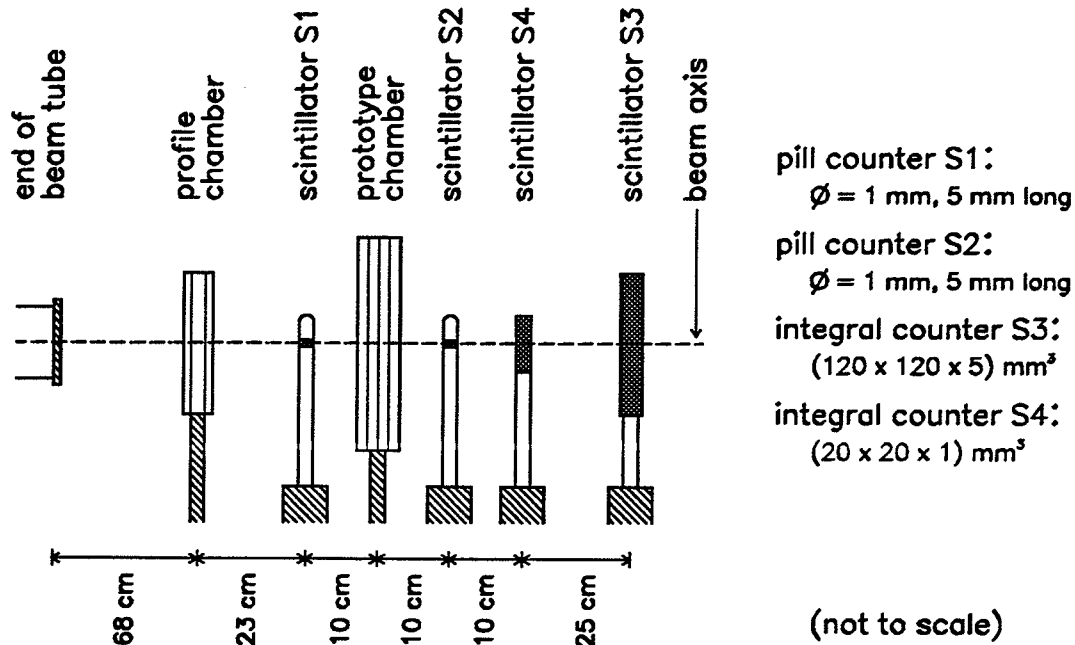


Figure 3.16: Experimental setup for the beam test with pions and electrons at incident momenta of 220 MeV/c.

( $\sim 15$  m). The time spectrum displayed in figure 3.17 was obtained with the S1 signal as "START" and the next accelerator RF-signal as "STOP".

The profile chamber in front of S1 was used for beam alignment and beam profile measurements. The beam intensity was monitored by the scintillators S3 and S4. At CPLEAR, with  $\sim 10^6$   $p\bar{p}$  annihilations per second and a mean charged particle multiplicity of  $\sim 3.1$ , the maximum flux density for PC1 ( $z=0$ ) is

$$\Phi_{PC1}^{max} \simeq 27 \text{ Hz/mm}^2 .$$

The measurements were performed at the following two beam intensities:

- "low rate" :  $\Phi_{low} \simeq 1.2 \text{ kHz/mm}^2$  ;  $\Phi_{low}/\Phi_{PC1}^{max} \simeq 45$  and
- "high rate" :  $\Phi_{high} \simeq 4.9 \text{ kHz/mm}^2$  ;  $\Phi_{high}/\Phi_{PC1}^{max} \simeq 180$  .

For the efficiency measurements, accidental coincidences between the gate, generated by "S1 AND S2", and the "OR" of the 32 anode wires must be accounted for. The chamber efficiency,  $\eta_{MWPC}$ , can be obtained from the equation

$$S = \eta_{MWPC} + \eta_{MWPC} (1 - \eta_{MWPC}) \cdot R_{beam} \cdot T_{gate} , \quad (3.24)$$

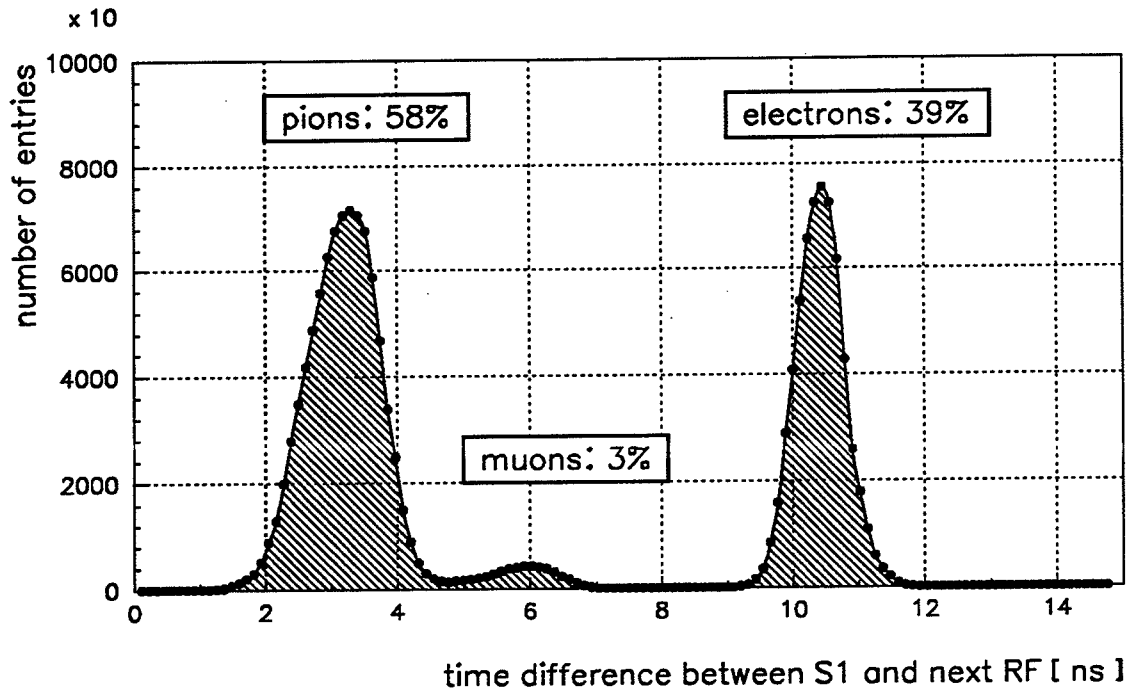


Figure 3.17: Beam composition, as determined by time of flight measurement.

with

$$S = \frac{CR(GATE, MWPC)}{CR(S1, S2)},$$

where  $R_{beam}$  is the total rate of charged particles on the 32 anode wires (1.0 MHz [4.1 MHz] for "low" ["high"] rate),  $T_{gate}$  is the gate width (150 ns),  $CR(S1, S2)$  is the coincidence rate between the scintillators S1 and S2 and  $CR(GATE, MWPC)$  is the coincidence rate between the gate and the "OR" of the 32 anode wires.

### 3.8.2.3 Anode Wire Efficiency Curve for two Gas Mixtures

As mentioned in section 3.3, we found, as a result of extensive gas tests with the prototype chamber, two equally good mixtures

- 79.5 % Argon, 20.0 % Isobutane, 0.5 % Freon and
- 69.0 % Argon, 30.0 % Ethane, 1.0 % Freon.

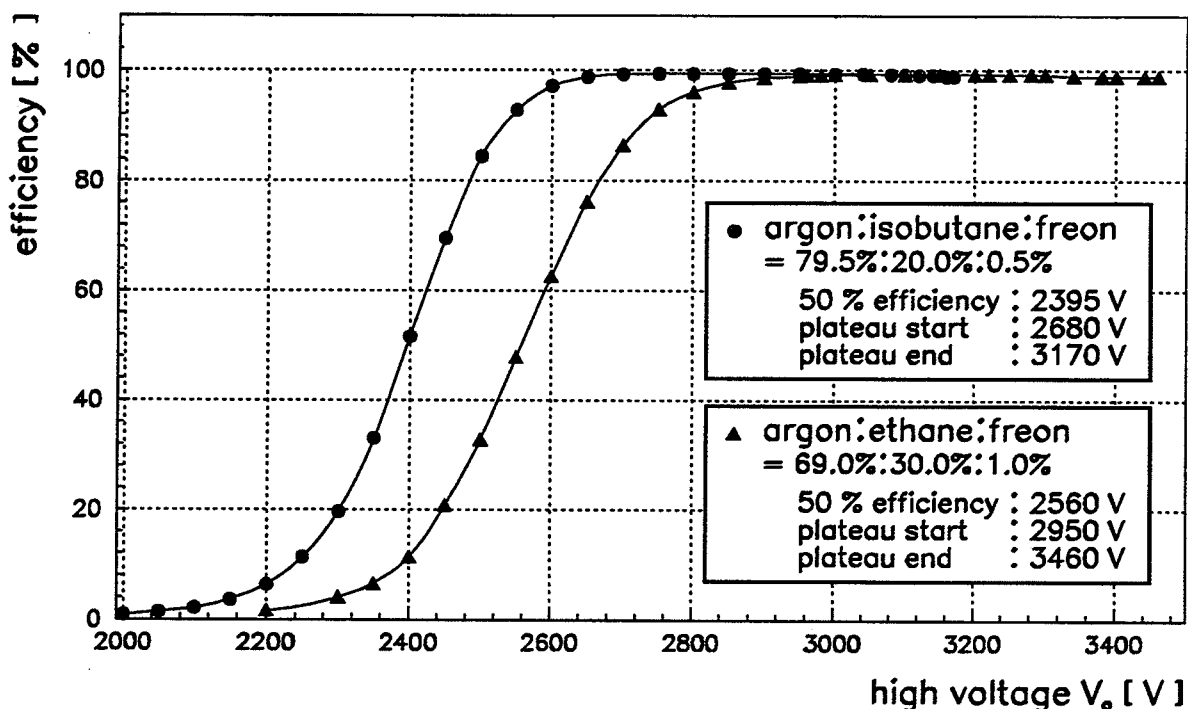


Figure 3.18: Anode wire efficiency curve for two gas mixtures. The lines are intended to guide the eye.

Figure 3.18 shows the anode wire efficiency curve for the two mixtures, measured with the test chamber and the  $^{90}\text{Sr}$  source. The lines connecting the data points are intended to guide the eye. We defined that the efficiency plateau is reached for an efficiency of 99 %, and that it ends if the chamber current exceeds the minimum current limit of the high voltage power supply.

For tracks perpendicular to the wire plane, the effective number of primary ion pairs,  $n_p^{eff}$ , is  $\sim 30$  for the isobutane mixture, and  $\sim 13$  for the ethane mixture (higher freon concentration). This explains the somewhat steeper rise of the efficiency curve for the gas mixture with isobutane (smaller relative fluctuations in the number of primary ion pairs) compared to the ethane mixture.



While the plateau length is almost equal for the two gases, the isobutane mixture reaches the plateau  $\sim 270$  V before the ethane mixture, thus allowing a lower working voltage.

### 3.8.2.4 Cathode Strip Efficiency Curve

The induced signal on the cathode is split between the two planes and distributed over several strips (see figure 3.3). The resulting pulse heights on the cathode strips are thus only a fraction of the anode wire pulse height.

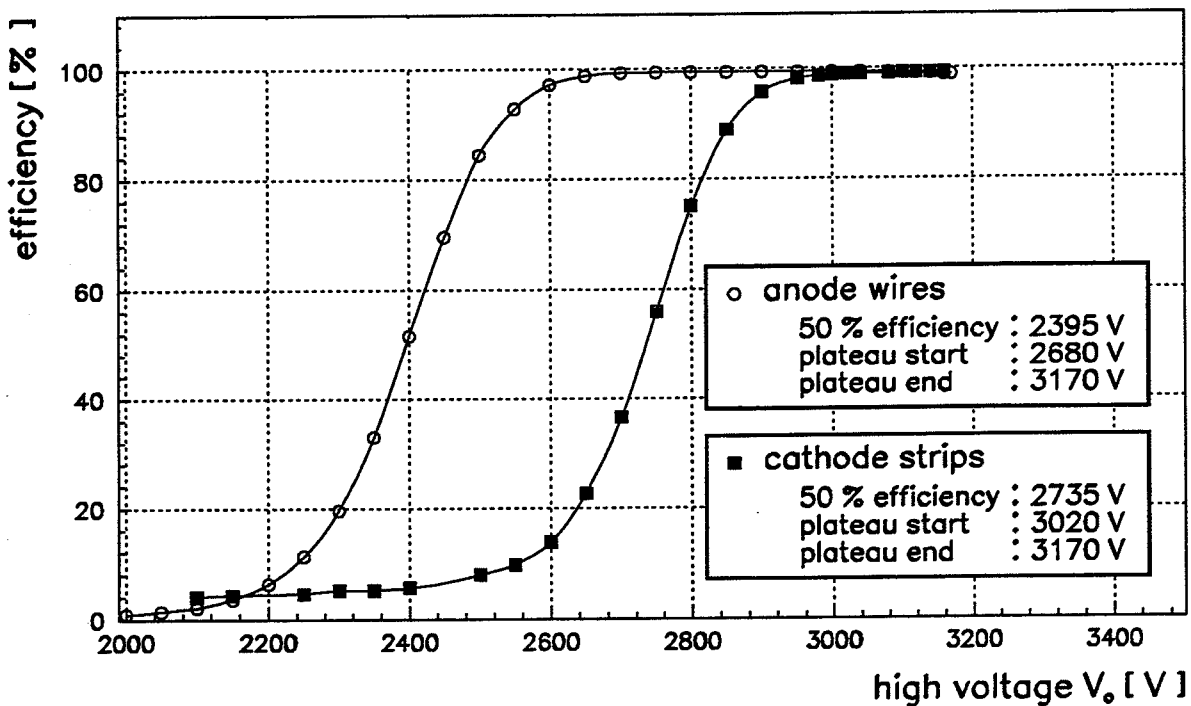


Figure 3.19: Comparison between anode wire and cathode strip efficiencies. The lines are intended to guide the eye.

In figure 3.19, the efficiency curves for anode wires and cathode strips are compared. Both curves are measured with the source test setup and the isobutane mixture. As expected, the cathode strips reach the efficiency plateau only for much higher gas amplifications. The resulting shift in high voltage is  $\sim 340$  V for the readout electronics used in our test setup which is not adequate for cathode strip signals. At CPLEAR, we intend to lower the plateau start voltage for the strips using low-noise preamplifiers.

### 3.8.2.5 Rate Dependence of Plateau Efficiency

The prototype chamber with the ethane gas mixture behaved very well under beam conditions. The anode efficiency curve measured with the  $^{90}\text{Sr}$  source was well reproduced for the "low rate" beam intensity which already corresponds to  $\sim 45$  times the maximum flux density for PC1 (see diagram 3.20). The beam test showed, that the expected charged particle flux at CPLEAR is uncritical for PC1 and PC2. This was confirmed by measurements during the first CPLEAR run periods (see section 3.8.1).

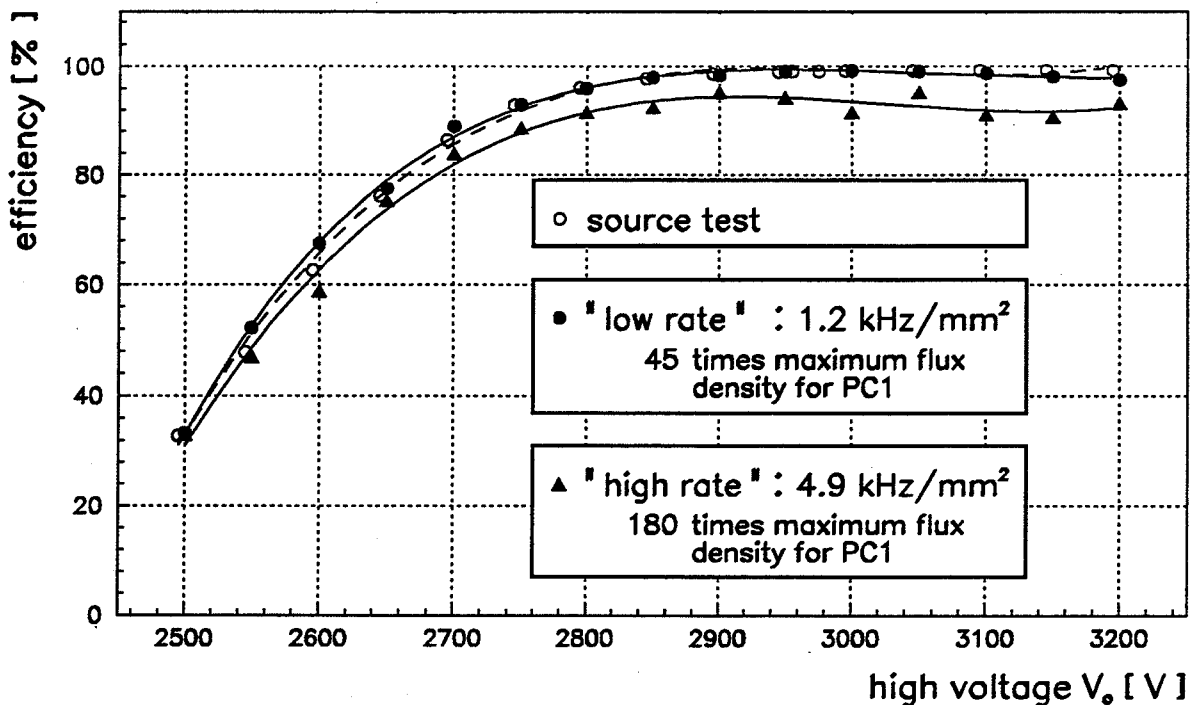


Figure 3.20: Anode efficiency for "low" and "high" beam intensities compared to source measurements. The lines are intended to guide the eye.

At even higher rates, space charge effects lower the maximum attainable efficiency. For the "high rate" beam intensity, the plateau efficiency is decreased by  $\sim 7\%$ .

### 3.8.2.6 Inefficiency due to Wire Supports

In the region of the wire supports (see section 3.5) gas amplification cannot take place and the proportional chambers are inefficient. To measure this effect, the prototype chamber was equipped with a wire support structure for the beam test.

Figure 3.21 shows that the region with reduced efficiency extends over  $\sim 10$  mm along the wires. At the support structure (5 mm wide), the efficiency drops below 10%.

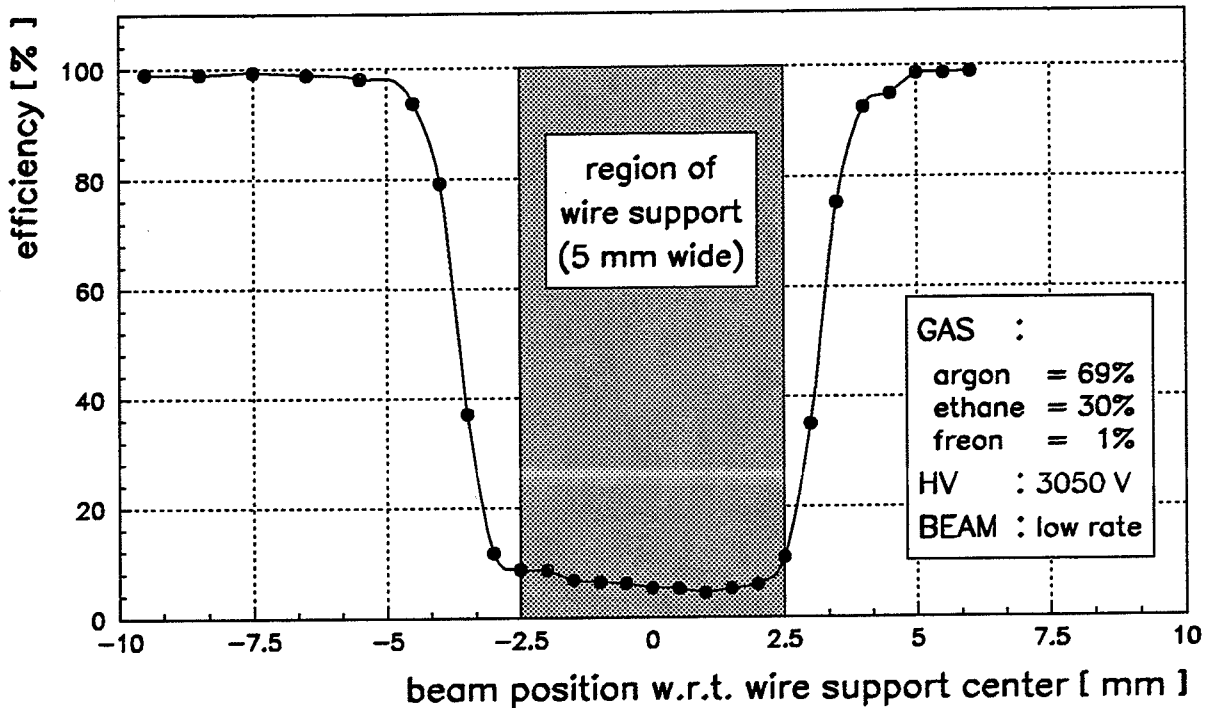


Figure 3.21: Chamber inefficiency due to the wire support structure. The line is intended to guide the eye.

Averaged over the active length of the chambers, i.e. for tracks perpendicular to the anode plane and uniformly distributed along the wires, the wire supports for the PC's (two per chamber) cause an detection inefficiency of  $\sim 2\%$ .

### 3.8.2.7 Efficiency of PC1 and PC2 for Run Periods 8 and 9

The performance of the proportional chambers during the run periods 8 and 9 was analysed by T.Ruf [22]. The data used in the analysis were taken with the "minimum bias" trigger (see 2.4) and no magnetic field. The operational parameters for PC1 and PC2 were

- a high voltage of 2700 V,
- a discriminator trigger threshold of  $0.4 \mu\text{A}$  ( $0.5 \mu\text{A}$ ) for PC1 (PC2) and
- a coincidence gate width of 80 ns (90 ns) for PC1 (PC2).

Straight tracks defined by the pattern recognition and track fit procedures were used to determine the chamber alignment with respect to the drift chambers, their efficiency and their spatial resolution. The tracks were required to pass within 2 cm of the origin in the  $xy$ -plane and have hits in all six drift chambers. The alignment and the spatial resolution will be discussed in the next section.

The detection efficiencies for the individual chambers, corrected for defect readout channels, were found to be

$$\begin{aligned}\eta_{PC1} &= (91.7 \pm 0.2)\% \quad \text{and} \\ \eta_{PC2} &= (92.2 \pm 0.2)\% .\end{aligned}$$

Note that the maximum attainable efficiency is  $\simeq 98\%$  due to the wire support structures. For the trigger decisions at the IDL level, one hit in either of the proportional chambers is sufficient. The efficiency for at least one hit in PC1 or PC2 was determined to be

$$\eta_{(PC1 \text{ or } PC2)} \simeq 99.5\% .$$

The  $\sim 6\%$  inefficiency of the chambers was due to the high voltage which was purposely kept low for these two run periods, for the following three reasons:

1. The relevant trigger efficiency  $\eta_{(PC1 \text{ or } PC2)}$  was already at a maximum (99.5 %).
2. The preamplifiers and discriminators were pending modification to improve the grounding and thus the signal to noise ratio, allowing a gain in efficiency by reducing the discriminator threshold.
3. In order to minimize aging effects.

### 3.8.3 Spatial Resolution

Prior to the spatial resolution analysis, the position of the proportional chambers with respect to the drift chambers has to be determined. The displacement of PC1 and PC2 is expressed by a shift in the  $x$ - and  $y$ - directions and a rotation of the cylinder by an angle  $\alpha$ . The values obtained for run period 8 are listed in table 3.6.

	PC1	PC2
$x$ -shift	+ 0.673 mm	+ 0.883 mm
$y$ -shift	- 0.313 mm	- 0.397 mm
rotation ( $\alpha$ )	+ 0.0635 rad	+ 0.0567 rad

Table 3.6: Results of the PC alignment analysis.

For the evaluation of the spatial resolution, all neighboring hits in the PC's with no more than one missing wire between are grouped together in hit clusters. The theoretically expected resolution,  $\sigma_{r\varphi}^{th}$ , for a wire pitch  $s$  and a mean cluster size  $\langle n_{hit} \rangle$  is given by

$$\sigma_{r\varphi}^{th} = \frac{\langle n_{hit} \rangle \cdot s}{\sqrt{12}} . \quad (3.25)$$

Under the operating conditions of the chambers during the data taking, the mean cluster size was  $\langle n_{hit} \rangle \simeq 1.17$ . Thus, the expected resolution is

$$\sigma_{r\varphi}^{th} \simeq 340 \mu\text{m} .$$

The experimentally determined spatial resolutions for the proportional chambers are

$$\begin{aligned} \sigma_{r\varphi}^{PC1} &= (382 \pm 26) \mu\text{m} \quad \text{and} \\ \sigma_{r\varphi}^{PC2} &= (294 \pm 27) \mu\text{m} . \end{aligned}$$

Until now, no explanation was found for the different resolutions of PC1 and PC2.

Using the constraint  $\sigma_{r\varphi}^{PC1} = \sigma_{r\varphi}^{PC2}$  (see [22]) in the analysis, a proportional chamber resolution of

$$\sigma_{r\varphi}^{PC} = (336 \pm 6) \mu\text{m}$$

was obtained, which is in good agreement with the expected value.

The spatial resolution along the wire direction obtained by the strips,  $\sigma_z$ , was analysed with the planar prototype chamber, using a 150 MeV/c momentum beam at PSI. The experimental setup and a detailed description of the analysis can be found in [23]. Two different methods were investigated to reconstruct the  $u$ - and  $v$ - coordinates (see figure 3.3) of the intersection point between the particle trajectory and the anode plane.

**analogue method:** The center of gravity of a strip hit cluster is approximated by the weighted average of the strip center coordinates, with the induced pulse heights as weights. This method requires a readout of the cathode strips with ADC's.

**digital method:** The cluster center is calculated with equal weights for all strips in the cluster. In this case a digital readout of the cathode strips is sufficient.

The resolutions obtained for the two methods are

$$\begin{aligned} \sigma_{u,v}^{analog} &= (229 \pm 55) \mu\text{m} \quad \text{and} \\ \sigma_{u,v}^{digital} &= (623 \pm 42) \mu\text{m} . \end{aligned}$$

The relationship between  $\sigma_{u,v}$  and  $\sigma_z$  is given by

$$\sigma_z = \frac{\sigma_{u,v}}{\sin \alpha} , \quad (3.26)$$

where  $\alpha$  is the angle between strips and wires. Inserting the values  $\alpha = 19.474$  (27.888) degrees, corresponding to PC1 (PC2), one expects the following resolutions in  $z$ -direction for the proportional chambers:

	PC1	PC2
$\sigma_z^{analog} :$	$(0.69 \pm 0.17) \text{ mm}$	$(0.49 \pm 0.12) \text{ mm}$
$\sigma_z^{digital} :$	$(1.87 \pm 0.13) \text{ mm}$	$(1.33 \pm 0.09) \text{ mm}$

## 4 Isospin Mass Splitting of the $K^*$ (892) Meson

The aim of this analysis is to determine the mass difference between the neutral and the charged states of the  $K^*$ (892) meson. The  $K^*$  mesons are members of the  $SU(3)$  vector meson octet. They are grouped into the two isospin doublets

- $K^{*+}, K^{*0}$  with strangeness  $S = +1$  and
- $\bar{K}^{*0}, K^{*-}$  with strangeness  $S = -1$ .

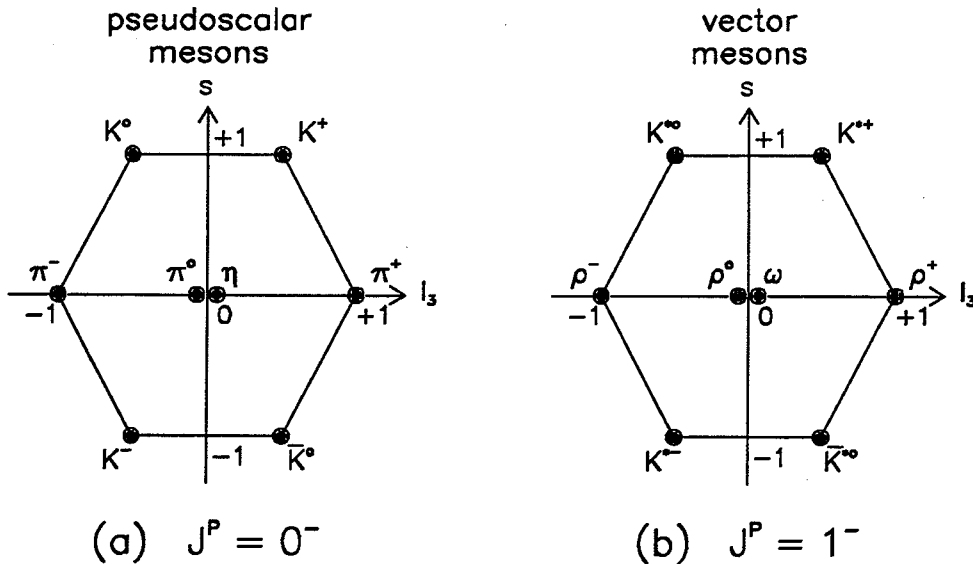


Figure 4.1:  $SU(3)$  octets for pseudoscalar (a) and vector (b) mesons.

Shown in figure 4.1 are the octets for the pseudoscalar and the vector mesons. The mass difference is defined to be

$$\Delta m_{K^*} \equiv m_{K^{*0}} - m_{K^{*\pm}} . \quad (4.1)$$

### 4.1 Physics Motivation

There are two reasons for a new measurement of the  $K^*$  mass difference:

1. The individual masses of the neutral and charged  $K^*$  mesons have been measured by many experiments and the values are well established. The average values listed in [4] are determined from about 20 measurements for each state. They are:

$$\begin{aligned} \langle m_{K^{*\pm}} \rangle &= (891.83 \pm 0.24) \text{ MeV}/c^2 & \text{and} \\ \langle m_{K^{*0}} \rangle &= (896.10 \pm 0.28) \text{ MeV}/c^2 . \end{aligned}$$

The  $K^*$  mass difference calculated from these averaged mass values is

$$\langle m_{K^{*0}} \rangle - \langle m_{K^{*\pm}} \rangle = (4.27 \pm 0.37) \text{ MeV}/c^2. \quad (4.2)$$

Most of the experiments measuring the  $K^*$  masses observe either the charged or the neutral state of the  $K^*$ , but not both. So far, only three experiments could detect both states simultaneously and measure  $\Delta m_{K^*}$  from the same data sample. They are:

**Barash et al., 1967 [24]:** Annihilations of antiprotons at rest in hydrogen were analysed by exposing a 30 inch bubble chamber to a low energy antiproton beam. From a sample of 851 events of the type  $p\bar{p}$  (at rest)  $\rightarrow K_S^0 K^\pm \pi^\mp$ , the neutral and charged  $K^*$  masses were determined by fitting the invariant mass distributions  $M_{inv}(K^\pm, \pi^\mp)$  and  $M_{inv}(K_S^0, \pi^\pm)$ , respectively, in the range of 0.68 to 1.1  $\text{GeV}/c^2$ . With a statistics of  $170 \pm 25$  ( $113 \pm 20$ ) events in the  $K^{*0}$  ( $K^{*\pm}$ ) peak, the value for the  $K^*$  mass difference was found to be

$$\Delta m_{K^*} = (6.3 \pm 6.1) \text{ MeV}/c^2 \quad (\text{enlarged error}). \quad (4.3)$$

**Aguilar et al., 1971 [25]:** Reactions of the type  $K^- p \rightarrow K^- \pi^+ n$ ,  $K^- p \rightarrow K^- \pi^0 p$  and  $K^- p \rightarrow \bar{K}^0 \pi^- p$  were analysed by exposing an 80 inch hydrogen bubble chamber to  $K^-$  beams of 3.9 and 4.6  $\text{GeV}/c^2$  incident momenta. The mass of  $\bar{K}^{*0}$  was obtained by a fit on the  $K^- \pi^+$  invariant mass spectrum in the region of  $0.8 \leq M_{inv}(K^- \pi^+) \leq 1.0 \text{ GeV}/c^2$ , while for the  $K^{*-}$ , the two spectra  $M_{inv}(K^- \pi^0)$  and  $M_{inv}(\bar{K}^0 \pi^-)$  were combined. The data analysed contained  $2934 \pm 109$  ( $4404 \pm 100$ )  $\bar{K}^{*0}$  ( $K^{*-}$ ) and the  $K^*$  mass difference was determined as

$$\Delta m_{K^*} = (5.7 \pm 1.8) \text{ MeV}/c^2 \quad (\text{enlarged error}). \quad (4.4)$$

**Aguilar et al., 1978 [26]:** This determination of the  $K^*$  mass difference is based on 6453 events of the type  $p\bar{p} \rightarrow K_S^0 K^\pm \pi^\mp$ . The data came from exposures of an 80 cm hydrogen bubble chamber to incident antiproton beams of 700 and 750  $\text{MeV}/c$  momenta. Fits were performed on the invariant mass distributions  $M_{inv}(K^\pm, \pi^\mp)$  and  $M_{inv}(K_S^0, \pi^\pm)$  in the range of 0.7 to 1.1  $\text{GeV}/c^2$ , yielding  $1180 \pm 100$  ( $1800 \pm 97$ ) events in the  $K^{*0}$  ( $K^{*\pm}$ ) peak and a mass difference of

$$\Delta m_{K^*} = (7.7 \pm 1.9) \text{ MeV}/c^2 \quad (\text{enlarged error}). \quad (4.5)$$

The quoted errors for  $\Delta m_{K^*}$  are enlarged following the procedure described in [4]. The minimum error on the determination of a resonance mass  $M$  with a width  $\Gamma$  from a sample of  $N$  events is assumed to be given by

$$\delta_{min}(M) = \frac{\Gamma}{\sqrt{N}}. \quad (4.6)$$

The average of  $\Delta m_{K^*}$  from these three experiments is then

$$\langle \Delta m_{K^*} \rangle = (6.6 \pm 1.3) \text{ MeV}/c^2. \quad (4.7)$$

Comparing the results of  $\langle m_{K^{*0}} \rangle - \langle m_{K^{*+}} \rangle$  and  $\langle \Delta m_{K^*} \rangle$ , one sees that the central values differ by  $2.3 \text{ MeV}/c^2$ , corresponding to 1.8 standard deviations.

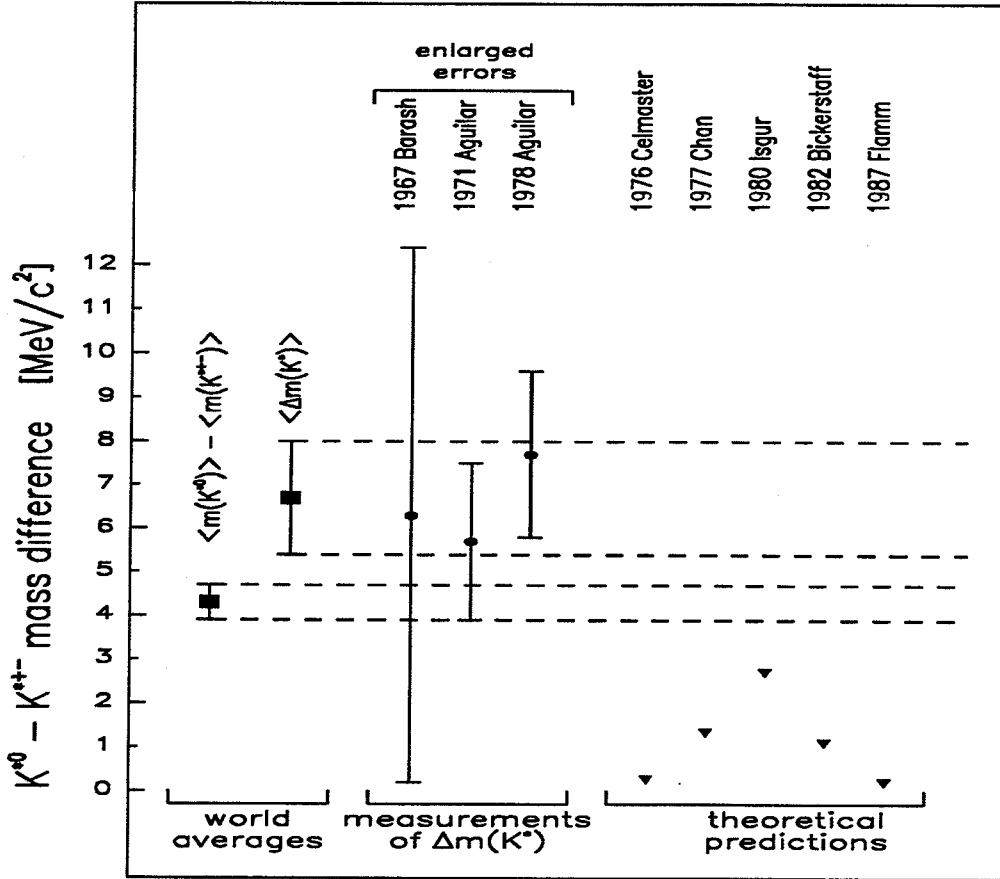


Figure 4.2: Overview of experimental measurements and theoretical predictions of the  $K^*$  mass difference.

- Theoretical models had always difficulties in explaining the  $K^*$  mass difference. The predictions are generally too low compared with either of the two experimental values given above. The difference is usually attributed to the large  $K^*$  width. In table 4.1 are summarized the results of some recent calculations.

The situation of isospin splitting in heavy meson systems has been reanalysed recently by Goity and Hou [32], taking into account the latest experimental results. Generally, the isospin splitting has two contributions:

$$\Delta M \equiv M_{Q\bar{d}} - M_{Q\bar{u}} = \Delta^m M + \Delta^\gamma M, \quad (4.8)$$

where



year	author	model	$\Delta m_{K^*}$ [MeV/c <sup>2</sup> ]
1976	Celmaster [27]	potential model	0.27
1977	Chan [28]	phenom. quark model	1.34
1980	Isgur [29]	potential model	2.70
1982	Bickerstaff et al. [30]	MIT bag model	1.11
1987	Flamm et al. [31]	potential model	0.20

Table 4.1: Some recent theoretical predictions for the  $K^*$  mass difference.

$M$  is the mass of the pseudoscalar meson ( $Q\bar{q}$ ),  
 $Q$  is the heavy quark  $c$  or  $b$  (or  $s$ ),  
 $\Delta^m M$  is the contribution from the mass difference of  $u$  and  $d$  quarks and  
 $\Delta^\gamma M$  is the contribution from QED effects .

From the experimental observation, given as [4],[33]

$$\begin{aligned}
m_{D^{*0}} - m_{D^0} &\simeq m_{D^{*+}} - m_{D^+} \simeq m_{D_s^*} - m_{D_s} \simeq 141 \text{ MeV}/c^2 \text{ and} \\
m_{B^*} - m_B &\simeq m_{B_s^*} - m_{B_s} \simeq 47 \text{ MeV}/c^2,
\end{aligned}$$

Goity and Hou conclude that

$$\Delta^m M \simeq \Delta^m M^* \quad (4.9)$$

for  $Q = c$  and  $b$ , where  $M^*$  is the mass of the vector meson ( $Q\bar{q}$ ). In the quark model,  $\Delta^\gamma M$  is given by electromagnetic hyperfine effects, which are small (several tenths of a  $\text{MeV}/c^2$ ) and comparable to experimental uncertainties. Neglecting this small electromagnetic effect, heavy vector mesons are then expected to have approximately the same isospin splitting as their pseudoscalar counterparts, i.e.

$$\Delta M \simeq \Delta M^* \quad (4.10)$$

for  $Q = c$  and  $b$ . Neither of the relations 4.9 and 4.10 can be substantiated theoretically for the  $K$  mesons. However, if one uses the value  $\langle m_{K^{*0}} \rangle - \langle m_{K^{*\pm}} \rangle$  (see equation 4.2) as the  $K^*$  mass difference, then one finds that relation 4.10 also seems to hold for the kaon system, i.e.

$$\begin{aligned}
\Delta m_K &\simeq (4.02 \pm 0.02) \text{ MeV}/c^2, \\
\Delta m_{K^*} &\simeq (4.27 \pm 0.37) \text{ MeV}/c^2,
\end{aligned}$$

and  $\Delta m_K \simeq \Delta m_{K^*}$ . This result allows two possible and very surprising conclusions:

(a)  $\Delta^m m_K - \Delta^m m_{K^*} \simeq 0$  and  $\Delta^\gamma m_K - \Delta^\gamma m_{K^*} \simeq 0$ , i.e.

relation 4.9 holds even if the heavy quark mass is lowered to the kaon mass.

In addition, the QED induced splitting in the K and the K\* system are approximately equal. This is amazing, since K and K\* are very different mesons. Unlike for D and B mesons,  $\Delta\gamma_{m_K} - \Delta\gamma_{m_{K^*}}$  cannot be calculated reliably in a simple quark model and does not need to be small.

$$(b) (\Delta^m_{m_K} - \Delta^m_{m_{K^*}}) \simeq -(\Delta\gamma_{m_K} - \Delta\gamma_{m_{K^*}})$$

where the two contributions to  $\Delta m_K - \Delta m_{K^*}$  cancel accidentally.

To clarify the situation of isospin mass splitting in the K and K\* systems, the experimental discrepancy for  $\Delta m_{K^*}$  should first be settled. The most promising way is an improved measurement of  $\Delta m_{K^*}$  by an experiment able to see both states of the K\*, in order to reduce the uncertainty of the average  $\langle \Delta m_{K^*} \rangle$  (see equation 4.7). If  $\Delta m_K \simeq \Delta m_{K^*}$  were experimentally confirmed, a reliable calculation of  $\Delta\gamma_{m_{K^*}}$  would then be needed to decide between the two possible conclusions mentioned above, where  $\Delta\gamma_{m_K}$  is well understood. A progress along this line would certainly deepen our knowledge of bound quark states and their theoretical treatment.

Figure 4.2 gives an overview of the experimental measurements and the theoretical predictions on the K\* mass difference.

## 4.2 Event Selection

At the CPLEAR experiment, one looks for the following final states of  $p\bar{p}$  annihilations at rest ("golden" events):

$$\begin{aligned} p\bar{p} &\rightarrow K^+\pi^-\bar{K}^0, \\ p\bar{p} &\rightarrow K^-\pi^+K^0. \end{aligned}$$

Figure 4.3 shows two basically different diagrams that can lead to these final states, i.e.  $p\bar{p}$  may annihilate either directly (a) or via an intermediate resonant state (b) into three final state particles.

The following resonances are relevant for the reaction  $p\bar{p}$  (at rest)  $\rightarrow K^+\pi^-\bar{K}^0$ :

$$\begin{aligned} p\bar{p} &\rightarrow \text{(direct)} \rightarrow K^+\pi^-\bar{K}^0 \\ p\bar{p} &\rightarrow K^+K^{*-} \rightarrow K^+(\pi^-\bar{K}^0) \\ p\bar{p} &\rightarrow K^{*0}\bar{K}^0 \rightarrow (K^+\pi^-)\bar{K}^0 \\ p\bar{p} &\rightarrow a_2^+\pi^- \rightarrow (K^+\bar{K}^0)\pi^- \\ p\bar{p} &\rightarrow a_0^+\pi^- \rightarrow (K^+\bar{K}^0)\pi^- \end{aligned}$$

The  $a_2$  refers to  $a_2(1320)$  and the  $a_0$  refers to  $a_0(980)$ . The corresponding list for the final state  $K^-\pi^+K^0$  can be obtained by exchanging particles and antiparticles.

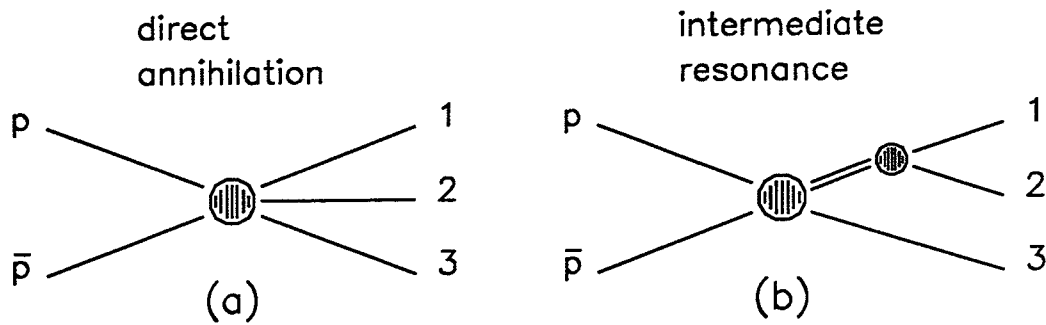


Figure 4.3: Two different diagrams leading to three-body final states.

The particles in parentheses are the decay products of the resonance. The quantum numbers and the approximate values for the mass and the width of the resonant states are listed in table 4.2.

resonance	I	J	L	S	P	quark composition	mass [MeV/c <sup>2</sup> ]	width [MeV/c <sup>2</sup> ]
$K^*(\bar{K}^*)$	1/2	1	0	1	-1	$u\bar{s}, d\bar{s}$ ( $s\bar{u}, s\bar{d}$ )	892	50
$a_2$	1	2	1	1	+1	$u\bar{d}, u\bar{u}, d\bar{d}$	1320	110
$a_0$	1	0	1	1	+1	$u\bar{d}, u\bar{u}, d\bar{d}$	980	57

Table 4.2: Quantum number assignments according to the standard quark-model and approximate values for the mass and the width for the resonances  $K^*(892)$ ,  $a_2(1320)$  and  $a_0(980)$ .

In the "golden" event sample, both charged and neutral states of the  $K^*$  can be observed, but only charged states of the  $a_2$  and  $a_0$ . Table 4.3 shows the decay modes for the  $K^*$  and the  $a_2$ , as given in [4].

#### 4.2.1 Event Type

The mass and the width of a resonance can be determined by analysing the invariant mass distribution of its decay products. In order to calculate the invariant masses, one needs to identify the particles and measure their momenta. Since the neutral kaon cannot be seen in the detector, the  $K^0(\bar{K}^0)$  momentum must be reconstructed from its decay products.

For the determination of the  $K^*$  mass difference,  $\Delta m_{K^*}$ , events with  $K^0(\bar{K}^0) \rightarrow \pi^+\pi^-$  decays are selected from trigger 233 data, i.e.

$$p\bar{p} \rightarrow K^\mp \pi^\pm K^0(\bar{K}^0), K^0(\bar{K}^0) \rightarrow \pi^+\pi^- \quad (\text{"golden } \pi^+\pi^- \text{ events}).$$

resonance	decay mode	fraction ( $\Gamma_i/\Gamma$ )
$K^{*\pm}$	$(K\pi)^\pm$	$(99.899\pm 0.009) \%$
	$K^\pm\gamma$	$(1.01\pm 0.09) \cdot 10^{-3}$
$K^{*0}, \bar{K}^{*0}$	$(K\pi)^0$	$(99.770\pm 0.020) \%$
	$K^0\gamma$	$(2.30\pm 0.20) \cdot 10^{-3}$
$a_2$	$\rho\pi$	$(70.1\pm 2.7) \%$
	$\eta\pi$	$(14.5\pm 1.2) \%$
	$\omega\pi$	$(10.6\pm 3.2) \%$
	$K\bar{K}$	$(4.9\pm 0.8) \%$
	$\pi^\pm\gamma$	$(2.7\pm 0.6) \cdot 10^{-3}$
	$\gamma\gamma$	$(8.2\pm 1.0) \cdot 10^{-6}$

Table 4.3: Decay modes of the  $K^*$  and the  $a_2$  mesons.

See section 2.4 for a description of the trigger 233. This event type is chosen for the following two reasons:

- $K^0(\bar{K}^0) \rightarrow \pi^+\pi^-$  is the only  $K^0(\bar{K}^0)$  decay with no neutral (unmeasured) secondary particles. This allows for best  $K^0(\bar{K}^0)$  momentum reconstruction.
- $\pi^+\pi^-$  decays come mainly from  $K_S^0$ . It is the only  $K_S^0$  decay mode (of any fraction) with charged particles in the final state. This means that all the other charged  $K^0(\bar{K}^0)$  decay modes seen in the detector are  $K_L^0$  decays. With an average neutral kaon momentum of  $\sim 550$  MeV/c, the mean decay length for the  $K_L^0$  is  $L_L \simeq 17$  m, while for the  $K_S^0$  it is  $L_S \simeq 3$  cm. Hence,  $K_L^0$  decays are strongly suppressed by the trigger 233.

## 4.2.2 Data Filtering

The data analysed in the present work were taken in run period 8 (October 90). The raw data were first passed through two standard filters, called FILTER7 and KAON4T. Two additional filters, called PREFILTER and 5CFIT, were then applied to select the final data sample.

The description of the filters assumes the following terminology and definitions:

- primary vertex =  $p\bar{p}$  annihilation vertex,
- secondary vertex = neutral kaon decay vertex,
- primary tracks = tracks originating from the primary vertex,

secondary tracks = tracks originating from the secondary vertex,

$E_{miss}$  = missing energy of the event, assuming a "golden  $\pi^+\pi^-$ " event

$$= 2m_p c^2 - E_K - E_\pi - E_{S1} - E_{S2} ,$$

$P_{miss}$  = missing momentum of the event

$$= | - (\vec{P}_K + \vec{P}_\pi + \vec{P}_{S1} + \vec{P}_{S2}) | ,$$

$M_{miss}$  = missing mass at the primary vertex

$$= \frac{1}{c^2} \sqrt{(2m_p c^2 - E_K - E_\pi)^2 - c^2 (\vec{P}_K + \vec{P}_\pi)^2} ,$$

$M_{inv}$  = invariant mass of the secondary tracks

$$= \frac{1}{c^2} \sqrt{(E_{S1} + E_{S2})^2 - c^2 (\vec{P}_{S1} + \vec{P}_{S2})^2} ,$$

Č flag = 0: no or ambiguous Čerenkov counter information,

= 1:  $\pi$  according to Čerenkov pulse height analysis,

= 2: K according to Čerenkov pulse height analysis,

$dE/dx$  flag (S1) = 0: no  $dE/dx$ -information,

= 1:  $\pi^\pm$  compatible, not  $K^\pm$  compatible,

= 2:  $K^\pm$  compatible, not  $\pi^\pm$  compatible,

= 3: not  $\pi^\pm$  compatible, not  $K^\pm$  compatible,

= 4:  $\pi^\pm$  compatible,  $K^\pm$  compatible,

where      subscript  $p$       means proton,  
              subscript  $K$       means primary charged kaon,  
              subscript  $\pi$       means primary pion,  
              subscript  $S1$      means first secondary pion,  
              subscript  $S2$      means second secondary pion,

$\pi^\pm$  compatible means the energy loss measured in the scintillator S1 is within 3 standard deviations from the expected energy loss for a charged pion and

$K^\pm$  compatible is explained as above.

#### 4.2.2.1 The FILTER7 and the KAON4T

A detailed description of these two filters can be found in [34]. The idea of FILTER7 and KAON4T is to verify that

- there are exactly 4 tracks,

- the sum of charges is zero,
- there is at least one kaon candidate,
- a primary vertex exists and
- a secondary vertex exists.

Two particles have an existing vertex if the tracks intersect in the transverse plane. The events passing these first two filters were written out to mini-DST's (Data Summary Tapes). The data used in this work comes from the tapes listed in table 4.4.

mini-DST	number of events	magnet polarity
HP0590	70'915	$\vec{B}$ parallel $\hat{z}$ -axis
HP0591	91'363	$\vec{B}$ antiparallel $\hat{z}$ -axis
HP0592	68'465	$\vec{B}$ antiparallel $\hat{z}$ -axis
HP0593	64'278	$\vec{B}$ antiparallel $\hat{z}$ -axis
HP0594	86'031	$\vec{B}$ antiparallel $\hat{z}$ -axis
all	381'052	

Table 4.4: The KAON4T mini-DST's from run period 8 used in this analysis.

#### 4.2.2.2 The PREFILTER

The purposes of the PREFILTER are:

- It ensures that all tracks are well measured and that the vertices are well defined.
- It looks for exactly one kaon candidate.
- It defines which are the primary and secondary tracks, and assigns a mass to each track.
- It ensures that the event kinematics agrees reasonably well with a "golden  $\pi^+\pi^-$ " hypothesis.

The complete list of the PREFILTER conditions is given below:

1. At least 2  $z$ -measurements for each track (DC + ST).
2. At least 4 wire hits for each track (PC + DC).
3. Exactly 1 kaon candidate, defined by
  - $\check{C}$  flag = 2,
  - $dE/dx$  flag  $\neq$  1 or 3 and
  - momentum  $\leq$  800 MeV/c.

4. No tracks other than the kaon candidate hit the same PID-sector.
5. The missing energy in the event,  $|E_{miss}|$ , is less than 250 MeV.
6. At least one primary pion candidate, defined by
  - opposite charge to the kaon candidate,
  - Č flag  $\neq 2$ ,
  - $dE/dx$  flag  $\neq 2$ ,
  - existing vertex with the kaon candidate,
  - this primary vertex is within a radius of 2 cm in the  $xy$ -plane from the detector center,
  - the  $z$ -coordinate of the primary vertex is within  $[-7 \text{ cm}, +9 \text{ cm}]$ ,
  - the minimum distance between the primary tracks and the primary vertex is less than 5 cm,
  - $\Delta M_{miss} = |M_{miss} - m_{K^0}| < 250 \text{ MeV}/c^2$  and
  - $\Delta M_{inv} = |M_{inv} - m_{K^0}| < 250 \text{ MeV}/c^2$ .

In case there is more than one primary pion candidate, the track with the smallest value of  $\Delta M_{miss} + \Delta M_{inv}$  is selected as the primary pion.

7. The remaining two tracks (secondary tracks) have an existing vertex and the minimum distance to this vertex is less than 5 cm.
8. None of the tracks is an electron candidate as defined by Čerenkov counter and scintillator S1 pulse height analysis for tracks with a momentum below 200 MeV/c.
9. The missing momentum of the event,  $P_{miss}$ , is less than 250 MeV/c.

#### 4.2.2.3 The 5CFIT

The filter 5CFIT is based on a kinematic fit with 5 constraints. It calculates for each event the confidence level for the hypothesis  $p\bar{p} \rightarrow K^\pm \pi^\mp K_S^0$ ,  $K_S^0 \rightarrow \pi^+ \pi^-$ . A description of the kinematic fit and its performance can be found in appendix A. The filter 5CFIT has two main effects:

- The background from other annihilation channels and from  $K_L^0$  decays is reduced.
- The measured momenta are corrected to satisfy the constraints, which improves the momentum resolution.

The following 5 constraints were used, requiring energy and momentum conservation and  $M_{miss} = m_{K^0}$ :

$$f_1 = E_K + E_\pi + E_{S1} + E_{S2} - 2 m_p c^2 = 0, \quad (4.11)$$

$$f_2 = P_K^x + P_\pi^x + P_{S1}^x + P_{S2}^x = 0, \quad (4.12)$$

$$f_3 = P_K^y + P_\pi^y + P_{S1}^y + P_{S2}^y = 0, \quad (4.13)$$

$$f_4 = P_K^z + P_\pi^z + P_{S1}^z + P_{S2}^z = 0, \quad (4.14)$$

$$f_5 = \frac{1}{m_{K^0} c^2} \left[ (2 m_p c^2 - E_K - E_\pi)^2 - c^2 (\vec{P}_K + \vec{P}_\pi)^2 \right] - m_{K^0} c^2 = 0. \quad (4.15)$$

A confidence level of more than 30 % was required for the final data sample used in the analysis.

Table 4.5 summarizes the data reduction for the various algorithms of the PRE-FILTER and the 5CFIT. The initial data sample on the KAON4T mini-DST's contained  $N_{total} = 381'052$  events.  $N_{left}$  is the number of events left after each filter condition and  $P = N_{left}/N_{total}$  is the corresponding ratio. The effect of each condition is further expressed by the number of rejected events,  $N_{cut}$ , and the reduction factor  $R = N_{cut}/N_{left}$  with respect to  $N_{left}$  of the previous condition.

filter	condition	$N_{cut}$	R	$N_{left}$	P [%]
KAON4T mini - DST's				381'052	100.0
PRE - FILTER	n°. of z-measurements	31'727	0.917	349'325	91.7
	n°. of xy-measurements	2'950	0.992	346'375	90.9
	kaon candidate	31'167	0.910	315'208	82.7
	PID sector	11'472	0.964	303'736	79.7
	missing energy	109'088	0.641	194'648	51.1
	primary pion	65'706	0.662	128'942	33.8
	secondary pions	16'791	0.870	112'151	29.4
	no electron candidate	2'899	0.974	109'252	28.7
	missing momentum	17'891	0.836	91'361	24.0
5CFIT	confidence level > 30 %	58'229	0.363	33'132	8.7

Table 4.5: Data reduction for the various algorithms of the PREFILTER and the 5CFIT.

### 4.2.3 Presentation of the Selected Data

This section is intended to show the effect of the filter 5CFIT on the data sample and to demonstrate the quality of the selected data.



Figure 4.4 shows scatter plots of the missing momentum  $P_{miss}$  versus the missing energy  $E_{miss}$  for events selected by the PREFILTER and for events left after the 5CFIT. For the data sample selected by the 5CFIT, the uncorrected particle momenta were used, since  $P_{miss}$  and  $E_{miss}$  (as well as  $M_{miss}$  and  $M_{inv}$ ) are determined by the constraints of the kinematic fit.

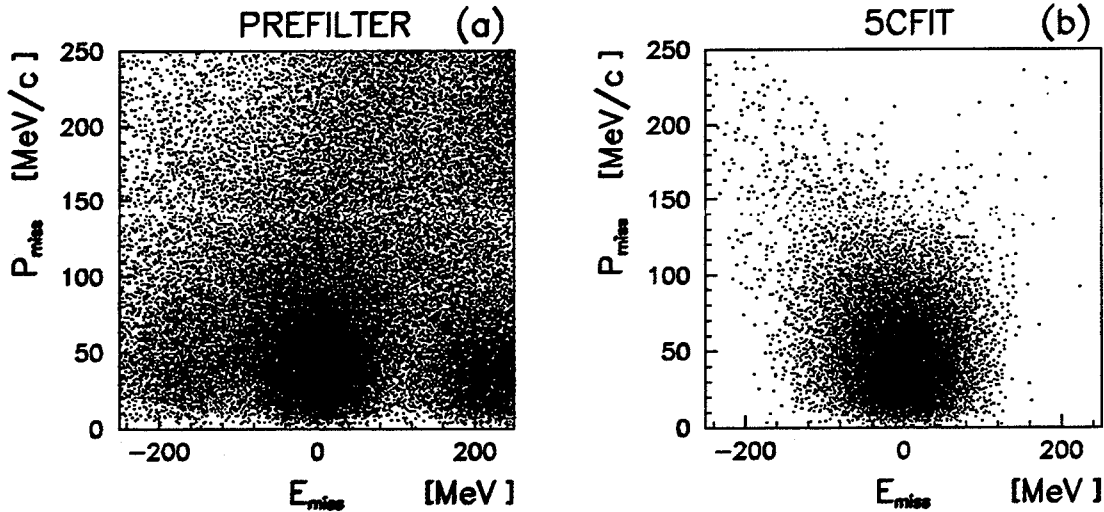
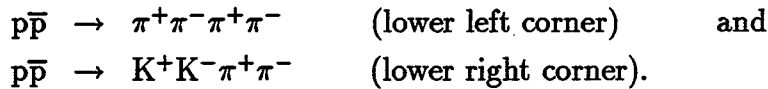


Figure 4.4: Missing momentum versus missing energy for the data samples selected by the PREFILTER (a) and the 5CFIT (b).

In the plot representing the PREFILTER data, an accumulation of events at the lower left and right corners is observed. These events are background events due to particle misidentification (see paragraph 4.2.4.3) and are mainly of the type



The filter 5CFIT removes these background events almost completely (see figure 4.4 (b)). The events passing the 5CFIT with  $P_{miss} > 120$  MeV/c are not background events, but contain one or more particles with badly measured momenta. This was demonstrated with the simulated "golden  $\pi^+\pi^-$ " sample MCT233, described in appendix B.1, where this type of events is also present.

The distributions of the missing mass at the primary vertex,  $M_{miss}$ , and the invariant mass of the secondary tracks,  $M_{inv}$ , are shown in figure 4.5. The distributions for the 5CFIT data, represented by the hatched histograms, are still asymmetric. Again, this is not due to background events, since the same asymmetries can be reproduced with the simulated "golden  $\pi^+\pi^-$ " data.

To test the detector resolution, a fit to the invariant mass distribution  $M_{inv}$  (5CFIT) with a Gaussian function plus a "background" parameterization to compensate for the

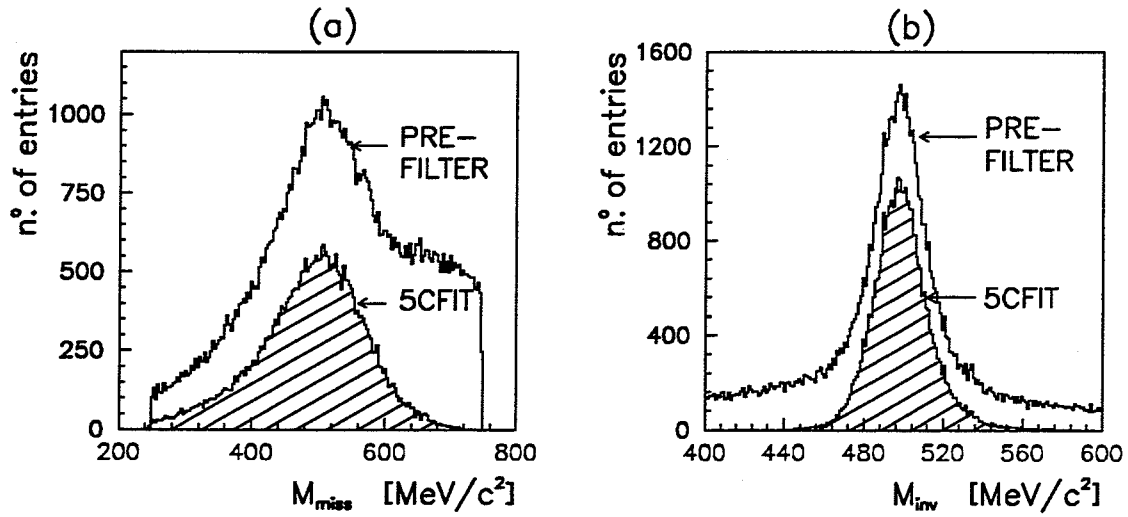


Figure 4.5: The distributions of the missing mass  $M_{miss}$  (a) and the invariant mass  $M_{inv}$  (b).

asymmetry was done. For the "background", another Gaussian function or polynomials of order 2, 3 and 4 in  $M_{inv}$  were tried.

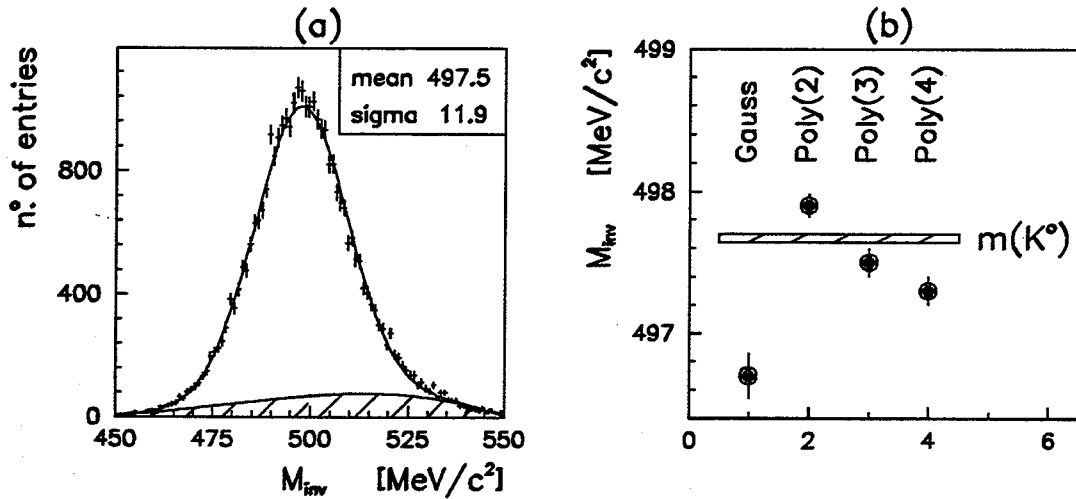


Figure 4.6: Fit example of the invariant mass distribution (a) and the results for the mean values of the Gaussian function (b).

Figure 4.6 (a) shows as an example the fit of the  $M_{inv}$  distribution with a polynomial of order 3 for the "background". Figure 4.6 (b) presents the values obtained for the mean of the main Gaussian function for the "background" parameterizations considered. The error bars represent a one standard deviation statistical error. All four mean values are within 1  $\text{MeV}/c^2$  of the neutral kaon mass  $m_{K^0} = (497.671 \pm 0.031) \text{MeV}/c^2$ , as given in [4].

The momentum spectra for the primary charged kaon ( $P_{K^\pm}$ ), the neutral kaon ( $P_{K^0} = |\vec{P}_{S1} + \vec{P}_{S2}|$ ), the primary pion ( $P_\pi$ ) and the combined spectrum for the two secondary pions ( $P_{S1}, P_{S2}$ ) are presented in figure 4.7, showing the corrected momenta for the data sample after the 5CFIT.

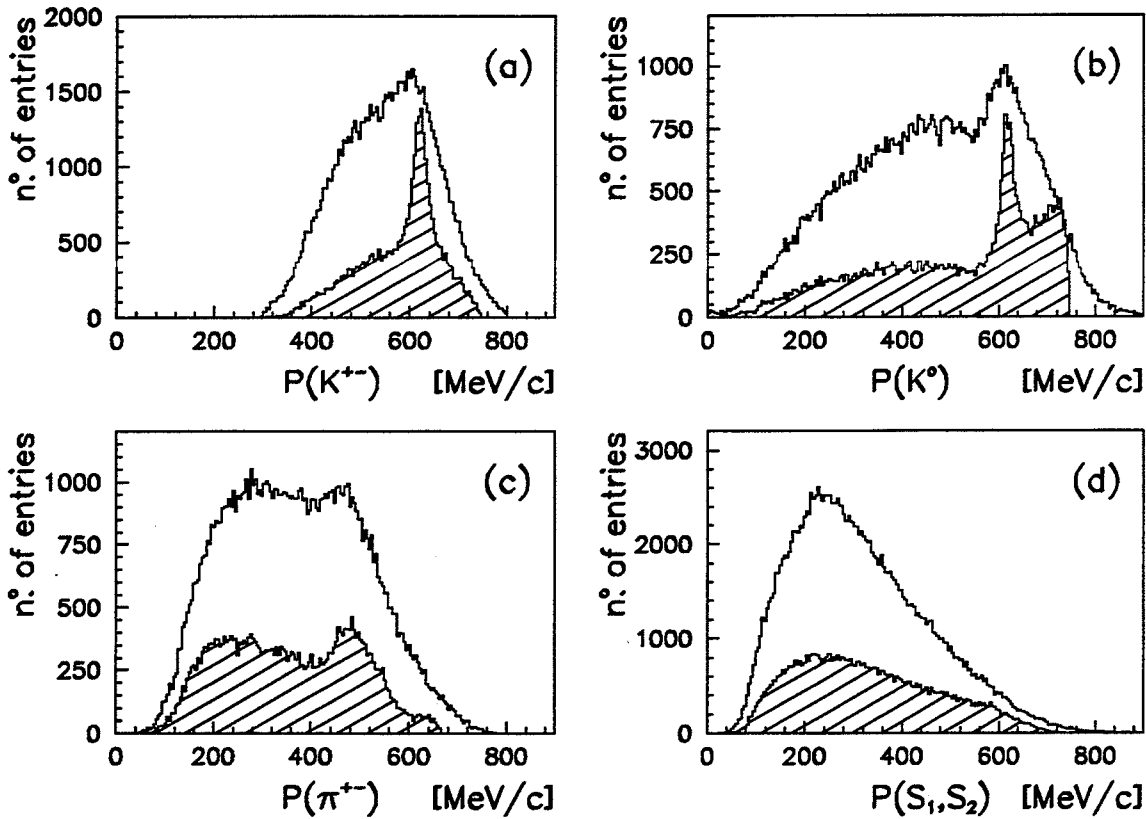


Figure 4.7: Momentum spectra for the primary charged kaon (a), the neutral kaon (b), the primary pion (c) and the combined spectrum for the two secondary pions (d).

While the typical peaks due to the resonant two-body decays of the protonium (see figure 4.3) are hardly visible in the distributions of the PREFILTER data, they are very clear after the 5CFIT. In addition, the 5CFIT confines the distribution to the kinematically allowed range.

The important quantities in the analysis are the invariant masses squared,  $M_{inv}^2(i, j)$ , of the two-particle combinations  $(K^0, \pi^\pm)$ ,  $(K^\pm, \pi^\mp)$  and  $(K^0, K^\pm)$ , given by

$$M_{inv}^2(i, j) = \frac{1}{c^4} \left[ (E_i + E_j)^2 - c^2 (\vec{P}_i + \vec{P}_j)^2 \right]. \quad (4.16)$$

If the particles  $(i, j)$  are the decay products of an intermediate resonance,  $M_{inv}^2(i, j)$  is equal to the resonance mass squared. In figure 4.8, the distributions of  $M_{inv}^2(i, j)$  and the Dalitz-plots  $M_{inv}^2(K^\pm, \pi^\mp)$  versus  $M_{inv}^2(K^0, \pi^\pm)$  are shown. In the final data sample, the resonances show up as clear peaks in the corresponding invariant mass squared distributions.

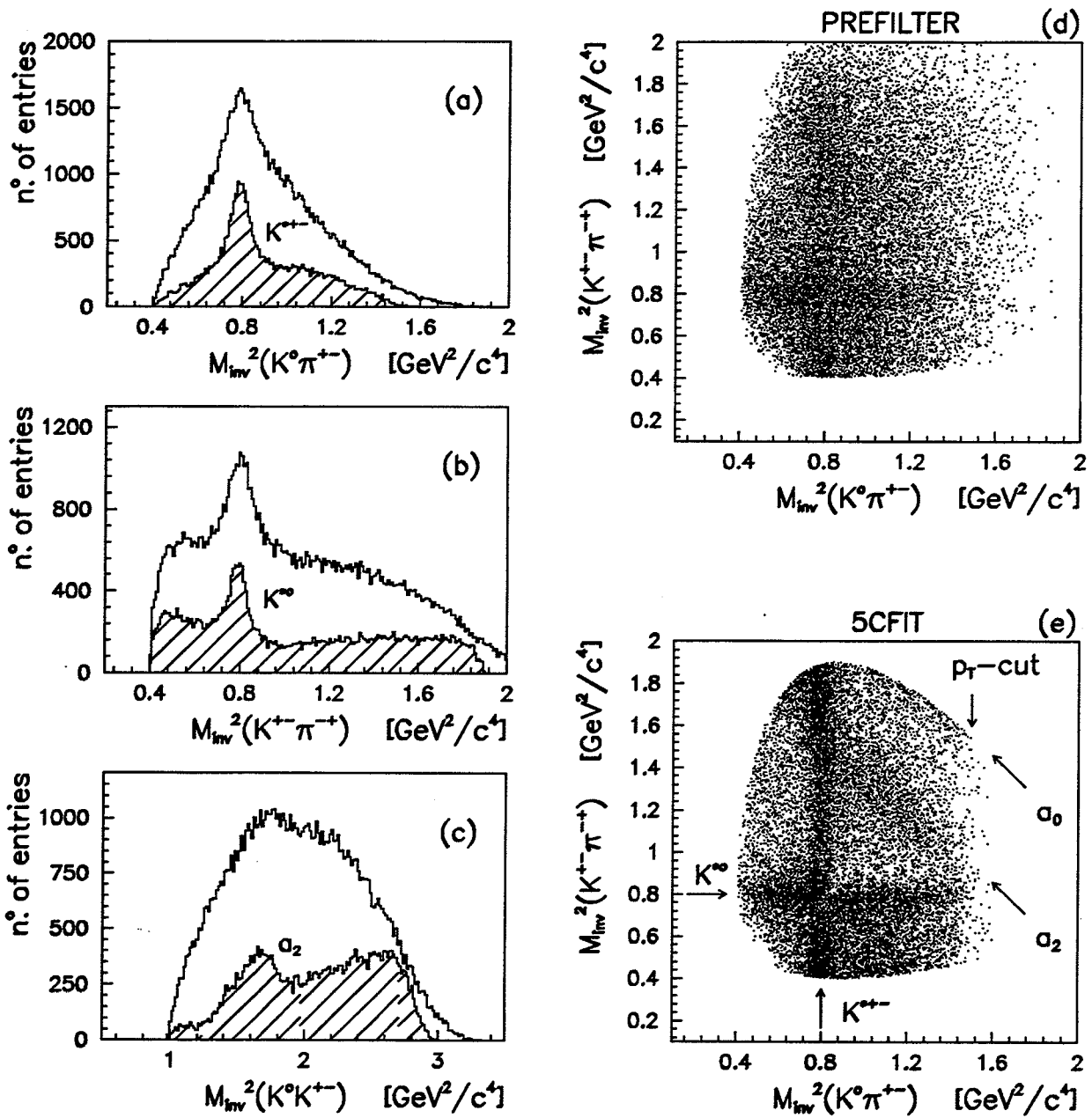


Figure 4.8: Invariant mass squared distributions  $M_{inv}^2(K^0, \pi^\pm)$  (a),  $M_{inv}^2(K^\pm, \pi^\mp)$  (b),  $M_{inv}^2(K^0, K^\pm)$  (c) and the Dalitz-plots  $M_{inv}^2(K^\pm, \pi^\mp)$  vs  $M_{inv}^2(K^0, \pi^\pm)$  [(d) and (e)].

The most valuable information is contained in the Dalitz-plot density distributions, where the following remarks can be made:

1. Here, the effect of the 5CFIT on the data sample is especially impressive. The structure of the Dalitz-plot is much clearer after the 5CFIT and the events are confined to the kinematically allowed region.

2. The mass range with  $M_{inv}^2(K^0, \pi^\pm) > 1.5 \text{ GeV}/c^4$  is missing due to the  $p_T$ -cut of the trigger.
3. The lower left corner of the Dalitz-plot is missing as well. The kinematics of this area corresponds to a maximum of  $M_{inv}^2(K^0, K^\pm)$  and hence to a minimum of the primary pion momentum  $P_\pi$ . The events in this area are lost because the primary pion cannot reach the PID.
4. The  $K^{*\pm}$  ( $K^{*0}, \bar{K}^{*0}$ ) resonances appear as clear vertical (horizontal) bands.
5. The  $a_2^\pm$  - band (and an indication of the  $a_0^\pm$  -band) is broader and runs along the diagonal.
6. There is interference between the two  $K^*$  - bands in the intersection region. An accumulation of events at the upper left side and a depletion at the lower right side of the intersection region can be seen.

#### 4.2.4 Background Analysis

There are several possible sources for background in the data. The following three are most important:

- $K_L^0$  decays into  $\pi^\pm e^\mp \nu$ ,  $\pi^\pm \mu^\mp \nu$  and  $\pi^+ \pi^- \pi^0$ .
- Events with an additional  $\pi^0$  from the  $p\bar{p}$  annihilation, i.e.
 
$$p\bar{p} \rightarrow K^\mp \pi^\pm K^0(\bar{K}^0) \pi^0, \quad K^0(\bar{K}^0) \rightarrow \pi^+ \pi^-.$$
- Misidentification of a kaon as a pion or vice versa. This leads to the misidentification of the following event types as "golden" events:

$$\begin{aligned} p\bar{p} &\rightarrow K^+ K^- \pi^+ \pi^- \quad \text{and} \\ p\bar{p} &\rightarrow \pi^+ \pi^- \pi^+ \pi^- \quad . \end{aligned}$$

##### 4.2.4.1 Semileptonic and three Pion Decays of $K_L^0$

The background from semileptonic and three pion decays was studied as follows:

1. By means of the simulation program described in appendix B.2, the fraction of "golden" events with  $K_L^0$  decays was estimated for trigger 233 raw data.
  - The branching ratios for the  $K_S^0$  and  $K_L^0$  decay modes were taken from [4].
  - The neutral kaon decay vertex was required to be inside the radius defined by the DC4 wire plane.

- The branching ratios for the different annihilation channels (direct annihilation into three final state particles or production of intermediate resonances) was varied and the resultant effect was found to be small.
  - The influence of the  $p_T$ -cut was investigated and no effect was found.
2. Since the filters FILTER7 and KAON4T do not contain any conditions which obviously prefer a special neutral kaon decay mode, it was assumed that they do not change the percentage of events with a  $K_L^0$  decay in the data.
  3. The simulated data sample MCT433, described in appendix B.1, was used to determine the reduction factors of the PREFILTER and the 5CFIT for the decay modes  $K_S^0 \rightarrow \pi^+\pi^-$ ,  $K_L^0 \rightarrow \pi^\pm e^\mp \nu$ ,  $K_L^0 \rightarrow \pi^\pm \mu^\mp \nu$  and  $K_L^0 \rightarrow \pi^+\pi^-\pi^0$ .

Table 4.6 summarizes the fractions of events with  $K_S^0$  and  $K_L^0$  decays in the raw, the PREFILTER and the 5CFIT data samples. A background of  $\sim 0.1$  % remains from semileptonic  $K_L^0$  decays.

decay mode	raw data fraction [%]	PREFILTER		5CFIT	
		reduction factor R	fraction [%]	reduction factor R	fraction [%]
$K_S^0 \rightarrow \pi^+\pi^-$	96.22	$1.59 \cdot 10^{-1}$	97.96	$6.05 \cdot 10^{-1}$	99.90
$K_L^0 \rightarrow \pi^\pm e^\mp \nu$	1.94	$8.97 \cdot 10^{-2}$	1.11	$3.37 \cdot 10^{-2}$	0.07
$K_L^0 \rightarrow \pi^\pm \mu^\mp \nu$	1.29	$8.84 \cdot 10^{-2}$	0.73	$2.95 \cdot 10^{-2}$	0.03
$K_L^0 \rightarrow \pi^+\pi^-\pi^0$	0.55	$5.58 \cdot 10^{-2}$	0.20	$5.88 \cdot 10^{-4}$	$\approx 0$

Table 4.6: Reduction of background from  $K_L^0$  decays due to the PREFILTER and the 5CFIT.

#### 4.2.4.2 Additional $\pi^0$ from the $p\bar{p}$ Annihilation

The invariant mass squared of an additional neutral particle in the event is given by

$$M_{inv}^2(\text{neutral}) = \frac{1}{c^4} \left[ (2m_p c^2 - E_K - E_\pi - E_{S1} - E_{S2})^2 - c^2 (\vec{P}_K + \vec{P}_\pi + \vec{P}_{S1} + \vec{P}_{S2})^2 \right] . \quad (4.17)$$

Figure 4.9 shows the distribution of  $M_{inv}^2(\text{neutral})$  for the final data sample, calculated using the uncorrected momenta. No indication is found for events with an additional  $\pi^0$ .

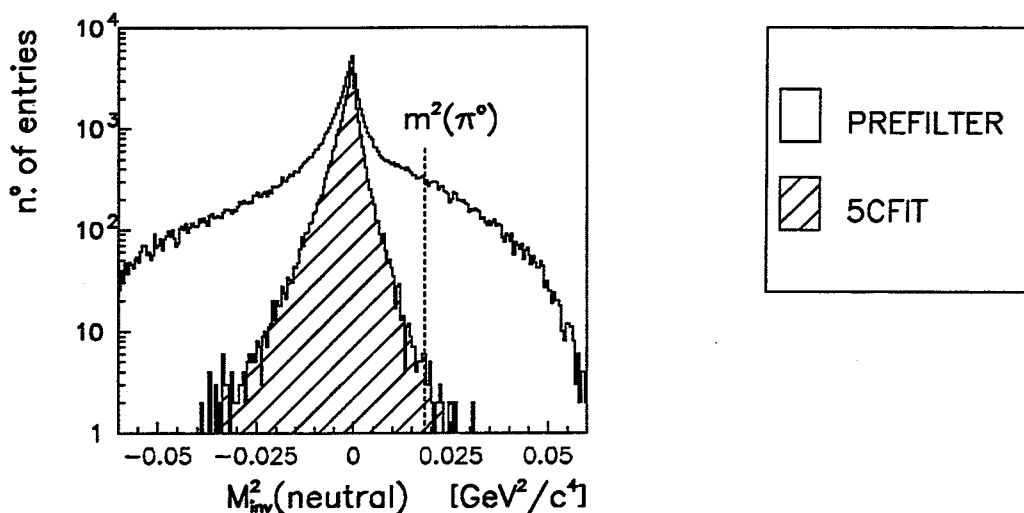


Figure 4.9: Invariant mass squared of a possible additional neutral particle in the event. No indication is found for events with an additional  $\pi^0$ .

#### 4.2.4.3 Particle Misidentification

Particle misidentification is the main source of background in the data sample after the PREFILTER. The two event-types

$$\begin{aligned} p\bar{p} &\rightarrow K^+K^-\pi^+\pi^- & \text{and} \\ p\bar{p} &\rightarrow \pi^+\pi^-\pi^+\pi^- \end{aligned}$$

are clearly visible in the plot  $P_{miss}$  vs  $E_{miss}$  (see fig. 4.4 (a)). The kinematics of these events is quite different from the "golden  $\pi^+\pi^-$ " events

$$p\bar{p} \rightarrow K^\mp\pi^\pm K^0(\bar{K}^0), \quad K^0(\bar{K}^0) \rightarrow \pi^+\pi^-$$

and hence this background is strongly suppressed by the filter 5CFIT (see fig. 4.4 (b)).

Another way to see this type of background is to plot the invariant mass squared distribution for each track, defined as

$$M_{inv}^2(\text{K-track}) \equiv \frac{1}{c^4} \left[ (2m_p c^2 - E_\pi - E_{S1} - E_{S2})^2 - c^2 (\vec{P}_\pi + \vec{P}_{S1} + \vec{P}_{S2})^2 \right], \quad (4.18)$$

$$M_{inv}^2(\pi\text{-track}) \equiv \frac{1}{c^4} \left[ (2m_p c^2 - E_K - E_{S1} - E_{S2})^2 - c^2 (\vec{P}_K + \vec{P}_{S1} + \vec{P}_{S2})^2 \right], \quad (4.19)$$

$$M_{inv}^2(\text{S1-track}) \equiv \frac{1}{c^4} \left[ (2m_p c^2 - E_K - E_\pi - E_{S2})^2 - c^2 (\vec{P}_K + \vec{P}_\pi + \vec{P}_{S2})^2 \right], \quad (4.20)$$

$$M_{inv}^2(\text{S2-track}) \equiv \frac{1}{c^4} \left[ (2m_p c^2 - E_K - E_\pi - E_{S1})^2 - c^2 (\vec{P}_K + \vec{P}_\pi + \vec{P}_{S1})^2 \right]. \quad (4.21)$$

In figure 4.10, these distributions are displayed for the data sample after the PREFILTER and the 5CFIT (hatched histograms), again using the uncorrected momenta

for the 5CFIT data. In the PREFILTER data sample, the misidentifications of kaons as pions ( $K^+K^-\pi^+\pi^-$  events are identified as "golden" events) shows up as a peak at  $m_K^2$  in the  $M_{inv}^2(\pi\text{-track})$  distribution. The peak in the  $M_{inv}^2(K\text{-track})$  distribution at  $\sim 0.6 \text{ GeV}^2/c^4$  is produced by the same events. The invariant mass squared of the kaon track is too high because of the wrong mass assignment for the pion track. The correlation between these two peaks can be seen in the scatter-plot  $M_{inv}^2(\pi\text{-track})$  versus  $M_{inv}^2(K\text{-track})$ , where the  $K^+K^-\pi^+\pi^-$  events appear in the upper right corner. The misidentification of pions as kaons ( $\pi^+\pi^-\pi^+\pi^-$  events) is less frequent. A small enhancement at the lower left corner of the scatter-plot is seen due to these events. The filter 5CFIT eliminates most of the events with misidentified particles.

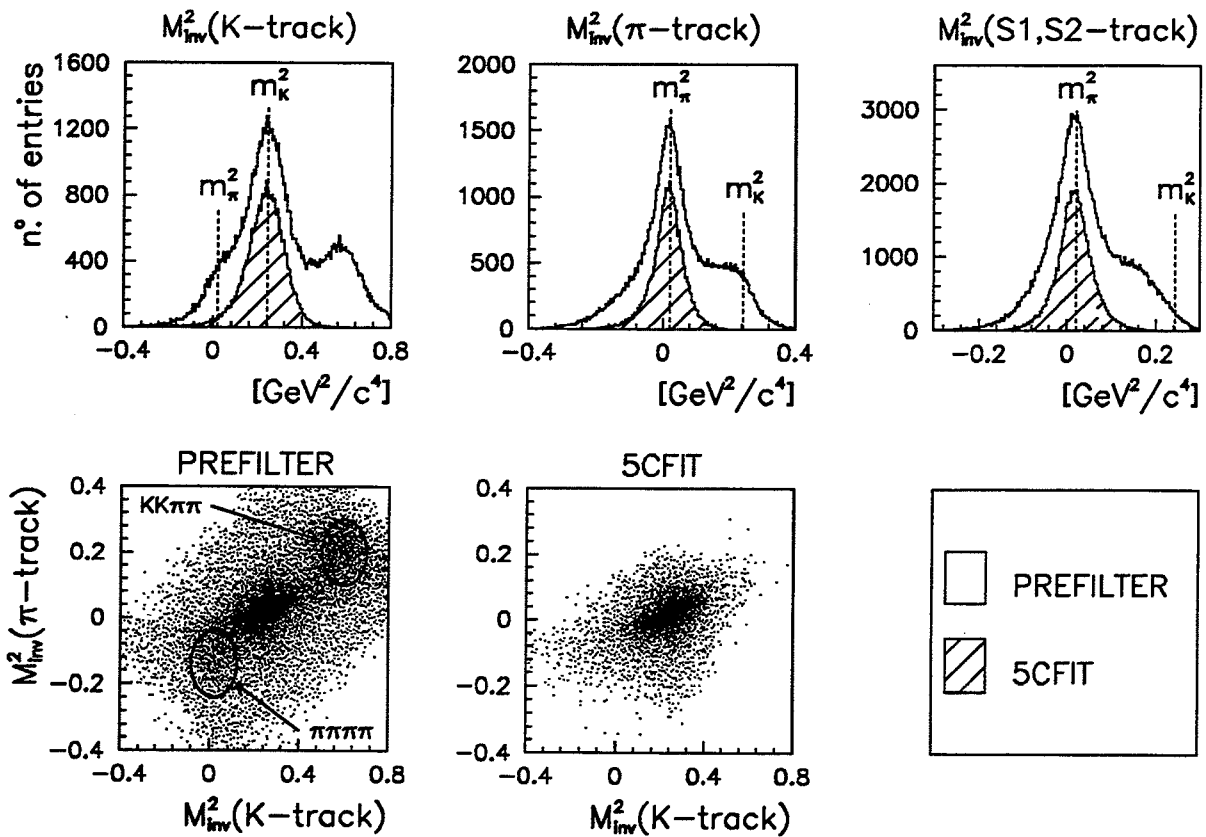


Figure 4.10: The invariant mass squared distributions for the primary tracks, the combined distribution for the secondary tracks and the scatter-plot  $M_{inv}^2(\pi\text{-track})$  vs  $M_{inv}^2(K\text{-track})$ . Particle misidentification is frequent in the PREFILTER data, but is almost absent after the filter 5CFIT.

### 4.3 Parameterization of the Dalitz-Plot Density

As mentioned already, the Dalitz-plot shown in figure 4.8 indicates interference between the two  $K^*$  bands. This is again demonstrated in figure 4.11, where slices of the



Dalitz-plot are projected. Close to the intersection region of the two  $K^*$  bands, the  $K^*$  peaks are shifted and distorted due to the interference.

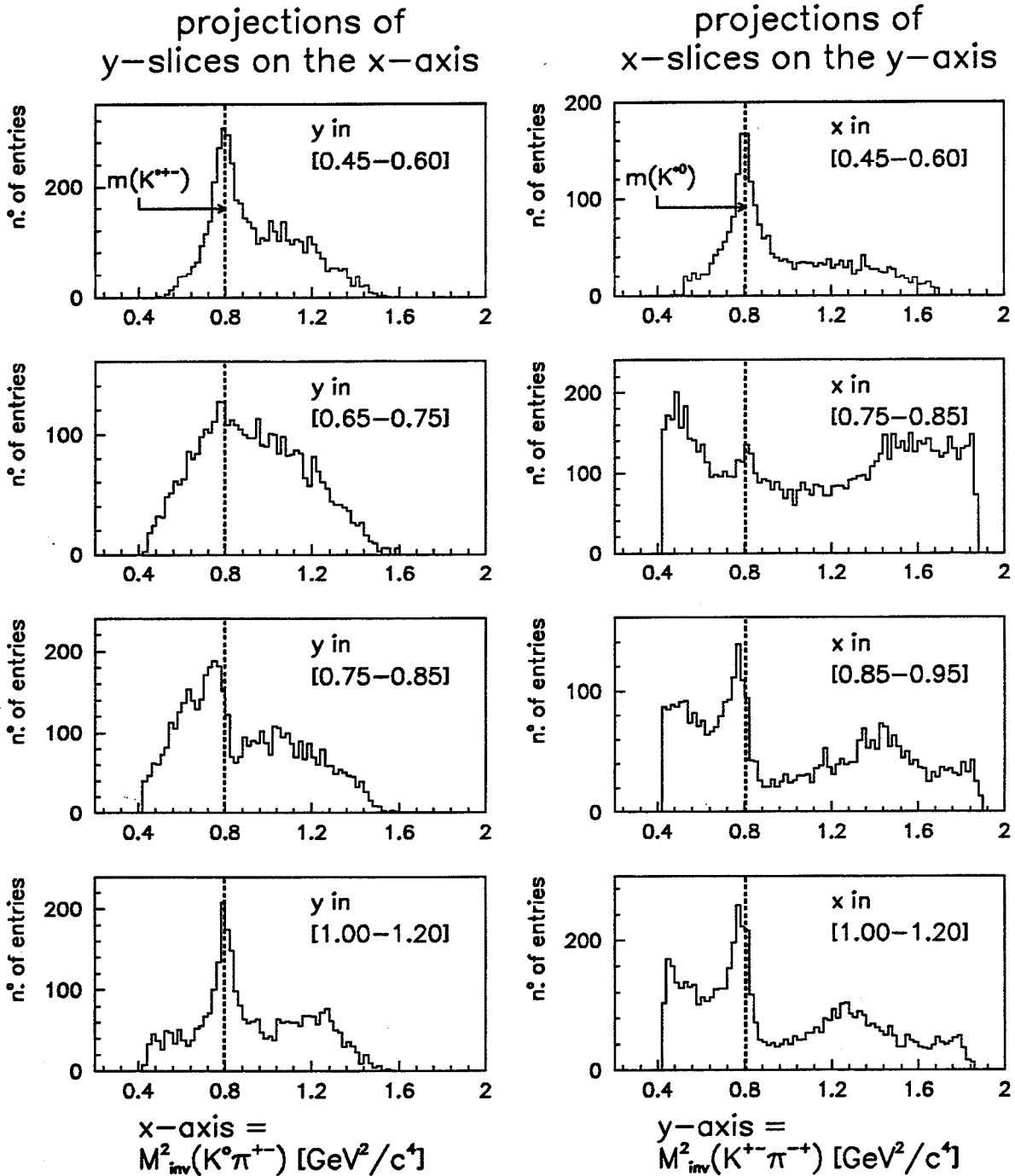


Figure 4.11: Projections of Dalitz-plot slices, indicating interference between the two  $K^*$  bands.

Because of this interference effect, it is impossible to determine the charged and neutral  $K^*$  masses with a fit to the corresponding invariant mass squared distributions

$M_{inv}^2(K^0, \pi^\pm)$  and  $M_{inv}^2(K^\pm, \pi^\mp)$ . For a measurement of the  $K^*$  resonance parameters  $m_{K^*}$  and  $\Gamma_{K^*}$ , a Dalitz-plot analysis is needed, with separate parameterizations of the resonances and the non-resonant part, and the possibility of interference between the different contributions.

Conforto et al. [35],[36] analysed  $p\bar{p}$  annihilations at rest of the type  $p\bar{p} \rightarrow K\bar{K}\pi$ , using data taken with a hydrogen bubble chamber. Since antiprotons annihilate mainly from an s-wave orbital of the protonium in liquid hydrogen [21], Conforto et al. considered only s-wave annihilations in their model and found 10 amplitudes contributing to the reaction  $p\bar{p} \rightarrow K^\mp \pi^\pm K^0(\bar{K}^0)$ .

At CPLEAR, the antiprotons are stopped in gaseous hydrogen at 15 bar pressure. The fraction of p-wave annihilations at this target density was measured to be [17],[37]

$$f_p = 0.38 \pm 0.09.$$

While  $p\bar{p}$  annihilations from atomic d-levels can always be neglected [38], one cannot neglect p-wave annihilations in the data used for this analysis.

In the first part of this section, an extension of the Conforto model to p-wave annihilations is discussed. The list of the amplitudes contributing to the reaction  $p\bar{p} \rightarrow K^\mp \pi^\pm K^0(\bar{K}^0)$  is given in appendix C. Unfortunately, the number of amplitudes becomes very large and one can no longer fit the Dalitz-plot density with all the amplitudes. The second part describes then the simplified parameterization used for a fit of the Dalitz-plot population.

#### 4.3.1 Expansion of the Conforto-Model to P-Wave Annihilations

In this section, the Conforto model and its extension to p-wave annihilations is presented. More detailed descriptions of the Conforto model itself can be found in [35] and especially in [36].

The  $p\bar{p}$  system at rest, the protonium, can be considered as an unstable meson with a mass equal to twice the proton mass. The transition matrix elements for the reaction  $p\bar{p} \rightarrow K\bar{K}\pi$  are then constructed in an analogous way to the decay matrix elements of a meson into three pseudoscalar mesons.

For the present analysis, the two final states  $K\bar{K}\pi = K^+\bar{K}^0\pi^-$  and  $K\bar{K}\pi = K^0\bar{K}^-\pi^+$  are of interest. The determination of the transition matrix elements for these two final states is equivalent and from now on only the reaction

$$p\bar{p} \text{ (at rest)} \rightarrow K^+\bar{K}^0\pi^-$$

shall be discussed.

In difference to a meson, the protonium is not in an eigenstate of

- the total isospin  $I$ ,
- the spin angular momentum  $S$ ,
- the orbital angular momentum  $L$  and
- the total angular momentum  $J$ ,

but is a mixture of such eigenstates. Allowing s- and p-wave annihilations, 12 possible initial states of the protonium have to be considered. Table 4.7 shows a list of the 12 initial  $p\bar{p}$  states, of which only 10 can contribute to the reaction  $p\bar{p} \rightarrow K^\mp \pi^\pm K^0(\bar{K}^0)$ .

For a nucleon-antinucleon system ( $N\bar{N}$ ), the eigenvalues for the discrete symmetries  $P, C$  and  $G$  are given by [21]

$$\text{parity} \quad P = (-1)^{L+1}, \quad (4.22)$$

$$\text{charge conjugation} \quad C = (-1)^{L+S} \quad \text{and} \quad (4.23)$$

$$\text{G-parity} \quad G = (-1)^{L+S+I}. \quad (4.24)$$

The four quantum numbers  $J, P, C$  and  $I$  can be chosen to characterize the initial  $p\bar{p}$  state in an unique way. These quantum numbers, as well as the G-parity, are conserved in the annihilation process. The invariant transition amplitudes are obtained by the projection of the final states with well defined quantum numbers  $J, P, C$  and  $I$  on the 12 possible initial states. The relevant  $S$ -matrix elements are then

$$A_I^{JPC} = \langle K\bar{K}\pi(JPCI) | S | p\bar{p}(JPCI) \rangle. \quad (4.25)$$

Assuming an incoherent mixture of  $J, P$  and  $C$  eigenstates and no polarization for the initial  $p\bar{p}$  system, the following expression for the transition rate is obtained:

$$d\Gamma = \frac{1}{(2\pi)^3} \frac{1}{32(2m_p)^3} \left| \langle p\bar{p} | S | K^+\bar{K}^0\pi^- \rangle \right|^2 dM_{inv}^2(\bar{K}^0, \pi^-) dM_{inv}^2(K^+, \pi^-) \quad (4.26)$$

with

$$\left| \langle p\bar{p} | S | K^+\bar{K}^0\pi^- \rangle \right|^2 = \sum_{JPC} \left| \alpha_{I=0} \cdot A_{I=0}^{JPC} + \alpha_{I=1} \cdot A_{I=1}^{JPC} \right|^2,$$

where  $\alpha_I$  are isospin factors, originating from the decomposition of the final state  $K^+\bar{K}^0\pi^-$  into eigenstates of the total isospin,  $I$ , and the isospin of the  $K\bar{K}$  subsystem,  $I_{K\bar{K}}$ . The isospin factors are of no further importance, since they are absorbed in the fit parameters (see equation 4.39).

Apart from effects of the detector, trigger and event selection acceptance (see section 4.4), the transition rate  $d\Gamma$  is proportional to the measured density in the Dalitz-plot  $M_{inv}^2(K^+, \pi^-)$  versus  $M_{inv}^2(\bar{K}^0, \pi^-)$ .

$p\bar{p}$ initial state $(2I+1)(2S+1)L_J$	discrete symmetries			S-matrix element
	P	C	G	$A_I^{JPC}$ structure
$^{11}S_0$ $^{31}S_0$	-	+	+	$A_0^{0-+}$ $A_1^{0-+}$ pseudoscalar
$^{13}S_1$ $^{33}S_1$	-	-	-	$A_0^{1--}$ $A_1^{1--}$ axial vector
$^{13}P_0$ $^{33}P_0$	+	+	+	not allowed
$^{11}P_1$ $^{31}P_1$	+	-	-	$A_0^{1+-}$ $A_1^{1+-}$ vector
$^{13}P_1$ $^{33}P_1$	+	+	+	$A_0^{1++}$ $A_1^{1++}$ vector
$^{13}P_2$ $^{33}P_2$	+	+	+	$A_0^{2++}$ $A_1^{2++}$ rank 2 tensor

Table 4.7: Discrete symmetry eigenvalues of the initial  $p\bar{p}$  states and the corresponding S-matrix elements.

#### 4.3.1.1 Symmetry Properties of the Transition Amplitudes

The G-parity of the final state  $K\bar{K}\pi$  and the  $K\bar{K}$  subsystem are given by [35]

$$G(K\bar{K}\pi) = G(K\bar{K}) \cdot G(\pi) \quad \text{and} \quad (4.27)$$

$$G(K\bar{K}) = (-1)^{I_{K\bar{K}} + l_{K\bar{K}}}, \quad (4.28)$$

where  $I_{K\bar{K}}$  is the isospin and  $l_{K\bar{K}}$  the relative orbital angular momentum of the  $K\bar{K}$  system. With  $G(\pi) = -1$  and  $I_{K\bar{K}} = 1$  for  $K\bar{K} = K^+\bar{K}^0$ , the G-parity of the final state  $K^+\bar{K}^0\pi^-$  is

$$G(K^+\bar{K}^0\pi^-) = (-1)^{l_{K\bar{K}}}. \quad (4.29)$$

With equation 4.24, the conservation of G-parity in the annihilation process imposes the condition

$$(-1)^{L+S+I} = (-1)^{l_{K\bar{K}}}. \quad (4.30)$$

The parity  $P$  of the final  $K\bar{K}\pi$  state is

$$\begin{aligned} P(K\bar{K}\pi) &= P(K) \cdot P(\bar{K}) \cdot P(\pi) \cdot (-1)^{L_i} \cdot (-1)^{l_{jk}} \\ &= (-1)^{L_i + l_{jk} + 1}, \end{aligned} \quad (4.31)$$

where  $(i, j, k)$  is a permutation of  $(K, \bar{K}, \pi)$ ,  $L_i$  is the relative angular momentum between particle  $i$  and the subsystem  $(jk)$  and  $l_{jk}$  is the relative angular momentum

between particle  $j$  and  $k$ . Using equation 4.22, parity conservation leads to the condition

$$(-1)^L = (-1)^{L_i + l_{jk}}. \quad (4.32)$$

The symmetry properties imposed by equations 4.30 and 4.32 on the transition matrix elements  $A_I^{JPC}$  are listed in table 4.8. The relative angular momentum  $l_{\bar{K}\bar{K}}$  indicates the symmetry of the matrix element under the exchange of the space variables of  $\bar{K}$  and  $\bar{K}$ . The reason why the initial states  $^{13}P_0$  and  $^{33}P_0$  cannot contribute to the reaction  $p\bar{p} \rightarrow K^\pm \pi^\mp K_S^0$  is the requirement  $L_i + l_{jk} = \text{odd}$  (equation 4.32), which is in contradiction to  $J = 0$ .

$(2I+1)(2S+1)L_J$	$A_I^{JPC}$	$G(p\bar{p})$	$G(K\bar{K})$	$l_{\bar{K}\bar{K}}$	$L_i + l_{jk}$	$L_\pi$
$^{11}S_0$	$A_0^{0-+}$	+	-	even	even	even
$^{31}S_0$	$A_1^{0-+}$	-	+	odd	even	odd
$^{13}S_1$	$A_0^{1--}$	-	+	odd	even	odd
$^{33}S_1$	$A_1^{1--}$	+	-	even	even	even
$^{11}P_1$	$A_0^{1+-}$	-	+	odd	odd	even
$^{31}P_1$	$A_1^{1+-}$	+	-	even	odd	odd
$^{13}P_1$	$A_0^{1++}$	+	-	even	odd	odd
$^{33}P_1$	$A_1^{1++}$	-	+	odd	odd	even
$^{13}P_2$	$A_0^{2++}$	+	-	even	odd	odd
$^{33}P_2$	$A_1^{2++}$	-	+	odd	odd	even

Table 4.8: Symmetry properties of the transition matrix elements  $A_I^{JPC}$ .

#### 4.3.1.2 Partial Wave Decomposition and Separation of the Angular Variables

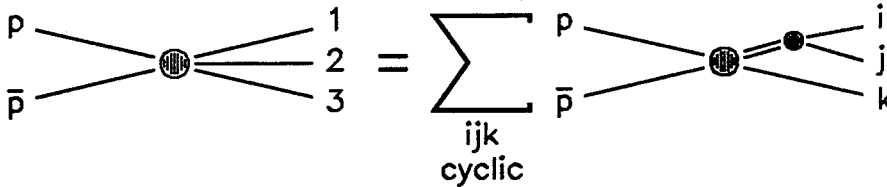


Figure 4.12: Two-body decomposition of the three-body annihilation.

With the assumption that the three-body annihilation process  $p\bar{p} \rightarrow K\bar{K}\pi$  can be decomposed in a series of two-body processes [35], as shown in figure 4.12, the matrix

elements  $A_I^{JPC}$  can then be decomposed as

$$\begin{aligned}
A_I^{JPC} &= \sum_{L_\pi, l_{K\bar{K}}} a_{L_\pi l_{K\bar{K}}}^{JPC}(s_{K\bar{K}}, \vartheta_{K\bar{K}}) \cdot \frac{e^{i\delta_{K\bar{K}}} \sin \delta_{K\bar{K}}}{p_{K\bar{K}}} \\
&+ \sum_{L_{\bar{K}}, l_{K\pi}, I_{K\pi}} b_{L_{\bar{K}} l_{K\pi}, I_{K\pi}}^{JPC}(s_{K\pi}, \vartheta_{K\pi}) \cdot \frac{e^{i\delta_{K\pi}} \sin \delta_{K\pi}}{p_{K\pi}} \\
&+ \sum_{L_K, l_{\bar{K}\pi}, I_{\bar{K}\pi}} c_{L_K l_{\bar{K}\pi}, I_{\bar{K}\pi}}^{JPC}(s_{\bar{K}\pi}, \vartheta_{\bar{K}\pi}) \cdot \frac{e^{i\delta_{\bar{K}\pi}} \sin \delta_{\bar{K}\pi}}{p_{\bar{K}\pi}}, \quad (4.33)
\end{aligned}$$

with

$$\begin{aligned}
\vec{p}_{jk} &= \frac{(m_j \cdot \vec{p}_k - m_k \cdot \vec{p}_j)}{(m_j + m_k)}, \\
\cos \vartheta_{jk} &= \frac{(\vec{p}_{jk} \cdot \vec{p}_i)}{(|\vec{p}_{jk}| \cdot |\vec{p}_i|)},
\end{aligned}$$

where  $\vec{p}_i, \vec{p}_j, \vec{p}_k$  are the momenta of the particles  $i, j, k$  in the  $p\bar{p}$  rest frame,  
 $\vec{p}_{jk}$  is the relative momentum of the particles  $j$  and  $k$  in the  $(jk)$  rest frame,  
 $\vartheta_{jk}$  is the decay angle of the system  $(ij)$  with respect to  $\vec{p}_i$  and  
 $s_{jk}$  is the invariant mass squared of the system  $(jk)$ .

Making use of the symmetry properties listed in table 4.8, the matrix elements with negative parity (s-wave annihilations) can be written as ( $L_i = l_{jk} = l$  or  $\lambda$ )

$$\begin{aligned}
A_I^{J-C} &= \sum_{\substack{l=\text{even} \\ (l=\text{odd})}} a_{ll}^{J-C}(s_{K\bar{K}}, \vartheta_{K\bar{K}}) \cdot \frac{e^{i\delta_{K\bar{K}}} \sin \delta_{K\bar{K}}}{p_{K\bar{K}}} \\
&+ \sum_{\lambda, I_{K\pi}} \left[ b_{\lambda\lambda}^{J-C}(s_{K\pi}, \vartheta_{K\pi}) \cdot \frac{e^{i\delta_{K\pi}} \sin \delta_{K\pi}}{p_{K\pi}} \right. \\
&\quad \left. \pm b_{\lambda\lambda}^{J-C}(s_{\bar{K}\pi}, \vartheta_{\bar{K}\pi}) \cdot \frac{e^{i\delta_{\bar{K}\pi}} \sin \delta_{\bar{K}\pi}}{p_{\bar{K}\pi}} \right], \quad (4.34)
\end{aligned}$$

while for the positive parity states (p-waves annihilations) one finds

$$\begin{aligned}
A_I^{J+C} &= \sum_{\substack{l_{K\bar{K}}=\text{odd}(\text{even}) \\ L_\pi=\text{even}(\text{odd})}} a_{L_\pi l_{K\bar{K}}}^{J+C}(s_{K\bar{K}}, \vartheta_{K\bar{K}}) \cdot \frac{e^{i\delta_{K\bar{K}}} \sin \delta_{K\bar{K}}}{p_{K\bar{K}}} \\
&+ \sum_{\substack{l_{K\pi}=\text{odd}(\text{even}) \\ L_{\bar{K}}=\text{even}(\text{odd}) \\ I_{K\pi}}} \left[ b_{L_{\bar{K}} l_{K\pi}}^{J+C}(s_{K\pi}, \vartheta_{K\pi}) \cdot \frac{e^{i\delta_{K\pi}} \sin \delta_{K\pi}}{p_{K\pi}} \right. \\
&\quad \left. \pm b_{L_K l_{\bar{K}\pi}}^{J+C}(s_{\bar{K}\pi}, \vartheta_{\bar{K}\pi}) \cdot \frac{e^{i\delta_{\bar{K}\pi}} \sin \delta_{\bar{K}\pi}}{p_{\bar{K}\pi}} \right]. \quad (4.35)
\end{aligned}$$

In the functions  $a_{L_i l_{jk}}^{JPC}(s_{jk}, \vartheta_{jk})$  and  $b_{L_i l_{jk}}^{JPC}(s_{jk}, \vartheta_{jk})$  the angular variables can be separated [35], e.g.

$$a_{L_i l_{jk}}^{JPC}(s_{jk}, \vartheta_{jk}) = \rho(s_{jk}) \cdot A_{ijk}^{JP} \quad (4.36)$$

where  $\rho(s_{jk})$  is a scalar function of  $s_{jk}$  and  $A_{ijk}^{JP}$  is the spin-parity factor, describing the dependence of the amplitude on the angular variables  $\vartheta_{jk}$ . Each amplitude  $A_I^{JPC}$  is then a sum of terms of the form

$$\rho(s_{jk}) \cdot \frac{e^{i\delta_{jk}} \sin \delta_{jk}}{p_{jk}} \cdot A_{ijk}^{JP} = A_{jk}^F \cdot A_{ijk}^{JP}, \quad (4.37)$$

where

$$A_{jk}^F = \rho(s_{jk}) \cdot \frac{e^{i\delta_{jk}} \sin \delta_{jk}}{p_{jk}} \quad (4.38)$$

is the form-factor, describing the energy dependence of the amplitude.

#### 4.3.1.3 The Spin-Parity Factors $A_{ijk}^{JP}$

Instead of spherical harmonics, states of definite angular momentum can be represented by symmetric and traceless tensors, composed of the Cartesian components of the particle momenta. The construction of such tensors and their covariant form for Lorentz transformations is explained in [39].

The spin-parity factors  $A_{ijk}^{JP}$  were constructed with this formalism of symmetric and traceless tensors. They are listed in table 4.9. Only angular momenta  $L_i, l_{jk} \leq 2$  were considered. The notation used in the expressions of the spin-parity factors is explained in figure 4.13 and is defined as:

$$\begin{aligned} Y^\mu &= P_j^\mu + P_k^\mu, & \text{is the 4-vector of the system } (jk), \\ X^\mu &= P_i^\mu + P_j^\mu + P_k^\mu, & \text{is the 4-vector of the protonium,} \\ g^{\mu\nu} &= \begin{pmatrix} 1 & & & \\ & -1 & & \\ & & -1 & \\ & & & -1 \end{pmatrix}, & \text{is the metric tensor,} \\ P_{jk}^\mu &= (P_j^\mu - P_k^\mu) - (P_j^\mu + P_k^\mu) \cdot \frac{(m_j^2 - m_k^2)}{s_{jk}}, \\ \bar{P}_i^\mu &= P_i^\mu - X^\mu \cdot \frac{(P_i^\nu X_\nu)}{m_x^2}, \\ T_i^{\mu\nu} &= \bar{P}_i^\mu \bar{P}_i^\nu - \frac{1}{3} \left( g^{\mu\nu} - \frac{X^\mu X^\nu}{m_x^2} \right) \bar{P}_i^\sigma \bar{P}_{i\sigma}, \\ T_{jk}^{\mu\nu} &= P_{jk}^\mu P_{jk}^\nu - \frac{1}{3} \left( g^{\mu\nu} - \frac{Y^\mu Y^\nu}{s_{jk}} \right) P_{jk}^\sigma P_{jk\sigma}, \end{aligned}$$

where  $P_i^\mu$ ,  $P_j^\mu$  and  $P_k^\mu$  are the energy-momentum 4-vectors for the particles  $i$ ,  $j$  and  $k$ , respectively, and  $\varepsilon^{\mu\nu\rho\sigma}$  is the completely antisymmetric tensor with 4 indices and  $\varepsilon^{0123} = -1$ .

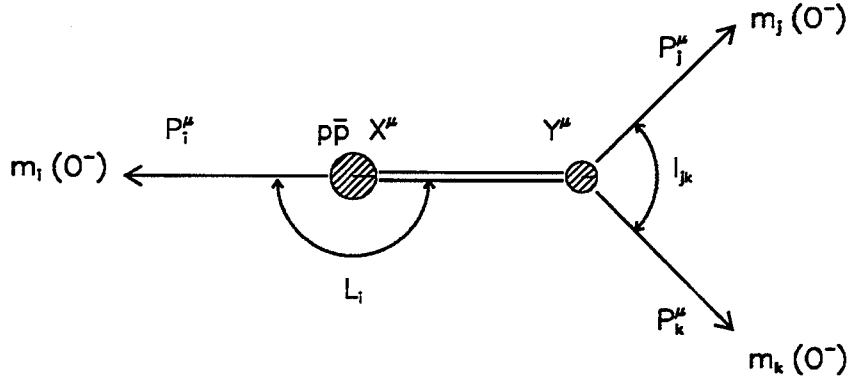


Figure 4.13: Explanation of the notation used for the spin-parity factors  $A_{ijk}^{JP}$ .

$J^P$	$L_i$	$l_{jk}$	spin-parity factor $A_{ijk}^{JP}$
$0^-$	0	0	1
	1	1	$P_{jk}^\mu \bar{P}_{i\mu}$
	2	2	$T_{jk}^{\mu\nu} T_{i\mu\nu}$
$1^+$	0	1	$P_{jk}^\mu$
	1	0	$\bar{P}_i^\mu$
	1	2	$T_{jk}^{\mu\nu} \bar{P}_{i\nu}$
	2	1	$T_i^{\mu\nu} P_{jk\nu}$
$1^-$	1	1	$\varepsilon^{\mu\nu\rho\sigma} P_j^\nu P_k^\rho P_i^\sigma$
	2	2	$\varepsilon^{\mu\nu\rho\sigma} P_j^\nu P_k^\rho P_i^\sigma (P_{jk}^\tau \bar{P}_{i\tau})$
$2^+$	1	2	$\varepsilon^{\mu\tau\rho\sigma} P_j^\tau P_k^\rho P_i^\sigma \cdot P_{jk}^\nu + P_{jk}^\mu \cdot \varepsilon^{\nu\tau\rho\sigma} P_j^\tau P_k^\rho P_i^\sigma$
	2	1	$\varepsilon^{\mu\tau\rho\sigma} P_j^\tau P_k^\rho P_i^\sigma \cdot \bar{P}_i^\nu + \bar{P}_i^\mu \cdot \varepsilon^{\nu\tau\rho\sigma} P_j^\tau P_k^\rho P_i^\sigma$

Table 4.9: The spin-parity factors  $A_{ijk}^{JP}$ .

#### 4.3.1.4 The Form Factors $A_{ijk}^F$

The following approximations are introduced for the expressions of the form factors:



- For the  $K\pi$  ( $\bar{K}\pi$ ) subsystem in an angular momentum state  $l_{K\pi}$  ( $l_{\bar{K}\pi}$ ) = 1, a Breit-Wigner function for the  $K^*$  ( $\bar{K}^*$ ) resonance is used.
- The form factor for the  $K\bar{K}$  subsystem in an angular momentum state  $l_{K\bar{K}} = 0(2)$  is described by a Breit-Wigner function for the  $a_0$  ( $a_2$ ) resonance. The Breit-Wigner function for the  $a_0$  contains a slight modification for a resonance produced near threshold [35].
- For all other angular momentum states, a scattering-length parameterization is assumed. Two independent scattering lengths are allowed for the two possible isospin states of the  $K\pi$  ( $\bar{K}\pi$ ) system.

Table 4.10 shows the form factors  $A_{jk}^F$  for the subsystems ( $K\pi$ ) and ( $K\bar{K}$ ). The expressions for the ( $\bar{K}\pi$ ) system are equivalent to those of ( $K\pi$ ). The following parameters are introduced:

- $m_{K^*}, m_{a_2}, m_{a_0}$  : for the masses of the  $K^*$ ,  $a_2$ , and  $a_0$  resonances,
- $\Gamma_{K^*}, \Gamma_{a_2}, \gamma$  : for the widths of the  $K^*$ ,  $a_2$ , and  $a_0$  resonances,
- $a_{1/2}, a_{3/2}$  : for the scattering lengths of the  $K\pi$  ( $\bar{K}\pi$ ) scattering with  $l_{K\pi}$  ( $l_{\bar{K}\pi}$ ) = 0 and  $I_{K\pi}$  ( $I_{\bar{K}\pi}$ ) = 1/2, 3/2,
- $c_{1/2}, c_{3/2}$  : for the scattering lengths of the  $K\pi$  ( $\bar{K}\pi$ ) scattering with  $l_{K\pi}$  ( $l_{\bar{K}\pi}$ ) = 2 and  $I_{K\pi}$  ( $I_{\bar{K}\pi}$ ) = 1/2, 3/2 and
- $b_1$  : for the scattering length of the  $K\bar{K}$  scattering with  $l_{K\bar{K}} = 1$ .

#### 4.3.1.5 Dalitz-Plot Parameterization with the Conforto-Model

The partial wave decomposition of the transition matrix elements  $A_I^{JPC}$  is shown in equation 4.34 and 4.35. With the spin-parity factors of table 4.9 and the form factors of table 4.10, one is now able to give explicit expressions for the terms appearing in the decomposition. The complete list of contributions  $C_k^{JPCI}$  to each of the matrix elements  $A_I^{JPC}$  is given in appendix C. The matrix element  $A_I^{JPC}$  can then be expressed by a sum over the corresponding contributions  $C_k^{JPCI}$ , each multiplied with a complex parameter  $\rho_k^{JPCI} e^{i\varphi_k^{JPCI}}$ .

Absorbing the isospin factors  $\alpha_I$  and the constant term  $[(2\pi)^3 \cdot 32(2m_p)^3]^{-1}$  of equation 4.26 in the parameters  $\rho_k^{JPCI}$ , the following expression for the transition rate  $d\Gamma$  is obtained:

$$d\Gamma = \sum_{JPC} |A_{I=0}^{JPC} + A_{I=1}^{JPC}|^2 ds_{K_s^0\pi} ds_{K^\pm\pi} \quad (4.39)$$

with

$$A_I^{JPC} = \sum_k \rho_k^{JPCI} e^{i\varphi_k^{JPCI}} \cdot C_k^{JPCI} . \quad (4.40)$$

(jk)	$l_{jk}$	interpretation	$I_{jk}$	form factor $A_{jk}^F$
(K $\pi$ )	0	s-wave scattering	$\frac{1}{2}$	$\frac{1}{1 - ia_{1/2}\sqrt{-p_{K\pi}^2/4}}$
			$\frac{3}{2}$	$\frac{1}{1 - ia_{3/2}\sqrt{-p_{K\pi}^2/4}}$
	1	K* resonance	$\frac{1}{2}$	$\frac{1}{s_{K\pi} - m_{K^*}^2 + im_{K^*}\Gamma_{K^*}}$
	2	d-wave scattering	$\frac{1}{2}$	$\frac{1}{1 - ic_{1/2}\sqrt{-p_{K\pi}^2/4}}$
			$\frac{3}{2}$	$\frac{1}{1 - ic_{3/2}\sqrt{-p_{K\pi}^2/4}}$
(K $\bar{K}$ )	0	$a_0$ resonance	1	$\frac{1}{s_{K\bar{K}} - m_{a_0}^2 + i\sqrt{-p_{K\bar{K}}^2} \gamma}$
	1	p-wave scattering	1	$\frac{1}{1 - ib_1\sqrt{-p_{K\bar{K}}^2/4}}$
	2	$a_2$ resonance	1	$\frac{1}{s_{K\bar{K}} - m_{a_2}^2 + im_{a_2}\Gamma_{a_2}}$

Table 4.10: The form factors  $A_{jk}^F$  for the (K $\pi$ ) and the (K $\bar{K}$ ) subsystems.

The total of 53 contributions to the transition rate (see appendix C) corresponds to 106 real parameters ( $\rho_k^{JPCI}$ 's and  $\varphi_k^{JPCI}$ 's). For each term  $|A_{l=0}^{JPC} + A_{l=1}^{JPC}|$ , one phase can be fixed, e.g.  $\varphi_1^{JPC0} = 0$ . The normalization of the decay rate gives one constraint for the parameters  $\rho_k^{JPCI}$ , which allows to set one  $\rho_k^{JPCI} = 1$ . This leaves 100 real fit parameters from the 53 complex coefficients  $\rho_k^{JPCI} e^{i\varphi_k^{JPCI}}$ . In addition, one has the following parameters from the form factors:

- 5 scattering lengths:  $a_{1/2}, a_{3/2}, b_1, c_{1/2}, c_{3/2}$ ,
- 4 resonance masses:  $m_{K^*\pm}, m_{K^*0}, m_{a_2^\pm}, m_{a_2^0}$  and
- 4 resonance widths:  $\Gamma_{K^*\pm}, \Gamma_{K^*0}, \Gamma_{a_2^\pm}, \gamma$ .

The extension of the Conforto-model to p-wave annihilations leads then to a fit of the Dalitz-plot density with a total of 113 free parameters. With our statistics of  $\sim 33'000$  events and an unmeasured part of the Dalitz-plot due to the  $p_T$ -cut of the trigger, it is impossible to determine all these parameters !

### 4.3.2 Simplified Parameterization of the Dalitz-Plot Density

The Conforto-parameterization, based on a model to describe the reactions  $p\bar{p} \rightarrow K\bar{K}\pi$ , is applicable for  $p\bar{p}$  annihilations in liquid hydrogen, where annihilations from s-wave orbitals are dominant. In this case, the number of contributing amplitudes is limited to 10. In the analysis of the CPLEAR data, one cannot neglect annihilations from atomic p-levels of the protonium [17],[37]. As shown in 4.3.1, the extension of the Conforto-parameterization to include p-wave annihilations increases the number of contributing amplitudes to 53. Therefore, a fit of this parameterization to the measured Dalitz-plot density is practically impossible.

The simpler distribution function presented in this section is not based on an amplitude analysis, but reflects the observed density distribution in the Dalitz-plot and reduces the number of free parameters considerably. The coordinate system used in this simplified parameterization is explained in diagram 4.14, and is defined as follows:

$$\begin{aligned}
 x &= s_{K_S^0\pi} && \text{is the invariant mass squared of } (K_S^0\pi), \\
 y &= s_{K^\pm\pi} && \text{is the invariant mass squared of } (K^\pm\pi), \\
 z &= s_{K_S^0K^\pm} && \text{is the invariant mass squared of } (K_S^0K^\pm) \quad \text{and} \\
 w &= \sqrt{2}(x-y).
 \end{aligned}$$

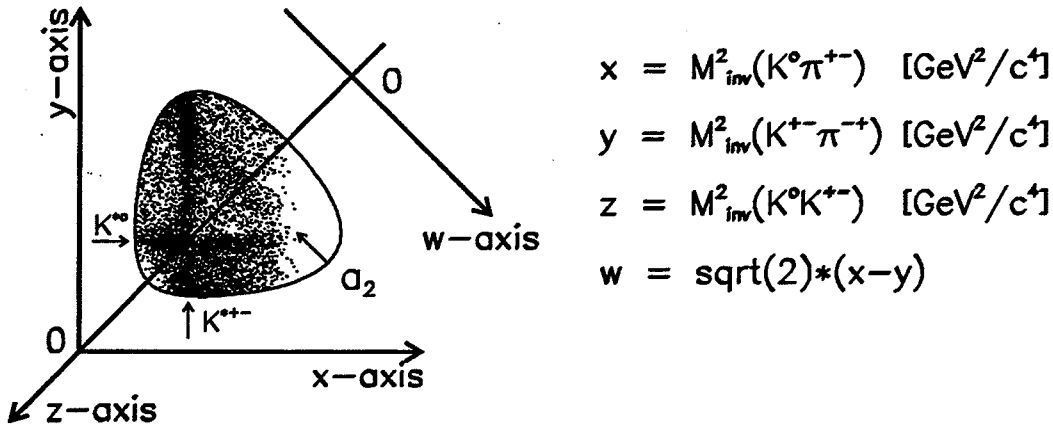


Figure 4.14: Definition of the coordinate system used in the simplified parameterization of the Dalitz-plot density.

Each of the resonances  $K^{*\pm}$ ,  $K^{*0}$  and  $a_2^\pm$  is parameterized by one Breit-Wigner function, multiplied with a polynomial to describe the variation along the resonance band. The resonant amplitudes are then

$$A_1 = BW(x) \cdot \text{Poly}(y, n_1) \quad \text{for the } K^{*\pm} \text{ - resonances ,} \quad (4.41)$$

$$A_2 = BW(y) \cdot \text{Poly}(x, n_2) \quad \text{for the } K^{*0}, \bar{K}^{*0} \text{ - resonances and} \quad (4.42)$$

$$A_3 = BW(z) \cdot \text{Poly}(w, n_3) \quad \text{for the } a_2^\pm \text{ - resonances .} \quad (4.43)$$

$\text{Poly}(t, n_i)$  is a polynomial in  $t$  of order  $n_i$ , i.e.

$$\text{Poly}(t, n_i) = \rho_1 + \rho_2 t + \dots + \rho_{n_i+1} t^{n_i}, \quad (4.44)$$

with  $t = y, x, w$  for  $K^{*\pm}, K^{*0}$  and  $a_2^\pm$ , respectively.  $\text{BW}(s)$  is the Breit-Wigner function with  $s = x, y, z$  for  $K^{*\pm}, K^{*0}$  and  $a_2^\pm$ , respectively, and is given by [26],[40]

$$\text{BW}(s) = \frac{m_o \Gamma_o}{(m_o^2 - s) - im_o \Gamma} \cdot \frac{q}{q_o} \quad (4.45)$$

with 
$$\Gamma = \Gamma_o \cdot \frac{m_o}{\sqrt{s}} \left( \frac{q}{q_o} \right)^{2l+1},$$

$$q = \frac{1}{2} \sqrt{\frac{(s - (m_1 + m_2)^2)(s - (m_1 - m_2)^2)}{s}},$$

where  $m_o, \Gamma_o$  = mass and width of the resonance,  
 $l$  = relative orbital angular momentum of the decay products,  
 $s$  = invariant mass squared of the decay products,  
 $m_1, m_2$  = masses of the decay products,  
 $q$  = momentum of the decay products in their CM-system and  
 $q_o = q(s = m_o^2)$ .

This Breit-Wigner function takes account of the resonance spin and is quite different to the function used by Conforto et al. [35]. In Figure 4.15, where the two functions are compared, the difference is clearly visible in the position of the maximum and the shape of the tails.

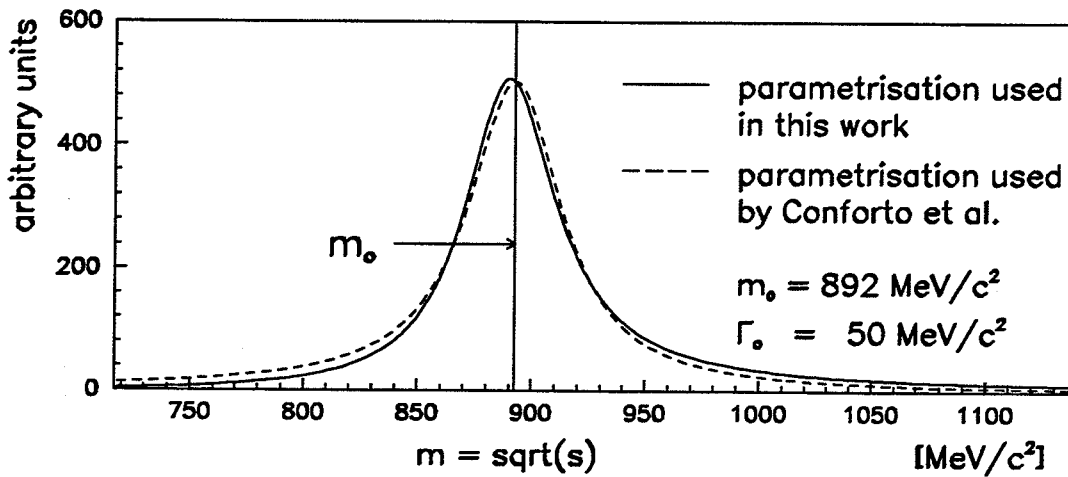


Figure 4.15: Comparison between the Breit-Wigner function used by Conforto et al. and the function used in this work.

For the non-resonant part, the scattering length approximation used by Conforto et al. is adopted, introducing one amplitude for each of the subsystems ( $K_S^0\pi$ ), ( $K^\pm\pi$ ) and ( $K_S^0K^\pm$ ). No distinction is made between the two possible isospin eigenstates  $I_{K\pi}$  ( $I_{\bar{K}\pi}$ ) = 1/2 and 3/2, nor between the two possible angular momentum states (s-wave or d-wave) for the subsystems ( $K_S^0\pi$ ) and ( $K^\pm\pi$ ). The spin-parity factors are replaced by polynomial functions. The three non-resonant contributions are

$$A_4 = \frac{1}{1 - iSL_{K_S^0\pi} \cdot q_{K_S^0\pi}} \cdot \text{Poly}(y, n_4) \quad \text{for } (K_S^0\pi) \text{ - scattering,} \quad (4.46)$$

$$A_5 = \frac{1}{1 - iSL_{K^\pm\pi} \cdot q_{K^\pm\pi}} \cdot \text{Poly}(x, n_5) \quad \text{for } (K^\pm\pi) \text{ - scattering and} \quad (4.47)$$

$$A_6 = \frac{1}{1 - iSL_{K_S^0K^\pm} \cdot q_{K_S^0K^\pm}} \cdot \text{Poly}(w, n_6) \quad \text{for } (K_S^0K^\pm) \text{ - scattering,} \quad (4.48)$$

where  $SL_{jk}$  is the scattering length for ( $jk$ ) - scattering and  $q_{jk}$  is the momentum of the particles  $j, k$  in their CM-system.

Two different modes are used to parameterize the Dalitz-plot density. The first mode (mode I) allows interference between the resonant and the non-resonant amplitudes, while in the second mode (mode II) the two do not interfere. The two expressions for the distribution function  $D(x, y, \vec{\theta})$  are then:

$$D_I(x, y, \vec{\theta}) = |A_1 + A_2e^{i\varphi_2} + A_3e^{i\varphi_3} + A_4 + A_5 + A_6|^2 \quad (\text{mode I}), \quad (4.49)$$

$$D_{II}(x, y, \vec{\theta}) = |A_1 + A_2e^{i\varphi_2} + A_3e^{i\varphi_3}|^2 + |A_4 + A_5 + A_6|^2 \quad (\text{mode II}), \quad (4.50)$$

where  $\varphi_2, \varphi_3$  are the relative phases of  $A_2$  and  $A_3$  with respect to  $A_1$ , and  $\vec{\theta}$  represents all fit parameters.

For each of the two modes I and II, 10 parameterizations were selected, differing in the orders of the polynomials. In general, more degrees of freedom were allowed in mode II for the non-resonant amplitudes than in mode I. Table 4.11 lists the polynomial orders of the 20 parameterizations chosen, together with the corresponding number of free parameters,  $N_{par}$ , including

- the coefficients of the polynomials,  $\rho_i$ ,
- the two phases  $\varphi_2$  and  $\varphi_3$ ,
- the three scattering lengths  $SL_{K_S^0\pi}$ ,  $SL_{K^\pm\pi}$  and  $SL_{K_S^0K^\pm}$ ,
- the three resonance masses, parameterized as  $m_{K^{*\pm}}$ ,  $\Delta m_{K^*}$  and  $m_{a_2}$  and
- the three resonance widths  $\Gamma_{K^{*\pm}}$ ,  $\Gamma_{K^{*0}}$  and  $\Gamma_{a_2}$ .

From the many types of parameterizations tested, the two functions of equation 4.49 and 4.50 give the highest confidence levels for least-squares fits. The other parameterizations investigated are obtained from equation 4.49 or 4.50 by one or several of the following modifications:

1. The amplitudes  $A_4$ ,  $A_5$  and  $A_6$  for mode I ( $A_5$  and  $A_6$  for mode II) are multiplied with a phase factor  $e^{i\varphi_i}$ .

parameterization mode	number	polynomial order for						n <sup>o</sup> . of free parameters N <sub>par</sub>
		resonances			non-res. amplitudes			
		K <sup>*±</sup>	K <sup>*0</sup>	A2	K <sub>s</sub> <sup>0</sup> π	K <sup>±</sup> π	K <sub>s</sub> <sup>0</sup> K <sup>±</sup>	
I	1	5	2	2	2	2	2	32
	2	5	2	2	3	2	2	33
	3	5	3	2	3	2	2	34
	4	5	3	2	3	2	3	35
	5	5	4	3	3	2	2	36
	6	5	3	3	3	3	3	37
	7	5	4	4	3	2	3	38
	8	5	4	4	3	3	3	39
	9	5	5	5	3	2	3	40
	10	5	5	5	3	3	3	41
II	1	5	1	2	3	2	2	32
	2	5	2	2	3	2	2	33
	3	5	2	2	4	2	2	34
	4	5	3	2	3	2	3	35
	5	5	2	2	4	3	3	36
	6	5	3	3	3	3	3	37
	7	5	3	2	5	3	3	38
	8	5	2	2	5	4	4	39
	9	5	3	3	4	4	4	40
	10	5	3	3	5	4	4	41

Table 4.11: Order of the polynomials  $\text{Poly}(t, n_i)$  and the number of free parameters for the 20 selected parameterizations.

- Two additional amplitudes and one scattering length are introduced to distinguish between s-wave and d-wave scattering for the subsystems ( $K_s^0\pi$ ) and ( $K^\pm\pi$ ).
- Instead of the polynomials  $\text{Poly}(t, n_i)$ , functions of the form

$$R(\vartheta_{jk}) = \rho_1 + \rho_2 \cos(\vartheta_{jk}) + \rho_3 \sin(\vartheta_{jk}) + \rho_4 \cos(2\vartheta_{jk}) + \rho_5 \sin(2\vartheta_{jk}) \quad (4.51)$$

are used, where  $\vartheta_{jk}$  is the decay angle of the subsystem ( $jk$ ) with respect to the momentum of particle  $i$ .

- In the Conforto-model, all amplitudes are either symmetric or antisymmetric in the exchange of K and  $\bar{K}$ . This is because the final state  $K\bar{K}\pi$  is composed of three bosons, and therefore the amplitudes for the reaction  $p\bar{p} \rightarrow K\bar{K}\pi$  have to be completely symmetric under the exchange of all variables, including isospin, between the two kaons. As a consequence, the isospin and the spatial parts of an amplitude have the same symmetry properties.

Analogous to the Conforto-model, the  $K^*$  resonance and the  $(K\pi)$ -scattering is parameterized by a symmetric and an antisymmetric amplitude, e.g. for the  $K^*$ :

$$A'_1 = BW(x) \cdot \text{Poly}(y, n_1) + BW(y) \cdot \text{Poly}(x, n_1) \quad (\text{symmetric}) \quad (4.52)$$

and

$$A'_2 = BW(x) \cdot \text{Poly}(y, n_2) - BW(y) \cdot \text{Poly}(x, n_2) \quad (\text{antisymmetric}). \quad (4.53)$$

If the functions  $R(\vartheta_{jk})$  are used instead of the polynomials  $\text{Poly}(t, n_i)$ , the amplitudes for the  $a_2$  - resonance and the  $(K\bar{K})$ -scattering can be split in a symmetric and an antisymmetric part as well, e.g. for the  $a_2$ :

$$A'_3 = BW(z) \cdot [\rho_1 + \rho_2 \sin(\vartheta_{K\bar{K}}) + \rho_3 \cos(2\vartheta_{K\bar{K}})] \quad (\text{symmetric}) \quad (4.54)$$

and

$$A'_4 = BW(z) \cdot [\rho_4 \cos(\vartheta_{K\bar{K}}) + \rho_5 \sin(2\vartheta_{K\bar{K}})] \quad (\text{antisymmetric}). \quad (4.55)$$

#### 4.4 Estimation of the Detector and Filter Acceptance

In order to describe the measured Dalitz-plot density, the distribution functions given in equation 4.49 and 4.50 have to be weighted with an acceptance function  $Acc(x, y)$ , describing the detector and filter acceptance.  $Acc(x_o, y_o)$  is the probability for a "golden  $\pi^+\pi^-$ " event, i.e.

$$p\bar{p} \rightarrow K^\pm \pi^\mp K_S^0, \quad K_S^0 \rightarrow \pi^+ \pi^-,$$

with  $x_o = s_{K_S^0 \pi}$  and  $y_o = s_{K^\pm \pi}$  to be recognized and accepted by the detector and the subsequent filters (see section 4.2).

To determine the acceptance function  $Acc(x, y)$ , the simulated "golden  $\pi^+\pi^-$ " sample MCT233 (see appendix B.1) is used. The events of MCT233 are generated with equal probability in the Dalitz-plot and the simulated trigger type is 233. The 151'508 events of MCT233 are passed through the PREFILTER and 5CFIT algorithms. Table 4.12 shows the data reduction, where  $N_{cut}$ ,  $R$ ,  $N_{left}$  and  $P$  are defined as for table 4.5 on page 72. The remaining 43'765 events are filled in a histogram  $AH(i, j)$ , the acceptance histogram, with an equal number of bins,  $n_{bin}$ , along the  $x$ - and  $y$ -axis in the range of 0.2 to 2.0  $\text{GeV}^2/c^4$ . Apart from statistical fluctuations, the bin content of the histogram  $AH(i, j)$  is proportional to the acceptance function  $Acc(x, y)$ , averaged over the bin area.

Since the statistics of the simulated data is quite poor, the fluctuations of  $AH(i, j)$  between neighboring bins are large, even for a rather coarse subdivision of the Dalitz-plot. In order to get a smoother acceptance function, the contents of neighboring bins are averaged according to the formula

$$AH'(i, j) = \frac{1}{9} \sum_{l=-1}^1 \sum_{k=-1}^1 AH(i+l, j+k), \quad (4.56)$$

filter	events rejected $N_{\text{cut}}$	reduction factor $R$	events left $N_{\text{left}}$	percentage left $P$ [%]
simulated data sample MCT233			151'508	100.0
PREFILTER	86'468	0.429	65'040	42.9
5CFIT	21'275	0.673	43'765	28.9

Table 4.12: Data reduction for the simulated data sample MCT233.

where  $AH'(i, j)$  is the smoothed acceptance histogram. The contents of bins outside the kinematic boundary of the Dalitz-plot are kept at zero.

For the final fits with the method of maximum likelihood, a "standard" acceptance histogram,  $AH^{sta}$ , is defined. To study the systematic effect on the fit results, introduced by this approximation of the acceptance function (see 4.5.3.3), six alternative acceptance histograms,  $AH_k^{alt}$  ( $k = 1, \dots, 6$ ), are produced, differing in the smoothness and the number of cells. These various acceptance histograms are obtained in two steps:

- Starting with the histogram  $AH(i, j)$  with  $n_{bin} \times n_{bin}$  cells, the smoothing procedure, described by equation 4.56, is repeated  $n_s$  times to obtain the smoothed histogram  $AH_s(i, j)$  with an equal number of cells as  $AH(i, j)$ .
- In order to get acceptance histograms with different cell sizes, but approximately the same smoothness, the histogram  $AH_s(i, j)$  is rebinned to  $n'_{bin} \times n'_{bin}$  cells. The smoothed and rebinned histogram,  $AH_{sr}(i', j')$ , is defined as

$$AH_{sr}(i', j') = AH_s(i, j), \quad (4.57)$$

where the center of the cell  $(i', j')$  is inside the bin  $(i, j)$ . The content of bins intersected by the kinematic boundary is set to zero.

The standard acceptance histogram  $AH^{sta}$  used for the maximum likelihood fits (see section 4.5.2) is obtained with the following parameters:

- original number of bins along  $x$  ( $y$ ):  $n_{bin} = 60 \rightarrow AH(i, j)$ ,
- number of smoothing cycles :  $n_s = 5 \rightarrow AH_s(i, j)$ ,
- final number of bins along  $x$  ( $y$ ) :  $n'_{bin} = 100 \rightarrow AH_{sr}(i, j) = AH^{sta}(i, j)$ .

The histograms  $AH(i, j)$ ,  $AH_s(i, j)$  and  $AH^{sta}(i, j)$  are compared in figure 4.16. Table 4.13 shows the parameters chosen for the six alternative acceptance histograms (number 2-7).



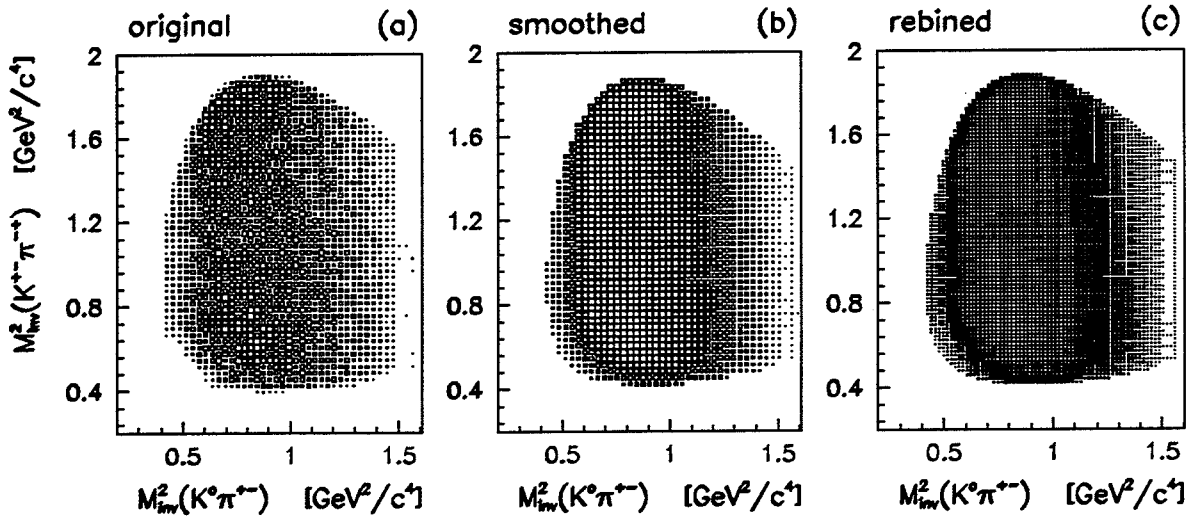


Figure 4.16: The original  $AH(i, j)$  (a), the smoothed  $AH_s(i, j)$  (b) and the rebinned  $AH_{sr}(i, j)$  (c) acceptance histograms.  $AH_{sr}(i, j)$  is used in the maximum likelihood fits as the standard acceptance histogram,  $AH^{sta}(i, j)$ .

acceptance histogram number	number of original bins $n_{bin}$	number of smoothing cycles $n_s$	number of final bins $n'_{bin}$
1 ( $AH^{sta}$ )	60	5	100
2 ( $AH_1^{alt}$ )	60	5	60
3 ( $AH_2^{alt}$ )	60	5	150
4 ( $AH_3^{alt}$ )	100	5	100
5 ( $AH_4^{alt}$ )	150	5	150
6 ( $AH_5^{alt}$ )	60	3	100
7 ( $AH_6^{alt}$ )	60	1	100
$\chi^2$ - fits	60	5	$n_\chi$

Table 4.13: The parameters chosen for the standard (1) and the six alternative (2-7) acceptance histograms. The last line shows the parameters used to produce the acceptance histograms for the least-squares fits.

For the least-squares fits with  $n_\chi$  bins along the  $x$ - and  $y$ -axis, the acceptance histograms were obtained with the parameters given in the last line of table 4.13.

## 4.5 Fit Results

In this section, the results obtained from the fits of the parameterizations described in section 4.3.2 to the measured density distribution in the Dalitz-plot are presented. The fits were performed with the function minimization and error analysis package MINUIT [41].

This section is divided into four parts:

1. Initially, least-squares fits are used with different cell sizes in the Dalitz-plot. Presented are some of the results, showing the systematic effect introduced by the bin size.
2. For the final fits, the method of maximum likelihood is used. The resulting distribution function for one of the parameterizations is shown in detail and compared to the data. Then the results are given for the  $K^*$  resonance parameters (masses and widths) for all 20 parameterizations.
3. In the third part, the statistical error of the  $K^*$  mass difference and the uncertainties introduced by the parameterization of the distribution function and the choice of the acceptance function are analysed.
4. Finally, the result obtained for the isospin mass splitting of the  $K^*$  (892) meson is presented and compared to earlier measurements.

### 4.5.1 Least-Squares Fits

Usually, the  $\chi^2$  - function for least-squares fits is defined as

$$\chi^2(\vec{\theta}) = \sum_{ij} \frac{(N_{ij}^{obs} - N_{ij}^{th})^2}{N_{ij}^{obs}}, \quad (4.58)$$

where  $N_{ij}^{obs}$  is the observed number of entries in the bin  $(i, j)$  and  $N_{ij}^{th}$  is the value of the theoretical distribution function at the center of  $(i, j)$ . This definition of the  $\chi^2$  - function introduces a bias in the fit parameters, since downward fluctuations in the data from the true expectation values are favoured, especially if  $N_{ij}^{th}$  is small ( $\leq 8$ ) [4]. This is because a fluctuation to smaller values will be assigned a smaller error and hence a greater weight than an equal fluctuation upward.

Therefore, the following modified  $\chi^2$  - function, which yields correct parameter values and error estimates for all values of  $N_{ij}^{th}$ , is used for the least-squares fits:

$$\chi^2(\vec{\theta}) = \sum_{i=1}^{n_x} \sum_{j=1}^{n_x} \left[ 2(N_{ij}^{th} - N_{ij}^{obs}) + 2N_{ij}^{obs} \ln \left( \frac{N_{ij}^{obs}}{N_{ij}^{th}} \right) \right], \quad (4.59)$$

with

$$N_{ij}^{th} = D(x_i, y_j, \vec{\theta}) \cdot AH_{sr}(i, j), \quad (4.60)$$

where  $D(x_i, y_j, \vec{\theta})$  is the distribution function defined in equation 4.49 or 4.50,  $AH_{sr}(i, j)$  is the acceptance histogram and  $(x_i, y_j)$  is the center of the bin  $(i, j)$ . The second term in equation 4.59 is set to zero if  $N_{ij}^{obs} = 0$ . The mass range of the Dalitz-plot with  $x > 1.5 \text{ GeV}^2/c^4$ , which is almost empty due to the  $p_T$ -cut of the trigger, is not considered in the fit.

The least-squares fits are performed for various number of bins  $n_x$  along the  $x$ - and  $y$ -axis in the range of 0.2 to 2.0  $\text{GeV}^2/c^4$ . The values for  $n_x$  are listed in table 4.14, together with the corresponding number of cells  $N_c$  inside the kinematic boundary and with  $x < 1.5 \text{ GeV}^2/c^4$ , the number of events  $N_e$  inside these cells, the average number of events per cell and the bin-width  $\Delta B$  in a linear energy scale at the  $K^*$  mass ( $\sqrt{x} = m_{K^*}$ ).

number of bins along x,y $n_x$	number of contributing cells $N_c$	number of considered events $N_e$	average cell content	bin width at $\sqrt{x} = m_{K^*}$ $\Delta B [\text{MeV}/c^2]$
30	350	30'690	87.7	34.2
35	490	30'956	63.2	28.9
40	636	31'342	49.3	25.0
45	819	31'238	38.1	22.6
50	1038	31'828	30.7	20.2
60	1500	32'038	21.4	16.9
70	2038	32'059	15.7	14.3
80	2674	32'220	12.0	12.6
90	3439	32'276	9.4	11.3
100	4249	32'381	7.6	10.0

Table 4.14: Some characteristic quantities for the least-squares fits with different cell sizes in the Dalitz-plot.

Figure 4.17 shows the results obtained for the  $K^*$  mass difference with the two parameterizations (see table 4.11)

- mode I, number 4 (I/4) and
- mode II, number 4 (II/4)

of the distribution function  $D(x, y, \vec{\theta})$ . Parameterizations of mode I allow interference between the resonant and the non-resonant amplitudes, while the two do not interfere in the functions of mode II. Both parameterizations have polynomials of order five, three and two (5 3 2) for the resonances  $K^{*\pm}$ ,  $K^{*0}(\bar{K}^{*0})$  and  $a_2^\pm$ , respectively, and

polynomials of order three, two, three (3 2 3) for the scattering of the subsystems ( $K_S^0\pi$ ), ( $K^\pm\pi$ ) and ( $K_S^0K^\pm$ ), respectively. The number of free parameters in the fit is  $N_{par} = 35$ .

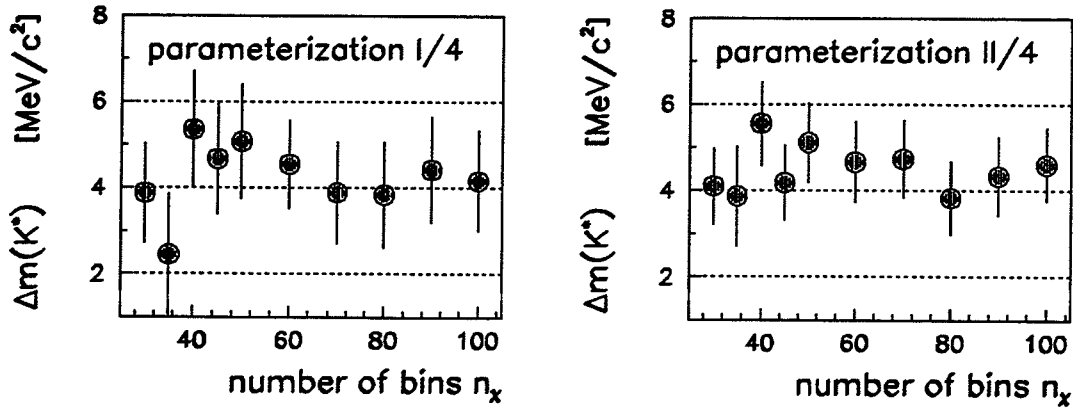


Figure 4.17: The  $K^*$  mass difference as obtained from least-squares fits of the two parameterizations I/4 and II/4 with  $n_x$  bins along  $x$  and  $y$  in the range of 0.2 to 2.0  $\text{GeV}^2/c^4$ .

The values obtained for  $\Delta m_{K^*}$  are given in table 4.15, together with the  $\chi^2$  of the fit and the reduced quantity  $\chi_{red}^2$ , defined as

$$\chi_{red}^2 = \frac{\chi^2}{N_{df}} = \frac{\chi^2}{(N_c - N_{par})}, \quad (4.61)$$

where  $N_c$  is the number of cells and  $N_{df} = (N_c - N_{par})$  is the number of degrees of freedom in the fit. The quoted errors, the "parabolic"  $1\sigma$  errors as given by the MINUIT program (see paragraph 4.5.3.2), are purely statistical.

Figure 4.17 shows large fluctuations in the results for  $\Delta m_{K^*}$  between the fits with a low number of bins  $n_x$ . This is due to the big bin width  $\Delta B$  of  $\sim 30 \text{ MeV}/c^2$ . By increasing  $n_x$ , the fit becomes more sensitive to the  $K^*$  peak position and the fluctuations in  $\Delta m_{K^*}$  are reduced. But even for  $n_x = 100$ ,  $\Delta B$  is still  $10 \text{ MeV}/c^2$ . In order to come down to a bin width of  $\Delta B \sim 5 \text{ MeV}/c^2$ , one needs  $n_x \sim 200$ , which leaves an average bin content of less than two. This example illustrates the limitation of the least-squares method. A way around this problem is the method of maximum likelihood, described in the next part.

Since the method of least-squares is less computer time intensive than the method of maximum likelihood, it was used to test many different parameterizations (see section 4.3.2), and to find good starting values for the final fits with the method of maximum likelihood.

number of bins $n_x$	parameterization I/4			parameterization II/4		
	$\Delta m_{K^*}$ [MeV/c <sup>2</sup> ]	$\chi^2$	$\chi_{\text{red}}^2$	$\Delta m_{K^*}$ [MeV/c <sup>2</sup> ]	$\chi^2$	$\chi_{\text{red}}^2$
30	3.88±1.16	495	1.57	4.10±0.88	572	1.81
35	2.45±1.41	660	1.45	3.87±1.16	740	1.63
40	5.35±1.36	826	1.37	5.55±0.97	895	1.49
45	4.67±1.29	1071	1.37	4.18±0.87	1180	1.51
50	5.07±1.33	1257	1.25	5.11±0.92	1364	1.36
60	4.55±1.02	1731	1.18	4.66±0.93	1822	1.24
70	3.89±1.18	2354	1.18	4.73±0.90	2472	1.23
80	3.84±1.23	3110	1.18	3.83±0.85	3221	1.22
90	4.42±1.23	3842	1.13	4.33±0.91	3973	1.17
100	4.16±1.17	4692	1.11	4.60±0.85	4788	1.14

Table 4.15: Results for the  $K^*$  mass difference obtained from least-squares fits with the two parameterizations I/4 and II/4.

#### 4.5.2 The Method of Maximum Likelihood

The method of maximum likelihood interprets the distribution function as a probability density function. One supposes that the measured events, characterized by their coordinates in the Dalitz-plot  $(x_n, y_n)$ , came from a particular probability density function  $P(x, y, \vec{\theta})$ , depending on the parameters  $\vec{\theta}$ . The principle of maximum likelihood states, that the best explanation for the data sample is provided by the set of parameters  $\vec{\theta}$ , which maximizes the joint probability density,  $\mathcal{L}(\vec{\theta})$ , of all events. The function  $\mathcal{L}(\vec{\theta})$ , called the likelihood function, is given by

$$\mathcal{L}(\vec{\theta}) = \prod_{\substack{n \\ \text{(all events)}}} P(x_n, y_n, \vec{\theta}). \quad (4.62)$$

This procedure can be simplified by minimizing the negative logarithm of the likelihood function,  $-\ln \mathcal{L}(\vec{\theta})$ . Again the MINUIT program was used to find the minimum of

$$-\ln \mathcal{L}(\vec{\theta}) = - \sum_{\substack{n \\ \text{(all events)}}} \ln P(x_n, y_n, \vec{\theta}), \quad (4.63)$$

with

$$P(x_n, y_n, \vec{\theta}) = D(x_n, y_n, \vec{\theta}) \cdot \text{Acc}(x_n, y_n) \cdot N(\vec{\theta}), \quad (4.64)$$

where  $D(x_n, y_n, \vec{\theta})$  is the distribution function of equation 4.49 or 4.50,  
 $\text{Acc}(x_n, y_n)$  is the acceptance function (see below),  
 $N(\vec{\theta})$  is the normalization factor (see below) and  
 $x_n (y_n)$  is the invariant mass squared  $s_{K^0\pi}$  ( $s_{K^\pm\pi}$ ) for event  $n$ .

To calculate the acceptance function  $Acc(x_n, y_n)$  at the event coordinates  $(x_n, y_n)$ , the acceptance histogram  $AH_{sr}(i, j)$  is interpolated in the  $x$  and  $y$  directions, according to the formula

$$Acc(x_n, y_n) = AH_{sr}(i, j) + \frac{1}{2} \left\{ \frac{|x_n - x_i|}{\Delta x} \cdot [AH_{sr}(k, j) - AH_{sr}(i, j)] + \frac{|y_n - y_j|}{\Delta y} \cdot [AH_{sr}(i, l) - AH_{sr}(i, j)] \right\}, \quad (4.65)$$

where  $AH_{sr}(i, j)$  is the acceptance histogram with  $n'_{bin} \times n'_{bin}$  cells,  
 $(i, j)$  is the bin that contains  $(x_n, y_n)$ ,  
 $(k, j)$  is the neighboring bin of  $(i, j)$  closest to  $(x_n, y_n)$  in  $x$  direction,  
 $(i, l)$  is the neighboring bin of  $(i, j)$  closest to  $(x_n, y_n)$  in  $y$  direction,  
 $x_i, y_j$  are the coordinates for the center of  $(i, j)$  and  
 $\Delta x, \Delta y$  are the bin-widths ( $\Delta x = \Delta y = (1.8/n'_{bin}) \text{ GeV}^2/c^4$ ).

This again introduces a dependance on the chosen bin size for the acceptance histogram. The "standard" acceptance histogram  $AH^{sta}(i, j)$  (see section 4.4) is used for the maximum likelihood fits, except in paragraph 4.5.3.3, where the dependance of the  $K^*$  mass difference on the acceptance function is investigated. Equation 4.63 is summed over all events contained in a bin inside the kinematic boundary of the Dalitz-plot. The condition  $x \leq 1.5 \text{ GeV}^2/c^4$  is dropped and the number of events considered in the fit is  $N_e = 32'469$ .

In order to get meaningful error estimates for the parameters  $\vec{\theta}$ , it is important that the function  $P(x, y, \vec{\theta})$  is normalized. Choosing the normalization as

$$\int_{\text{Dalitz-plot}} P(x, y, \vec{\theta}) dx dy = 1, \quad (4.66)$$

the normalization factor  $N(\vec{\theta})$  of equation 4.64 is defined and approximated as

$$N(\vec{\theta}) \equiv \left[ \int_{\text{Dalitz-plot}} D(x, y, \vec{\theta}) \cdot Acc(x, y) dx dy \right]^{-1} \quad (4.67)$$

$$\approx \left[ \sum_{i=1}^{n'_{bin}} \sum_{j=1}^{n'_{bin}} D(x_i, y_j, \vec{\theta}) \cdot AH_{sr}(i, j) \Delta x \Delta y \right]^{-1}.$$

The normalization factor  $N(\vec{\theta})$  must be calculated each time the parameters  $\vec{\theta}$  are changed, i.e. in each MINUIT function call.

#### 4.5.2.1 An Example of a Distribution Function

At the example of parameterization I/10 (see table 4.11), the probability density function  $P(x, y, \vec{\theta})$ , obtained with the method of maximum likelihood, is presented. The parameterization I/10 is characterized by polynomials of order five for the resonances, order three for the non-resonant amplitudes, interference between the resonant and non-resonant amplitudes and a total of  $N_{par} = 41$  free parameters.

In order to compare the function  $P(x, y, \vec{\theta})$  with the measured density distribution in the Dalitz-plot, the theoretical distribution  $P(x, y, \vec{\theta})$  is normalized to the number of events considered in the fit, i.e.

$$\int_{\text{Dalitz-plot}} P(x, y, \vec{\theta}) dx dy = N_e = 32'469, \quad (4.68)$$

and the Dalitz-plot is subdivided in 60 bins along the  $x$  ( $y$ )-axis in the range of 0.2 to 2.0  $\text{GeV}^2/c^4$ .

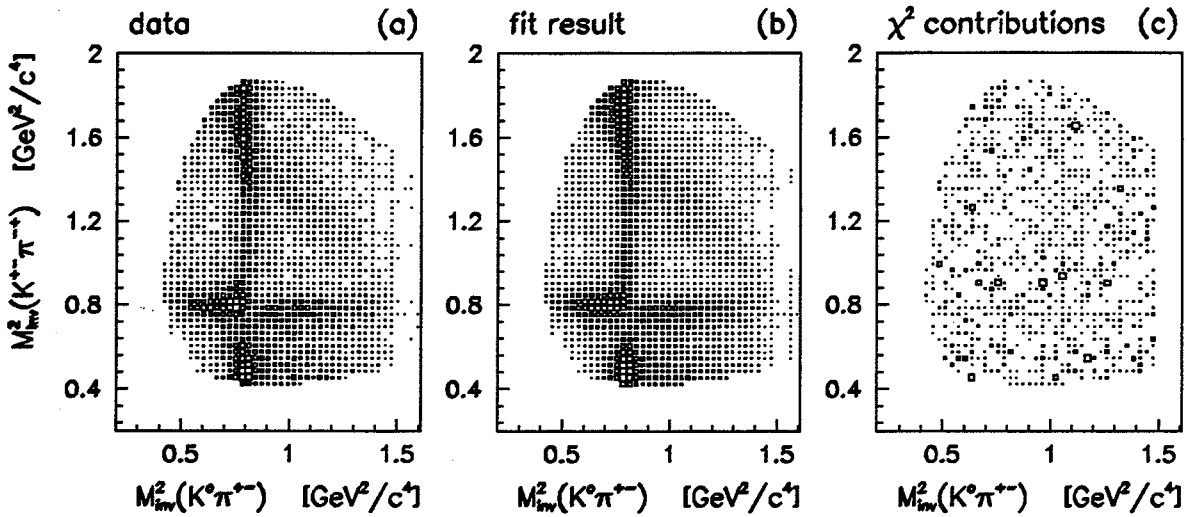
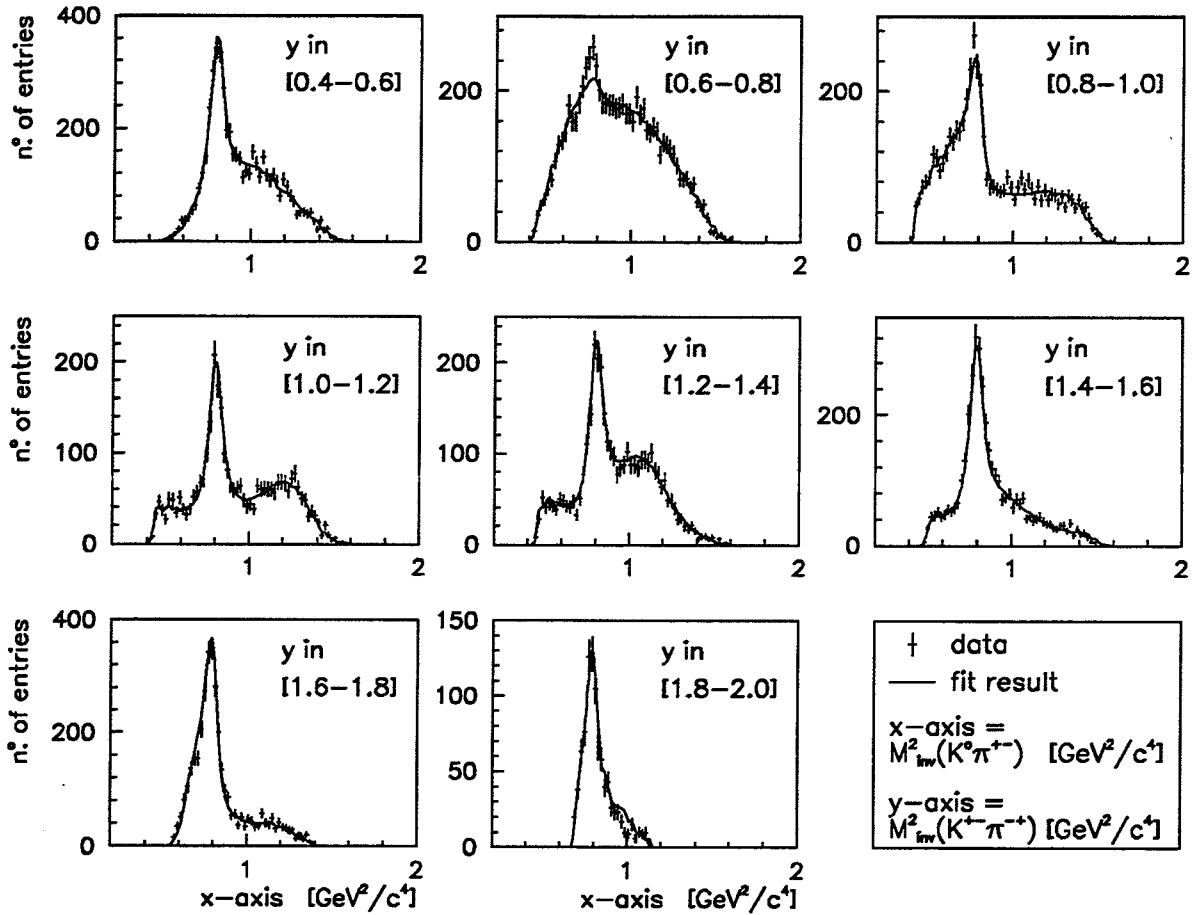


Figure 4.18: Experimental (a) and theoretical (b) distributions in the Dalitz-plot. In (c), the contribution per cell to the  $\chi^2$ -function is shown.

Figure 4.18 shows the experimental distribution in the Dalitz-plot (a), the theoretical function  $P(x_i, y_i, \vec{\theta})$  (b) and the contributions of each cell to the  $\chi^2$ -function defined in equation 4.59, with  $N_{ij}^{th} = P(x_i, y_i, \vec{\theta})$  (c). The rather homogeneous distribution in figure 4.18 (c) demonstrates that  $P(x_i, y_i, \vec{\theta})$  follows the data well in all parts of the Dalitz-plot, even in the intersection region of the two  $K^*$  bands.

In figure 4.19, projections of squared mass intervals (slices) in  $x$  and  $y$  are compared. Good agreement is found between the measured distribution and  $P(x, y, \vec{\theta})$ .

projections of  $y$ -slices on the  $x$ -axis



projections of  $x$ -slices on the  $y$ -axis

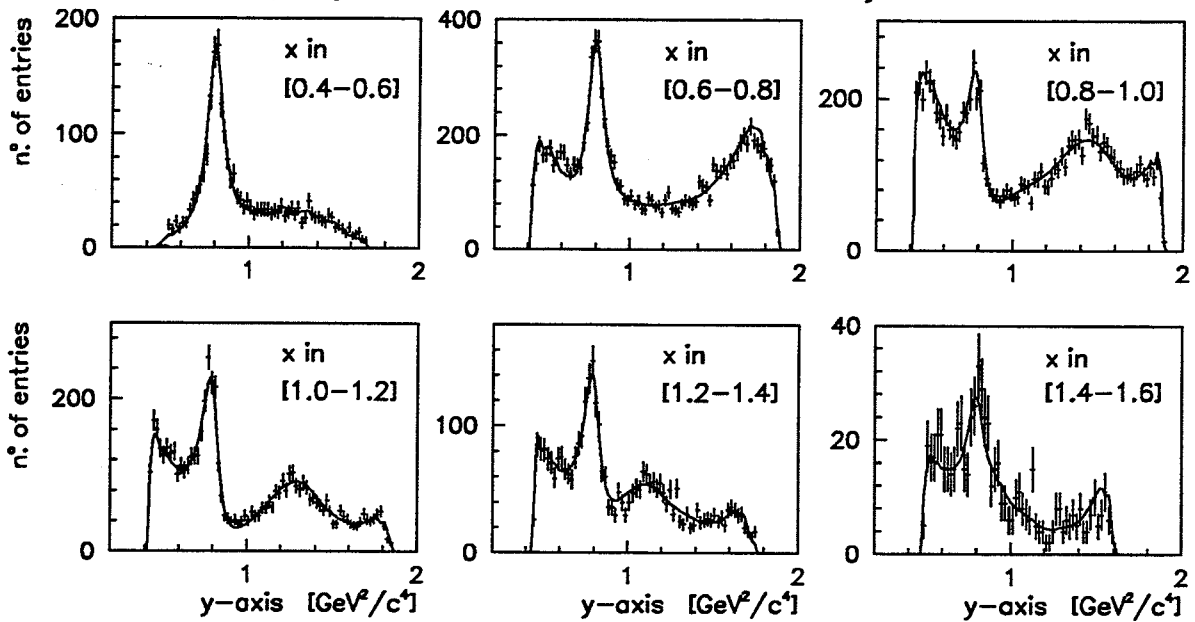


Figure 4.19: Projections of Dalitz-plot slices in  $x$  and  $y$  for the experimental and the theoretical distributions.



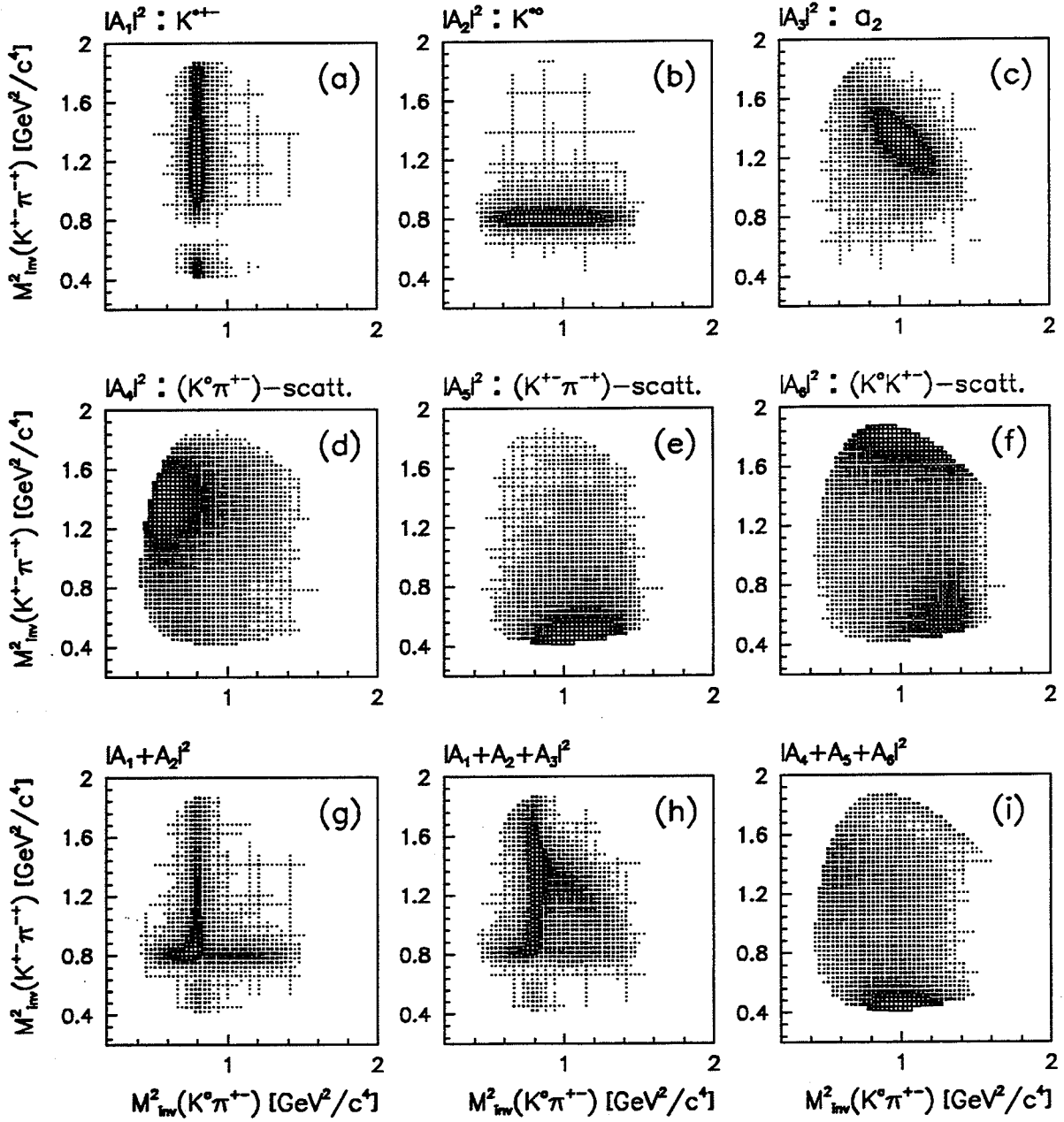


Figure 4.20: The individual contributions  $C_i(x, y, \vec{\theta})$  of the six amplitudes  $A_i(x, y, \vec{\theta})$  to the theoretical distribution in the Dalitz-plot [(a) to (f)], and the combined contributions of the  $K^*$  resonances (g), all resonances (h) and all non-resonant amplitudes (i).

The individual contribution of each amplitude  $A_i(x, y, \vec{\theta})$  ( $i = 1, \dots, 6$ ) to  $P(x, y, \vec{\theta})$ , defined as (neglecting interference effects)

$$C_i(x, y, \vec{\theta}) = |A_i(x, y, \vec{\theta})|^2 \cdot Acc(x, y), \quad (4.69)$$

is displayed in figure 4.20 (a) to (f). In addition, the combined contributions of

- the two  $K^*$  resonances :  $|A_1 + A_2 e^{i\varphi_2}|^2 \cdot Acc$ ,
- all resonances :  $|A_1 + A_2 e^{i\varphi_2} + A_3 e^{i\varphi_3}|^2 \cdot Acc$  and
- all non-resonant amplitudes :  $|A_4 + A_5 + A_6|^2 \cdot Acc$

are shown in (g) to (h).

#### 4.5.2.2 Results for the Resonance Parameters

The results for the resonance parameters, obtained by fitting all 20 parameterizations to the experimental distribution in the Dalitz-plot, are shown in figure 4.21 as a function of the number of free parameters,  $N_{par}$ . The central values for the  $K^*$  resonance parameters and the statistical errors are listed in table 4.16.

parameterization mode	n°.	$\Delta m_{K^*}$	$m_{K^{*\pm}}$	$m_{K^{*0}}$	$\Gamma_{K^{*\pm}}$	$\Gamma_{K^{*0}}$
		[MeV/c <sup>2</sup> ]	[MeV/c <sup>2</sup> ]	[MeV/c <sup>2</sup> ]	[MeV/c <sup>2</sup> ]	[MeV/c <sup>2</sup> ]
I	1	5.09±1.16	897.58±0.73	902.67±0.79	58.34±1.45	65.15±1.98
	2	4.23±1.18	897.44±0.74	901.67±0.85	57.45±1.53	66.58±2.15
	3	4.23±1.18	897.44±0.74	901.67±0.86	57.45±1.53	66.60±2.16
	4	4.32±1.18	897.44±0.73	901.76±0.87	57.18±1.49	66.20±2.09
	5	4.32±1.16	897.68±0.73	901.99±0.86	56.95±1.48	66.15±2.07
	6	4.22±1.16	897.85±0.74	902.07±0.87	56.87±1.49	66.07±2.11
	7	4.47±1.17	897.72±0.73	902.19±0.88	55.97±1.50	67.29±2.17
	8	4.34±1.17	897.65±0.73	901.99±0.89	55.90±1.49	67.37±2.17
	9	4.09±1.16	897.27±0.72	901.36±0.88	55.75±1.47	67.21±2.16
	10	4.02±1.16	897.22±0.72	901.24±0.89	55.73±1.46	67.11±2.16
II	1	4.72±0.89	891.47±0.61	896.19±0.70	47.38±1.13	55.49±2.16
	2	4.59±0.89	891.45±0.61	896.04±0.70	47.43±1.12	55.41±2.11
	3	4.53±0.87	891.35±0.60	895.88±0.70	47.48±1.12	52.57±2.24
	4	4.55±0.89	891.23±0.61	895.78±0.71	47.58±1.13	55.98±2.18
	5	4.44±0.87	891.31±0.61	895.75±0.70	47.86±1.14	53.16±2.26
	6	3.67±0.92	892.03±0.65	895.70±0.70	48.97±1.22	55.58±2.11
	7	4.41±0.88	891.32±0.62	895.73±0.70	47.78±1.16	53.03±2.30
	8	4.67±0.92	891.30±0.65	895.97±0.71	48.37±1.25	55.60±2.31
	9	3.76±0.92	891.84±0.65	895.60±0.71	48.67±1.25	53.68±2.31
	10	4.34±0.92	891.56±0.65	895.90±0.71	48.55±1.25	55.53±2.31

Table 4.16: Results for the  $K^*$  resonance parameters and their statistical errors, as obtained by the fits with the method of maximum likelihood.

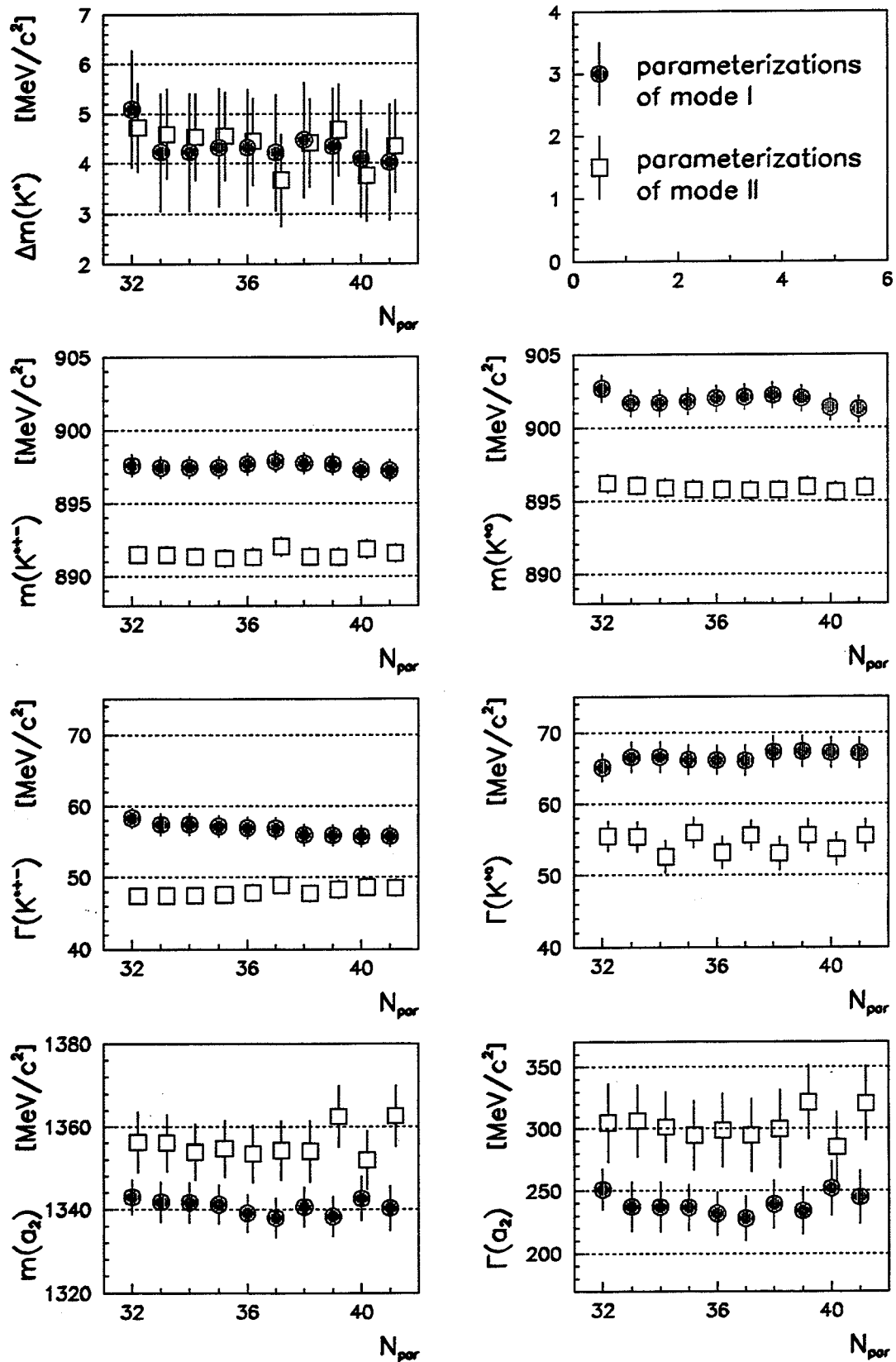


Figure 4.21: The results for the resonance parameters shown as a function of  $N_{par}$ , the number of free parameters in the fit.

As can be seen from the figure, the values for mass and width of the resonances are quite stable within a given parameterization mode, but differ a lot between mode I and mode II. Going from mode I to mode II changes on average the values for

the  $K^*$  masses by  $\sim -6 \text{ MeV}/c^2$ ,  
the  $K^*$  widths by  $\sim -10 \text{ MeV}/c^2$ ,  
the  $a_2$  mass by  $\sim +15 \text{ MeV}/c^2$ ,  
the  $a_2$  width by  $\sim +64 \text{ MeV}/c^2$ .

Although the  $K^*$  masses  $m_{K^{*\pm}}$  and  $m_{K^{*0}}$  change, the mass difference  $\Delta m_{K^*}$  is rather constant for the 20 parameterizations.

#### 4.5.3 Mean Value and Error Analysis for the $K^*$ Mass Difference

In this section, the mean value and the error analysis for the  $K^*$  mass difference is presented. The contributions considered to the error of  $\Delta m_{K^*}$  are

- the statistical error,  $\sigma_{stat}$ ,
- the uncertainty due to the parameterization,  $\sigma_{para}$ , and
- the error introduced by the approximation of the acceptance function,  $\sigma_{acc}$ .

In addition, the effect of a different Breit-Wigner parameterization on  $\Delta m_{K^*}$  is tested.

##### 4.5.3.1 Mean Value for the $K^*$ Mass Difference and Uncertainty due to the Parameterization

To demonstrate the independence of the  $K^*$  mass difference on the fit mode, the weighted average of  $\Delta m_{K^*}$  for mode I and mode II parameterizations are calculated separately. By taking the inverse squared of the errors given in table 4.16 as the weights, one gets

$$\langle \Delta m_{K^*} \rangle_{\text{mode I}} = 4.33 \text{ MeV}/c^2 \quad \text{for mode I} \quad \text{and} \quad (4.70)$$

$$\langle \Delta m_{K^*} \rangle_{\text{mode II}} = 4.38 \text{ MeV}/c^2 \quad \text{for mode II} . \quad (4.71)$$

The two mean values are in excellent agreement and no systematic shift of  $\Delta m_{K^*}$  is observed between mode I and II. The agreement between the values of  $\Delta m_{K^*}$  within a parameterization mode can be expressed by the quantity

$$\frac{\chi^2}{N-1} = \frac{1}{(N-1)} \sum_{i=1}^N \frac{[\Delta m_{K^*}(i) - \langle \Delta m_{K^*} \rangle]^2}{\sigma^2(\Delta m_{K^*}(i))} , \quad (4.72)$$

where  $N = 10$  is the number of parameterizations within a mode and  $\Delta m_{K^*}(i)$  and  $\sigma(\Delta m_{K^*}(i))$  are given in table 4.16. The results obtained are

$$\left(\frac{\chi^2}{N-1}\right)_{\text{mode I}} = 0.07 \quad \text{and} \quad \left(\frac{\chi^2}{N-1}\right)_{\text{mode II}} = 0.16. \quad (4.73)$$

For the final mean value of the  $K^*$  mass difference, the weighted average of all  $N = 20$  parameterizations is taken, giving

$$\langle \Delta m_{K^*} \rangle = 4.36 \text{ MeV}/c^2 \quad \text{with} \quad \left(\frac{\chi^2}{N-1}\right)_{\text{mode I+II}} = 0.11. \quad (4.74)$$

As can be seen from table 4.16, the maximum deviation of the central values from  $\langle \Delta m_{K^*} \rangle$  is

$$\begin{aligned} &+ 0.73 \text{ MeV}/c^2 \text{ for parameterization mode I} \quad (\text{number 1}) \text{ and} \\ &- 0.69 \text{ MeV}/c^2 \text{ for parameterization mode II} \quad (\text{number 6}). \end{aligned}$$

For the uncertainty due to the parameterization,  $\sigma_{para}$ , the maximum deviation of all 20 values for  $\Delta m_{K^*}$  (mode I and mode II) from  $\langle \Delta m_{K^*} \rangle$  is taken, giving

$$\sigma_{para} = 0.73 \text{ MeV}/c^2. \quad (4.75)$$

#### 4.5.3.2 Statistical Error and Correlations

The shape of the likelihood function  $\mathcal{L}(\vec{\theta})$  in the neighborhood of the maximum contains information about the statistical uncertainties of the parameter values at the maximum and the correlations between the parameters.

For a very large data sample,  $\mathcal{L}(\vec{\theta})$  is expected to approach a multidimensional Gaussian function [4], i.e.

$$\mathcal{L}(\vec{\theta}) \propto \exp \left[ -\frac{1}{2} \sum_{i,j=1}^M (\theta_i - \theta_{oi})(\theta_j - \theta_{oj})(V^{-1})_{ij} \right], \quad (4.76)$$

where  $V$  is the covariance matrix,  $\vec{\theta}_o$  is the parameter set that maximizes  $\mathcal{L}(\vec{\theta})$  and  $M$  is the dimension of the vector  $\vec{\theta}$ . The  $M \times M$  covariance matrix  $V$  is defined as

$$V \equiv \begin{pmatrix} \text{var}(\theta_1) & \text{cov}(\theta_1, \theta_2) & \dots & \text{cov}(\theta_1, \theta_n) \\ \text{cov}(\theta_2, \theta_1) & \text{var}(\theta_2) & \dots & \text{cov}(\theta_2, \theta_n) \\ \vdots & \vdots & \ddots & \vdots \\ \text{cov}(\theta_n, \theta_1) & \text{cov}(\theta_n, \theta_2) & \dots & \text{var}(\theta_n) \end{pmatrix}, \quad (4.77)$$

with

$$\text{var}(\theta_i) \equiv E[(\theta_i - \theta_{oi})^2] = \sigma_i^2 \quad , \quad (4.78)$$

$$\text{cov}(\theta_i, \theta_j) \equiv E[(\theta_i - \theta_{oi})(\theta_j - \theta_{oj})] = \rho_{ij} \sigma_i \sigma_j \quad , \quad (4.79)$$

where  $E[f(\vec{\theta})]$  is the expectation value of  $f(\vec{\theta})$  and  $\rho_{ij}$  is the correlation coefficient for  $\theta_i$  and  $\theta_j$  with  $|\rho_{ij}| \leq 1$ . Hence, the symmetric and positive definite covariance matrix  $V$  contains in the diagonal elements the variance of the parameters and in the off-diagonal elements the correlation coefficients between parameter pairs.

Another useful quantity is the global correlation coefficient  $R(\theta_i)$ , defined as the maximum correlation coefficient between  $\theta_i$  and any linear combination of all other parameters  $\theta_j$ ,  $j \neq i$  [42].  $R(\theta_i)$  is a measure of the total amount of correlation between  $\theta_i$  and all other parameters, and is given by

$$R(\theta_i) = \sqrt{1 - [V_{ii} \cdot (V^{-1})_{ii}]^{-1}} \quad . \quad (4.80)$$

Assuming a Gaussian shape for the likelihood function,  $\ell(\vec{\theta}) = -\ln \mathcal{L}(\vec{\theta})$  becomes an  $M$ -dimensional parabola, i.e.

$$\ell(\vec{\theta}) = \frac{1}{2} \sum_{i,j=1}^M (\theta_i - \theta_{oi})(\theta_j - \theta_{oj})(V^{-1})_{ij} + \text{const.} \quad (4.81)$$

The "score" functions [4], defined as

$$S_i(\vec{\theta}) \equiv \frac{\partial \ell(\vec{\theta})}{\partial \theta_i} = \sum_{j=1}^M (\theta_j - \theta_{oj})(V^{-1})_{ij} \quad , \quad (4.82)$$

are then linear in  $\vec{\theta}$ , and the covariance matrix elements may be calculated from

$$(V^{-1})_{ij} = \frac{\partial^2 \ell(\vec{\theta})}{\partial \theta_i \partial \theta_j} = H_{ij} \quad , \quad (4.83)$$

where  $H$  is the matrix of second derivatives of  $\ell(\vec{\theta})$  (the Hesse matrix), which is independent of  $\vec{\theta}$  in this case.

Hence, for a Gaussian shape of  $\mathcal{L}(\vec{\theta})$ , the equation

$$\mathcal{L}(\vec{\theta}) = \mathcal{L}(\vec{\theta}_o) \cdot e^{-s^2/2} \quad \text{or equivalent} \quad \ell(\vec{\theta}) = \ell(\vec{\theta}_o) + \frac{s^2}{2} \quad (4.84)$$

defines a  $M$ -dimensional ellipsoid in parameter space. The extreme limits of this ellipsoid parallel to the  $\theta_i$ -axis give an  $s$ -standard deviation error interval in  $\theta_i$ :

$$I_{\theta_i}(s) = [\theta_{oi} - s \cdot \sigma_i, \theta_{oi} + s \cdot \sigma_i] \quad . \quad (4.85)$$

The MINUIT program offers two possibilities to estimate the statistical errors of the fit parameters:

1. The "parabolic" errors are calculated from the covariance matrix  $V$ , which is obtained by inversion of the Hesse matrix  $H$  (equation 4.83). As explained above, this procedure assumes a parabolic shape of  $\ell(\vec{\theta})$  (or  $\chi^2(\vec{\theta})$ ) at the minimum. Therefore, the parabolic errors include the correlations between all the fit parameters, but do not take account of non-linearities in the score functions  $S_i(\vec{\theta})$ . The  $2\sigma$ -errors are by definition exactly twice as big as the  $1\sigma$ -errors, and the positive and negative errors are equal (symmetric error interval).
2. The MINOS processor of the MINUIT program calculates numerically the contour defined by (see equation 4.84)

$$\begin{aligned} \bullet \ell(\vec{\theta}) &= \ell(\vec{\theta}_0) + \frac{s^2}{2} && \text{(for method of maximum likelihood)} \quad \text{or} \\ \bullet \chi^2(\vec{\theta}) &= \chi^2(\vec{\theta}_0) + s^2 && \text{(for method of least squares)} \end{aligned}$$

in order to estimate the  $s\sigma$  error intervals. Thus, the errors quoted by MINOS take into account both parameter correlations and non-linearities and are usually asymmetric.

MINOS errors are generally more reliable than parabolic errors, but their determination requires a lot of computer time. The statistical errors quoted in table 4.16 are  $1\sigma$  errors and are obtained as follows:

- For all parameterizations, the MINOS errors are calculated for the charged  $K^*$  mass,  $m_{K^{*\pm}}$ , and the mass difference,  $\Delta m_{K^*}$ . The larger of the negative or positive MINOS error is taken.
- For some parameterizations, the MINOS errors are determined for all resonance parameters, especially when the parabolic errors seem unrealistic.
- Otherwise, the parabolic errors are used.
- The error of  $m_{K^{*0}} = m_{K^{*\pm}} + \Delta m_{K^*}$  is calculated according to

$$\sigma(m_{K^{*0}}) = \sqrt{\sigma_i^2 + \sigma_j^2 + 2\sigma_i\sigma_j\rho_{ij}}, \quad (4.86)$$

where  $i = m_{K^{*\pm}}$  and  $j = \Delta m_{K^*}$ .

In figure 4.22, the parabolic values are compared to the MINOS values for the  $1\sigma$ ,  $2\sigma$  and  $3\sigma$  errors (parameterization I/10). The two error estimates were found to agree well for the  $K^*$  resonance parameters. However, the errors for  $m_{a_2}$  and  $\Gamma_{a_2}$  are slightly asymmetric.

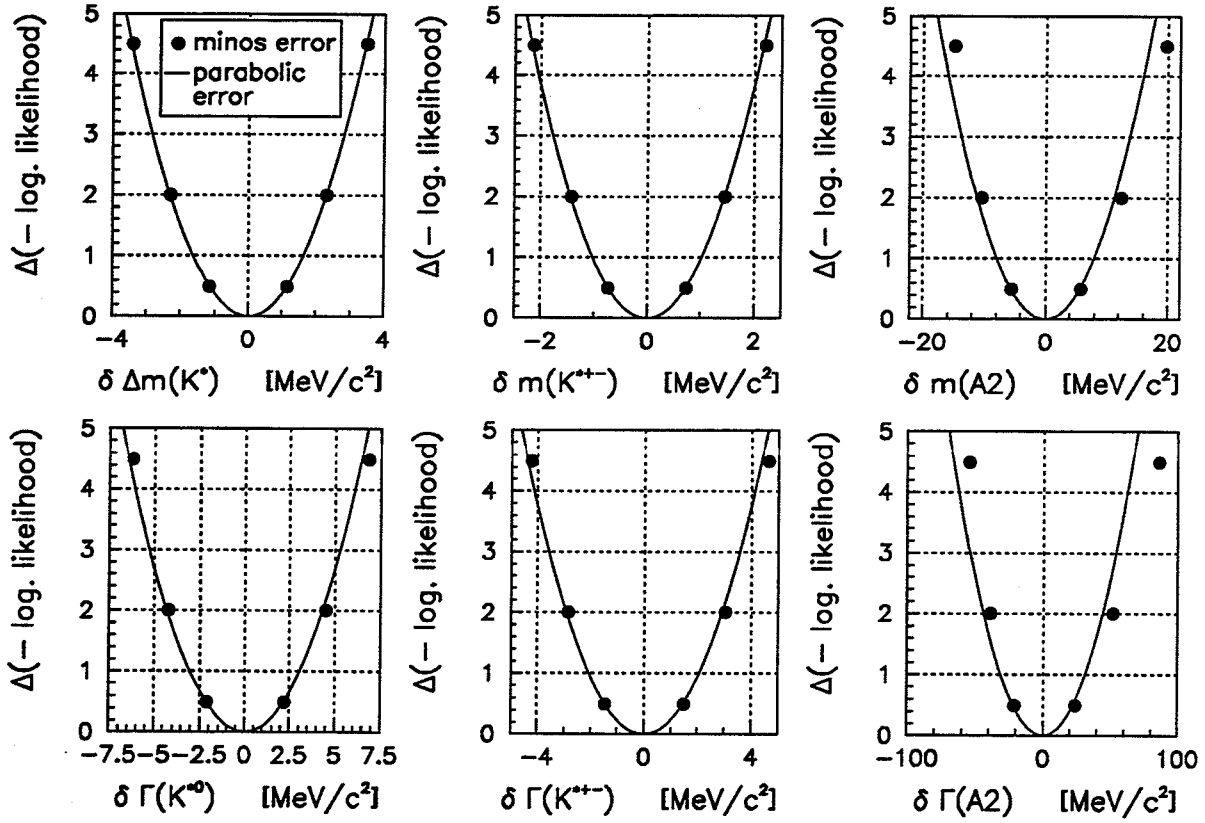


Figure 4.22: Comparison between parabolic and MINOS values for  $1\sigma$ ,  $2\sigma$  and  $3\sigma$  errors (parameterization I/10).

As already mentioned on page 63, equation 4.6, the minimum statistical errors in the determination of the resonance masses  $m_{K^{*\pm}}$  and  $m_{K^{*0}}$  are given by [4]

$$\delta_{min}(m_{K^{*\pm}[K^{*0}]}) = \frac{\Gamma_{K^{*\pm}[K^{*0}]}}{\sqrt{N_{K^{*\pm}[K^{*0}]}}}, \quad (4.87)$$

where  $N_{K^{*\pm}[K^{*0}]}$  is the number of events in the  $K^{*\pm}$  ( $K^{*0}$ ) peak. Neglecting interference effects,  $N_{K^{*\pm}[K^{*0}]}$  can be estimated by (see equation 4.69)

$$N_{K^{*\pm}[K^{*0}]} = \int_{\text{Dalitz-plot}} C_{1[2]}(x, y, \vec{\theta}) dx dy, \quad (4.88)$$

where  $C_{1[2]}(x, y, \vec{\theta})$  is the contribution of the  $K^{*\pm}$  ( $K^{*0}$ ) resonance to the distribution function  $P(x, y, \vec{\theta})$  in the Dalitz-plot, with  $P(x, y, \vec{\theta})$  normalized to  $N_e$ , the number of events considered in the fit (see equation 4.68). The values for  $N_{K^{*\pm}[K^{*0}]}$  are stable within a parameterization mode, but different between mode I and II. Therefore  $\langle N_{K^{*\pm}[K^{*0}]} \rangle$ , the average value within a mode, is used to calculate the minimum statistical error

$$\delta_{min}(m_{K^{*\pm}[K^{*0}]}) \simeq \frac{\Gamma_{K^*}}{\sqrt{\langle N_{K^{*\pm}[K^{*0}]} \rangle}} \quad (4.89)$$



for each mode separately, assuming  $\Gamma_{K^*} = \Gamma_{K^{*\pm}} = \Gamma_{K^{*0}} = 50 \text{ MeV}/c^2$ .

	$\langle N_{K^{*\pm}} \rangle$	$\frac{\langle N_{K^{*\pm}} \rangle}{N_e}$	$\delta_{\min}(m_{K^{*\pm}})$ [MeV/c <sup>2</sup> ]	$\langle N_{K^{*0}} \rangle$	$\frac{\langle N_{K^{*0}} \rangle}{N_e}$	$\delta_{\min}(m_{K^{*0}})$ [MeV/c <sup>2</sup> ]
mode I	5'426	0.167	0.68	10'809	0.333	0.48
mode II	8'656	0.267	0.54	8'504	0.262	0.54

Table 4.17: The minimum statistical errors of the  $K^*$  masses for mode I and mode II parameterizations.

Table 4.17 gives the values for  $\langle N_{K^{*\pm}[K^{*0}]} \rangle$ , the ratios  $\langle N_{K^{*\pm}[K^{*0}]} \rangle / N_e$  and  $\delta_{\min}(m_{K^{*\pm}[K^{*0}]})$  for the two parameterization modes. A comparison with table 4.16 shows that the statistical errors quoted for  $m_{K^{*\pm}}$  and  $m_{K^{*0}}$  are well above the minimum errors  $\delta_{\min}(m_{K^{*\pm}[K^{*0}]})$ .

As the statistical error of the  $K^*$  mass difference, the maximum of the errors listed in table 4.16 for  $\Delta m_{K^*}$  is taken, which is

$$\sigma_{stat} = 1.18 \text{ MeV}/c^2. \quad (4.90)$$

At the example of the parameterizations I/4, I/10, II/4 and II/10, table 4.18 gives the correlation coefficients between the mass difference  $\Delta m_{K^*}$  and the other physical parameters, together with the global correlation of  $\Delta m_{K^*}$ . For the  $K^*$  mass difference, the correlations are very similar within a parameterization mode, but there are some differences between mode I and II. Generally one can say:

- The global correlation,  $R(\Delta m_{K^*})$ , is larger for mode I ( $\simeq 0.86$ ) than for mode II ( $\simeq 0.75$ ). This leads to the larger statistical errors of  $\Delta m_{K^*}$  for mode I parameterizations.
- The  $K^*$  mass difference is strongest correlated to  $m_{K^{*\pm}}$ .
- The other significant correlations are between  $\Delta m_{K^*}$  and the  $K^*$  - widths  $\Gamma_{K^{*\pm}}$  and  $\Gamma_{K^{*0}}$ , as well as the two phases  $\varphi_2$  and  $\varphi_3$ .
- For mode I,  $\Delta m_{K^*}$  is correlated to the scattering length  $SL_{K_S^0\pi}$ .
- For mode II,  $\Delta m_{K^*}$  is correlated to the  $a_2$  mass,  $m_{a_2}$ .
- The correlations between  $\Delta m_{K^*}$  and the coefficients of the polynomials,  $\rho_i$ , are small.

correlation between $\Delta m_{K^*}$ and	parameterization			
	I/4	I/10	II/4	II/10
$m_{K^{*\pm}}$	-0.680	-0.644	-0.604	-0.592
$\Gamma_{K^{*\pm}}$	-0.212	-0.228	-0.094	-0.129
$\Gamma_{K^{*0}}$	0.157	0.171	0.209	0.190
$m_{a_2}$	-0.082	-0.082	0.258	0.244
$\Gamma_{a_2}$	-0.056	-0.088	0.060	0.062
$SL_{K_S^0\pi}$	0.198	0.180	0.033	-0.014
$SL_{K^{\pm}\pi}$	0.039	0.014	-0.073	-0.067
$SL_{K_S^0K^{\pm}}$	-0.029	-0.038	0.029	-0.021
$\varphi_2$	0.472	0.410	0.290	0.242
$\varphi_3$	0.389	0.355	0.196	0.170
<b>R(<math>\Delta m_{K^*}</math>) (global)</b>	<b>0.867</b>	<b>0.854</b>	<b>0.752</b>	<b>0.740</b>

Table 4.18: Correlation coefficients between  $\Delta m_{K^*}$  and other physical parameters.

#### 4.5.3.3 Uncertainty due to the Acceptance Function

The systematic error of  $\Delta m_{K^*}$  introduced by approximating the acceptance function  $Acc(x, y)$  with the "standard" acceptance histogram,  $AH^{sta}$ , is analysed with six alternative acceptance histograms,  $AH_k^{alt}$  ( $k = 1, \dots, 6$ ), differing from  $AH^{sta}$  in the cell size as well as the smoothness. The various acceptance histograms are described in section 4.4.

To estimate the systematic error due to the acceptance function,  $\sigma_{acc}$ , the maximum likelihood fits were repeated with the six alternative acceptance histograms for the following parameterizations (see table 4.11):

**I/2 and II/2:** Both have polynomials of order (5 2 2) for the resonances and (3 2 2) for the scattering amplitudes. The number of free parameters is  $N_{par} = 33$ .

**I/6 and II/6:** Both have polynomials of order (5 3 3) for the resonances and (3 3 3) for the scattering amplitudes. The number of free parameters is  $N_{par} = 37$ .

In figure 4.23, the values for  $\Delta m_{K^*}$  obtained with the standard acceptance histogram,  $\Delta m_{K^*}(AH^{sta})$ , are compared to the values obtained with the alternative acceptance histograms,  $\Delta m_{K^*}(AH_k^{alt})$ . Table 4.19 summarizes the results and gives in the last line the maximum deviations

$$\delta(\Delta m_{K^*}) \equiv \max \left\{ \left| \Delta m_{K^*}(AH^{sta}) - \Delta m_{K^*}(AH_k^{alt}) \right|, k = 1, \dots, 6 \right\} \quad (4.91)$$

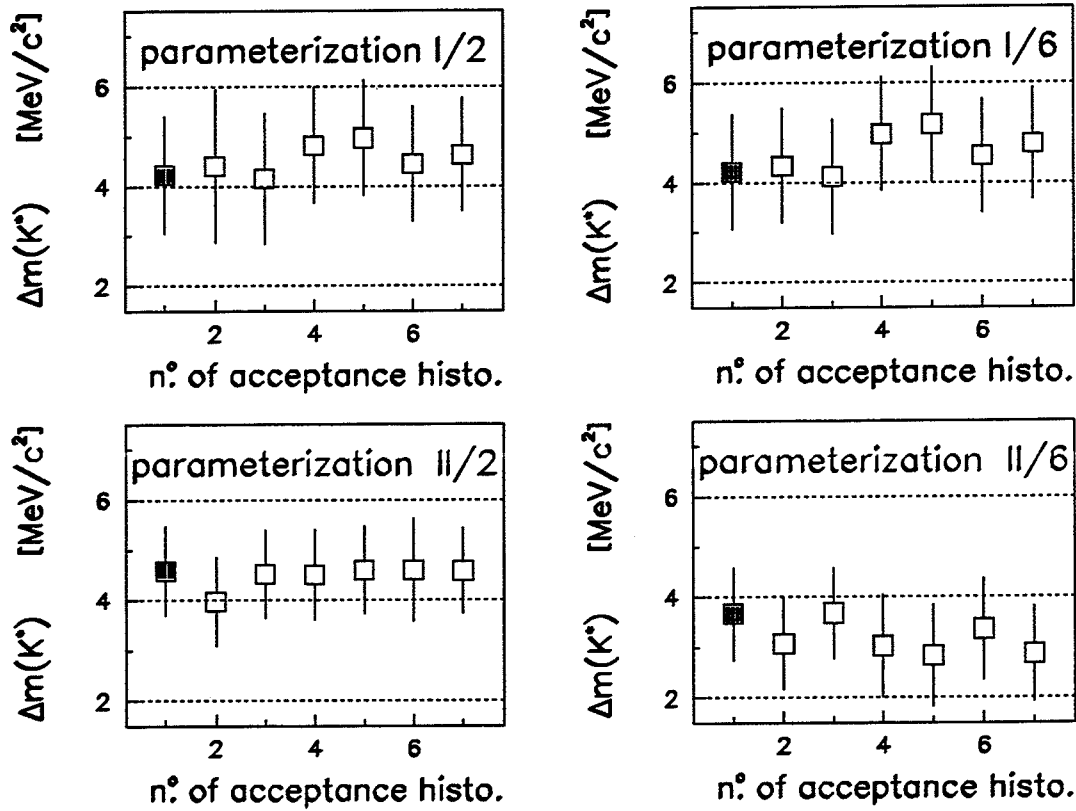


Figure 4.23: The values for  $\Delta m_{K^*}$  obtained with the standard (1) and the six alternative (2-7) acceptance histograms for the parameterizations I/2, I/6, II/2 and II/6.

within each parameterization.

For the selected parameterizations, all values  $\Delta m_{K^*}(AH_k^{alt})$  ( $k = 1, \dots, 6$ ) are within  $1\sigma$  of  $\Delta m_{K^*}(AH^{sta})$ . As an estimate for the systematic error of  $\Delta m_{K^*}$  due to the acceptance function, the maximum of the values for  $\delta(\Delta m_{K^*})$  listed in table 4.19 is taken, yielding

$$\sigma_{acc} = 0.95 \text{ MeV}/c^2. \quad (4.92)$$

#### 4.5.3.4 Effect of a Different Breit-Wigner Parameterization

The maximum likelihood fits were also repeated for all 20 parameterizations with the Breit-Wigner function used by Conforto et al. (see paragraph 4.3.1.4, table 4.10). A comparison between the Conforto parameterization and the one used in this work is shown in figure 4.15 on page 92. This plot suggests lower values for the resonance masses when using the Conforto parameterization.

In figure 4.24, the standard values for  $\Delta m_{K^*}$  are compared to the results obtained with the Conforto parameterization of the Breit-Wigner function. Notice that the standard

acceptance histogram number	$\Delta m_{K^*}$ [MeV/c <sup>2</sup> ] for parameterization			
	I/2	I/6	II/2	II/6
1	4.23	4.22	4.59	3.67
2	4.41	4.34	3.98	3.08
3	4.15	4.12	4.52	3.68
4	4.82	4.98	4.51	3.03
5	4.97	5.17	4.60	2.83
6	4.45	4.54	4.60	3.36
7	4.63	4.78	4.58	2.87
maximum deviation $\delta(\Delta m_{K^*})$ [MeV/c <sup>2</sup> ]				
	0.74	0.95	0.61	0.84

Table 4.19: The results for  $\Delta m_{K^*}$  obtained with the standard (1) and the six alternative acceptance histograms (2-7) for the parameterizations I/2, I/6, II/2 and II/6. The maximum deviations from the standard values (1) are listed in the last line.

values for  $\Delta m_{K^*}$  are independent of the parameterization mode (see 4.5.3.1), while the Breit-Wigner function used in the work of Conforto et al. yields results for  $\Delta m_{K^*}$  which are different for parameterization mode I and mode II.

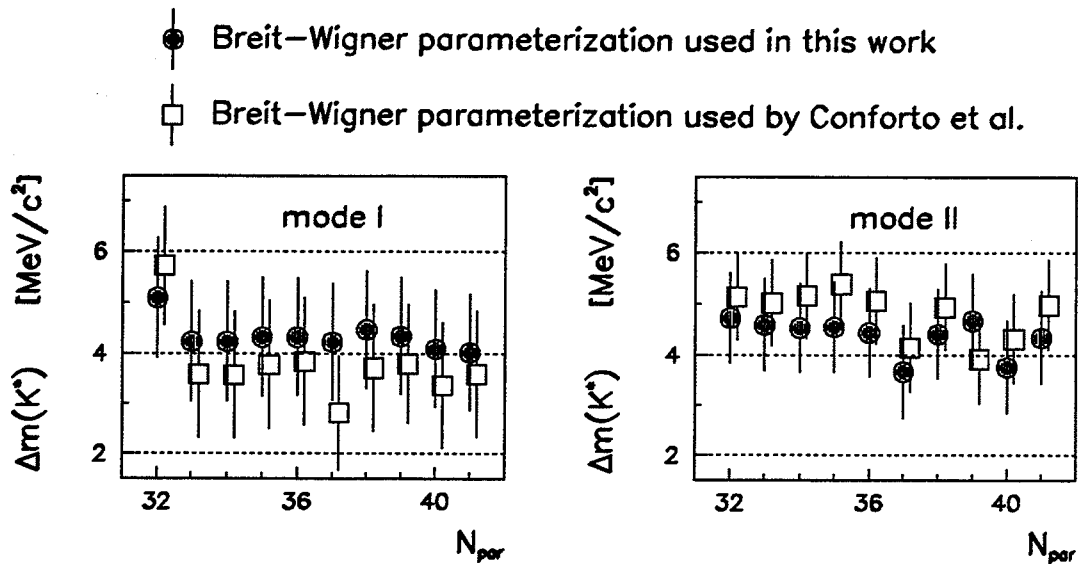


Figure 4.24: Results for the  $K^*$  mass difference obtained with two different Breit-Wigner functions. The function used in this work yields parameterization mode independent results, while the Conforto parameterization introduces a systematic shift of  $\Delta m_{K^*}$  between mode I and mode II.

In table 4.20 are listed the weighted mean values of the resonance parameters for each parameterization mode and each Breit-Wigner function separately, as well as the difference between these mean values, defined as

$$\delta(\theta) = \langle \theta \rangle_{\text{Conforto}} - \langle \theta \rangle_{\text{standard}}, \quad (4.93)$$

where  $\theta$  is one of the resonance parameters.

resonance parameter $\theta$	standard mean value [MeV/c <sup>2</sup> ]		Conforto mean value [MeV/c <sup>2</sup> ]		difference $\delta(\theta)$ [MeV/c <sup>2</sup> ]	
	mode I	mode II	mode I	mode II	mode I	mode II
$\Delta m_{K^*}$	4.33	4.38	3.79	4.82	-0.54	+0.44
$m_{K^{*\pm}}$	897.53	891.48	891.64	888.18	-5.89	-3.30
$m_{K^{*0}}$	901.87	895.85	895.25	893.00	-6.62	-2.85
$\Gamma_{K^{*\pm}}$	56.76	47.96	55.43	48.06	-1.33	+0.10
$\Gamma_{K^{*0}}$	66.54	54.64	63.26	56.00	-3.28	+1.36
$m_{a_2}$	1340.68	1355.83	1289.11	1289.85	-51.57	-65.98
$\Gamma_{a_2}$	238.89	302.61	139.64	164.05	-99.25	-138.56

Table 4.20: The effect of the Breit-Wigner function used by Conforto et al. on the weighted mean values of the resonance parameters.

The effect of the different Breit-Wigner function is small for  $\Delta m_{K^*}$  ( $\sim \pm 0.5 \text{ MeV}/c^2$ ), but quite substantial for the other resonance parameters, especially the mass and width of the  $a_2$ .

Many different Breit-Wigner parameterizations exist for a resonance with spin and they are all very similar to the one chosen in this work. On the other hand, the parameterization used by Conforto et al. does not take into account the spin of the resonance and is quite different to this parameterization. Nevertheless, the effect on the  $K^*$  mass difference is small. Because of these reasons, the uncertainty due to the Breit-Wigner function is neglected in the error estimate of  $\Delta m_{K^*}$ .

#### 4.5.4 Result for the Isospin Mass Splitting of the $K^*$ (892) Meson

The value found in this analysis for the  $K^*$  mass difference  $\Delta m_{K^*} \equiv m_{K^{*0}} - m_{K^{*\pm}}$  is

$$\Delta m_{K^*}^{\text{CPLEAR}} = [4.36 \pm 1.18 (\text{stat.}) \pm 1.20 (\text{syst.})] \text{ MeV}/c^2. \quad (4.94)$$

The systematic error is given by

$$\sigma_{\text{syst}}^2 = \sigma_{\text{para}}^2 + \sigma_{\text{acc}}^2, \quad (4.95)$$

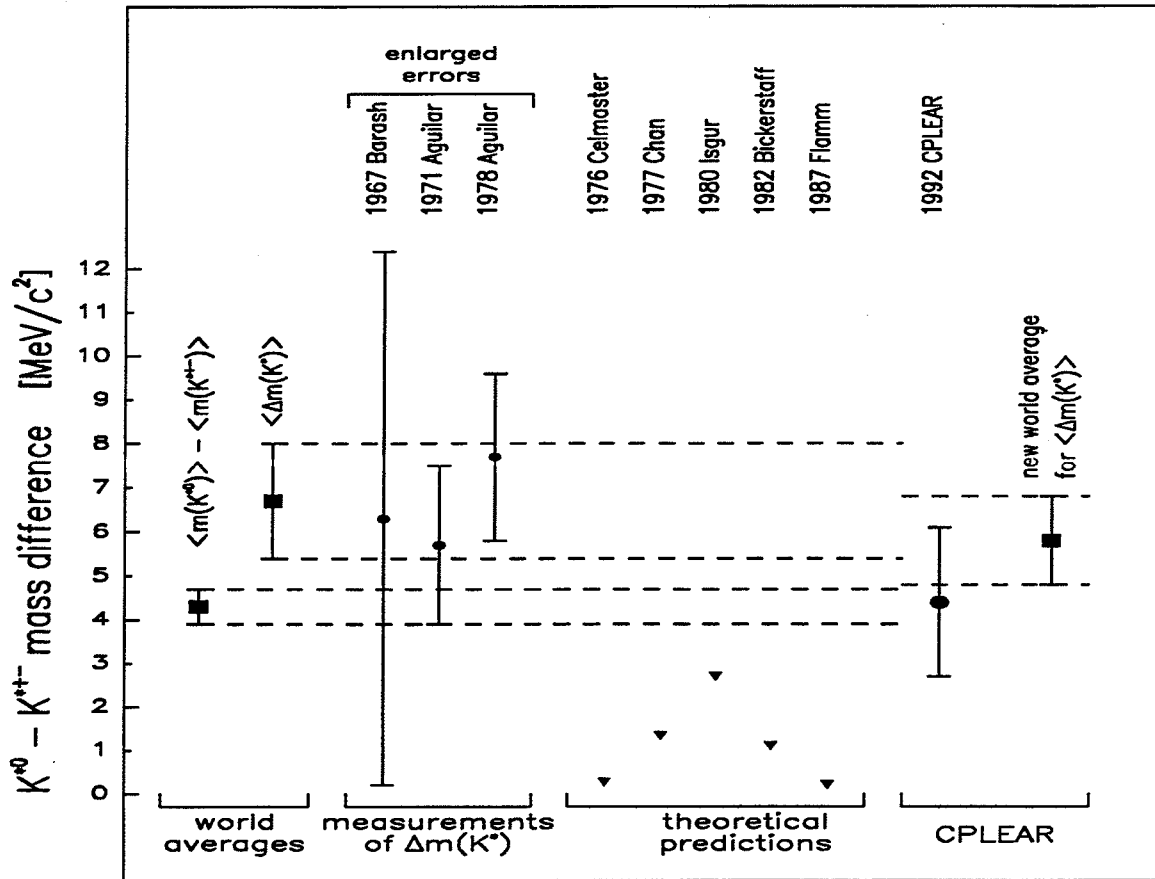


Figure 4.25: Comparison between the value found in this analysis for the  $K^*$  mass difference and results of earlier measurements and theoretical predictions.

where  $\sigma_{para} = 0.73 \text{ MeV}/c^2$  is the uncertainty of  $\Delta m_{K^*}$  due to the parameterization of the Dalitz-plot density and  $\sigma_{acc} = 0.95 \text{ MeV}/c^2$  is the error introduced by the approximation of the detector and trigger acceptance function.

This result for  $\Delta m_{K^*}$  is in excellent agreement with the world average (see 4.1)

$$\langle m_{K^{*0}} \rangle - \langle m_{K^{*\pm}} \rangle = (4.27 \pm 0.37) \text{ MeV}/c^2, \quad (4.96)$$

as can be seen in figure 4.25, where  $\Delta m_{K^*}^{CPLEAR}$  is compared to earlier measurements and theoretical predictions of the  $K^*$  mass difference. On the other hand,  $\Delta m_{K^*}^{CPLEAR}$  is not in sincere disagreement ( $\sim 1.0$  standard deviations) with the world average

$$\langle \Delta m_{K^*} \rangle = (6.6 \pm 1.3) \text{ MeV}/c^2. \quad (4.97)$$

Including  $\Delta m_{K^*}^{CPLEAR}$  in the world average of the  $\Delta m_{K^*}$  measurements, i.e. the average of the four results

year	experiment	$\Delta m_{K^*}$ [MeV/c <sup>2</sup> ]
1967	Barash et. al. [24]	$6.3 \pm 6.1$ (enlarged error)
1971	Aguilar et. al. [25]	$5.7 \pm 1.8$ (enlarged error)
1978	Aguilar et. al. [26]	$7.7 \pm 1.9$ (enlarged error)
1992	CPLEAR (this work)	$4.4 \pm 1.7$ ,

one finds

$$\langle \Delta m_{K^*} \rangle_{\text{new}} = (5.8 \pm 1.0) \text{ MeV}/c^2 . \quad (4.98)$$

Thereby, the previous discrepancy of  $\sim 1.8$  standard deviations between  $\langle m_{K^{*0}} \rangle - \langle m_{K^{*\pm}} \rangle$  and  $\langle \Delta m_{K^*} \rangle$  is reduced to  $\sim 1.4$  standard deviations for the new value  $\langle \Delta m_{K^*} \rangle_{\text{new}}$ .

## 5 Conclusion

The isospin mass splitting of the  $K^*(892)$  meson was analysed with a sample of 33'132 events of the type  $p\bar{p} \rightarrow K^\mp \pi^\pm K^0(\bar{K}^0)$ ;  $K^0(\bar{K}^0) \rightarrow \pi^+\pi^-$ , recorded by the CPLEAR collaboration in October 1990.

The data were taken with a trigger that favored  $K_S^0$  decays and thereby reduced the background from  $K_L^0$  decays. The information provided by the scintillators and the Čerenkov-counters was used for the kaon/pion separation. The final data sample was selected by a constraint fit, requiring energy and momentum conservation and a missing mass at the annihilation vertex equal to the neutral kaon mass.

The Dalitz-plot,  $M_{inv}^2(K^\pm, \pi^\mp)$  vs  $M_{inv}^2(K^0, \pi^\pm)$ , shows interference between the neutral and charged  $K^*$  bands, which makes it impossible to measure the  $K^*$  masses by a fit of the corresponding invariant mass distributions. Hence, a study of the Dalitz-plot population is required. An amplitude analysis leads to a large number of contributions and is not suited for a fit, because there are too many parameters to be determined. Therefore, a parameterization is chosen with one amplitude for each of the resonances  $K^{*\pm}$ ,  $K^{*0}(\bar{K}^{*0})$ , and  $a_2$  plus three amplitudes for the non-resonant part. The resonant amplitudes are constructed as the product of a Breit-Wigner function and a polynomial, while a scattering-length parameterization multiplied with a polynomial is used for the non-resonant contributions. Using the method of maximum likelihood, 20 parameterizations differing in the order of the polynomials, are fitted to the experimental Dalitz-plot. This yields the average result

$$\Delta m_{K^*} \equiv m_{K^{*0}} - m_{K^{*\pm}} = [4.36 \pm 1.18 \text{ (stat.)} \pm 1.20 \text{ (syst.)}] \text{ MeV}/c^2.$$

The systematic error of  $\Delta m_{K^*}$  includes the uncertainty in the parameterization,  $\sigma_{para} = 0.73 \text{ MeV}/c^2$ , and the error introduced by an approximation of the acceptance function for the detector and the trigger,  $\sigma_{acc} = 0.95 \text{ MeV}/c^2$ . The acceptance function was estimated with a simulated data sample.

The result found for  $\Delta m_{K^*}$  is in excellent agreement with the difference between the world averages for the neutral and charged  $K^*$  masses,  $\langle m_{K^{*0}} \rangle - \langle m_{K^{*\pm}} \rangle = (4.27 \pm 0.37) \text{ MeV}/c^2$ , and is lower by one standard deviation than the average value of three previous measurements of the  $K^*$  mass splitting,  $\langle \Delta m_{K^*} \rangle = (6.6 \pm 1.3) \text{ MeV}/c^2$ .

Including the result of this work, the new world average for  $\Delta m_{K^*}$  becomes

$$\langle \Delta m_{K^*} \rangle_{\text{new}} = (5.8 \pm 1.0) \text{ MeV}/c^2,$$

and the difference between  $\langle m_{K^{*0}} \rangle - \langle m_{K^{*\pm}} \rangle$  and  $\langle \Delta m_{K^*} \rangle$  is lowered from  $\sim 1.8$  standard deviations to  $\sim 1.4$  standard deviations. Therefore, the experimental discrepancy in the determination of the  $K^*$  mass splitting is reduced by this work and may be considered as settled.



# A The Kinematic Fit

The kinematic fit used for the filter 5CFIT (see section 4.2.2.3) is a least squares fit with conditions (constraints). In this appendix are briefly described the principle of this kind of fit, its application to the "golden  $\pi^+\pi^-$ " event selection and finally the effect of the fit on the momentum and invariant mass resolution of the detector. A detailed description of the method of least squares fits with constraints can be found in [43].

## A.1 Principle of Least Squares Fits with Constraints

The method of least squares with constraints is often used for one or several of the following reasons:

- To improve the measurement precision.
- To estimate unmeasured parameters.
- To have a statistical test of the hypothesis, that the measured data are consistent with an assumed model.

An example, where this method is very helpful, are elementary reactions in particle physics. Energy and momentum conservation, as well as geometrical conditions, permit the formulation of constraint equations. The unmeasured parameters may come from unseen particles in the reaction. In general, least squares fits with constraints apply to the following situation:

- One has a set of  $n$  random variables  $y_i$  ( $i = 1, \dots, n$ ), where the values are assumed to be measurements of true values,  $\bar{y}_i$ , without bias, i.e.

$$E[y_i] = \bar{y}_i, \quad (\text{A.1})$$

where  $E[y_i]$  is the expectation value of  $y_i$ .

- For the measurements  $y_i$ , one knows the corresponding  $n \times n$  covariance matrix  $V(y)$ :

$$V(y) \equiv \begin{pmatrix} \text{var}(y_1) & \text{cov}(y_1, y_2) & \dots & \text{cov}(y_1, y_n) \\ \text{cov}(y_2, y_1) & \text{var}(y_2) & \dots & \text{cov}(y_2, y_n) \\ \vdots & \vdots & \ddots & \vdots \\ \text{cov}(y_n, y_1) & \text{cov}(y_n, y_2) & \dots & \text{var}(y_n) \end{pmatrix}, \quad (\text{A.2})$$

where  $\text{var}(y_i) \equiv E[(y_i - \bar{y}_i)^2]$  is the variance of  $y_i$  and  $\text{cov}(y_i, y_j) \equiv E[(y_i - \bar{y}_i)(y_j - \bar{y}_j)]$  is the covariance of  $y_i$  and  $y_j$ .

- The underlying model for the measurements  $y_i$  depends on  $p$  additional parameters  $a_j$  ( $j = 1, \dots, p$ ), with true values  $\bar{a}_j$ .
- The model can be formulated with a set of  $m$  equations (the constraints) of the type

$$f_k(\bar{a}, \bar{y}) = 0 \quad (k = 1, \dots, m), \quad (\text{A.3})$$

where  $\bar{a}$  is the vector of the true parameter values  $\bar{a}_j$ , and  $\bar{y}$  is the vector of the true variables  $\bar{y}_i$ .

If  $m > p$ , the constraints cannot be fulfilled with the measured values  $y_i$  and an appropriate set of parameters  $a_j$ . In this case, one has to determine corrections  $\Delta y_i$  and parameters  $a_j$  such that

$$f_k(a, y^*) = 0 \quad (k = 1, \dots, m), \quad (\text{A.4})$$

where  $y^* = y + \Delta y$  are the corrected values of the measured variables, and the weighted sum of squares

$$S(y^*) \equiv \Delta y^T W \Delta y \quad \text{with} \quad W = V(y)^{-1} \quad (\text{A.5})$$

attains a minimum. This problem can be solved by the method of Lagrangian multipliers. An additional parameter  $\lambda_k$  (Lagrange multiplier) is introduced for each constraint, and a new function

$$L(y^*) \equiv S(y^*) + 2 \sum_{k=1}^m \lambda_k f_k(a, y^*) \quad (\text{A.6})$$

is defined. The condition for a minimum of  $L(y^*)$  with respect to all parameters  $y^*$ ,  $a$  and  $\lambda$  is equivalent to the condition for a minimum of  $S(y^*)$  under the constraints  $f_k(a, y^*) = 0$ .

In the general case of nonlinear conditions, one can find the solution by linearization of the conditions and subsequent iterations. The formulae for the resulting iterative algorithm can be found in [43].

If one has a correct model, linear conditions and measured data that are gaussian distributed around the true values, then the expectation value for  $S(y^*)$  at the minimum is given by

$$E(\hat{S}) = (m - p), \quad (\text{A.7})$$

where  $\hat{S}$  is the minimum of  $S(y^*)$ , and  $\hat{S}$  follows a  $\chi^2$  - distribution with  $n_{df} = m - p$  degrees of freedom. The confidence level  $CL(\hat{S})$  for the measurements  $y_i$  is obtained by integrating the tail of the  $\chi^2$  - function, i.e.

$$CL(\hat{S}) = \int_{\hat{S}}^{\infty} f(x, n_{df}) dx, \quad (\text{A.8})$$

where  $f(x, n_{df})$  is the  $\chi^2$  - function for  $n_{df}$  degrees of freedom. For a correct model, the confidence level expresses the probability that a random repeat of the measurement would give a worse  $\hat{S}$ . In this case,  $CL(\hat{S})$  is equally distributed in the range of 0 to 1.

## A.2 Application to "Golden $\pi^+\pi^-$ " Event Selection

The model (or hypothesis) for the events analysed in the filter 5CFIT is a  $p\bar{p}$  annihilation into  $K^\pm \pi^\mp K_S^0$  with a subsequent neutral kaon decay into  $\pi^+\pi^-$ . The set of  $n$  measured values,  $y_i$ , are the 12 cartesian components of the charged particle momenta:

$$P_K^i, P_\pi^i, P_{S1}^i, P_{S2}^i \quad (i = x, y, z), \quad (\text{A.9})$$

where  $K$  is the primary charged kaon,  $\pi$  is the primary pion and  $S1, S2$  are the two secondary pions. The model contains no additional unmeasured parameters  $a_j$ , because no undetected final particles are in this event type. The hypothesis can be express by the following  $m = 5$  constraints:

$$f_1 = E_K + E_\pi + E_{S1} + E_{S2} - 2 m_p c^2 = 0, \quad (\text{A.10})$$

$$f_2 = P_K^x + P_\pi^x + P_{S1}^x + P_{S2}^x = 0, \quad (\text{A.11})$$

$$f_3 = P_K^y + P_\pi^y + P_{S1}^y + P_{S2}^y = 0, \quad (\text{A.12})$$

$$f_4 = P_K^z + P_\pi^z + P_{S1}^z + P_{S2}^z = 0, \quad (\text{A.13})$$

$$f_5 = \frac{1}{m_{K^0} c^2} \left[ (2 m_p c^2 - E_K - E_\pi)^2 - c^2 (\vec{P}_K + \vec{P}_\pi)^2 \right] - m_{K^0} c^2 = 0. \quad (\text{A.14})$$

The first equation requires the energy conservation in the reaction. The conditions  $f_2, f_3$  and  $f_4$  express the momentum conservation. With the constraint  $f_5$  one requires the missing mass at the  $p\bar{p}$  annihilation vertex to be equal to the neutral kaon mass. These five conditions imply as well, that the invariant mass of the secondary particles  $S1, S2$  is equal to  $m_{K^0}$ . The number of degrees of freedom in this model is then

$$n_{df} = m - p = 5 \quad (\text{5C-fit}). \quad (\text{A.15})$$

Similar conditions for other event types, e.g.

$$\begin{aligned} \bullet p\bar{p} &\rightarrow K^\pm \pi^\mp K_L^0, & K_L^0 &\rightarrow \pi^\pm e^\mp \nu, \\ \bullet p\bar{p} &\rightarrow K^\pm \pi^\mp K_L^0, & K_L^0 &\rightarrow \pi^\pm \mu^\mp \nu, \\ \bullet p\bar{p} &\rightarrow K^\pm \pi^\mp K_L^0, & K_L^0 &\rightarrow \pi^+ \pi^- \pi^0 \quad \text{and} \\ \bullet p\bar{p} &\rightarrow K^\pm \pi^\mp K_S^0 \pi^0, & K_S^0 &\rightarrow \pi^+ \pi^- \end{aligned}$$

can also be formulated, but in all these reactions, one neutral particle is unmeasured. The momentum components of this particle are introduced as  $p = 3$  unmeasured parameters in the model. By adjusting these parameters, three of the five constraints can be fulfilled immediately. This leaves an effective number of two conditions, which is expressed by the number of degrees of freedom  $n_{df} = m - p = 2$  (2C-fit). Such a 2C-fit is less selective and the improvement of the data not as good as for the 5C-fit.

For testing, the constraint fits for the different reaction types were first applied to data produced with the small simulation program described in appendix B.2. In

figure A.1 (a), the  $\hat{S}$  distribution obtained for simulated "golden  $\pi^+\pi^-$ " data and a correct hypothesis is shown, together with the expected  $\chi^2$  function with 5 degrees of freedom. The corresponding confidence levels  $CL(\hat{S})$ , presented in figure A.1 (b), are distributed with equal probability between 0 and 1.

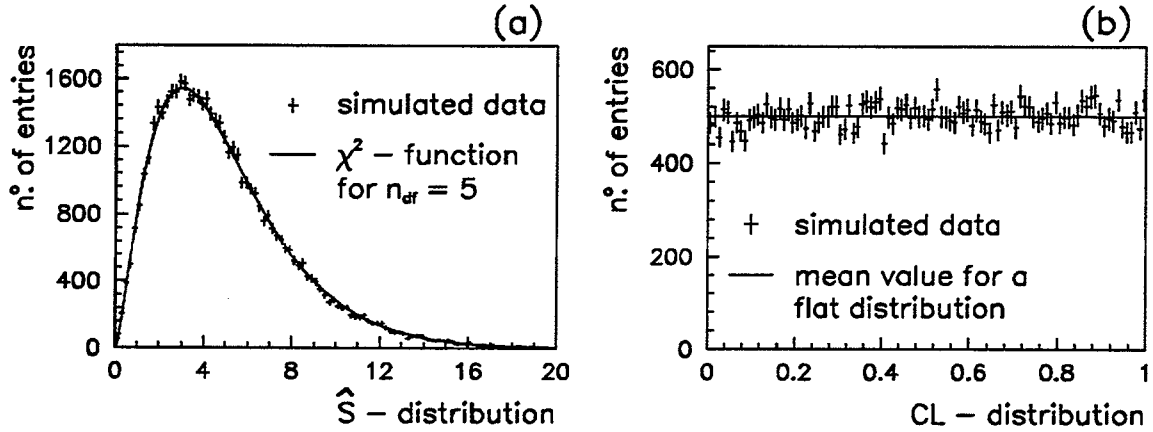


Figure A.1: The distributions of  $\hat{S}$  (a) and the confidence level  $CL(\hat{S})$  (b) for the kinematic 5C-fit of simulated "golden  $\pi^+\pi^-$ " events with the right hypothesis.

### A.3 Improvement of the Measured Variables

The effect of the constraint fit on the momentum and invariant mass resolution is analysed with the data sample MCT433, described in appendix B.1. MCT433 consists of "golden  $\pi^+\pi^-$ " events, produced with a trigger 433 simulation. For trigger 433, the average number of measured points along the secondary particle tracks is smaller than for trigger 233, and hence the momentum resolution is worse. The sample MCT233, where the simulated trigger is 233, could not be used, since the "true" (i.e. generated) values for the particle momenta were not written out to the mini-DST's.

The data sample MCT433 was passed through the PREFILTER and the 5CFIT (see section 4.2), and for the selected events the following deviations from the "true" values were determined:

$$\Delta P_i^{(\text{un})\text{corr}} = (\vec{P}^{\text{true}} - \vec{P}^{(\text{un})\text{corr}})_i \quad (i = x, y, z), \quad (\text{A.16})$$

$$\Delta P_{\text{T}}^{(\text{un})\text{corr}} = (\vec{P}^{\text{true}} - \vec{P}^{(\text{un})\text{corr}})_{\text{T}} \quad (\text{A.17})$$

$$\begin{aligned} &= \sqrt{(\Delta P_x^{(\text{un})\text{corr}})^2 + (\Delta P_y^{(\text{un})\text{corr}})^2}, \\ \Delta P^{(\text{un})\text{corr}} &= |\vec{P}^{\text{true}} - \vec{P}^{(\text{un})\text{corr}}| \quad (\text{A.18}) \\ &= \sqrt{(\Delta P_x^{(\text{un})\text{corr}})^2 + (\Delta P_y^{(\text{un})\text{corr}})^2 + (\Delta P_z^{(\text{un})\text{corr}})^2} \end{aligned}$$

and

$$\Delta M_{inv}(K_S^0, \pi^\pm)^{(un)corr} = M_{inv}(K_S^0, \pi^\pm)^{true} - M_{inv}(K_S^0, \pi^\pm)^{(un)corr}, \quad (A.19)$$

$$\Delta M_{inv}(K^\pm, \pi^\mp)^{(un)corr} = M_{inv}(K^\pm, \pi^\mp)^{true} - M_{inv}(K^\pm, \pi^\mp)^{(un)corr}, \quad (A.20)$$

$$\Delta M_{inv}(K_S^0, K^\pm)^{(un)corr} = M_{inv}(K_S^0, K^\pm)^{true} - M_{inv}(K_S^0, K^\pm)^{(un)corr}, \quad (A.21)$$

where the superscript "true" means the generated values, "corr" means the reconstructed values including the corrections from the 5CFIT and "uncorr" means the uncorrected reconstructed values.

In figure A.2 are shown the residuals for the neutral kaon momentum, where the uncorrected  $K_S^0$  momentum is calculated as

$$\vec{P}_{K_S^0}^{uncorr} = -\vec{P}_{K^\pm}^{uncorr} - \vec{P}_{\pi^\mp}^{uncorr}. \quad (A.22)$$

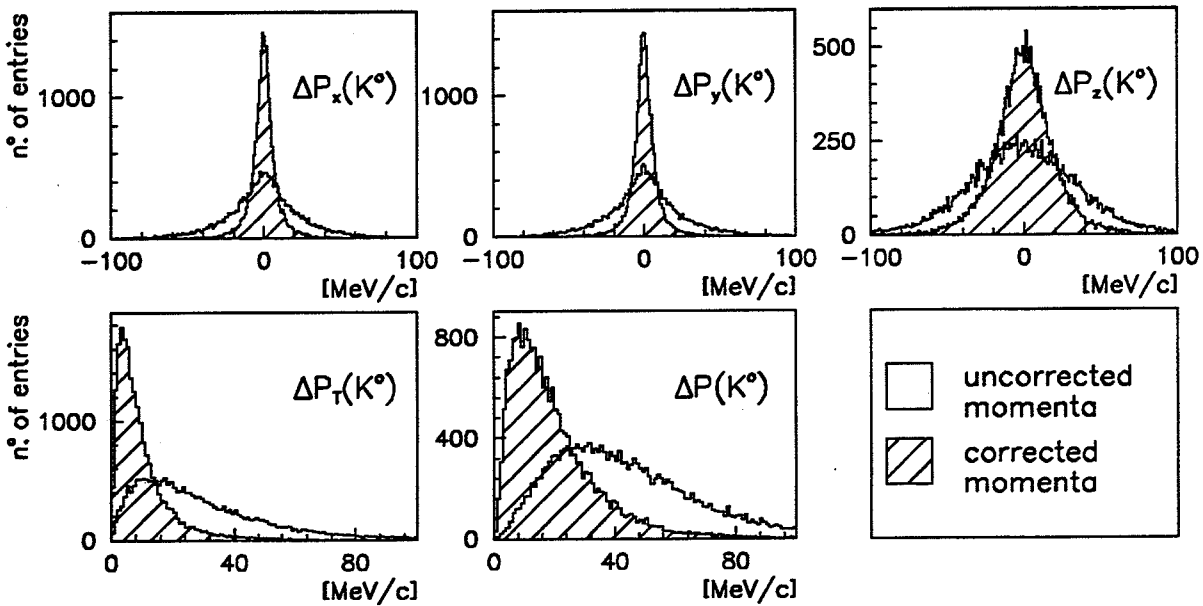


Figure A.2: Distributions of  $\Delta P_i^{(un)corr}$  ( $i = x, y, z$ ),  $\Delta P_T^{(un)corr}$  and  $\Delta P^{(un)corr}$  for the neutral kaon momentum  $\vec{P}_{K_S^0}$ .

The full width at half maximum (FWHM) for the distributions  $\Delta P_i^{(un)corr}$  ( $i = x, y, z$ ) are listed in table A.1. One sees that the FWHM values are reduced by a factor of almost two for the charged kaon and a factor of three for the neutral kaon due to the kinematic fit. The effect on the pion momenta is not that large.

The distributions of  $\Delta M_{inv}(i, j)^{(un)corr}$  and the scatter plots  $\Delta M_{inv}(K^\pm, \pi^\mp)^{(un)corr}$  versus  $\Delta M_{inv}(K_S^0, \pi^\pm)^{(un)corr}$  are presented in figure A.3. Table A.2 summarizes the corresponding FWHM values. Here, the improvement due to the kinematic fit is even larger. One gains a factor of 2.5 to 3 for the  $(K \pi)$  combinations and a factor of 5 for the  $(K\bar{K})$  pair.

FWHM of [Mev/c]	uncorrected momenta			corrected momenta			ratios		
	$\Delta P_x$	$\Delta P_y$	$\Delta P_z$	$\Delta P_x$	$\Delta P_y$	$\Delta P_z$	$\frac{\Delta P_x^{\text{uncorr}}}{\Delta P_x^{\text{corr}}}$	$\frac{\Delta P_y^{\text{uncorr}}}{\Delta P_y^{\text{corr}}}$	$\frac{\Delta P_z^{\text{uncorr}}}{\Delta P_z^{\text{corr}}}$
$K^\pm$	12.5	12.4	59.1	6.7	6.6	32.6	1.87	1.88	1.81
$\pi^\pm$	7.6	7.9	32.3	5.8	6.1	25.3	1.31	1.30	1.28
$K_S^0$	32.7	30.6	78.0	10.0	10.3	33.8	3.27	2.97	2.31
S1,S2	9.2	9.4	35.4	6.8	6.8	19.5	1.35	1.38	1.82

Table A.1: FWHM of the distributions  $\Delta P_i^{(\text{un})\text{corr}}$  ( $i = x, y, z$ ) and the improvement factors due to the constraint fit.

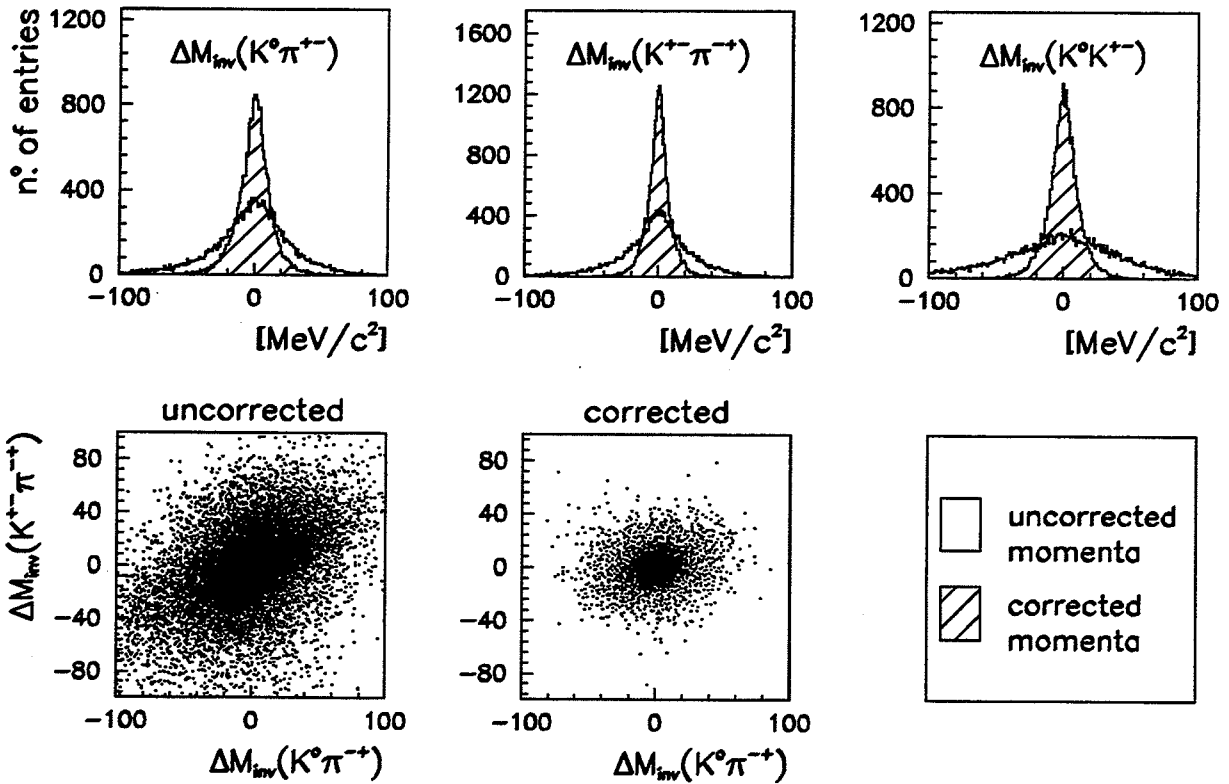


Figure A.3: Distributions of  $\Delta M(i, j)^{(\text{un})\text{corr}}$  and the scatter plots  $\Delta M_{inv}(K^\pm, \pi^\mp)^{(\text{un})\text{corr}}$  versus  $\Delta M_{inv}(K_S^0, \pi^\pm)^{(\text{un})\text{corr}}$ .

FWHM of	$\Delta M_{\text{inv}}^{\text{uncorr}}$ [MeV/c <sup>2</sup> ]	$\Delta M_{\text{inv}}^{\text{corr}}$ [MeV/c <sup>2</sup> ]	$\frac{\Delta M_{\text{inv}}^{\text{uncorr}}}{\Delta M_{\text{inv}}^{\text{corr}}}$
( $K_S^0 \pi^\pm$ )	46.3	18.7	2.48
( $K^\pm \pi^\mp$ )	34.6	11.8	2.93
( $K_S^0 K^\pm$ )	90.8	18.4	4.93

Table A.2: FWHM of the distributions  $\Delta M_{\text{inv}}(i, j)^{(\text{un})\text{corr}}$  and the improvement factors due to the constraint fit.

## B The Simulated Data Samples

The aim of this appendix is to describe the different simulated data samples used in the analysis. The data samples were produced with two programs:

1. CPGEANT, written by the CPLEAR offline group and based on GEANT 3 [44], is the dedicated simulation program for the CPLEAR experiment. With CPGEANT, the detector and trigger response for various event types can be simulated in great detail. An introduction to CPGEANT can be found in [45].
2. In order to test kinematic event selection algorithms, especially the constraint fits, a simpler simulation program was written with the following two advantages over CPGEANT:
  - The production of one event requires much less computer time and hence good statistics can be produced in a short time.
  - The generated data is ideal in the sense that detector and trigger inefficiencies are not simulated.

In the first part, the data samples produced with CPGEANT are described, while the second part explains the simplified simulation program in more detail.

### B.1 Data Samples Produced with CPGEANT

To estimate the reduction factors of the PREFILTER and the 5CFIT for the different  $K_S^0$  and  $K_L^0$  decay modes (see section 4.2.4.1), and in order to demonstrate the improvement of the momentum and invariant mass resolution due to the 5CFIT (see appendix A.3), a sample called **MCT433** is used. These data are produced with the following characteristics:

- The simulated trigger type is 433.
- Direct and resonant  $p\bar{p}$  annihilations are simulated. The percentages for the different annihilation channels, at the example of the  $K^+\pi^-\bar{K}^0$  final state, are given below:

$p\bar{p}$	$\rightarrow$	(direct)	$\rightarrow$	$K^+\pi^-\bar{K}^0$	BR = 33.1 % ,
$p\bar{p}$	$\rightarrow$	$K^{*0}\bar{K}^0$	$\rightarrow$	$(K^+\pi^-)\bar{K}^0$	BR = 30.6 % ,
$p\bar{p}$	$\rightarrow$	$K^+K^{*-}$	$\rightarrow$	$K^+(\pi^-\bar{K}^0)$	BR = 19.1 % ,
$p\bar{p}$	$\rightarrow$	$\pi^-a_2^+$	$\rightarrow$	$\pi^-(K^+\bar{K}^0)$	BR = 12.4 % ,
$p\bar{p}$	$\rightarrow$	$\pi^-a_0^+$	$\rightarrow$	$\pi^-(K^+\bar{K}^0)$	BR = 4.8 % .



- The possible neutral kaon decay modes are

$$K_S^0 \rightarrow \pi^+\pi^-, \quad K_L^0 \rightarrow \pi^\pm e^\mp \nu, \quad K_L^0 \rightarrow \pi^\pm \mu^\mp \nu \quad \text{and} \quad K_L^0 \rightarrow \pi^+\pi^-\pi^0.$$

- The probability distributions for the  $K_S^0$  and  $K_L^0$  decay eigentime are equal and constant.

The data sample MCT433 was generated at CERN. The events were written on separate mini-DST's for each  $K_S^0$  and  $K_L^0$  decay mode. Besides the reconstructed values, the mini-DST's also contained the "true" values for the particle momenta and vertex positions. At the time of this analysis, no similar data was available for trigger 233.

In the present evaluation of the detector and trigger acceptance (see section 4.4) and for a comparison of the real data sample with the corresponding simulated data (see section 4.2.3) the sample MCT233 is used.

- The simulated trigger is 233.
- Only direct annihilations  $p\bar{p} \rightarrow K^\mp \pi^\pm K^0(\bar{K}^0)$  are generated, according to an equal probability in the Dalitz-plot  $M_{inv}^2(K^\pm, \pi^\mp)$  versus  $M_{inv}^2(K^0, \pi^\pm)$ .
- The neutral kaon always decays into two pions:  $K^0 \rightarrow \pi^+\pi^-$ .

The data sample MCT233 was produced by the University of Ljubljana. The "true" values were not written on the mini-DST's.

## B.2 The Simplified Simulation Program

In the simplified program, the detector and trigger response is simulated with much less detail than in CPGEANT. The particles are not individually tracked through the detector, and their interaction with the detector material is only roughly approximated. Figure B.1 shows the flow diagram of the program. Some of the points are described in more detail below:

1. The  $p\bar{p}$  annihilation vertex is generated according to the distribution obtained from real data.
2. The branching ratios can be specified for the annihilation channels listed below (for the  $K^+\pi^-\bar{K}^0$  final state):

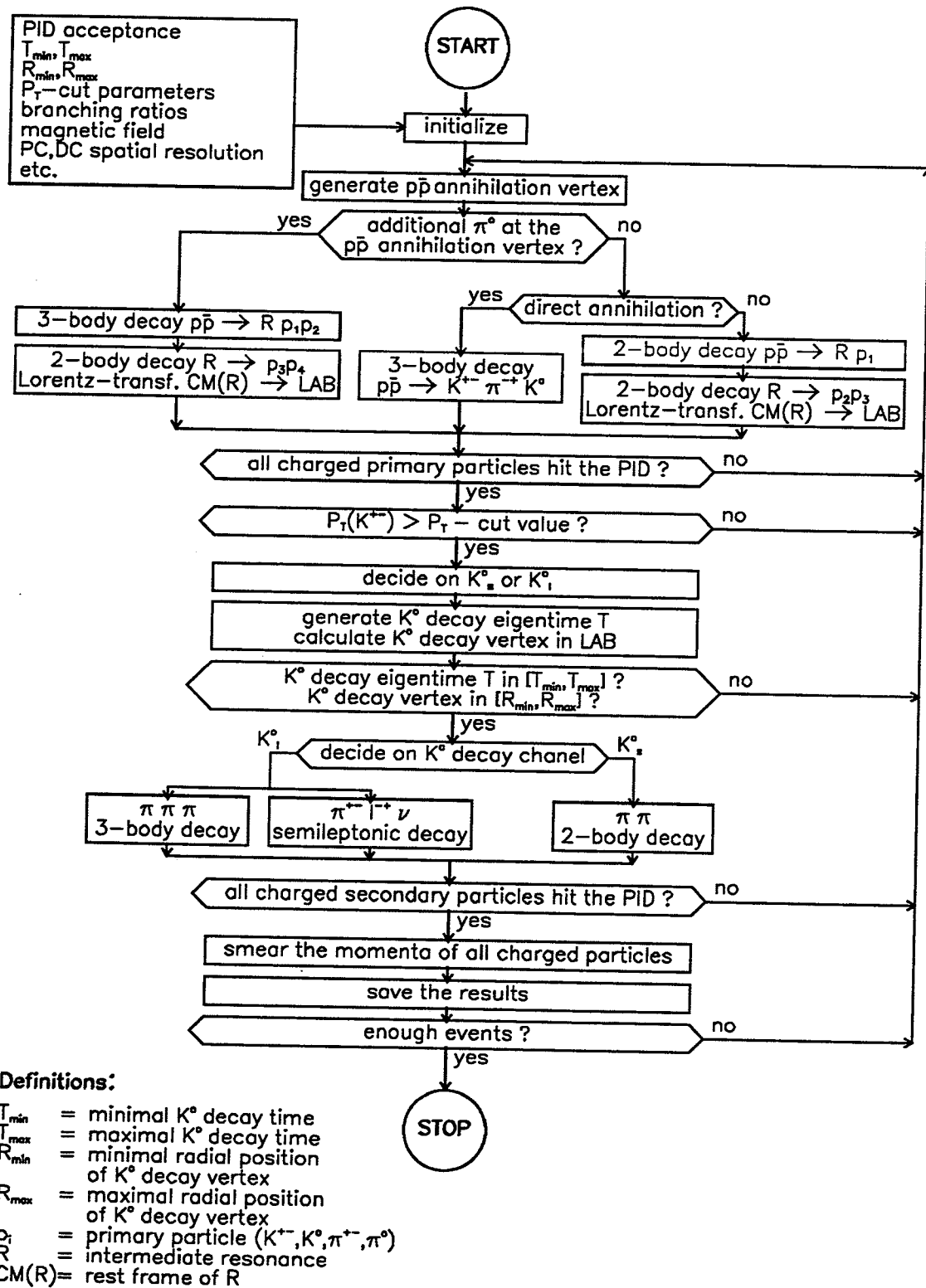


Figure B.1: Flow diagram for the simplified simulation program.

• for "golden" events:

$$\begin{array}{llll}
p\bar{p} & \rightarrow & (\text{direct}) & \rightarrow & K^+\pi^-\bar{K}^0 \\
p\bar{p} & \rightarrow & K^{*0}\bar{K}^0 & \rightarrow & (K^+\pi^-)\bar{K}^0 \\
p\bar{p} & \rightarrow & K^+K^{*-} & \rightarrow & K^+(\pi^-\bar{K}^0) \\
p\bar{p} & \rightarrow & \pi^-a_2^+ & \rightarrow & \pi^-(K^+\bar{K}^0)
\end{array}$$

• for events with an additional  $\pi^0$  at the  $p\bar{p}$  annihilation vertex:

$$\begin{array}{llll}
p\bar{p} & \rightarrow & K^+K^{*-}\pi^0 & \rightarrow & K^+(\pi^-\bar{K}^0)\pi^0 \\
p\bar{p} & \rightarrow & \bar{K}^0K^{*+}\pi^- & \rightarrow & \bar{K}^0(K^+\pi^0)\pi^- \\
p\bar{p} & \rightarrow & K^{*0}\bar{K}^0\pi^0 & \rightarrow & (K^+\pi^-)\bar{K}^0\pi^0 \\
p\bar{p} & \rightarrow & \bar{K}^{*0}K^+\pi^- & \rightarrow & (\bar{K}^0\pi^0)K^+\pi^-
\end{array}$$

3. All charged particles are required to hit the scintillator S2 of the PID. Hence, the particle tracks must intersect with a cylinder parallel to the  $z$ -axis, having a radius of 74.2 cm and a length of 210 cm.
4. For each event, a random  $p_T$ -cut value is generated according to a Gaussian distribution with  $\langle p_T \rangle = 400$  MeV/c and  $\sigma(p_T) = 40$  MeV/c.
5. The branching ratios for  $K_S^0$  and  $K_L^0$  decays can be specified for the decay modes

$$\begin{array}{llll}
K_S^0 \rightarrow \pi^+\pi^-, & K_S^0 \rightarrow \pi^0\pi^0, & \text{and} & \\
K_L^0 \rightarrow \pi^\pm e^\mp \nu, & K_L^0 \rightarrow \pi^\pm \mu^\mp \nu, & K_L^0 \rightarrow \pi^+\pi^-\pi^0, & K_L^0 \rightarrow \pi^0\pi^0\pi^0.
\end{array}$$

6. The three-body decays  $M \rightarrow p_1 p_2 p_3$  (except the semileptonic  $K_L^0$  decays) are generated with an equal probability in the Dalitz-plot  $M_{inv}^2(p_1 p_3)$  vs  $M_{inv}^2(p_1 p_2)$ .
7. The semileptonic decays are generated according to the (not normalized) density distribution  $\rho(T_\pi, T_l)$  given below [4]:

$$\begin{aligned}
\rho(T_\pi, T_l) = & -4(1 + \xi_+ T_\pi)^2 T_l^2 & (B.1) \\
& + 4T_l \left[ (1 + \xi_+ T_\pi)^2 (-T_\pi + W + U) + \xi_0 U P (1 + \xi_+ T_\pi) \right] \\
& + \left[ (1 + \xi_+ T_\pi)^2 (U T_\pi - (1 + U)^2) \right. \\
& \quad \left. + 2\xi_0 U P (1 + \xi_+ T_\pi) (T_\pi + P - W - U) \right. \\
& \quad \left. + \xi_0^2 U P^3 (T_\pi - U) \right],
\end{aligned}$$

where  $T_\pi(T_l)$  = kinetic energy of the pion (lepton),

$$\begin{aligned}
U &= \frac{m_l^2}{2m_{K^0}m_\pi}, \\
P &= \frac{m_{K^0}^2 - m_\pi^2}{2m_{K^0}m_\pi},
\end{aligned}$$

$$\begin{aligned}
W &= \frac{m_{K^0}^2 + m_\pi^2}{2m_{K^0}m_\pi}, \\
\xi_+ &= 2\lambda_+ \frac{m_{K^0}}{m_\pi}, \\
\xi_o &= 2(\lambda_o - \lambda_+) \frac{m_{K^0}}{m_\pi}, \\
\lambda_+ &= 0.030 \quad (0.034) \quad \text{for } \pi^\pm e^\mp \nu \quad (\pi^\pm \mu^\mp \nu) \text{ and} \\
\lambda_o &= 0.0 \quad (0.025) \quad \text{for } \pi^\pm e^\mp \nu \quad (\pi^\pm \mu^\mp \nu).
\end{aligned}$$

8. The momentum smearing for the charged tracks is calculated with the Gluckstern formulas [46] [47]:

$$\left(\frac{\sigma_{p_T}}{p_T}\right)^2 = \left(\frac{R \cdot \sigma_{r\varphi}}{L_p^2}\right)^2 \cdot \frac{720}{N+5} + \frac{1.43 \cdot R^2 K}{L_p} \left(\frac{p}{p_T}\right)^3, \quad (\text{B.2})$$

$$\sigma_\varphi^2 = \left(\frac{\sigma_{r\varphi}}{L_p}\right)^2 \cdot \frac{192}{N+4.9} + 0.229 \cdot K L_p \left(\frac{p}{p_T}\right)^3, \quad (\text{B.3})$$

$$\sigma_\theta^2 = \left(\frac{\sigma_z}{L}\right)^2 \left(\frac{p_T}{p}\right)^2 \cdot \frac{12N}{(N+1)(N+2)} + \frac{1.11 \cdot KL}{3}, \quad (\text{B.4})$$

with

$$R = \frac{p_T}{0.3B},$$

$$K = \left(\frac{0.015}{p \cdot \beta}\right)^2 \cdot \frac{1}{X_o},$$

where

- $\sigma_{p_T}$  = transverse momentum resolution,
- $\sigma_\varphi, \sigma_\theta$  = azimuthal and polar angular momentum resolutions  
( $p_x = p_T \cdot \cos \varphi$ ;  $p_y = p_T \cdot \sin \varphi$ ;  $p_z = p_T \cdot \cot \theta$ ),
- $\sigma_{r\varphi}, \sigma_z$  = tracking chamber resolutions in  $r\varphi$  (wires) and  $z$  (strips),
- $p, p_T$  = particle momentum and component in transverse plane at the production vertex,
- $L, L_p$  = track length in space and in transverse plane between first and last measured point,
- $N+1$  = number of measured points along the particle track,
- $R$  = bending radius of the particle track,
- $B$  = magnetic field strength,
- $\beta$  = particle velocity  $v/c$  and
- $X_o$  = thickness of the traversed material in radiation lengths.

Lengths are given in meter, momentum in GeV/c and the field strength in tesla. The first term in the three equations describes the momentum smearing due to the measurement errors. The second term takes account of the multiple scattering.

In order to determine the covariance matrix for the constraint fits, no correlation between the parameters  $p_T$ ,  $\varphi$  and  $\theta$  is assumed, i.e.

$$V(p_T, \varphi, \theta) = \begin{pmatrix} \sigma_{p_T}^2 & 0 & 0 \\ 0 & \sigma_\varphi^2 & 0 \\ 0 & 0 & \sigma_\theta^2 \end{pmatrix}. \quad (\text{B.5})$$

The covariance matrix for the cartesian components  $p_x, p_y, p_z$  is then obtained from

$$V(p_x, p_y, p_z) = T V(p_T, \varphi, \theta) T^T \quad (\text{B.6})$$

with

$$T = \begin{pmatrix} \frac{\partial p_x}{\partial p_T} & \frac{\partial p_x}{\partial \varphi} & \frac{\partial p_x}{\partial \theta} \\ \frac{\partial p_y}{\partial p_T} & \frac{\partial p_y}{\partial \varphi} & \frac{\partial p_y}{\partial \theta} \\ \frac{\partial p_z}{\partial p_T} & \frac{\partial p_z}{\partial \varphi} & \frac{\partial p_z}{\partial \theta} \end{pmatrix} = \begin{pmatrix} \cos \varphi & -p_T \sin \varphi & 0 \\ \sin \varphi & p_T \cos \varphi & 0 \\ \cot \theta & 0 & -p_T / \sin^2 \theta \end{pmatrix}. \quad (\text{B.7})$$

## C The Amplitudes Contributing to the Reaction $p\bar{p} \rightarrow K\bar{K}\pi$

In section 4.3.1, a theoretical model developed by Conforto et al. [35],[36] for the description of  $p\bar{p}$  annihilations of the type  $p\bar{p} \rightarrow K\bar{K}\pi$  is presented and its extension to include p-wave annihilations is discussed. The transition matrix elements  $A_I^{JPC}$  between states with well defined quantum numbers for the angular momentum  $J$ , the parity  $P$ , the charge conjugation  $C$  and the isospin  $I$  are decomposed as

$$\begin{aligned} A_I^{JPC} &\equiv \langle K\bar{K}\pi(JPCI) | S | p\bar{p}(JPCI) \rangle \\ &= \sum_k \rho_k^{JPCI} e^{i\varphi_k^{JPCI}} \cdot C_k^{JPCI}, \end{aligned}$$

where each contribution  $C_k^{JPCI}$  is the product of a spin-parity factor  $A_{ijk}^{JP}$  and a form-factor  $A_{jk}^F$ , listed in table 4.9 and 4.10, respectively. Each matrix element  $A_I^{JPC}$  corresponds to an initial protonium state with quantum numbers  $(2I+1)(2S+1)L_J$ , where  $S$  is the spin and  $L$  the orbital angular momentum.

In this appendix, the contributions  $C_k^{JPCI}$  to the matrix elements  $A_I^{JPC}$  are given for the final states  $K\bar{K}\pi=K^+\bar{K}^0\pi^-$  and  $K\bar{K}\pi=K^0\bar{K}^-\pi^+$ , taking into account the restrictions imposed by the symmetry properties of  $A_I^{JPC}$  (see table 4.8).

### C.1 Contributions to $A_0^{0-+}$ (initial $p\bar{p}$ state is $^1S_0$ )

$K\pi (\bar{K}\pi)$   $l_{K\pi} (l_{\bar{K}\pi}) = 0$   $L_{\bar{K}} (L_K) = 0$   $I_{K\pi} (I_{\bar{K}\pi}) = \frac{1}{2}$  s-wave scattering

$$C_1^{0-+0} = \frac{1}{1 - ia_{1/2}\sqrt{-p_{K\pi}^2/4}} + \frac{1}{1 - ia_{1/2}\sqrt{-p_{\bar{K}\pi}^2/4}}$$

$l_{K\pi} (l_{\bar{K}\pi}) = 1$   $L_{\bar{K}} (L_K) = 1$   $I_{K\pi} (I_{\bar{K}\pi}) = \frac{1}{2}$   $K^*$  - resonance

$$C_2^{0-+0} = \frac{P_{K\pi}^\mu \bar{P}_{\bar{K}\mu}}{s_{K\pi} - m_{K^*}^2 + im_{K^*}\Gamma_{K^*}} + \frac{P_{\bar{K}\pi}^\mu \bar{P}_{K\mu}}{s_{\bar{K}\pi} - m_{K^*}^2 + im_{K^*}\Gamma_{K^*}}$$

$l_{K\pi} (l_{\bar{K}\pi}) = 2$   $L_{\bar{K}} (L_K) = 2$   $I_{K\pi} (I_{\bar{K}\pi}) = \frac{1}{2}$  d-wave scattering

$$C_3^{0-+0} = \frac{T_{K\pi}^{\mu\nu} T_{\bar{K}\mu\nu}}{1 - ic_{1/2}\sqrt{-p_{K\pi}^2/4}} + \frac{T_{\bar{K}\pi}^{\mu\nu} T_{K\mu\nu}}{1 - ic_{1/2}\sqrt{-p_{\bar{K}\pi}^2/4}}$$

$K\bar{K}$   $l_{K\bar{K}} = 0$   $L_\pi = 0$   $a_0$  - resonance

$$C_4^{0-+0} = \frac{1}{s_{K\bar{K}} - m_{a_0}^2 + i\sqrt{-p_{K\bar{K}}^2} \gamma}$$

$$l_{\overline{K}\overline{K}} = 2 \quad L_\pi = 2 \quad a_2 - \text{resonance}$$

$$C_5^{0-+0} = \frac{T_{\overline{K}\overline{K}}^{\mu\nu} T_{\pi\mu\nu}}{s_{\overline{K}\overline{K}} - m_{a_2^\pm}^2 + im_{a_2^\pm} \Gamma_{a_2^\pm}}$$

## C.2 Contributions to $A_1^{0-+}$ (initial $p\overline{p}$ state is $^3S_0$ )

$K\pi (\overline{K}\pi)$   $l_{K\pi} (l_{\overline{K}\pi}) = 0$   $L_{\overline{K}} (L_K) = 0$   $I_{K\pi} (I_{\overline{K}\pi}) = \frac{1}{2}$  s-wave scattering

$$C_1^{0-+1} = \frac{1}{1 - ia_{1/2} \sqrt{-p_{K\pi}^2/4}} - \frac{1}{1 - ia_{1/2} \sqrt{-p_{\overline{K}\pi}^2/4}}$$

$l_{K\pi} (l_{\overline{K}\pi}) = 0$   $L_{\overline{K}} (L_K) = 0$   $I_{K\pi} (I_{\overline{K}\pi}) = \frac{3}{2}$  s-wave scattering

$$C_2^{0-+1} = \frac{1}{1 - ia_{3/2} \sqrt{-p_{K\pi}^2/4}} - \frac{1}{1 - ia_{3/2} \sqrt{-p_{\overline{K}\pi}^2/4}}$$

$l_{K\pi} (l_{\overline{K}\pi}) = 1$   $L_{\overline{K}} (L_K) = 1$   $I_{K\pi} (I_{\overline{K}\pi}) = \frac{1}{2}$   $K^*$  - resonance

$$C_3^{0-+1} = \frac{P_{K\pi}^\mu \overline{P}_{\overline{K}\mu}}{s_{K\pi} - m_{K^*}^2 + im_{K^*} \Gamma_{K^*}} - \frac{P_{\overline{K}\pi}^\mu \overline{P}_{K\mu}}{s_{\overline{K}\pi} - m_{K^*}^2 + im_{K^*} \Gamma_{K^*}}$$

$l_{K\pi} (l_{\overline{K}\pi}) = 2$   $L_{\overline{K}} (L_K) = 2$   $I_{K\pi} (I_{\overline{K}\pi}) = \frac{1}{2}$  d-wave scattering

$$C_4^{0-+1} = \frac{T_{K\pi}^{\mu\nu} T_{\overline{K}\mu\nu}}{1 - ic_{1/2} \sqrt{-p_{K\pi}^2/4}} - \frac{T_{\overline{K}\pi}^{\mu\nu} T_{K\mu\nu}}{1 - ic_{1/2} \sqrt{-p_{\overline{K}\pi}^2/4}}$$

$l_{K\pi} (l_{\overline{K}\pi}) = 2$   $L_{\overline{K}} (L_K) = 2$   $I_{K\pi} (I_{\overline{K}\pi}) = \frac{3}{2}$  d-wave scattering

$$C_5^{0-+1} = \frac{T_{K\pi}^{\mu\nu} T_{\overline{K}\mu\nu}}{1 - ic_{3/2} \sqrt{-p_{K\pi}^2/4}} - \frac{T_{\overline{K}\pi}^{\mu\nu} T_{K\mu\nu}}{1 - ic_{3/2} \sqrt{-p_{\overline{K}\pi}^2/4}}$$

$\overline{K}\overline{K}$   $l_{\overline{K}\overline{K}} = 1$   $L_\pi = 1$  p-wave scattering

$$C_6^{0-+1} = \frac{P_{\overline{K}\overline{K}}^\mu \overline{P}_{\pi\mu}}{1 - ib_1 \sqrt{-p_{\overline{K}\overline{K}}^2/4}}$$

## C.3 Contributions to $A_0^{1--}$ (initial $p\overline{p}$ state is $^3S_0$ )

$K\pi (\overline{K}\pi)$   $l_{K\pi} (l_{\overline{K}\pi}) = 1$   $L_{\overline{K}} (L_K) = 1$   $I_{K\pi} (I_{\overline{K}\pi}) = \frac{1}{2}$   $K^*$  - resonance

$$C_1^{1--0} = \varepsilon^{\mu\nu\rho\sigma} P_K^\nu P_\pi^\rho P_{\bar{K}}^\sigma \left( \frac{1}{s_{K\pi} - m_{K^*}^2 + im_{K^*}\Gamma_{K^*}} + \frac{1}{s_{\bar{K}\pi} - m_{\bar{K}^*}^2 + im_{\bar{K}^*}\Gamma_{\bar{K}^*}} \right)$$

$$l_{K\pi}(l_{\bar{K}\pi}) = 2 \quad L_{\bar{K}}(L_K) = 2 \quad I_{K\pi}(I_{\bar{K}\pi}) = \frac{1}{2} \quad \text{d-wave scattering}$$

$$C_2^{1--0} = \varepsilon^{\mu\nu\rho\sigma} P_K^\nu P_\pi^\rho P_{\bar{K}}^\sigma \left( \frac{P_{K\pi}^\tau \bar{P}_{\bar{K}\tau}}{1 - ic_{1/2}\sqrt{-p_{K\pi}^2/4}} + \frac{P_{\bar{K}\pi}^\tau \bar{P}_{K\tau}}{1 - ic_{1/2}\sqrt{-p_{\bar{K}\pi}^2/4}} \right)$$

$$\mathbf{K\bar{K}} \quad l_{K\bar{K}} = 1 \quad L_\pi = 1 \quad \text{p-wave scattering}$$

$$C_3^{1--0} = \frac{\varepsilon^{\mu\nu\rho\sigma} P_K^\nu P_{\bar{K}}^\rho P_\pi^\sigma}{1 - ib_1\sqrt{-p_{K\bar{K}}^2/4}}$$

#### C.4 Contributions to $A_1^{1--}$ (initial $p\bar{p}$ state is ${}^{33}S_1$ )

$$\mathbf{K\pi}(\mathbf{K\bar{\pi}}) \quad l_{K\pi}(l_{\bar{K}\pi}) = 1 \quad L_{\bar{K}}(L_K) = 1 \quad I_{K\pi}(I_{\bar{K}\pi}) = \frac{1}{2} \quad \mathbf{K^* - resonance}$$

$$C_1^{1--1} = \varepsilon^{\mu\nu\rho\sigma} P_K^\nu P_\pi^\rho P_{\bar{K}}^\sigma \left( \frac{1}{s_{K\pi} - m_{K^*}^2 + im_{K^*}\Gamma_{K^*}} - \frac{1}{s_{\bar{K}\pi} - m_{\bar{K}^*}^2 + im_{\bar{K}^*}\Gamma_{\bar{K}^*}} \right)$$

$$l_{K\pi}(l_{\bar{K}\pi}) = 2 \quad L_{\bar{K}}(L_K) = 2 \quad I_{K\pi}(I_{\bar{K}\pi}) = \frac{1}{2} \quad \text{d-wave scattering}$$

$$C_2^{1--1} = \varepsilon^{\mu\nu\rho\sigma} P_K^\nu P_\pi^\rho P_{\bar{K}}^\sigma \left( \frac{P_{K\pi}^\tau \bar{P}_{\bar{K}\tau}}{1 - ic_{1/2}\sqrt{-p_{K\pi}^2/4}} - \frac{P_{\bar{K}\pi}^\tau \bar{P}_{K\tau}}{1 - ic_{1/2}\sqrt{-p_{\bar{K}\pi}^2/4}} \right)$$

$$l_{K\pi}(l_{\bar{K}\pi}) = 2 \quad L_{\bar{K}}(L_K) = 2 \quad I_{K\pi}(I_{\bar{K}\pi}) = \frac{3}{2} \quad \text{d-wave scattering}$$

$$C_3^{1--1} = \varepsilon^{\mu\nu\rho\sigma} P_K^\nu P_\pi^\rho P_{\bar{K}}^\sigma \left( \frac{P_{K\pi}^\tau \bar{P}_{\bar{K}\tau}}{1 - ic_{3/2}\sqrt{-p_{K\pi}^2/4}} - \frac{P_{\bar{K}\pi}^\tau \bar{P}_{K\tau}}{1 - ic_{3/2}\sqrt{-p_{\bar{K}\pi}^2/4}} \right)$$

$$\mathbf{K\bar{K}} \quad l_{K\bar{K}} = 2 \quad L_\pi = 2 \quad \mathbf{a_2 - resonance}$$

$$C_4^{1--1} = \frac{\varepsilon^{\mu\nu\rho\sigma} P_K^\nu P_{\bar{K}}^\rho P_\pi^\sigma (P_{K\bar{K}}^\tau \bar{P}_{\pi\tau})}{s_{K\bar{K}} - m_{a_2^\pm}^2 + im_{a_2^\pm}\Gamma_{a_2^\pm}}$$

#### C.5 Contributions to $A_0^{1+-}$ (initial $p\bar{p}$ state is ${}^{11}P_1$ )

$$\mathbf{K\pi}(\mathbf{K\bar{\pi}}) \quad l_{K\pi}(l_{\bar{K}\pi}) = 0 \quad L_{\bar{K}}(L_K) = 1 \quad I_{K\pi}(I_{\bar{K}\pi}) = \frac{1}{2} \quad \text{s-wave scattering}$$



$$C_1^{1+-0} = \frac{\bar{P}_{\bar{K}}^\mu}{1 - ia_{1/2}\sqrt{-p_{K\pi}^2/4}} - \frac{\bar{P}_K^\mu}{1 - ia_{1/2}\sqrt{-p_{K\pi}^2/4}}$$

$$l_{K\pi}(l_{\bar{K}\pi}) = 1 \quad L_{\bar{K}}(L_K) = 0 \quad I_{K\pi}(I_{\bar{K}\pi}) = \frac{1}{2} \quad \mathbf{K^* - resonance}$$

$$C_2^{1+-0} = \frac{P_{K\pi}^\mu}{s_{K\pi} - m_{K^*}^2 + im_{K^*}\Gamma_{K^*}} - \frac{P_{\bar{K}\pi}^\mu}{s_{\bar{K}\pi} - m_{K^*}^2 + im_{K^*}\Gamma_{K^*}}$$

$$l_{K\pi}(l_{\bar{K}\pi}) = 1 \quad L_{\bar{K}}(L_K) = 2 \quad I_{K\pi}(I_{\bar{K}\pi}) = \frac{1}{2} \quad \mathbf{K^* - resonance}$$

$$C_3^{1+-0} = \frac{T_{\bar{K}}^{\mu\nu} P_{K\pi\nu}}{s_{K\pi} - m_{K^*}^2 + im_{K^*}\Gamma_{K^*}} - \frac{T_K^{\mu\nu} P_{\bar{K}\pi\nu}}{s_{\bar{K}\pi} - m_{K^*}^2 + im_{K^*}\Gamma_{K^*}}$$

$$l_{K\pi}(l_{\bar{K}\pi}) = 2 \quad L_{\bar{K}}(L_K) = 1 \quad I_{K\pi}(I_{\bar{K}\pi}) = \frac{1}{2} \quad \mathbf{d-wave scattering}$$

$$C_4^{1+-0} = \frac{T_{K\pi}^{\mu\nu} \bar{P}_{\bar{K}\nu}}{1 - ic_{1/2}\sqrt{-p_{K\pi}^2/4}} - \frac{T_{\bar{K}\pi}^{\mu\nu} \bar{P}_{K\nu}}{1 - ic_{1/2}\sqrt{-p_{K\pi}^2/4}}$$

$$\mathbf{K\bar{K}} \quad l_{K\bar{K}} = 1 \quad L_\pi = 0 \quad \mathbf{p-wave scattering}$$

$$C_5^{1+-0} = \frac{P_{K\bar{K}}^\mu}{1 - ib_1\sqrt{-p_{K\bar{K}}^2/4}}$$

$$l_{K\bar{K}} = 1 \quad L_\pi = 2 \quad \mathbf{p-wave scattering}$$

$$C_6^{1+-0} = \frac{T_\pi^{\mu\nu} P_{K\bar{K}\nu}}{1 - ib_1\sqrt{-p_{K\bar{K}}^2/4}}$$

## C.6 Contributions to $A_1^{1+-}$ (initial $p\bar{p}$ state is $^3P_1$ )

$$\mathbf{K\pi}(\bar{\mathbf{K}}\pi) \quad l_{K\pi}(l_{\bar{K}\pi}) = 0 \quad L_{\bar{K}}(L_K) = 1 \quad I_{K\pi}(I_{\bar{K}\pi}) = \frac{1}{2} \quad \mathbf{s-wave scattering}$$

$$C_1^{1+-1} = \frac{\bar{P}_{\bar{K}}^\mu}{1 - ia_{1/2}\sqrt{-p_{K\pi}^2/4}} + \frac{\bar{P}_K^\mu}{1 - ia_{1/2}\sqrt{-p_{K\pi}^2/4}}$$

$$l_{K\pi}(l_{\bar{K}\pi}) = 0 \quad L_{\bar{K}}(L_K) = 1 \quad I_{K\pi}(I_{\bar{K}\pi}) = \frac{3}{2} \quad \mathbf{s-wave scattering}$$

$$C_2^{1+-1} = \frac{\bar{P}_{\bar{K}}^\mu}{1 - ia_{3/2}\sqrt{-p_{K\pi}^2/4}} + \frac{\bar{P}_K^\mu}{1 - ia_{3/2}\sqrt{-p_{K\pi}^2/4}}$$

$$l_{K\pi}(l_{\bar{K}\pi}) = 1 \quad L_{\bar{K}}(L_K) = 0 \quad I_{K\pi}(I_{\bar{K}\pi}) = \frac{1}{2} \quad \mathbf{K^* - resonance}$$

$$C_3^{1+-1} = \frac{P_{\mu}^{K\pi}}{s_{K\pi} - m_{K^*}^2 + im_{K^*}\Gamma_{K^*}} + \frac{P_{\mu}^{\bar{K}\pi}}{s_{\bar{K}\pi} - m_{\bar{K}^*}^2 + im_{\bar{K}^*}\Gamma_{\bar{K}^*}}$$

$$l_{K\pi}(l_{\bar{K}\pi}) = 1 \quad L_{\bar{K}}(L_K) = 2 \quad I_{K\pi}(I_{\bar{K}\pi}) = \frac{1}{2} \quad K^* \text{ - resonance}$$

$$C_4^{1+-1} = \frac{T_{\bar{K}}^{\mu\nu} P_{K\pi\nu}}{s_{K\pi} - m_{K^*}^2 + im_{K^*}\Gamma_{K^*}} + \frac{T_K^{\mu\nu} P_{\bar{K}\pi\nu}}{s_{\bar{K}\pi} - m_{\bar{K}^*}^2 + im_{\bar{K}^*}\Gamma_{\bar{K}^*}}$$

$$l_{K\pi}(l_{\bar{K}\pi}) = 2 \quad L_{\bar{K}}(L_K) = 1 \quad I_{K\pi}(I_{\bar{K}\pi}) = \frac{1}{2} \quad \text{d-wave scattering}$$

$$C_5^{1+-1} = \frac{T_{K\pi}^{\mu\nu} \bar{P}_{\bar{K}\nu}}{1 - ic_{1/2}\sqrt{-p_{K\pi}^2/4}} + \frac{T_{K\pi}^{\mu\nu} \bar{P}_{\bar{K}\nu}}{1 - ic_{1/2}\sqrt{-p_{\bar{K}\pi}^2/4}}$$

$$l_{K\pi}(l_{\bar{K}\pi}) = 2 \quad L_{\bar{K}}(L_K) = 1 \quad I_{K\pi}(I_{\bar{K}\pi}) = \frac{3}{2} \quad \text{d-wave scattering}$$

$$C_6^{1+-1} = \frac{T_{K\pi}^{\mu\nu} \bar{P}_{\bar{K}\nu}}{1 - ic_{3/2}\sqrt{-p_{K\pi}^2/4}} + \frac{T_{K\pi}^{\mu\nu} \bar{P}_{\bar{K}\nu}}{1 - ic_{3/2}\sqrt{-p_{\bar{K}\pi}^2/4}}$$

$$K\bar{K} \quad l_{K\bar{K}} = 0 \quad L_{\pi} = 1 \quad a_0 \text{ - resonance}$$

$$C_7^{1+-1} = \frac{\bar{P}_{\pi}^{\mu}}{s_{K\bar{K}} - m_{a_0}^2 + i\sqrt{-p_{K\bar{K}}^2} \gamma}$$

$$l_{K\bar{K}} = 2 \quad L_{\pi} = 1 \quad a_2 \text{ - resonance}$$

$$C_8^{1+-1} = \frac{T_{K\bar{K}}^{\mu\nu} \bar{P}_{\pi\nu}}{s_{K\bar{K}} - m_{a_2^{\pm}}^2 + im_{a_2^{\pm}}\Gamma_{a_2^{\pm}}}$$

### C.7 Contributions to $A_0^{1++}$ (initial $p\bar{p}$ state is $^{13}P_1$ )

The contributions are the same as for  $A_1^{1+-}$  (initial  $p\bar{p}$  state is  $^{31}P_1$ ):

$$C_k^{1++0} = C_k^{1+-1} \quad (k = 1, \dots, 8). \quad (C.1)$$

### C.8 Contributions to $A_1^{1++}$ (initial $p\bar{p}$ state is $^{33}P_1$ )

The contributions are the same as for  $A_0^{1+-}$  (initial  $p\bar{p}$  state is  $^{11}P_1$ ):

$$C_k^{1++1} = C_k^{1+-0} \quad (k = 1, \dots, 6). \quad (C.2)$$

### C.9 Contributions to $A_0^{2++}$ (initial $p\bar{p}$ state is $^{13}P_2$ )

$K\pi (\bar{K}\pi)$   $l_{K\pi} (l_{\bar{K}\pi}) = 1$   $L_{\bar{K}} (L_K) = 2$   $I_{K\pi} (I_{\bar{K}\pi}) = 12$   $K^*$  - resonance

$$C_1^{2++0} = \frac{\varepsilon^{\mu\tau\rho\sigma} P_K^\tau P_\pi^\rho P_{\bar{K}}^\sigma \cdot \bar{P}_{\bar{K}}^\nu + \bar{P}_{\bar{K}}^\mu \cdot \varepsilon^{\nu\tau\rho\sigma} P_K^\tau P_\pi^\rho P_{\bar{K}}^\sigma}{s_{K\pi} - m_{K^*}^2 + im_{K^*}\Gamma_{K^*}}$$

$$+ \frac{\varepsilon^{\mu\tau\rho\sigma} P_{\bar{K}}^\tau P_\pi^\rho P_K^\sigma \cdot \bar{P}_{\bar{K}}^\nu + \bar{P}_{\bar{K}}^\mu \cdot \varepsilon^{\nu\tau\rho\sigma} P_{\bar{K}}^\tau P_\pi^\rho P_K^\sigma}{s_{\bar{K}\pi} - m_{\bar{K}^*}^2 + im_{\bar{K}^*}\Gamma_{\bar{K}^*}}$$

$l_{K\pi} (l_{\bar{K}\pi}) = 2$   $L_{\bar{K}} (L_K) = 1$   $I_{K\pi} (I_{\bar{K}\pi}) = \frac{1}{2}$   $d$ -wave scattering

$$C_2^{2++0} = \frac{\varepsilon^{\mu\tau\rho\sigma} P_K^\tau P_\pi^\rho P_{\bar{K}}^\sigma \cdot P_{K\pi}^\nu + P_{K\pi}^\mu \cdot \varepsilon^{\nu\tau\rho\sigma} P_K^\tau P_\pi^\rho P_{\bar{K}}^\sigma}{1 - ic_{1/2}\sqrt{-p_{K\pi}^2}/4}$$

$$+ \frac{\varepsilon^{\mu\tau\rho\sigma} P_{\bar{K}}^\tau P_\pi^\rho P_K^\sigma \cdot P_{\bar{K}\pi}^\nu + P_{\bar{K}\pi}^\mu \cdot \varepsilon^{\nu\tau\rho\sigma} P_{\bar{K}}^\tau P_\pi^\rho P_K^\sigma}{1 - ic_{1/2}\sqrt{-p_{\bar{K}\pi}^2}/4}$$

$K\bar{K}$   $l_{K\bar{K}} = 2$   $L_\pi = 1$   $a_2$  - resonance

$$C_3^{2++0} = \frac{\varepsilon^{\mu\tau\rho\sigma} P_K^\tau P_\pi^\rho P_{\bar{K}}^\sigma \cdot P_{K\bar{K}}^\nu + P_{K\bar{K}}^\mu \cdot \varepsilon^{\nu\tau\rho\sigma} P_K^\tau P_\pi^\rho P_{\bar{K}}^\sigma}{s_{K\bar{K}} - m_{a_2^\pm}^2 + im_{a_2^\pm}\Gamma_{a_2^\pm}}$$

### C.10 Contributions to $A_1^{2++}$ (initial $p\bar{p}$ state is $^{33}P_2$ )

$K\pi (\bar{K}\pi)$   $l_{K\pi} (l_{\bar{K}\pi}) = 1$   $L_{\bar{K}} (L_K) = 2$   $I_{K\pi} (I_{\bar{K}\pi}) = \frac{1}{2}$   $K^*$  - resonance

$$C_1^{2++1} = \frac{\varepsilon^{\mu\tau\rho\sigma} P_K^\tau P_\pi^\rho P_{\bar{K}}^\sigma \cdot \bar{P}_{\bar{K}}^\nu + \bar{P}_{\bar{K}}^\mu \cdot \varepsilon^{\nu\tau\rho\sigma} P_K^\tau P_\pi^\rho P_{\bar{K}}^\sigma}{s_{K\pi} - m_{K^*}^2 + im_{K^*}\Gamma_{K^*}}$$

$$- \frac{\varepsilon^{\mu\tau\rho\sigma} P_{\bar{K}}^\tau P_\pi^\rho P_K^\sigma \cdot \bar{P}_{\bar{K}}^\nu + \bar{P}_{\bar{K}}^\mu \cdot \varepsilon^{\nu\tau\rho\sigma} P_{\bar{K}}^\tau P_\pi^\rho P_K^\sigma}{s_{\bar{K}\pi} - m_{\bar{K}^*}^2 + im_{\bar{K}^*}\Gamma_{\bar{K}^*}}$$

$l_{K\pi} (l_{\bar{K}\pi}) = 2$   $L_{\bar{K}} (L_K) = 1$   $I_{K\pi} (I_{\bar{K}\pi}) = \frac{1}{2}$   $d$ -wave scattering

$$C_2^{2++1} = \frac{\varepsilon^{\mu\tau\rho\sigma} P_K^\tau P_\pi^\rho P_{\bar{K}}^\sigma \cdot P_{K\pi}^\nu + P_{K\pi}^\mu \cdot \varepsilon^{\nu\tau\rho\sigma} P_K^\tau P_\pi^\rho P_{\bar{K}}^\sigma}{1 - ic_{1/2}\sqrt{-p_{K\pi}^2}/4}$$

$$- \frac{\varepsilon^{\mu\tau\rho\sigma} P_{\bar{K}}^\tau P_\pi^\rho P_K^\sigma \cdot P_{\bar{K}\pi}^\nu + P_{\bar{K}\pi}^\mu \cdot \varepsilon^{\nu\tau\rho\sigma} P_{\bar{K}}^\tau P_\pi^\rho P_K^\sigma}{1 - ic_{1/2}\sqrt{-p_{\bar{K}\pi}^2}/4}$$

$l_{K\pi} (l_{\bar{K}\pi}) = 2$   $L_{\bar{K}} (L_K) = 1$   $I_{K\pi} (I_{\bar{K}\pi}) = \frac{3}{2}$   $d$ -wave scattering

$$C_3^{2++1} = \frac{\varepsilon^{\mu\tau\rho\sigma} P_K^\tau P_\pi^\rho P_{\bar{K}}^\sigma \cdot P_{K\pi}^\nu + P_{K\pi}^\mu \cdot \varepsilon^{\nu\tau\rho\sigma} P_K^\tau P_\pi^\rho P_{\bar{K}}^\sigma}{1 - ic_{3/2} \sqrt{-p_{K\pi}^2/4}} - \frac{\varepsilon^{\mu\tau\rho\sigma} P_{\bar{K}}^\tau P_\pi^\rho P_K^\sigma \cdot P_{\bar{K}\pi}^\nu + P_{\bar{K}\pi}^\mu \cdot \varepsilon^{\nu\tau\rho\sigma} P_{\bar{K}}^\tau P_\pi^\rho P_K^\sigma}{1 - ic_{3/2} \sqrt{-p_{\bar{K}\pi}^2/4}}$$

**K $\bar{K}$**

$$l_{K\bar{K}} = 1$$

$$L_\pi = 2$$

**p-wave scattering**

$$C_4^{2++1} = \frac{\varepsilon^{\mu\tau\rho\sigma} P_K^\tau P_{\bar{K}}^\rho P_\pi^\sigma \cdot \bar{P}_\pi^\nu + \bar{P}_\pi^\mu \cdot \varepsilon^{\nu\tau\rho\sigma} P_K^\tau P_{\bar{K}}^\rho P_\pi^\sigma}{1 - ib_1 \sqrt{-p_{K\bar{K}}^2/4}}$$

## References

- [1] L.Wolfenstein, *Ann. Rev. Nucl. and Part. Sci.* 36 (1986) 137.
- [2] F.Halzen and A.D.Martin, *Quarks and Leptons*, John Wiley and Sons Inc. 1984.
- [3] F.J.Gilman and Y.Nir, *Ann. Rev. Nucl. and Part. Sci.* 40 (1990) 213.
- [4] Review of Particle Properties, Particle Data Group, *Phys. Lett. B* 239 (1990).
- [5] E.D.Commins and P.H.Bucksbaum, *Weak Interactions of Leptons and Quarks*, Cambridge University Press 1983.
- [6] D.C.Cheng and G.K.O'Neill, *Elementary Particle Physics*, Addison-Wesley Publishing Company 1979.
- [7] K.Kleinknecht, *Ann. Rev. Nucl. Sci.* 26 (1976) 1.
- [8] T.Nakada, PSI-PR-91-02, 1991.
- [9] T.T.Wu and C.N.Yang, *Phys. Rev. Lett.* 13 (1964) 380.
- [10] CPLEAR Proposal, CERN/PSCC/85-6.
- [11] R.Adler et al., LEAP '90, Proc. First Biennial Conference on Low Energy Antiproton Physics, Stockholm, 1990, 414.
- [12] M.Dejardin, Ph.D. thesis, Universite de Paris 7 (1992).
- [13] A.Angelopoulos et al., *Nucl. Instrum. Methods A*311 (1992), 78.
- [14] P.Bloch et al., *Nucl. Instrum. Methods A*297 (1990), 126.
- [15] D.Tröster et al., *Nucl. Instrum. Methods A*279 (1989), 285.
- [16] L.Sacks (CPLEAR), AIP Conf. Proc. 243, "Interactions between particle and nuclear physics", Tucson, 1992, 408.
- [17] Ch.Witzig, Ph.D. thesis, ETH Zurich (1990).
- [18] F.Sauli, Principles of Operation of Multiwire Proportional and Drift Chambers, CERN-Report 77-09, 1977.
- [19] Ch.Bula, diploma thesis, ETH Zurich, unpublished, 1987.
- [20] Jan J.Tuma, *Handbook of physical Calculations*, McGraw-Hill Book Company, 1976.
- [21] R.Armenteros and B.French in "High Energy Physics" Vol. 4, p 237, Editor E.H.S.Burhop, Academic Press 1969.

- [22] T.Ruf, internal report, Geneva 1991.
- [23] T.Burwick, diploma thesis, ETH Zurich, unpublished, 1987.
- [24] N.Barash et al., Phys. Rev. 156 (1967) 1399.
- [25] M.Aguilar-Benitez et al., Phys. Rev. D 4 (1971) 2583.
- [26] M.Aguilar-Benitez et al., Nucl. Phys. B141 (1978) 101.
- [27] W.Celmaster, Phys. Rev. Lett. 37 (1976) 1042.
- [28] L.H.Chan, Phys. Rev. D 15 (1977) 2478.
- [29] N.Isgur, Phys. Rev. D 21 (1980) 779.
- [30] R.P.Bickerstaff and A.W.Thomas, Phys. Rev. D 25 (1982) 1869.
- [31] D.Flamm, F.Schöberl, H. Uematsu, Nuovo Cim. 98A (1987) 559.
- [32] J.L.Goity, W.S.Hou, PSI-PR-91-19, 1991, to be published in Phys. Lett. B.
- [33] J.Lee-Franzini et al. (CUSB Collaboration), Phys. Rev. Lett. 65 (1990) 2947.
- [34] P.Bloch, CPLEAR P8 Production Summary (CP/SW/034), Geneva 1991.
- [35] B.Conforto et al., Nucl. Phys. B3 (1967) 496.
- [36] M.Della Negra, Ph.D. thesis, University of Paris (1967).
- [37] CPLEAR Collab., R.Adler et al., Phys. Lett. B 267 (1991) 154.
- [38] J.M.Richard and M.E.Sainio, Phys. Lett. 110 B (1982) 349.
- [39] Ch.Zemach, Phys. Rev. 133 (1964) B1201.
- [40] M.Abramovich et al., Nucl. Phys. B20 (1970) 209.
- [41] Minuit, CERN Program Library entry D506, CERN, Geneva 1989.
- [42] W.T.Eadie, D.Drijard, F.E.James, M.Roos, B.Sadoulet, Statistical Methods in Experimental Physics, North-Holland Publishing Company, 1971.
- [43] V.Blobel, Formulae and Methods in experimental Data Evaluation, Vol. 3, Part I, p. I23, European Physical Society.
- [44] Geant 3, DD/EE 84-1, Data Handling Division, CERN, Geneva 1987.
- [45] CPLEAR Offline Group, CPGEANT User Manual, Geneva 1991.
- [46] R.L.Gluckstern, Nucl. Inst. and Meth. 24 (1963) 381.
- [47] A.Wagner, Physica Scripta 23 (1981) 446.

## List of Figures

2.1	The Wu-Yang triangle . . . . .	11
2.2	The expected asymmetry function $A_{\pi\pi}(t)$ . . . . .	14
2.3	Definition of the CPLEAR coordinate system . . . . .	16
2.4	Side view of the CPLEAR detector . . . . .	17
2.5	Transverse view of the CPLEAR detector . . . . .	20
2.6	Principle of the $p_T$ -cut logic . . . . .	25
3.1	Geometrical parameters of a multi wire proportional chamber . . . . .	27
3.2	Electrical potential and electric field strength for PC1 and PC2 . . . . .	29
3.3	Pulse height distribution on anode wires and cathode strips . . . . .	30
3.4	Transverse view of a chamber wall section . . . . .	31
3.5	Cut along the $z$ -axis through both chambers . . . . .	37
3.6	Preparation of a kapton foil . . . . .	38
3.7	Design for the anode and cathode print sector . . . . .	40
3.8	Support structure for the proportional chambers . . . . .	43
3.9	Sag of the proportional chambers . . . . .	44
3.10	Result of the stress test . . . . .	46
3.11	Readout chain for the proportional chamber wires . . . . .	47
3.12	Active gas volume defined by the mean free path for electron capture . . . . .	50
3.13	Track length in the active gas volume . . . . .	50
3.14	PC1 chamber current versus $p\bar{p}$ annihilation rate . . . . .	51
3.15	Experimental setup for the source test with the prototype chamber . . . . .	53
3.16	Experimental setup for the beam test . . . . .	54
3.17	Beam composition, as determined by time of flight measurement . . . . .	55
3.18	Anode wire efficiency curve for two gas mixtures . . . . .	56
3.19	Comparison between anode wire and cathode strip efficiencies . . . . .	57
3.20	Anode efficiency for "low" and "high" beam intensities . . . . .	58
3.21	Chamber inefficiency due to the wire support structure . . . . .	59
4.1	SU(3) octets for pseudoscalar and vector mesons . . . . .	62
4.2	Overview of experimental measurements and theoretical predictions of the $K^*$ mass difference . . . . .	64
4.3	Two different diagrams leading to three-body final states . . . . .	67
4.4	Missing momentum versus missing energy . . . . .	73
4.5	Missing mass and invariant mass distributions . . . . .	74
4.6	Fit of the invariant mass distribution . . . . .	74
4.7	Momentum spectra for the particles in "golden $\pi^+\pi^-$ " events . . . . .	75
4.8	Invariant mass squared distributions and the Dalitz-plot . . . . .	76
4.9	Invariant mass squared of a possible additional neutral particle . . . . .	79
4.10	Invariant mass squared distributions for charged tracks . . . . .	80
4.11	Projections of Dalitz-plot slices, indicating interference between the two $K^*$ bands . . . . .	81
4.12	Two-body decomposition of the three-body annihilation . . . . .	85
4.13	Explanation of the notation used for the spin-parity factors . . . . .	88

4.14	The coordinate system used in the simplified parameterization . . . . .	91
4.15	Comparison between two Breit-Wigner functions . . . . .	92
4.16	Original, smoothed and rebined acceptance histograms . . . . .	97
4.17	$K^*$ mass difference as obtained from least-squares fits . . . . .	100
4.18	Experimental and theoretical distributions in the Dalitz-plot . . . . .	103
4.19	Projections of Dalitz-plot slices for experimental and theoretical distributions . . . . .	104
4.20	Contributions of the six amplitudes to the density in the Dalitz-plot . .	105
4.21	Results for the resonance parameters . . . . .	107
4.22	Comparison between parabolic and MINOS errors . . . . .	112
4.23	Dependence of $\Delta m_{K^*}$ on the acceptance histogram . . . . .	115
4.24	Effect of a different Breit-Wigner function on the $K^*$ mass difference . .	116
4.25	Comparison with earlier measurements and theoretical predictions . . .	118
A.1	Distributions of $\hat{S}$ and the confidence level $CL(\hat{S})$ . . . . .	124
A.2	Residuals of the neutral kaon momentum . . . . .	125
A.3	Residuals of the invariante masses squared . . . . .	126
B.1	Flow diagram for the simplified simulation program . . . . .	130



## List of Tables

2.1	Expected precision for various CP violating and other parameters . . . .	16
2.2	Some physical parameters of the CPLEAR subdetectors . . . . .	20
2.3	The main stages of the CPLEAR trigger . . . . .	23
3.1	Electrostatic and gas amplification properties of PC1 and PC2 . . . . .	31
3.2	Geometrical parameters for PC1 and PC2 . . . . .	32
3.3	Different contributions to the surface density of a chamber . . . . .	35
3.4	Properties of the materials used in the construction of PC1 and PC2 . .	35
3.5	Gas amplification factors for different high voltage values . . . . .	51
3.6	Results of the PC alignment analysis . . . . .	60
4.1	Some recent theoretical predictions for the $K^*$ mass difference . . . . .	65
4.2	Quantum number assignments for $K^*(892)$ , $a_2(1320)$ and $a_0(980)$ . . . .	67
4.3	Decay modes of the $K^*$ and the $a_2$ mesons . . . . .	68
4.4	The KAON4T mini-DST's from run period 8 used in this analysis . . .	70
4.5	Data reduction due to the PREFILTER and the 5CFIT . . . . .	72
4.6	Reduction of background from $K_L^0$ decays . . . . .	78
4.7	Discrete symmetry eigenvalues of the initial $p\bar{p}$ states . . . . .	84
4.8	Symmetry properties of the transition matrix elements . . . . .	85
4.9	The spin-parity factors . . . . .	88
4.10	The form factors . . . . .	90
4.11	Order of the polynomials for the selected parameterizations . . . . .	94
4.12	Data reduction for the simulated data sample MCT233 . . . . .	96
4.13	Parameters for the standard and the alternative acceptance histograms	97
4.14	Some characteristic quantities for the least-squares fits . . . . .	99
4.15	Results for the $K^*$ mass difference obtained from least-squares fits . . .	101
4.16	Results for the $K^*$ resonance parameters . . . . .	106
4.17	The minimum statistical errors of the $K^*$ masses . . . . .	113
4.18	Correlation coefficients between $\Delta m_{K^*}$ and other parameters . . . . .	114
4.19	Dependence of $\Delta m_{K^*}$ on the acceptance histogram . . . . .	116
4.20	Effect of a different Breit-Wigner function on the resonance parameters	117
A.1	FWHM of the momentum residuals . . . . .	126
A.2	FWHM of the invariante mass squared residuals . . . . .	127

## Curriculum Vitae

- date of birth: November 7, 1961
- 1968 - 1974: Primarschule Birch in Seuzach, Switzerland
- 1974 - 1976: Sekundarschule Halden in Seuzach
- 1976 - 1980: Mathematisch Naturwissenschaftliches Gymnasium at the Kantonsschule im Lee, Winterthur, Switzerland
- 1981 - 1987: Physics study at the Eidgenössische Technische Hochschule (ETH) in Zürich, Switzerland.  
Gained diploma in experimental physics.
- 1987 - 1992: Ph. D. student in experimental particle physics at ETH, based at the Paul Scherrer Institute (PSI).

## Acknowledgments

This thesis would not have been possible without the assistance, encouragement and help from many people. Only some of them will be mentioned here, but no one is forgotten.

I am very grateful to Professor Dr. H.-J. Gerber for giving me the opportunity to accomplish this thesis and for his guidance and support in the last five years.

My special thanks go to Dr. Tatsuya Nakada and Peter-Raymond Kettle. Tatsuya, with his profound knowledge in elementary particle physics and his experience in data analysis, provided the necessary guidance in the physics analysis part of this work. Peter introduced me to the instrumental side of the experiment. With his knowledge in experimental techniques, he found solutions for many tricky problems that came up during the construction, installation and testing of the proportional chambers. Due to his optimism and humor, even the most desperate situations were endurable.

I would like to thank Nicolas Lordong and Sabine Heyer for their great help in the construction of the proportional chambers and for showing me that there is a way out of everyday life.

I am very thankful to Dr. Peter Weber for a careful reading of this manuscript and many suggested improvements, to Dr. Wulf Fetscher and Dr. Theodoros Karapiperis for many fruitful discussions, as well as to Rosa Bächli and Liz Furrer for their help in administration and L<sup>A</sup>T<sub>E</sub>X.

The hard work of the whole CPLEAR collaboration is gratefully acknowledged. In particular I want to mention Dr. Philippe Bloch who was always open for all kinds of questions and the people from the University of Ljubljana, especially Dr. Danilo Zavrtnik and Dr. Marko Mikuz, who provided me with the Monte Carlo data.

I also wish to express my appreciation to the PSI computing division for providing a smooth operation of the VAX cluster.

Finally, I want to thank my family, my parents and all my friends for their constant encouragement and support, their patience and all the fun we have together.

